UNIVERSITY OF SOUTHAMPTON

Faculty of Engineering and Physical Sciences
School of Engineering

The soluble lead flow battery: Numerical modelling for enhanced design of cell architecture

by

Ewan Joseph Fraser
MEng
ORCiD: 0000-0001-9592-9071

A thesis for the degree of
Doctor of Philosophy

April 2022

University of Southampton

Abstract

Faculty of Engineering and Physical Sciences
School of Engineering

Doctor of Philosophy

The soluble lead flow battery: Numerical modelling for enhanced design of cell architecture

by Ewan Joseph Fraser

This thesis describes a two-dimensional numerical model, based on the conservation of mass, charge, momentum and energy, and the main electrode reactions and a single simplified side reaction and their kinetics for the soluble lead flow battery (SLFB). The model is developed to include a change in morphology as solid deposits form at the electrode, on both flat planar electrodes and porous carbon foam electrodes, and to include a framework for modelling the anion-, cation-exchange membrane and separator divided SLFB along with a semi-empirical method to predict electrolyte conductivity at different electrolyte concentrations. All models are validated against experimental work presented in this thesis or from the literature.

The change in morphology on flat electrodes leads to a significant decrease in distance between the electrode surfaces causing a reduction in cell resistance and a decrease in volumetric electrolyte flow. This approach could be easily adapted for any battery with a metal/metal ion electrode reaction.

Anion exchange membranes were found to have a reduced potential drop at low states of charge but an increased potential drop at high states of charge when compared to cation exchange membranes. Porous separators were found to have an order of magnitude lower potential drops for separators of the same thickness. However, they do not provide any selectivity for electrolyte additives.

A method of manipulating computed tomography images of reticulated vitreous carbon electrodes (RVC), using a voxel dilation technique to simulate the deposition of Pb and PbO_2 at various states of charge are converted to homogeneous electrode domains for use in the numerical model of the SLFB. It is shown that the current distribution in the domain varies at different states of charge both perpendicular and parallel to the electrodes. However, adding a porous separator in place of a free electrolyte domain to divide the electrode domains mitigates this variation, especially along the length of the electrodes. An improved voltage efficiency of over 80 % is seen when RVC electrodes are used.

Contents

List of Figures ix

List of Tables xvii

List of Additional Material xix

Declaration of Authorship xxi

Acknowledgements xxiii

1 Introduction 1
- 1.1 Claims for Novelty . . . 1
- 1.2 Publications . . . 2
- 1.3 Background . . . 2
  - 1.3.1 Energy Storage . . . 4
- 1.4 Batteries . . . 9
  - 1.4.1 Primary Batteries . . . 10
  - 1.4.2 Secondary batteries . . . 11
- 1.5 Redox flow batteries . . . 13
- 1.6 Soluble lead flow battery . . . 19

2 Literature Review 23
- 2.1 History of Lead-based Batteries . . . 23
- 2.2 Electrolyte . . . 25
  - 2.2.1 Composition . . . 25
  - 2.2.2 Recycled electrolyte . . . 26
- 2.3 Deposits . . . 28
  - 2.3.1 Lead . . . 28
  - 2.3.2 Lead Dioxide . . . 30
- 2.4 Additives . . . 34
  - 2.4.1 Negative Electrode . . . 34
  - 2.4.2 Positive Electrode . . . 36
- 2.5 Performance . . . 36
- 2.6 Electrodes . . . 38
- 2.7 Electrochemical Theory . . . 40
  - 2.7.1 Definition of terms . . . 40
  - 2.7.2 Thermodynamics . . . 42
  - 2.7.3 Kinetics . . . 43

2.7.4 Mass transport 43
2.8 Modelling and Simulation 44
2.8.1 Battery modelling 44
2.8.2 Lead battery modelling 46
2.8.3 Flow battery modelling 48
2.8.3.1 Electrolyte flow 49
2.8.3.2 Laminar flow between plates 50
2.8.3.3 Flow in porous media 51
2.8.3.4 Conductivity 52
2.8.3.5 Porous electrodes 54
2.8.3.6 Membranes 54
2.8.3.7 Nernst-Planck-Poisson 55
2.8.3.8 Including Donnan potentials and electrolneutrality 56
2.8.3.9 Fully selective membrane 57
2.8.3.10 Deposition and dissolution 58
2.8.3.11 Soluble lead flow battery modelling 59
2.9 Engineering and Scale-up 64
2.10 Summary 67

3 Experimental setup **69**
3.1 100 cm^2 cell 70
3.2 10 cm^2 cell 72

4 Model setup **75**
4.1 Assumptions 79
4.2 Governing Equations 80
4.2.1 Free Electrolyte 81
4.2.1.1 Density 82
4.2.1.2 Viscosity 82
4.2.2 Solid Electrode 82
4.2.3 Porous Electrode 83
4.2.3.1 Electrolyte 83
4.2.3.2 Electrode 84
4.2.4 Membrane 85
4.3 Boundary Conditions 86
4.3.1 Inlet and Outlet 86
4.3.2 Kinetics 86
4.3.3 Electrodes 88
4.3.4 Membrane 88
4.4 Mesh Sensitivity 89

5 Moving Mesh **91**
5.1 Density, Conductivity and Viscosity 94
5.2 Parameters and Variables 94
5.2.1 Initial values 94
5.2.2 Parameters 95
5.3 Solver 95

5.4 Rate constant 97
5.5 Simulated cycling regime 98
5.6 Current distribution 107
5.7 Comparison with experimental results 112
5.8 Micro-Computed Tomography 114
5.9 Conclusions 118

6 Electrolyte Conductivity 119
6.1 Parameters 120
6.2 Conductivity Results 121
6.3 Summary 124

7 Modelling the divided soluble lead flow battery 125
7.1 Membrane 126
7.2 Two-dimensional model 126
7.3 Parameters 127
7.4 Microporous separator 127
7.5 Anion-exchange membrane 131
    7.5.1 Effect of current density 133
    7.5.2 Effect of porosity 134
    7.5.3 Effect of charge distribution 136
7.6 Cation-exchange membrane 137
    7.6.1 Effect of current density 138
    7.6.2 Effect of porosity 139
    7.6.3 Effect of charge distribution 140
7.7 Additive crossover 141
    7.7.1 Effect of additive valence 143
    7.7.2 Effect of additive diffusion coefficient 145
    7.7.3 Effect of additive concentration 146
    7.7.4 Effect of membrane charge distribution 147
7.8 Divided cell two-dimensional model 149
7.9 Summary 154

8 Image based modelling of porous RVC electrodes 155
8.1 Initial conditions 156
8.2 Parameters 157
8.3 Input data (computed tomography) 158
8.4 Results and Discussion 164
    8.4.1 Undivided cell 164
    8.4.2 Divided cell 172
8.5 Validation 178
8.6 Conclusions 179

9 Conclusions 181

10 Future work 183

Appendix A Justification of the soluble lead flow battery based on an existing lead supply chain 185
- Appendix A.1 Lead Recycling 185
  - Appendix A.1.1 Existing Process 186
    - Appendix A.1.1.1 Paste 186
    - Appendix A.1.1.2 Sulfuric acid from lead-acid batteries 186
    - Appendix A.1.1.3 Effluent Treatment 186
- Appendix A.2 Proposed Process 187
- Appendix A.3 Sulfate plant 187
- Appendix A.4 Electrolytic Leaching 188
- Appendix A.5 Electroplating Lead 188
- Appendix A.6 Summary 189

Appendix B Adaptive mesh vs moving mesh 191

Appendix C Mesh Sensitivity 193
- Appendix C.1 Moving mesh 194
- Appendix C.2 Static mesh 195
- Appendix C.3 Two-dimensional divided cell 196

Appendix D Gold 199
- Appendix D.1 Cell efficiencies 200
- Appendix D.2 Cell failure 203
- Appendix D.3 Economics 204
- Appendix D.4 Conclusions 207

References 209

List of Figures

1.1 Global electricity demand and generation mix by IEA scenario. Reproduced from IEA (2018) World Energy Outlook. All rights reserved. . . . 4
1.2 A simple example of a fictional demand profile and generation mix including baseload (orange), solar (green), wind (purple) and gas (yellow) without (A) and with (B) energy storage. The shaded area represents the difference between generation and demand facilitated by charging/discharging energy storage. 6
1.3 Comparison of required CCGT generation with (shown in red) and without (shown in black) storage for the same example demand profile used in previous figure. 7
1.4 Modified Ragone Plot comparing some of the key forms of electricity storage technologies. 8
1.5 Schematic of a typical two-electrolyte redox flow cell/battery. Positive (shown in red) and negative (shown in blue) electrolytes are contained in separate reservoirs and are circulated through cells which are divided by ion exchange membranes. 15
1.6 Representation of a single cell, two-electrolyte hybrid (type 2) flow battery. Positive (shown in red) and negative (shown in blue) electrolytes are contained in separate reservoirs and are circulated through cells which are divided by ion exchange membranes. A metal/metal oxide is deposited at one electrode. 16
1.7 Representation of a single cell, air-breathing (type 4) flow battery. A single electrolyte flows through one half of the cell. An air breathing electrode is used as the other half cell. The two half cells are separated by a divider. Metal my be deposited at the negative electrode. 17
1.8 Representation of a single cell soluble lead flow battery. A single electrolyte is circulated through an undivided cell. Solid deposits form at both electrodes during charge. 20

2.1 Cyclic voltammograms for the first and two hundredth cycle of the Pb^{2+}/Pb redox couple in 1.5 $mol\,dm^{-3}$ MSA on a glassy carbon electrode. A temperature of 295 K was maintained and the initial Pb^{2+} concentration was 10 $mol\,dm^{-3}$. 29
2.2 The effect of Pb^{2+} concentration on the morphology of Pb deposited at the negative electrode in an unstirred Hull cell for 2 hours. (a) and (b) show deposits from 0.5 $mol\,dm^{-3}$ Pb^{2+}, 1.0 $mol\,dm^{-3}$ MSA and 5 $mmol\,dm^{-3}$ HDTMA. (c) and (d) show deposits from 1.5 $mol\,dm^{-3}$ Pb^{2+}, 1.0 $mol\,dm^{-3}$ MSA and 5 $mmol\,dm^{-3}$ HDTMA. 30

2.3 The effect of H^+ concentration on the morphology of Pb deposited at the negative electrode in an unstirred Hull cell for 2 hours. (a) and (b) show deposits from 0.3 mol dm^{-3} Pb^{2+}, 1.0 mol dm^{-3} MSA and 5 mmol dm^{-3} HDTMA. (c) and (d) show deposits from 0.3 mol dm^{-3} Pb^{2+}, 2.4 mol dm^{-3} MSA and 5 mmol dm^{-3} HDTMA 31

2.4 Cyclic voltammograms for the first (A), fifth (B), twenty fifth (C), fiftieth (D), seventy fifth (E) and hundredth (F) cycle of the $Pb^{2+}/Pb)_2$ redox couple in 1.5 mol dm^{-3} MSA and 0.5 mol dm^{-3} Pb^{2+} on a glassy carbon electrode. 32

2.5 The effect of H^+ concentration on the morphology of PbO_2 deposited at the positive electrode in an unstirred Hull cell for 2 hours at current densities of 20 mA cm^{-2} ((a) and (c)) and 50 mA cm^{-2} ((b) and (d)). (a) and (b) show deposits from 1.5 mol dm^{-3} Pb^{2+}, 0.15 mol dm^{-3} MSA and 5 mmol dm^{-3} HDTMA. (c) and (d) show deposits from 1.5 mol dm^{-3} Pb^{2+}, 1.5 mol dm^{-3} MSA and 5 mmol dm^{-3} HDTMA. 33

2.6 Schematics of cells used by Pletcher et al. 35

2.7 Example of 3D electrodes used by Banerjee et al. in the SLFB. The negative electrode shown is a 30 ppi reticulated vitreous carbon electrode and the positive electrode is a corrugated graphite plate. 39

2.8 A typical electrochemical device. At the cathode, the active species A is reduced from a higher to a lower valence (n+ to (n-1)+) by the addition of an electron from the cathode. The active species B is oxidised to a higher valence (m+ to (m+1)+) liberating an electron which is collected by the anode. 41

2.9 Classification of battery modelling over a range of length scales. 45

2.10 Validation of the numerical model by Shah et al. Experimental and simulated charge-discharge curves at varying current densities (10, 20 and 30 mA cm^{-2}. 61

2.11 Validation of the numerical model by Nandanwar and Kumar. Experimental and simulated charge-discharge curves with and without a constraint on the availability of deposits at the electrodes. An average current density of 20 mA cm^{-2} was used. 62

2.12 Validation of the numerical model by Bates et al. Experimental and simulated charge-discharge curves at a current density of 15 mA cm^{-2}. Simulated results at 10, 20 and 25 mA cm^{-2} are also included. 63

2.13 Validation of the numerical model by Oury et al. Experimental charge-discharge curves are compared with the simulation results over 6 cycles. An average current density of 10 mA cm^{-2} was used. 63

3.1 Flow field of 100 cm^2 flow cell. Electrolyte flows in via the inlet at the bottom of the frame, then from bottom to top of the electrode area and out via the outlet at the top of the frame. Manifolds allow electrolyte to pass through to the opposite flow field. 71

3.2 Schematic showing a cross-section of the 100 cm^2 flow cell. components from outside to centre: Steel endplates, PEEK outer frames, current collectors, electrodes, PEEK inner frames, gasket. 72

3.3 Schematic showing a cross-section of the 10 cm^2 flow cell. Components from outside to centre: Steel endplates, hard norprene insulating gaskets, current collectors, electrodes, silicone gaskets, acrylic flow field. 73

3.4 Exploded view of 10 cm^2 flow cell. 74

4.1 Schematic showing the general geometry, including domains and boundaries used in simulations. Where electrode domains are included, these are described in the relevant chapter. 77
4.2 Maximum local current density magnitude (solid lines) and computational time (dashed lines) recorded with when number of elements are varied for the divided SLFB with RVC electrodes model. 90

5.1 Geometry as it changes from clean electrodes (left) to electrodes with deposits combined into a single solid domain at each electrode (right). G_{ie} is the inter-electrode gap, d_{ep} and d_{en} are the positive and negative solid domain thicknesses respectively. Subscript 0 represents before cycling, c represents after charging and d after discharging. 93
5.2 A snapshot of the mesh used for all simulations. The full mesh is shown on the left and a zoomed section is shown on the right. The mesh shown is at t = 0 93
5.3 A simple flowchart describing the process taken by the solver, where U^i is the dependent variable for each equation $f(U^i)$ for iteration i at time t. 96
5.4 Simulated cell potential vs time of the second charged cycle at 20 mA cm^{-2} with a varied forward rate constant, $k_{0f,PbO}$, for the side reaction from 2 to 2×10^{-6} mol m^2 s^{-1}. 97
5.5 A simulated cell voltage vs time at 20 mA cm^{-2} using a moving mesh. Two charge-discharge cycles are simulated each with a 24 hour charge, a 2 minute rest at open circuit and a discharge to 1.2 V. The two-step charging mechanism is included in the second charge. 99
5.6 Simulated cell voltage vs time for one cycle a for static (red dashed line) and moving (black solid line) meshes at 20 (A) and 30 (B) mA cm^{-2}. Inset is zoomed into the region at the end of charge. 100
5.7 Cell and electrolyte resistance vs time for static and moving mesh simulations. The cell resistance includes the resistance of the electrolyte deposits and the carbon electrode. Both resistances are measured across the electrolyte inlet. The cell was run at 20 mA cm^{-2}. Charging is shown with a red dotted background and discharge with a blue striped background. . 102
5.8 Concentration profiles of the SLFB with and without a simulated change in geometry. A current density of 20 mA cm^{-2} is used. 103
5.9 Progression of the moving mesh from clean electrodes (a) to 1 charge (b) then 1 discharge (c), 2 charges (d) and 2 discharges (e). The negative electrode is on the left side of each cell and the positive electrode is on the right. 104
5.10 Simulated volumetric flow rate vs time of the cell cycled at 20 mA cm^{-3} for both the static mesh (dashed line) and the moving mesh (solid line). 105
5.11 Simulated velocity profile of the electrolyte before the first charge, after the first charge and after the first discharge. 106
5.12 Simulated current density along the y-direction of the electrodes. Y=0 is at the inlet. 108
5.13 Simulated equilibrium potential during charge (solid black line) and discharge (dashed red line) along the y-direction of the electrodes. Y=0 is at the inlet. 109

5.14 Simulated overpotential along the y-direction of the electrodes. Y=0 is at the inlet. 110
5.15 Simulated concentration in the y-direction of the electrodes during charge (solid black line) and discharge (red dashed line). Y=0 is at the inlet. . . 111
5.16 A comparison of simulated cell potential (solid black line) using a moving mesh during the second charge with average values seen in the literature (dashed red line) and experimentally measured cell potential (dotted green line) for the second charge-discharge cycle at a constant current density of 20 mA cm^{-2}. 114
5.17 Reconstructions of CT scans of deposits over the first three cycles in a static electrolyte cell with 2 cm × 4 cm electrodes. 115
5.18 Voltage time curve of the divided static electrolyte cell. 116
5.19 Reconstruction of the CT scan after the second charge. The left deposit (negative electrode) has largely separated from the electrode surface. . . 117

6.1 Simulated (red dashed line) and experimental (solid black line) electrolyte conductivity vs concentration of Pb^{2+} and H^+ ions. 123
6.2 Bulk conductivity calculated using the modified method vs electrolyte state of charge. The starting concentrations are 0.7 mol dm^{-3} Pb^{2+} and 1.0 mol dm^{-3} H^+. 124

7.1 Experimental (red dashed line) and simulated potential drop mimicking the experimental technique (black solid line) an simulated potential drop measured directly (black dotted line) across an FF60 microporous separator. A current density of 171 mA cm^{-2} is used. 129
7.2 Simulated potential drop across a porous separator with varied porosity at different simulated electrolyte states of charge: $[Pb^{2+}]$=1 mol m^{-3} & $[H^+]$ = 2398 mol m^{-3} (black solid line), $[Pb^{2+}]$ = 230 mol m^{-3} & $[H^+]$ = 1940 mol m^{-3} (red dashed line), $[Pb^{2+}]$ = 460 mol m^{-3} & $[H^+]$ = 1480 mol m^{-3} (blue dotted line) and $[Pb^{2+}]$ = 700 mol m^{-3} & $[H^+]$ = 1000 mol m^{-3} (green dot-dashed line). 130
7.3 Simulated potential drop across a porous separator with varied thickness at different simulated electrolyte states of charge: $[Pb^{2+}]$ = 1 mol m^{-3} & $[H^+]$ = 2398 mol m^{-3} (black solid line), $[Pb^{2+}]$ = 230 mol m^{-3} & $[H^+]$ = 1940 mol m^{-3} (red dashed line), $[Pb^{2+}]$ = 460 mol m^{-3} & $[H^+]$ = 1480 mol m^{-3} (blue dotted line) and $[Pb^{2+}]$ = 700 mol m^{-3} & $[H^+]$ = 1000 mol m^{-3} (green dot-dashed line). 131
7.4 Experimental (red dashed line) and simulated potential drop mimicking the experimental technique (black solid line) an simulated potential drop measured directly (black dotted line) across an FAP-450 anion-exchange membrane. A current density of 171 mA cm^{-2} is used. 132
7.5 Simulated potential drop across an anion-exchange membrane with varied current density at different simulated electrolyte states of charge: $[Pb^{2+}]$ = 1 mol m^{-3} & $[H^+]$ = 2398 mol m^{-3} (black solid line), $[Pb^{2+}]$ = 230 mol m^{-3} & $[H^+]$ = 1940 mol m^{-3} (red dashed line), $[Pb^{2+}]$ = 460 mol m^{-3} & $[H^+]$ = 1480 mol m^{-3} (blue dotted line) and $[Pb^{2+}]$ = 700 mol m^{-3} & $[H^+]$ = 1000 mol m^{-3} (green dot-dashed line). 133

7.6 Simulated potential drop across an anion-exchange membrane with varied membrane porosity at different simulated electrolyte states of charge: $[Pb^{2+}]$ = 1 mol m^{-3} & $[H^{+}]$ = 2398 mol m^{-3} (black solid line), $[Pb^{2+}]$ = 230 mol m^{-3} & $[H^{+}]$ = 1940 mol m^{-3} (red dashed line), $[Pb^{2+}]$ = 460 mol m^{-3} & $[H^{+}]$ = 1480 mol m^{-3} (blue dotted line) and $[Pb^{2+}]$ = 700 mol m^{-3} & $[H^{+}]$ = 1000 mol m^{-3} (green dot-dashed line). 135

7.7 Simulated potential drop across an anion-exchange membrane with varied fixed charge concentration at different simulated electrolyte states of charge: $[Pb^{2+}]$ = 1 mol m^{-3} & $[H^{+}]$ = 2398 mol m^{-3} (black solid line), $[Pb^{2+}]$ = 230 mol m^{-3} & $[H^{+}]$ = 1940 mol m^{-3} (red dashed line), $[Pb^{2+}]$ = 460 mol m^{-3} & $[H^{+}]$ = 1480 mol m^{-3} (blue dotted line) and $[Pb^{2+}]$ = 700 mol m^{-3} & $[H^{+}]$ = 1000 mol m^{-3} (green dot-dashed line). 136

7.8 Experimental (red dashed line) and simulated potential drop mimicking the experimental technique (black solid line) an simulated potential drop measured directly (black dotted line) across a Nafion 115 membrane. A current density of 171 mA cm^{-2} is used. 137

7.9 Simulated electrolyte potential using a reference of 0 V at the maximum value for X. Values for electrolyte simulating 100 % (solid black line), 66 % (red short dashed line), 33 % (green dashed line) and 0 % (blue long dashed line) Pb^{2+} utilisation are included. 138

7.10 Simulated potential drop across an cation-exchange membrane with varied current density at different simulated electrolyte states of charge: $[Pb^{2+}]$ = 1 mol m^{-3} & $[H^{+}]$ = 2398 mol m^{-3} (black solid line), $[Pb^{2+}]$ = 230 mol m^{-3} & $[H^{+}]$ = 1940 mol m^{-3} (red dashed line), $[Pb^{2+}]$ = 460 mol m^{-3} & $[H^{+}]$ = 1480 mol m^{-3} (blue dotted line) and $[Pb^{2+}]$ = 700 mol m^{-3} & $[H^{+}]$ = 1000 mol m^{-3} (green dot-dashed line). 139

7.11 Simulated potential drop across an anion-exchange membrane with varied membrane porosity at different simulated electrolyte states of charge: $[Pb^{2+}]$ = 1 mol m^{-3} & $[H^{+}]$ = 2398 mol m^{-3} (black solid line), $[Pb^{2+}]$ = 230 mol m^{-3} & $[H^{+}]$ = 1940 mol m^{-3} (red dashed line), $[Pb^{2+}]$ = 460 mol m^{-3} & $[H^{+}]$ = 1480 mol m^{-3} (blue dotted line) and $[Pb^{2+}]$ = 700 mol m^{-3} & $[H^{+}]$ = 1000 mol m^{-3} (green dot-dashed line). 140

7.12 Simulated potential drop across an anion-exchange membrane with varied fixed charge concentration at different simulated electrolyte states of charge: $[Pb^{2+}]$ = 1 mol m^{-3} & $[H^{+}]$ = 2398 mol m^{-3} (black solid line), $[Pb^{2+}]$ = 230 mol m^{-3} & $[H^{+}]$ = 1940 mol m^{-3} (red dashed line), $[Pb^{2+}]$ = 460 mol m^{-3} & $[H^{+}]$ = 1480 mol m^{-3} (blue dotted line) and $[Pb^{2+}]$ = 700 mol m^{-3} & $[H^{+}]$ = 1000 mol m^{-3} (green dot-dashed line). 141

7.13 Simulated flux of additive through the membrane vs valence of the additive ion at different simulated stated of charge: $[Pb^{2+}]$ = 1 mol m^{-3} & $[H^{+}]$ = 2398 mol m^{-3} (black solid line), $[Pb^{2+}]$ = 230 mol m^{-3} & $[H^{+}]$ = 1940 mol m^{-3} (red dashed line), $[Pb^{2+}]$ = 460 mol m^{-3} & $[H^{+}]$ = 1480 mol m^{-3} (blue dotted line) and $[Pb^{2+}]$ = 700 mol m^{-3} & $[H^{+}]$ = 1000 mol m^{-3} (green dot-dashed line). 144

7.14 Simulated flux of additive through the membrane vs diffusion coefficient of the additive ion at different simulated stated of charge: [Pb^{2+}] = 1 mol m^{-3} & [H^+] = 2398 mol m^{-3} (black solid line), [Pb^{2+}] = 230 mol m^{-3} & [H^+] = 1940 mol m^{-3} (red dashed line), [Pb^{2+}] = 460 mol m^{-3} & [H^+] = 1480 mol m^{-3} (blue dotted line) and [Pb^{2+}] = 700 mol m^{-3} & [H^+] = 1000 mol m^{-3} (green dot-dashed line). 146

7.15 Simulated flux of additive through the membrane vs concentration of the additive ion at different simulated states of charge: [Pb^{2+}] = 1 mol m^{-3} & [H^+] = 2398 mol m^{-3} (black solid line), [Pb^{2+}] = 230 mol m^{-3} & [H^+] = 1940 mol m^{-3} (red dashed line), [Pb^{2+}] = 460 mol m^{-3} & [H^+] = 1480 mol m^{-3} (blue dotted line) and [Pb^{2+}] = 700 mol m^{-3} & [H^+] = 1000 mol m^{-3} (green dot-dashed line). 147

7.16 Simulated flux of additive through the membrane vs fixed charge concentration in the membrane at different simulate states of charge: [Pb^{2+}] = 1 mol m^{-3} & [H^+] = 2398 mol m^{-3} (black solid line), [Pb^{2+}] = 230 mol m^{-3} & [H^+] = 1940 mol m^{-3} (red dashed line), [Pb^{2+}] = 460 mol m^{-3} & [H^+] = 1480 mol m^{-3} (blue dotted line) and [Pb^{2+}] = 700 mol m^{-3} & [H^+] = 1000 mol m^{-3} (green dot-dashed line). A negative fixed charge represents a cation exchange membrane and a positive fixed charge represents an anion exchange membrane. 149

7.17 Simulated concentration profiles for each species, $CH_3SO_3^-$ (black solid line), H^+ (red dotted line) and Pb^{2+} (blue dashed line), over the width of the cell with an applied current density of 50 mA cm^{-2}. A spike/trough in each of the species is seen in the membrane. The negative electrode region is shaded in blue, the positive electrode region is shaded in red and the membrane is shaded in grey. 151

7.18 Simulated electrolyte potential distribution across the midpoint of the cell at 10 mA cm^{-2} (solid black line), 20 mA cm^{-2} (dotted red line), 30 mA cm^{-2} (dashed blue line), and 50 mA cm^{-2} (dot-dashed green line). The negative electrode region is shaded in blue, the positive electrode region is shaded in red and the membrane is shaded in grey. 152

8.1 Images from CT data of 30 ppi RVC, thresholded into RVC and electrolyte, with further voxel dilation to form artificial deposit phases. The original RVC dataset is dilated by 1 voxel, then to a total solid volume fraction of 10 %, 20 %, 30 %, 50 % and 80 %. Pore space (electrolyte) is shown in black, RVC in grey and deposit in white. 159

8.2 A comparison of different methods for estimating a porous electrode surface area: A solid sphere in a liquid matrix (blue dot-dot-dashed line), a liquid sphere in a solid matrix (red dashed line), a solid cylinder in a liquid matrix (green dotted line), a liquid cylinder in a solid matrix (dark blue dot dashed line) and a CT estimate based on a scan of 80 ppi RVC (black solid line). 163

8.3 Schematic showing the geometries used to model the SLFB with porous electrodes. 164

8.4 Simulated velocity profile across the mid-height of the electrodes of the undivided cell using 10 ppi RVC and an applied current density of 20 mA cm^{-2} at time=50 s(solid black line), time=3600 s (red dashed line) and time=7320 s (blue dotted line). The negative (left, blue) and positive (right, red) electrodes domains are highlighted. 165

8.5 Simulated current distribution in the x-direction at the mid height of the electrodes for the undivided configuration of the 10 ppi electrodes with an applied current density of 20 mA cm^{-2}. The negative (left, blue) and positive (right, red) electrodes domains are highlighted. 167
8.6 Simulated current distribution in the y-direction taken as a slice at the midpoint of the electrode domains for the 10 ppi electrodes. y=0 is at the inlet at the bottom of the cell. In both electrodes there is a significantly increased current density in the first 1 cm of the domain. Current density varies with time as the current is not even in the x-direction. 168
8.7 Simulated velocity distribution in the y-direction at the midpoint of the 10 ppi electrodes. The velocity begins at over 1 cm s^{-1} near the inlet in both electrodes, but rapidly reduces with increased distance from the inlet. The change in velocity levels off after approximately 4 cm and remains relatively constant between 1.5 and 3 mm s^{-1} in both electrodes. 169
8.8 Simulated Pb^{2+} concentration distribution near the end of the first charge for the 50 mA cm^{-2} cell using 10 ppi electrodes. The entire simulated domain (x-y plane) is shown. Red shows a higher concentration and blue shows a low concentration. 171
8.9 Simulated distribution of Pb^{2+} concentration in the x-direction at the mid height of the electrodes for the undivided configuration of the 10 ppi electrodes with an applied current density of 20 mA cm^{-2}. The negative (left, blue) and positive (right, red) electrodes domains are highlighted. . 172
8.10 Simulated current density distribution in the y-direction at the midpoint of the electrodes of the divided cell during the first charge. 174
8.11 Simulated current distribution in the x-direction at the mid height of the electrodes for the divided configuration of the 10 ppi electrodes with an applied current density of 20 mA cm^{-2}. The negative (left, blue) and positive (right, red) electrodes domains are highlighted. 175
8.12 Simulated Pb^{2+} concentration distribution in the x-direction at the mid height of the electrodes for the divided configuration of the 10 ppi electrodes with an applied current density of 20 mA cm^{-2}. The negative (left, blue) and positive (right, red) electrodes domains are highlighted. 176
8.13 Simulated current distribution in the x-direction at the mid height of the electrodes for the divided configuration with an applied current density of 20 mA cm^{-2}. The negative (left, blue) and positive (right, red) electrodes domains are highlighted. 177
8.14 Simulated cell potential vs time for different grades of RVC with an applied current density of 20 mA cm^{-2}. 178
8.15 Cell potential from the experimental and simulated 10 cm^{-2} cells. The cells were divided and used 80 ppi RVC electrodes. 179

Appendix A.1 Proposed process for electrochemically recovering lead from spent lead acid batteries. 187

Appendix B.1 Comparison of meshes from simulations using a moving mesh and an adaptive mesh. The times shown are t=0, after a charge step and after a subsequent discharge step. The simulations ran for 24 hours at 20 mA cm^{-2}. 192

Appendix C.1 An example mesh showing elements in each dimension. A full mesh is shown on the left and a zoomed region to highlight the boundary layer elements is shown on the right. In this example, there are 5 horizontal elements, 20 vertical elements, 5 boundary layer elements and a growth factor of 1.3. 194
Appendix C.2 Maximum local current density magnitude (solid lines) and computational time (dashed lines) recorded with when number of elements are varied for the moving mesh model. 195
Appendix C.3 Maximum local current density magnitude (solid lines) and computational time (dashed lines) recorded with when number of elements are varied for the static mesh model. 196
Appendix C.4 Maximum local current density magnitude (solid lines) and computational time (dashed lines) recorded with when number of elements are varied for the SLFB with two-dimensional divided model. . . 197

Appendix D.1 Charge, voltage and energy efficiencies for each cycle of cells charged at 10 mA cm^{-2} for 15 minutes and discharged to 0.3 V. 201
Appendix D.2 Charge, voltage and energy efficiencies for each cycle of cells using gold leaf plated carbon-polymer electrodes at single electrode only. Cells were charged at 10 mA cm^{-2} for 15 minutes and discharged to 0.3 V 202
Appendix D.3 Cell potential vs time for the three cycles post failure. 203
Appendix D.4 Proportion of cell cost by material using current and a future prediction for the cost of Nafion 206

List of Tables

1.1 Summary of proposed RFB chemistries 18

3.1 Summary of chemicals used to produce electrolyte for experimental work. 69

5.1 Initial values of parameters used in the model. 95
5.2 Summary of parameters used in all simulations. 95

6.1 Parameters for conductivity simulations 121

7.1 Default values for parameters used in the simulations of the divided soluble lead flow battery 127
7.2 Concentrations at simulated states of charge. 128
7.3 Default values of parameters used in for simulating an anion exchange membrane. 132
7.4 Default values of parameters used in for simulating additive crossover in a membrane divided SLFB. 142
7.5 Breakdown of potential drop across the membrane during charge and discharge. Current densities of 10, 20, 30 and 50 mA cm^{-2} are used. . . . 153

8.1 Initial conditions used for modelling three dimensional electrodes 157
8.2 Parameters used for modelling three dimensional electrodes 158

List of Additional Material

Dataset for PhD thesis ″The soluble lead flow battery: Numerical modelling for enhanced design of cell architecture″ DOI: 10.5258/SOTON/D2183

Declaration of Authorship

I declare that this thesis and the work presented in it is my own and has been generated by me as the result of my own original research.

I confirm that:

1. This work was done wholly or mainly while in candidature for a research degree at this University;
2. Where any part of this thesis has previously been submitted for a degree or any other qualification at this University or any other institution, this has been clearly stated;
3. Where I have consulted the published work of others, this is always clearly attributed;
4. Where I have quoted from the work of others, the source is always given. With the exception of such quotations, this thesis is entirely my own work;
5. I have acknowledged all main sources of help;
6. Where the thesis is based on work done by myself jointly with others, I have made clear exactly what was done by others and what I have contributed myself;
7. Parts of this work have been published as:
    - E. J. Fraser, R. G. Wills, and A. J. Cruden, "The use of gold impregnated carbon-polymer electrodes with the soluble lead flow battery," *Energy Reports*, vol. 6, pp. 19–24, 2020
    - E. J. Fraser, K. R. Dinesh, and R. Wills, "Development of a two-dimensional, moving mesh treatment for modelling the reaction chamber of the soluble lead flow battery as a function of state of charge for Pb and PbO_2 deposition and dissolution," *Journal of Energy Storage*, vol. 31, p. 101484, 2020

- E. Fraser, K. Ranga Dinesh, and R. Wills, "A two dimensional numerical model of the membrane-divided soluble lead flow battery," *Energy Reports*, vol. 7, pp. 49–55, 2021, sI: 5th AC-CDTESA

Signed:.. Date:..................

Acknowledgements

Firstly, my thanks must go to my supervisor Dr Richard Wills for supporting me over the last few years. Your enthusiasm and optimism often renewed my confidence and motivation for my work. Your door was always open when I needed to pick your brain.

They must also go to Prof Andy Cruden, your encouragement and pearls of wisdom in the fundamentals of research, especially when I first started have been most valuable.

Dr Ranga Dinesh Kahanda Koralage, thank you for the time you spent with me and the effort you put into helping me to get to grips with numerical modelling.

Dr Mohamed Torbati, thank you for the opportunities you have given me to develop my skills around my research. Dr Richard Boardman, Dr Keletso Orapeleng and Dr Luis Fernando Arenas, I am grateful for your help with gathering and interpreting imaging data.

Prof Carlos Ponce de Leon, I'd like to thank you for sparking my interest in energy storage during my undergraduate individual project and for continuing to help me around the lab. I'd also like to thank Prof Frank Walsh and Dr Muthu Krishna for your guidance and for the opportunity to collaborate with you so soon after starting my research.

To all those from the CDT, thank you. To those who taught me in the first year for giving me a solid grounding and knowledge of a wide area on which to build with my research. Sharon and Tracey, your hard work in keeping things running smoothly and in creating and maintaining a community to be a part of is greatly appreciated. To the students of the CDT, past and present your friendship has been invaluable. Tom, George, Alex and Hannes, you showed me the route ahead. Andreas, you always seemed to have the right tool for the job and Harriet your trinkets of knowledge from your experimental experience have been a great help, and thank you to you both for making the first year of the CDT such an enjoyable experience. Ben, our chats, in and out of the office, and impromptu phone calls were always a pleasure. Nick, you made the office an enjoyable place to be and your knowledge of the university has proved useful on more than one occasion. To James, especially, thank you. You've been there every step of the way; to go through this process together has been a pleasure.

Robin Idle and all those at HJ Enthoven & Sons., thank you for offering me a placement and for making me feel welcome during the time I spent with you.

To my friends, especially James, Joe, Luke, Michael, Alex C, Hugh, Ali and Emmo, thank you for leaving me be when I needed to work and for keeping me entertained when I didn't.

Helmi, thank you for your companionship, all the cups of tea and for keeping me going even with the task of writing looming. It has helped enormously.

Finally, to my family, thank you for the experiences that got me here in the first place, all the phone calls and messages, the opportunity to relax when at home and your interest and encouragement in whatever I have chosen to do.

Nomenclature

Abbreviations

2D	Two-dimensional
3D	Three-dimensional
AGM	Absorbent Glass Mat
ARPA-e	Advanced Research Projects Agency–Energy
BDF	Backward Differentiation Formula
BMS	Battery Management System
CAES	Compressed Air Energy Storage
CCGT	Combined Cycle Gas Turbine
CFD	Computational Fluid Dynamics
CT	Computed Tomography
DECC	Department of Energy and Climate Change
DFT	Density Function Theory
DoD	Depth of Discharge
DoE	Department of Energy
DTI	Department of Trade and Industry
EC	European Comission
EDTA	Ethylenediaminetetraacetic acid

EEC	Equivalent Electrical Circuit
EV	Electric Vehicle
FEA	Dinite Element Analysis
GB	Great Britain
HDTMA	Hexadecyl Trimethyl Ammonium Hydroxide
LAB	Lead Acid Battery
LBM	Lattice-Boltzmann Method
MSA	Methanesulfonic Acid
MUMPS	Multifrontal Massively Parallel Sparse Solver
NASA	National Aeronautics and Space Administration
NPP	Nernst-Planck-Poisson
PEEK	Polyether ether ketone
PEM	Proton Exchange Membrane
PHS	Pumped Hydro Energy Storage
ppi	Pores per Inch
PVDF	Polyvinylidene Difluoride
RFB	Redox Flow Battery
RVC	Reticulated Vitreous Carbon
SEM	Scanning Electron Microscope
SHE	Standard Hydrogen Electrode
SLFB	Soluble Lead Flow Battery
SMES	Superconducting Mangentic Energy Storage
SoC	State of Charge
SoH	State of Health

UPS	Uninterruptible Power Supply	
VRB	Vanadium Redox Flow Battery	
VRLAB	Valve Regulated Lead Acid Battery	
ZBFB	Zinc Bromine Flow Battery	

Symbols

α	Correction exponent	
δ	Empirical Constant	
ϵ	Permittivity	$\mathrm{F\,m^{-1}}$
η	Overpotential	V
γ	Activity Coefficient	
γ_{corr}	Correction Factor	
Λ	Molar Conductivity	$\mathrm{S\,m^{2}\,mol^{-1}}$
μ	Dynamic Viscosity	Pa s
$\overline{\mu_i}$	Electrochemical potential	V
ϕ	Domain Potential	V
ρ	Density	$\mathrm{kg\,m^{-3}}$
ρ_c	Charge Density	$\mathrm{C\,m^{-3}}$
σ	Conductivity	$\mathrm{S\,m^{-1}}$
τ	Tortuosity of Porous Domain	
ε	Volume Fraction of Porous Media	

A	Empirical Constant	$\mathrm{mol^{0.5}\,m^{-1.5}}$
a	Transfer Coefficient	
a_0	Empirical Constant	

A_e	Electrode Area	m^2
a_v	Volumetric Surface Area of Porous Electrode	m^{-1}
B	Empirical Constant	$mol^{0.5}\,m^{-1.5}$
c	Concentration	$mol\,m^{-3}$
D	Diffusion Coefficient	$m^2\,s^{-1}$
d	Deposit Thickness	m
E	Potential	V
F	Faraday's Constant	$C\,mol^{-1}$
G_{ie}	Inter-electrode Gap	m
I	Ionic Strength	$mol\,m^{-3}$
i	Current Density	$A\,m^{-2}$
IR	Ohmic Voltage Drop	V
K	Hydraulic Permeability	m^{-2}
k	Rate Constant	$m\,s^{-1}$
L	Length	m
M	Molar Mass	$kg\,mol^{-1}$
N_A	Avogadro's Number	
p	Pressure	Pa
Q	Reaction Quotient	
q	Charge	C
R	Gas Constant	$J\,K^{-1}mol^{-1}$
r	Radius	m
Re	Reynold's Number	
S	Surface Area	m^2

T	Temperature	K
t	time	s
u	x-component of Velocity	$\mathrm{m\,s^{-1}}$
u_m	Mobility	$\mathrm{s\,mol\,kg^{-1}}$
V	Volume	$\mathrm{m^3}$
v	y-component of Velocity	$\mathrm{m\,s^{-1}}$
W	Work Done	J
x	Distance in the x-direction	m
x_A	Ion Atmosphere Thickness	m
y	Distance in the y-direction	m
z	Valence	

$\mathbf{N}$	Molar Flux	$\mathrm{mol\,m^{-2}\,s^{-1}}$
$\mathbf{n}$	Normal Vector	
$\mathbf{u}$	Fluid Velocity	$\mathrm{m\,s^{-1}}$

Subscripts

$+$	Positive Value
0	Initial Value
b	Backward Reaction
c	During Charge
$cell$	Relating to a Full Cell
d	During Discharge
eff	Effective value, corrected for use in a porous domain
eq	At Equilibrium

f	Forward Reaction
fix	Relating to a Fixed Charge in a Membrane
H^+	Relating to a proton
i	Species in Electrolyte. Pb^{2+}, H^+ and $CH_3SO_3^-$
l	Relating to the Liquid or Electrolyte Domain
mob	Relating to a Mobile Charge
neg	Relating to the Negative Reaction
o	Oxidation
p	Particle
Pb	Relating to the Negative Reaction or Electrode
Pb^{2+}	Relating to the ion Pb^{2+}
PbO	Relating to PbO or the Side Reaction
PbO_2	Relating to the Positive Reaction or Electrode
pos	Relating to the Positive Reaction
r	Relating to Reduction
ref	Reference Value
s	Relating to the Solid or Electrode Domain
-	Negative Value

Chapter 1

Introduction

1.1 Claims for Novelty

Novel Contributions	**Associated Chapter**	**Associated Publication**
The use of a moving mesh technique to model the deposit formation in the soluble lead flow battery.	Chapter 5	E. J. Fraser, K. R. Dinesh, and R. Wills, "Development of a two-dimensional, moving mesh treatment for modelling the reaction chamber of the soluble lead flow battery as a function of state of charge for Pb and PbO_2 deposition and dissolution," *Journal of Energy Storage*, vol. 31, p. 101484, 2020
Development of a model to compare the requirements of separators in the soluble lead flow battery.	Chapter 7	E. Fraser, K. Ranga Dinesh, and R. Wills, "A two dimensional numerical model of the membrane-divided soluble lead flow battery," *Energy Reports*, vol. 7, pp. 49–55, 2021, sI: 5th AC-CDTESA
Improvement of existing SLFB models with the inclusion of semi-empirical conductivity equations.	Chapter 6	
Development of a numerical model for simulating the SLFB with porous electrodes.	Chapter 8	E. J. Fraser, J. P. Le Houx, K. R. Dinesh, and R. Wills, "Image-based modelling of porous electrodes and simulating their performance in the soluble lead flow battery," submitted to the Journal of Energy Storage
Using a voxel dilation technique to estimate properties of porous electrodes in the SLFB at various states of charge.	Chapter 8	

1.2 Publications

In publication 1, I provided wrote section 11. Modelling and simulation and contributed a considerable portion of the concluding remarks and provided general comments throughout. In publication 2, 3 and 4, I completed all experimental and modelling work. In publication 5, I completed all experimental and modelling work other than the use of the software OpenImpala.

1. M. Krishna, E. J. Fraser, R. G. A. Wills, and F. C. Walsh, "Developments in soluble lead flow batteries and remaining challenges: An illustrated review," *Journal of Energy Storage*, vol. 15, pp. 69–90, 2018
2. E. J. Fraser, K. R. Dinesh, and R. Wills, "Development of a two-dimensional, moving mesh treatment for modelling the reaction chamber of the soluble lead flow battery as a function of state of charge for Pb and PbO_2 deposition and dissolution," *Journal of Energy Storage*, vol. 31, p. 101484, 2020
3. E. J. Fraser, R. G. Wills, and A. J. Cruden, "The use of gold impregnated carbon-polymer electrodes with the soluble lead flow battery," *Energy Reports*, vol. 6, pp. 19–24, 2020
4. E. Fraser, K. Ranga Dinesh, and R. Wills, "A two dimensional numerical model of the membrane-divided soluble lead flow battery," *Energy Reports*, vol. 7, pp. 49–55, 2021, sI: 5th AC-CDTESA
5. E. J. Fraser, J. P. Le Houx, K. R. Dinesh, and R. Wills, "Image-based modelling of porous electrodes and simulating their performance in the soluble lead flow battery," submitted to the Journal of Energy Storage

1.3 Background

The United Nations estimate for the global population in 2019 is 7.7 billion. By 2050, they estimate the population will rise to almost 10 billion [6]. This increase in population, coupled with growing economies, is projected to cause the global demand for electricity to continue to rise [7]. In 2016, globally, 63 % of electricity was generated using fossil fuels [8]. The continued use of fossil fuels as a source of energy since the industrial revolution has led to a significant increase in greenhouse gas emissions [9]. This increase in human-made greenhouse gas emissions is widely accepted as the cause of an increase in average global temperature. This higher temperature has led to significant variations in local weather patterns and other potentially detrimental effects, the consequences of which can be severe and widespread [10]. Burning fossil fuels also produces other undesirable emissions, including ultrafine particulate matter, nitrogen oxides (NO_x), volatile organic compounds and low level ozone (O_3) which can reduce local air quality. The Royal College of Physicians has associated 40,000 deaths per year with poor air quality in the UK. These deaths are primarily attributed to the burning of fossil fuels [11].

In recent years, there has been an increasing demand for the development and deployment of low-carbon energy technologies. Nuclear fission, wind turbines, solar photovoltaics and hydroelectric generators have been the most widespread low-carbon energy generation technologies [12]. By 2050, IEA projections show a 70 % to 100 % low carbon electricity generation in three scenarios: Net Zero Emissions by 2050, where 100 % of generation is zero emissions, Announced Pledges Scenario where pledges currently announced by countries to reach net zero emissions are met and Stated Policies Scenario where only measures already in place are considered. Figure 1.1 shows the contribution by technology in each of these scenarios. More information on the scenarios is given in the World Energy Outlook 2021 [13].

While hydropower can be varied to follow demand, nuclear generation is often deemed to be inflexible and, although modern reactors are technically capable of load following to some extent, the high capital costs compared to fuel costs mean it often only has an economic case if it is operated at a very high capacity factor [14]. Wind and solar are at the mercy of the weather and only have the option of being curtailed to aid with demand matching. Of these technologies, only hydro and nuclear can provide grid inertia if they are connected with synchronous generators. However, both have substantial capital costs and require large volumes of CO_2 emitting concrete [15, 16]. Hydropower is limited in the locations it can be installed and poses other environmental issues due to the destruction of the landscape, interference with aquatic life and it can emit substantial volumes of greenhouse gases during construction and by causing flooding.

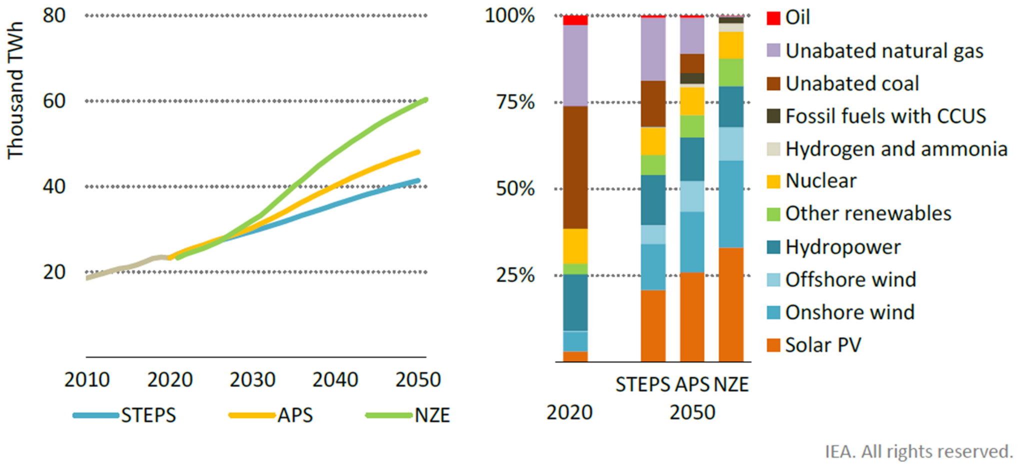

FIGURE 1.1: Global electricity demand and generation mix by IEA scenario. Scenarios are: Stated Policies Scenarios (STEPS), Announced Pledges Scenario (APS) and Net Zero Emissions by 2050 (NZE). Reproduced from IEA (2018) World Energy Outlook [13]. All rights reserved.

Homan et al., [17], show that between 2014 and 2018, there was a steady increase in the number of frequency events in the GB grid, defined as a deviation of frequency outside the range of 49.8 – 50.2 Hz and a corresponding increase in gird frequency standard deviation. The authors also show that there is a strong correlation between frequency standard deviation and the combined wind and solar penetration over the same period. In a simulated scenario with the complete absence of synchronous generation and a 25 % reduction in demand side inertia, there is an order of magnitude increase in the number of frequency events predicted. However, with suitably fast frequency response combined with introducing synthetic inertia, this effect can be largely mitigated. There is, then, a clear need for clean generation to be coupled with other technologies to aid in their widespread use while keeping a high quality, reliable supply of electricity that can react quickly and closely follow demand.

1.3.1 Energy Storage

Energy storage is one such set of technologies that has been identified by the US Department of Energy (DoE), the European Commission (EC) and the UK National Grid as being a vital part of a future low-carbon electricity grid [18–20]. Demand for these technologies is already growing [21]. Energy storage can provide several services on top of renewables capacity firming. The National Renewable Energy Laboratory, a laboratory of the US DoE, has defined the following as major grid applications of energy storage [22]:

- **Load levelling/arbitrage** The storage of energy during periods of low-cost or over-generation and selling the energy back to the grid during periods of high price or under generation. This creates a more consistent generation profile reducing the need for peaking plants that may have a low efficiency.
- **Capacity firming** The assurance of sufficient generation capacity at peak demand. This is essentially the current role of peaking generators.
- **Operating reserve** Frequency response or spinning reserve responds to short time scale, unpredictable fluctuations in demand, or a sudden change in generating capacity or demand such as generator failure.
- **Ramping/load following** The following of longer-term, generally predictable, changes in demand over hours.
- **Transmission and distribution replacement or deferral** A lessening of the peak loading on transmission and distribution systems. Because these networks are designed for peak demand, any increase in peak demand will require an upgraded system. Storage can reduce the impact of the increased demand allowing for a delay in upgrading the system.
- **Black-start** A limited use of storage technology, used for restarting conventional generators after a widespread failure.

Figure 1.2 gives an example of a fictitious demand profile and generation mix required to meet it. When storage is included, Figure 1.2 (B) gives an example of energy storage used in a load levelling application.

The peak demand is reduced and, notably, the demand on the load following combined cycle gas turbine (CCGT) is flattened, see Figure 1.3. Were the CCGT to have a limited capacity, the energy storage in this scenario would also be providing capacity firming for the peak demand.

Currently, the vast majority ($\sim$88 GW, $\sim$1.2 TW h, $\sim$90 % by power) of grid-connected energy storage, globally, is in the form of pumped hydro energy storage (PHS) [23]. PHS

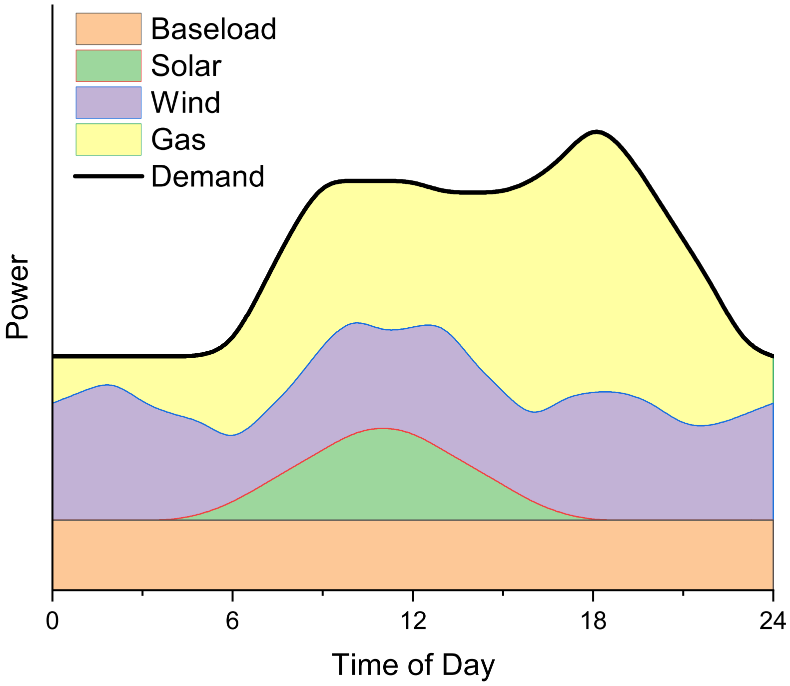

(A) Without storage

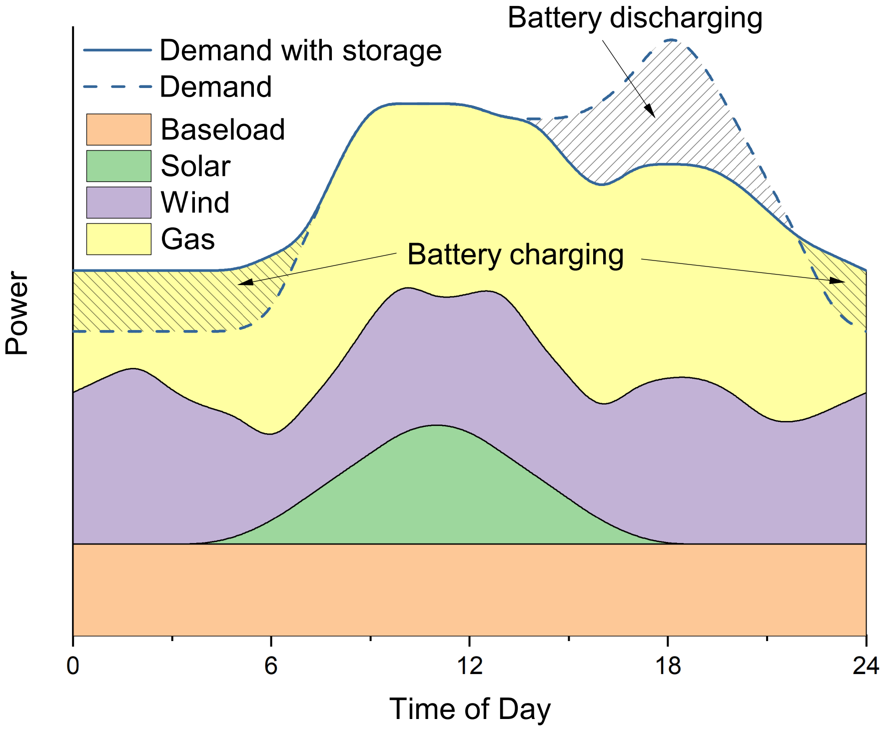

(B) With storage

FIGURE 1.2: A simple example of a fictional demand profile and generation mix including baseload (orange), solar (green), wind (purple) and gas (yellow) without (A) and with (B) energy storage. The shaded area represents the difference between generation and demand facilitated by charging/discharging energy storage.

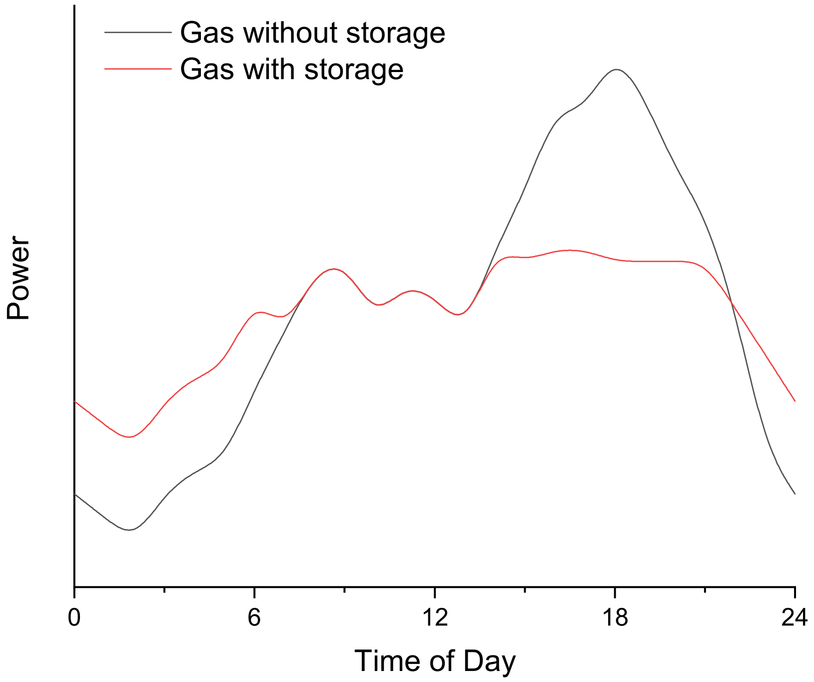

FIGURE 1.3: Comparison of required CCGT generation with (shown in red) and without (shown in black) storage for the same example demand profile used in previous figure.

stores energy by pumping water from one reservoir to another reservoir at a higher altitude, which can then be released through a turbine to generate electricity. Battery storage is the second most prominent form of energy storage in terms of installed capacity [18]. While its capacity is still small compared to PHS, battery storage can be used in a more diverse array of applications. There are numerous small projects using battery storage. Lead-acid batteries are the oldest secondary battery. While they remain the most popular in terms of global sales, research and development of batteries is dominated by lithium ion due to its high specific energy and power and versatility. The cost of lithium-ion has dropped dramatically in recent years largely due to its prominence in portable electronics and, more recently, in electric vehicles [24]. Both have grid connected applications (Lead-acid ∼180 MW, ∼165 MW h; lithium-ion ∼500 MW, ∼870 MW h) [23]. However, several other electrical energy storage technologies exist, each with different advantages for different applications. Molten salt storage (∼4.8 GW, ∼32 GW h, [23]), for example, allows for harnessing solar energy with dispatchable electricity generation. Sunlight is concentrated and is used to heat molten salt. Sensible heat is released from the slat on demand to power a steam turbine when electricity generation is required. Supercapacitors and flywheels (∼500 MW, ∼11.5 MW h, [23]) can provide high power for a short duration, making them ideal for frequency response.

Superconducting magnetic energy storage (SMES) can provide very high power for a short period and has a long cycle life. However, its high cost and requirement for very low temperatures means commercial applications may be a long way off. Other applications require specific terrain, such as compressed air energy storage (CAES) (∼430 MW, ∼33 GW h, [23]), which uses caverns to store compressed air, and gravimetric energy storage which raises and lowers large masses in abandoned mineshafts to store energy. Other technologies, such as pumped heat energy storage, also exist. Several of these technologies only have niche applications or even no commercial application to date.

Each form of electrical energy storage can be described in terms of rated power (the maximum power at which the system is designed to operate) and capacity, the amount of energy that it stores. Using these metrics as logarithmic axes, a Ragone plot allows for a comparison of technologies over a range of scales. An example of this is seen in Figure 1.4.

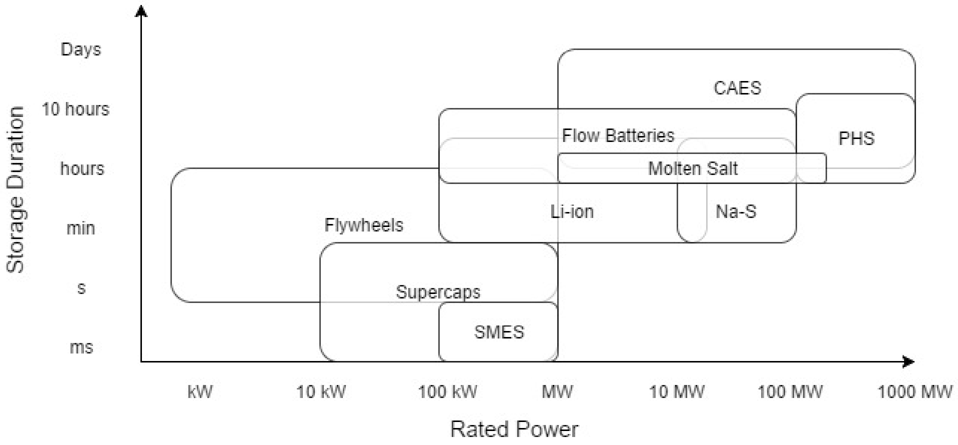

FIGURE 1.4: Modified Ragone Plot comparing some of the key forms of electricity storage technologies. CAES is Compressed Air Energy Storage, PHS is Pumped Hydro Energy Storage, SMES is Superconducting Magnetic Energy Storage, Li-ion is Lithium-ion Batteries, and Na-S is Sodium Sulphur Batteries. Data from [25].

Using this plot, suitable energy storage technology candidates for a given application can easily be found. For applications requiring the ability to supply high power (>MW) for several hours, along with CAES and PHS, redox flow batteries (RFBs) are a promising option.

1.4 Batteries

Batteries are electrochemical devices containing multiple electrochemical cells electrically connected in series and/or parallel. Each cell consists of a positive and a negative electrode divided by one or more electrolytes and often a separator. Energy is stored in active species, which is released via redox reactions at the electrodes. The amount of energy a cell can store is determined by the capacity, the amount of charge which can be released by the battery and the cell potential. The cell capacity can be determined by Faraday's law:

$$q = \frac{Fzm}{M} \tag{1.1}$$

Where q is charge held in a certain mass m, with valence z, and molar mass M, and F is Faraday's constant. The power available from each cell is determined by the current and potential.

The cell potential is determined from the sum of the equilibrium potential, the overpotential of each electrode and the cell resistance.

$$E_{cell} = E_{eq} + \eta^{+} - \eta^{-} + IR_{cell} \tag{1.2}$$

Where E_{cell} is the cell potential, E_{eq} is the equilibrium potential, η^{+} is the overpotential at the positive electrode, η^{-} is the overpotential at the negative electrode and IR_{cell} is the ohmic drop across the cell. Any electrode and electrolyte combination will have a specific potential when zero current flows. This is known as the equilibrium potential. During operation of a cell, as the composition of the electrolyte changes, the equilibrium potential will change. This change in potential can be calculated using the Nernst equation.

$$E_{eq} = E_0 - \frac{RT}{zF} \ln Q \tag{1.3}$$

Where E_0 is the standard potential and Q is the reaction quotient, a value which described the relative activities of the reactants and products. For the example reaction in Equation 1.4, with α moles of A, β moles of B, γ moles of C and δ moles of D, the reaction coefficient can be approximated using the concentrations, as in Equation 1.5.

$$\alpha A + \beta B \rightleftharpoons \gamma C + \delta D \tag{1.4}$$

$$Q = \frac{c_C^{\gamma} c_D^{\delta}}{c_A^{\alpha} c_B^{\beta}} \tag{1.5}$$

The overpotential at each electrode is determined by the temperature and the current.

$$\eta = \frac{RT}{nF} \ln \frac{j}{j_0} \tag{1.6}$$

Where η is the overpotential, R is the universal gas constant, T is temperature, n is the number of electrons involved in the reaction, F is Faraday's constant, j is current density and j_0 is the exchange current density. Batteries can be broadly divided into primary (single use) and secondary (rechargeable) chemistries.

1.4.1 Primary Batteries

Primary or single-use batteries have chemistries that are not reversible. Often primary batteries have a higher specific energy than secondary batteries but are commonly used in applications with a low current requirement. Zinc-Carbon and alkaline batteries are common chemistries for primary batteries and are often used in portable electronics [26].

Silver oxide batteries typically use monovalent silver oxide at the cathode and a zinc anode. Divalent silver was used in the past. However, environmental considerations mean their use has been rescinded. Silver oxide batteries have a high energy density, good shelf life and flat discharge curve. However, their high cost limits their use to low power applications such as watches [26].

Zinc-air batteries use oxygen as one active species, so they have a high energy density but require exposure to air to operate. Typical applications are hearing aids [27].

Primary lithium batteries have been available commercially for over 50 years and have found use in low power electronics [28]. Cathode chemistries include lithium sulphur dioxide, lithium-polycarbon monofluoride, lithium manganese oxide and polyvinylpyridine (PVP).

1.4.2 Secondary batteries

Secondary or rechargeable batteries contain reversible redox reactions at both electrodes. Generally, secondary batteries have a lower energy density than primary batteries. However, the advantages of being reusable are obvious. The efficiency of a secondary battery is an important metric. There are three primary methods of determining efficiency of a secondary battery:

Coulombic efficiency: Coulombic efficiency is the ratio of charge transferred during charge and discharge. The charge transferred is calculated by integrating current with respect to time.

$$\frac{q_d}{q_c} = \frac{\int I_d dt}{\int I_c dt} \tag{1.7}$$

Where q_d is the charge transferred during discharge, q_c is the charge transferred during charge, I_d is the current during discharge, I_c is the current during charge and t is time.

Voltage efficiency: Voltage efficiency is the ratio of average cell potential during charge and discharge.

$$\frac{\overline{E_d}}{\overline{E_c}} \tag{1.8}$$

Where E_d is the cell potential during discharge and E_c is the cell potential during charge.

Energy efficiency: Energy efficiency combines coulombic and voltage efficiencies to give an overall ratio of the energy transferred during charge and discharge. This is calculated by integrating power with respect to time.

$$\frac{W_d}{W_c} = \frac{\int I_d E_d dt}{\int I_c E_c dt} \tag{1.9}$$

Where W_d is energy transferred during discharge, W_c is energy transferred during charge.

A number of different secondary battery chemistries have been developed to varying levels of maturity.

Nickel-cadmium is a mature battery chemistry with high energy density and low maintenance. However, the cycle life is only circa 2000 cycles, the chemistry has a high cost, cadmium is toxic and the batteries must be regularly fully discharged due to their memory effect. Applications include portable electric and electronic devices and uninterruptable power supply (UPS). However, in many of these applications, this chemistry has now been replaced by other chemistries [26].

The term lithium ion encompasses several chemistries where the cathode is a lithium metal oxide. Often the anode is graphite and the electrolyte is organic. Lithium ion batteries have become highly popular since their commercial introduction in 1990. They have high energy density and power density, can have cycle lives of 10,000, have high efficiency and the cost has reduced dramatically in recent years. The main concerns of lithium ion are the availability of the chemicals required to manufacture them. Cobalt, used cathodes of the prevalent $LiCoO_2$ chemistry, has significant political and potential ethical considerations. Thermal runaway – the spontaneous combustion of the battery – releases toxic gases. Lithium-ion batteries have a large range of uses, commonly used in portable electronics, electric vehicles, and increasingly grid applications [26, 29].

Sodium-ion batteries have a similar working principle to lithium-ion. However, they are based on sodium which is abundant and low cost. The battery also has high efficiency and does not risk thermal runaway. Energy density is slightly lower than that of lithium-ion and the operating voltage is lower [30, 31].

Lead acid batteries (LABs) are the oldest secondary battery chemistry. This technology is very mature and is the most popular chemistry in terms of sales. Solid lead is used as the negative electrode and solid lead dioxide as the positive electrode. The electrolyte is sulphuric acid and lead sulphate is formed during discharge. LABs can discharge at high power, but due to the high elemental mass of lead and the relatively large volume of water-based electrolyte required, the specific energy of LABs is low. LABs are generally safe; however, the sulphuric acid used is corrosive, lead and its compounds are toxic and an electrolysis reaction may occur during charge creating hydrogen and oxygen, causing a risk of explosion. LABs are commonly found in automotive applications as power for starter motor and vehicle electrics. Other applications include UPS and traction batteries.

Sodium sulphur batteries consist of molten sodium as the positive electrode and molten sulphur as the negative electrode, separated by a solid alumina electrolyte. Na-S batteries have relatively low cycle lives ($\sim$2500) and moderate energy and power densities. Sodium sulphur batteries are able to supply high power for short periods during normal operation. This allows a single battery to be used for both peak shaving and as operating reserve. These batteries have high capital costs and although there has been research on room temperature opeartion [32], they normally require a high temperature to ensure the electrodes remain molten [26, 33].

1.5 Redox flow batteries

A redox flow battery (RFB) is an electrochemical energy storage device that stores energy within an electrolyte stored externally to the cell in separate reservoirs. RFBs have the potential to be a low-cost [34], durable, and environmentally friendly [35], method of energy storage for large applications [36]. An RFB is a stack of redox flow cells connected electrically in series. Each of these cells typically consists of two electrodes, a positive and a negative, separated by a flow channel and usually an ion exchange membrane or separator. Externally to the stack, there are two electrolyte reservoirs, one for each of the positive and negative electrolytes. The electrolyte in these reservoirs then flows through each of the cells where redox reactions occur, either capturing or liberating electrons, allowing a current to flow. This is shown schematically in Figure 1.5 as a single cell (A) and three cell stack (B).

During charging, an RFB reduces the negative active species at the negative electrode and oxidises the positive active species at the positive electrode. Both the positive electrolyte and the negative electrolyte are circulated continuously during this process. During discharge, the electrolyte continues to circulate through the battery, but the current reverses direction and the negative and positive active species are spontaneously oxidised and reduced, respectively.

Modern research on RFBs began in the 1970s with the formation of the Lewis Research Center, a centre created by the National Aeronautics and Space Administration (NASA) specifically for researching RFBs [37]. Initially, NASA worked on the iron/chromium system. Since this initial work by NASA, there have been many proposed chemistries for RFBs [38]. Table 1.1 shows a summary, but not an exhaustive list, of proposed systems, and their level of maturity.

RFBs can be divided into four categories:

- **Type 1.** A Redox Flow Battery. This is the conventional RFB with positive and negative redox couples that remain in solution regardless of their oxidation state. An example of this is the all-vanadium flow battery [39]. Schematically shown in Figure 1.5 (A).
- **Type 2.** Hybrid flow battery. Phase change occurs at one electrode to plate either a metal or metal oxide onto one of the electrodes. The other electrode uses a conventional redox couple that remains in solution at all used oxidation states (i.e. at all states of charge). An example of this is the zinc-bromine flow battery [40]. Schematically shown in Figure 1.6.
- **Type 3.** Metal Flow Battery. Phase change occurs at both electrodes, with metal plating at one electrode and a metal oxide at the other. An example of this is the soluble lead flow battery [5]. Schematically shown in Figure 1.8.
- **Type 4.** Air Breathing Flow Battery. One electrode is a conventional redox couple in this system; the other is an air-breathing electrode similar to those used in proton exchange membrane (PEM) hydrogen fuel cells. An example of this is the zinc-air flow battery [41]. Schematically shown in Figure 1.7.

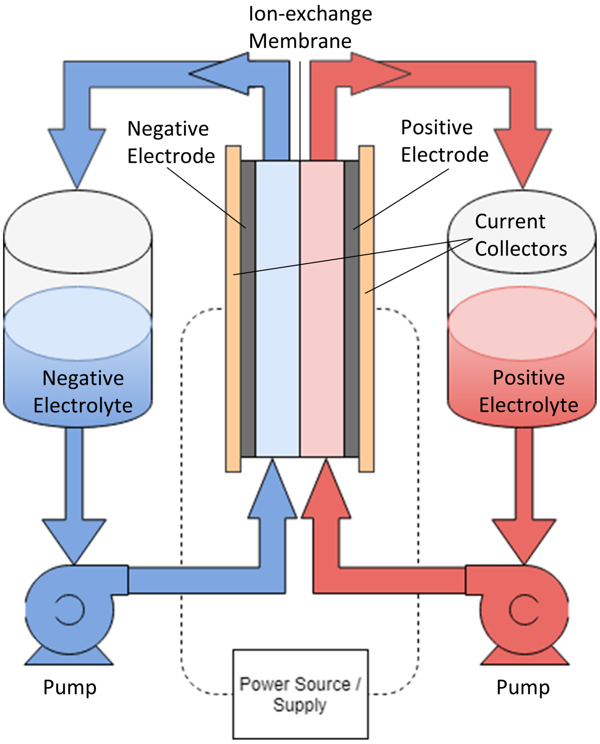

(A) Single cell

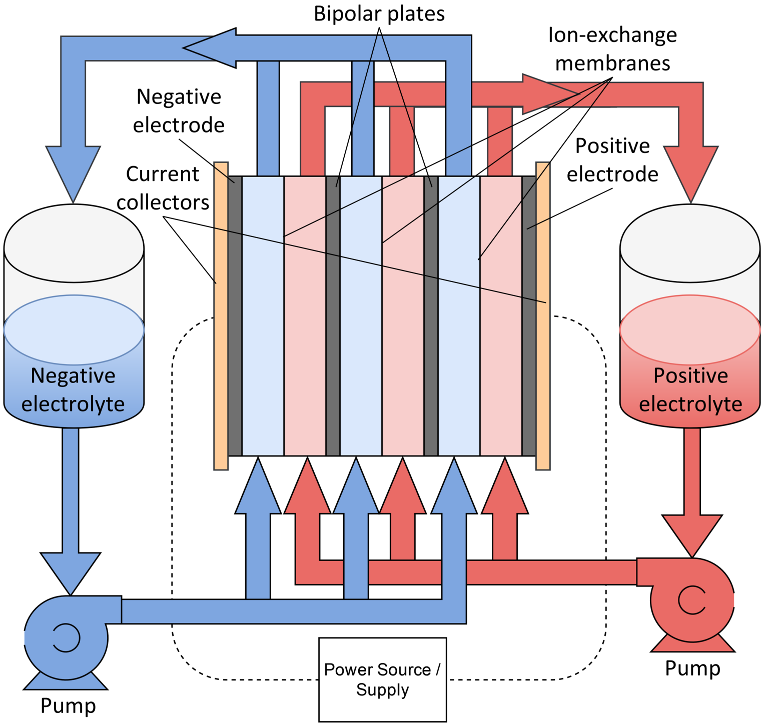

(B) Three cell stack

FIGURE 1.5: Schematic of a typical two-electrolyte redox flow cell/battery. Positive (shown in red) and negative (shown in blue) electrolytes are contained in separate reservoirs and are circulated through cells which are divided by ion exchange membranes.

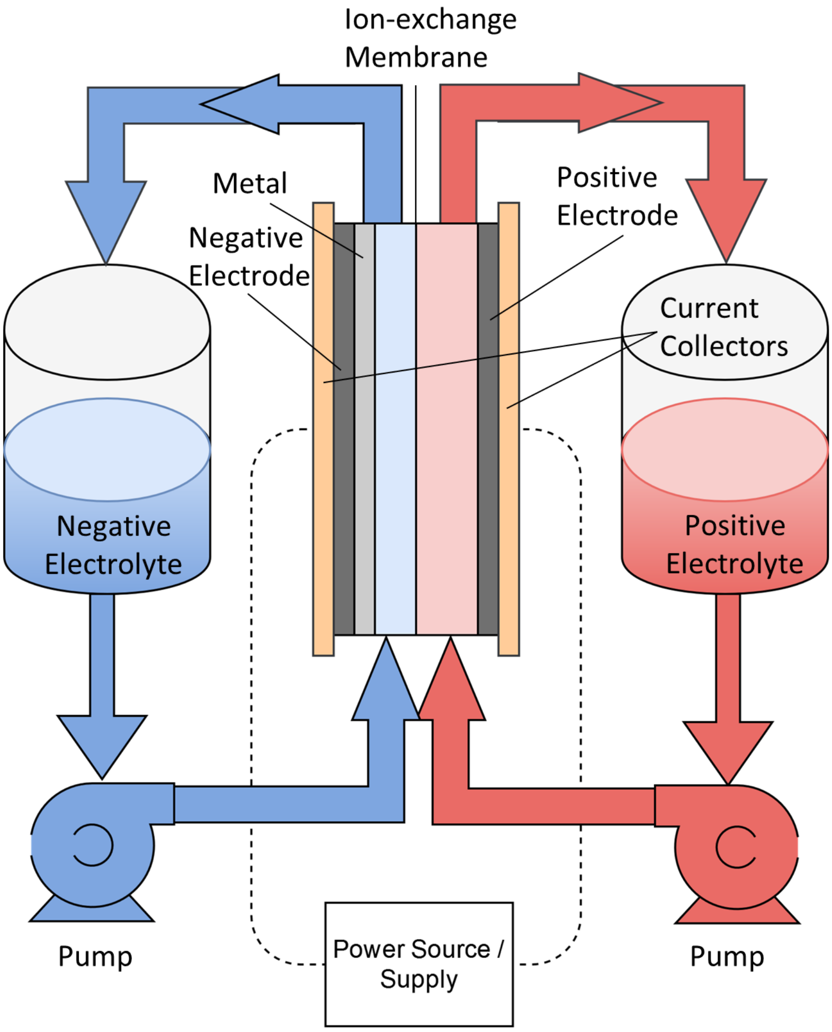

FIGURE 1.6: Representation of a single cell, two-electrolyte hybrid (type 2) flow battery. Positive (shown in red) and negative (shown in blue) electrolytes are contained in separate reservoirs and are circulated through cells which are divided by ion exchange membranes. A metal/metal oxide is deposited at one electrode.

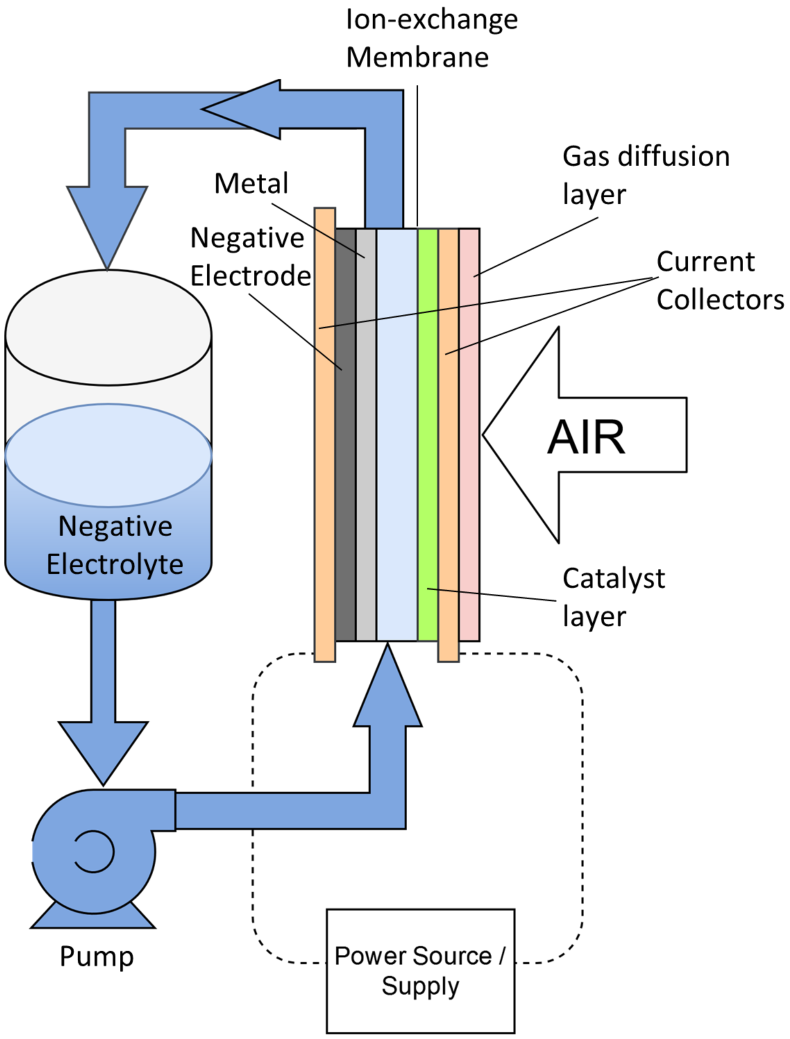

FIGURE 1.7: Representation of a single cell, air-breathing (type 4) flow battery. A single electrolyte flows through one half of the cell. An air breathing electrode is used as the other half cell. The two half cells are separated by a divider. Metal my be deposited at the negative electrode.

TABLE 1.1: Summary of proposed RFB chemistries

System	**Chemistry (Forward is charge)**	**Cell Potential (V)**	**Level of Maturity**	**Reference**
Iron-Chromium	$Cr^{3+} + Fe^{2+} \rightleftharpoons Cr^{2+} + Fe^{3+}$	1.18	Pilot-scale	[42]
Zinc Bromine	$Zn^{2+} + 2Br^{-} \rightleftharpoons Zn^{0} + Br_2$	1.85	Commercial	[43]
All-Vanadium	$VO^{2+} + H_2O + V^{3+} \rightleftharpoons VO_2 + +2H^{+} + V^{2+}$	1.26	Commercial	[43]
Zinc Cerium	$Zn^{2+} + 2Ce^{3+} \rightleftharpoons Zn^{0} + 2Ce^{4+}$	2.20	Lab-based research	[43]
Soluble Lead	$2Pb^{2+} \rightleftharpoons Pb^{4+} + Pb^{0}$	1.59	Lab based research / Pilot scale	[44]
Vanadium Air	$4V^{2+} + O_2 + 4H^{+} \rightleftharpoons 4V^{3+} + 2H_2O$	1.49	Early research	[45]
Organic	Typically Quinone Based	1.0	Early research	[46]

RFBs are easily scalable in terms of both energy and power. In a conventional, type 1, RFB where the active species remain in solution throughout, the system's power and capacity are decoupled. To increase the capacity of an RFB system, more electrolyte or a higher concentration of the electrolyte is required. To increase the power of a system, a larger electrode area or stack size is needed. However, in type 2 or 3 systems, such as the soluble lead flow battery, the electrodes are involved in the reaction, so the extent to which energy and power are decoupled is limited.

1.6 Soluble lead flow battery

The soluble lead flow battery (SLFB) is a type 3 flow battery, or metal flow battery, consisting of solid lead and lead dioxide deposits on the negative and positive electrodes. This is shown schematically in Figure 1.8. In its most common arrangement, the system consists of just a single electrolyte which, in its most basic form, is Pb^{2+} ions dissolved in methanesulfonic acid (MSA). At the positive electrode, during charging, the Pb^{2+} ions are oxidised to form PbO_2 (lead dioxide), which deposits as a solid material on the electrode surface. During charging, the Pb^{2+} ions are reduced to form solid lead metal at the negative electrode, which also deposits onto the electrode surface. For each mole of lead dioxide that is deposited, two moles of electrons are stripped from the Pb^{2+} ions in solution, where they flow around an external circuit to the negative electrode to reduce a further mole of Pb^{2+} ions forming one mole of solid lead. During discharge, the current reverses direction and the lead and lead dioxide are oxidised and reduced respectively back to Pb^{2+} ions in solution [44]. This is represented by the following equations, where left to right indicates charging the cell:

$$Positive \quad Pb^{2+} + 2H_2O \rightleftharpoons PbO_2 + 4H^+ + 2e^- \quad E^0 = +1.46 V vs SHE \tag{1.10}$$

$$Negative \quad Pb^{2+} + 2e^- \rightleftharpoons Pb \quad E^0 = -0.13 V vs SHE \tag{1.11}$$

$$Cell \quad 2Pb^{2+} + 2H_2O \rightleftharpoons Pb + PbO_2 + 4H^+ \quad E^0_{cell} = +1.59V \tag{1.12}$$

Compared to more conventional RFBs, such as the all-vanadium redox flow battery (VRB), the SLFB has several advantages and disadvantages. The main disadvantages are related to the formation of solid deposits at the electrodes. Because deposits form at the electrodes, the extent to which energy and power can be decoupled is limited. There

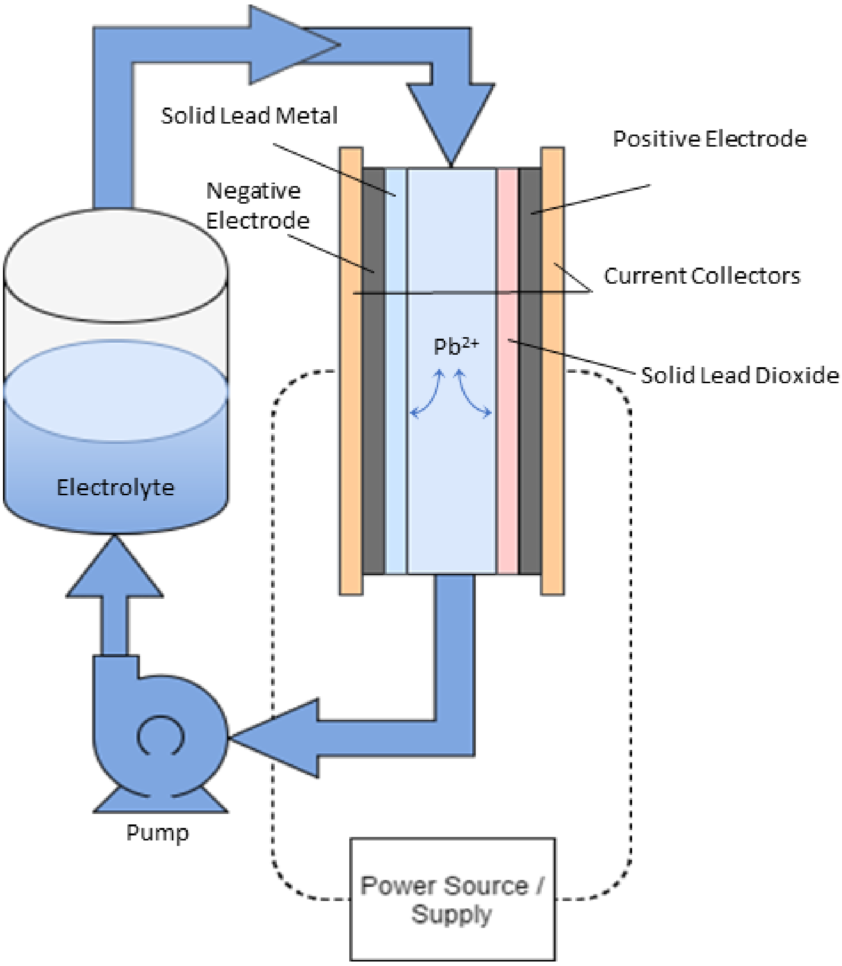

FIGURE 1.8: Representation of a single cell soluble lead flow battery. A single electrolyte is circulated through an undivided cell. Solid deposits form at both electrodes during charge.

is a maximum thickness of electrode deposit which will limit the energy for a given electrode area. A further disadvantage is the toxicity of lead. However, compared to competing systems such as the all vanadium or lithium-ion batteries, this is relatively trivial. There are two main advantages because of the common electrolyte of both the positive and the negative redox couples. The first is that the SLFB can operate without a membrane or separator. The second is that because the system uses just a single electrolyte, the number of storage tanks, pumps, and pipework required can be reduced. There is, therefore, the potential for a significant reduction in the cost of the system. Lead is also an abundant material that can be easily recovered from spent lead-acid batteries, for which there is an existing supply chain.

The SLFB has shown a specific energy of up to 40 Wh kg^{-1} of electrolyte at a concentration of 1.5 mol dm^{-3} Pb^{2+}, [47], a value higher than that of the VRB at 25-35 Wh kg^{-1} [43].

However, it is still less than that of the zinc-bromine flow battery (ZBFB) at 70 Wh kg^{-1} [48]. Theoretically, as the solubility limit of lead methanesulfonate is 2.6 mol dm^{-3} [49], the SLFB could have a specific energy of 59 Wh kg^{-1}. However, at high concentrations, the cycle life of the cell declines dramatically [49].

Chapter 2

Literature Review

2.1 History of Lead-based Batteries

The lead-acid battery was the first secondary battery to be conceived [50]. In 1859, Gaston Planté designed a lead-acid battery that could be recharged [51]. Since then, the lead-acid battery has become the world's most popular battery with a wide variety of uses. The battery has been used in electric vehicles. Fritchle's lead-acid battery-electric vehicle could travel over 100 miles on a single charge [44]. The battery currently has electric vehicle use in applications such as forklift traction batteries [52]. It has also been used in uninterruptible power supply (UPS) systems. However, the most common use in the modern era is in the automotive industry as an auxiliary power supply and to power starter motors for internal combustion engines.

The earliest and simplest lead-acid battery design is the flooded battery. In this system, the positive and negative electrodes are submerged in sulfuric acid and are divided with a separator. During discharge, at the negative and positive electrodes, lead and lead dioxide, respectively, are converted to insoluble lead sulphate [26].

Towards the end of the 20th century, the valve-regulated lead-acid battery (VRLAB) was developed [52]. There are two types of VRLAB, the absorbed glass mat (AGM) and the gel battery. The AGM uses a porous glass matt structure as a cell divider and the electrolyte is held within the pores of the matt. The gel battery is undivided, but silica is used as part of the electrolyte to form a gel-like substance.

With the dramatic increase in demand for lead acid batteries in automotive vehicles, recovery of lead from LABs became common. Today, more than 85 % of secondary lead comes from lead acid batteries, with secondary lead accounting for a higher proportion of production than primary lead [53]. Traditional methods using a pyrometallurgical process (the extraction or purification of metals via the application of heat) for secondary lead production remain in use and have remained largely unchanged for a considerable amount of time [54, 55]; however, since the 1990s, methods using leaching and electrowinning as a cleaner method of lead recovery have grown in popularity as an area of research [56, 57].

Soluble lead species were first used in primary batteries, where acid was added to the battery shortly before use. Subsequently, patents for soluble lead box cells and button cells were filed before the arrival of flow cells [58–60].

All these early cells used acids that were used in the lead plating industry as electrolytes. These included hexafluorosilicic ($H_2(SiF_6)$) and amidosulfonic (H_3NO_3) acids as well as perchloric ($HClO_4$) and fluoroboric (HBF_4) acids. The current acid used in the electrolyte is methanesulfonic acid (MSA) (CH_3SO_3H), which was used in conjunction with hexafluorosilicic acid by Henk et al. [60] but was first used as the sole acid in the electrolyte by Hazza et al. [44].

Zhang et al. [61] define several critical differences between the SLFB and the LAB. In the SLFB, lead in a +2 oxidation state is soluble in the electrolyte, whereas, in the LAB, the Pb^{2+} is in the form of solid lead sulphate. The methanesulfonic acid used in the SLFB is more environmentally friendly than the sulfuric acid used in the LAB (discussed further in Section 2.2.1) [62]. While, in its current state, the SLFB lags behind the LAB in efficiency with higher overpotentials and significantly shorter cycle life, further development of the cell and stack design is likely to mitigate these issues. Significantly, a preliminary study on maintenance cycles has shown great promise on extending the cycle life with over 7000 full cycles achieved before failure [63].

2.2 Electrolyte

2.2.1 Composition

The SLFB uses an acidic electrolyte, where the acid used is methanesulfonic acid (MSA). Pure MSA has a molar mass of 96.11 g mol^{-1} and a density of 1.481 g cm^{-3}. MSA can be broken down by microbial degradation into sulphate and carbon dioxide [64]. Hence, it is more environmentally friendly than other electrolytes, including fluorosilic and fluoroboric acids which are used in the lead plating industry and sulfuric acid which is used in electrochemical applications. In an electrochemical environment, storing, transporting and using MSA in a cell is more straightforward and safer than sulfuric acid [65]. Díaz-Urrutia and Ott have described a mechanism which can produce MSA using abundantly available methane as a feedstock [66].

The acid in an electrolyte is used to provide H^+ ions to balance the cell and to allow conduction across the electrolyte. A high electrolyte conductivity offers a reduced cell resistance and hence lower overpotentials and a higher voltage efficiency. A high conductivity will also increase the leakage currents (in a multi-cell stack, currents which flow though the electrolyte manifold bypassing one or more electrodes), as the resistance of the electrolyte bypassing the cell will also reduce, however. MSA has a conductivity of 285 mS cm^{-1} at a concentration of 1 mol dm^{-3} and a temperature of 298 K [49]. This is comparable to 332 mS cm^{-1} for HCl, [67], but slightly lower than 390 mS cm^{-1} for sulfuric acid [68].

The solubility of Pb^{2+} ions in the electrolyte is also important, as this determines the maximum energy density of the electrolyte. The lead salt used in the SLFB is typically lead methanesulfonate, which has a solubility limit of 2.6 mol dm^{-3} in water [62]. As the concentration of MSA increases, the solubility of lead methanesulfonate decreases. In 8 mol dm^{-3} MSA, lead methanesulfonate is virtually insoluble [44]. It is unclear why there is a steep decline in solubility with acid concentration.

The conductivity, the viscosity and the diffusion coefficients of the electrolyte can have a significant impact on the performance of the system. Higher conductivity allows for larger inter-electrode gaps and lower ohmic losses and more even current distribution.

Faster diffusion coefficients allow for faster kinetics and lower viscosity decreases the pressure drop across the cell [69].

2.2.2 Recycled electrolyte

Orapeleng et al. [70] have investigated methods to recover Pb^{2+} from spent LABs for use in the SLFB. A spent LAB is defined as one with a state of health (SoH) of 80 % or lower. Six electrolytes are prepared, each by dissolving the LAB electrodes in 2.5 mol dm^{-3} MSA. H_2O_2 was added to four of the electrolytes to oxidise the Pb electrode and reduce the PbO_2 electrode to Pb^{2+}. H_2O_2 was added to two electrolytes to a concentration of 0.09 mol dm^{-3} and to a further two to a concentration of 0.9 mol dm^{-3}, creating three pairs of electrolytes, 2.5 mol dm^{-3} MSA only, 2.5 mol dm^{-3} MSA and 0.09 mol dm^{-3} H_2O_2, and 2.5 mol dm^{-3} MSA and 0.9 mol dm^{-3} H_2O_2. H_2O_2 is unusual because it can act as both a reducing agent and an oxidising agent. Here it aids in reducing PbO_2 and oxidising Pb to soluble Pb^{2+} [71].

One of each pair of electrodes was then heated to 303 K and the remaining electrolytes were heated to 313 K. Both solutions with 0.9 mol dm^{-3} H_2O_2 were able to recover 0.9 – 1.5 mol dm^{-3} Pb^{2+} over 6 hours successfully. A comparison of standard and recovered electrolyte in a flow battery yielded identical voltage efficiencies of 64 % and comparable charge efficiencies of 85 % using fresh electrolyte and 81 % with recovered electrolyte. In a further study by the same authors [72], extended testing is completed comparing electrolyte recovered from spent LABs with reagent grade or fresh electrolyte. Comparisons were conducted on both flow cells and static electrolyte cells. In these experiments, static cells using recovered electrolyte had significantly higher charge, voltage and energy efficiencies and failed after a greater number of cycles.

When used in flow cells, figures for efficiencies and cycles before failure were generally comparable. However, at a current density of 10 mA cm^{-2} and a Pb^{2+} concentration of 0.7 mol dm^{-3}, 187 cycles were achieved before the charge efficiency dropped below 60 % for the cell using recovered electrolyte compared with 101 cycles for the reagent grade electrolyte. Dissolved trace elements in the recovered electrolyte may aid in the performance of the SLFB, or a decreased concentration of other elements, such as nickel, in the recycled electrolyte may explain its improved performance compared to reagent grade electrolyte. However, further work is needed in this area.

Several processes have been proposed to electrochemically recover lead from waste lead acid batteries as a cleaner alternative to secondary smelting, particularly if low-carbon electricity is used in the process. Each of these processes uses a slurry of leady material, or a solvated lead electrolyte. Hence, it may be possible to incorporate the SLFB directly into the lead recycling process if electrochemically recovered lead becomes a commercial success.

The proportion of lead sulphate in a spent lead acid battery varies. However, it is typically the component with the largest proportion of the battery mass [73]. When dissolving lead sulphate using Orapeleng et al.'s method, it is likely to become sulphuric acid, creating a mixed acid electrolyte. The effect of this is unknown in the SLFB. To deal with the large volumes of lead sulfate, Spijkerman and Groenen [74] patented a process which takes a slurry of lead sulphate and, using fine lead particles as a fluidised electrode, reduce the lead sulphate to lead metal. The cell consists of an anodic (positive) chamber and a cathodic (negative) chamber which are separated by an ion-exchange membrane. The cathodic side consists of the fluidised electrode. At the anode, water is electrolysed into O_2 and H^+ ions. The H^+ ions are combined with the sulphate ions from the cathode to produce clean H_2SO_4. As dilute sulphuric acid is recovered from the anodic side, water is added to complete the mass balance.

Developed by Engitec, the FAST® process is a method for recovering lead from waste lead-acid battery paste electrochemically. The patented system first removes the sulphur from the paste by reaction with ammonium carbonate. The desulphurised paste is then leached first with ammonium chloride then the residue is reductively leached with a solution of ammonium chloride and hydrogen peroxide. This solution is then passed through an electrolytic cell to recover lead metal [75].

Cambridge Enterprise Limited developed a process to convert lead paste into an aqueous lead citrate solution. Lead is then recovered electrochemically from this solution. The process requires the addition of a reducing agent to convert all the paste to lead citrate. The lead citrate can then be converted to Pb or PbO, either by electrowinning or by calcination. The preferred method is by calcination. If electrowinning is used, some further processing may be required to increase the solubility of the lead [76].

Aqua Metals have produced a process which recovers lead from paste. First, the paste is treated with a base, for example, NaOH, to remove the sulphur and convert $PbSO_4$ to

$Pb(OH)_2$. The resulting Na_2SO_4 is regenerated to NaOH by the use of an electrolytic cell. The desulphurised paste is then leached in a solution of methanesulphonic acid, hydrogen peroxide and a chelating agent, ethylenediaminetetraacetic acid (EDTA). This solution is then passed through the electrochemical cell to recover metallic lead. The cathode onto which the lead is plated is rotating. A portion of the electrode is submerged in the electrolyte. As the electrode rotates, it moves past a scraper which removes the lead from the electrode surface continuously. This allows for near-continuous operation. However, the high frequency of lead removal will lead to a large volume of electrolyte drag out. Hence, the electrolyte will need to be regularly topped up to replace the lost volume.

In Appendix A, a process for recovering lead from spent LABs electrochemically is proposed. This process would produce SLFB electrolyte as a mid stage in the process, allowing for efficient integration of the SLFB with LAB recycling. The process is described with the case study of the Ecobat's Darley Dale smelter [77].

2.3 Deposits

2.3.1 Lead

Lead is a heavy metal with a face centred cubic crystalline form, a molar mass of 207.2 $g\,mol^{-1}$, a density of 11.34 $g\,cm^{-3}$ at 20 °C, a melting point of 327.4 °C and an electrical resistivity of 20 $\mu\Omega\,cm^{-1}$ [26].

In a study to understand the negative electrode, cyclic voltammetry of lead deposition in the SLFB was conducted by Wallis & Wills [78]. This was conducted in a three-electrode glass cell containing 25 cm^3 of electrolyte. A 0.07 cm^2, glassy carbon working electrode was rotated at 900 rpm. The counter electrode was Pt wire and the reference electrode was a saturated calomel electrode. All voltammetry was conducted at 295 K.

The results show a typical metal deposition-dissolution reaction with a sharp oxidation peak and only a small difference between the first and 200th scan, as shown in Figure 2.1. It can, therefore, be concluded that the Pb/Pb^{2+} redox reaction is highly efficient with low overpotentials and fast kinetics and is highly repeatable.

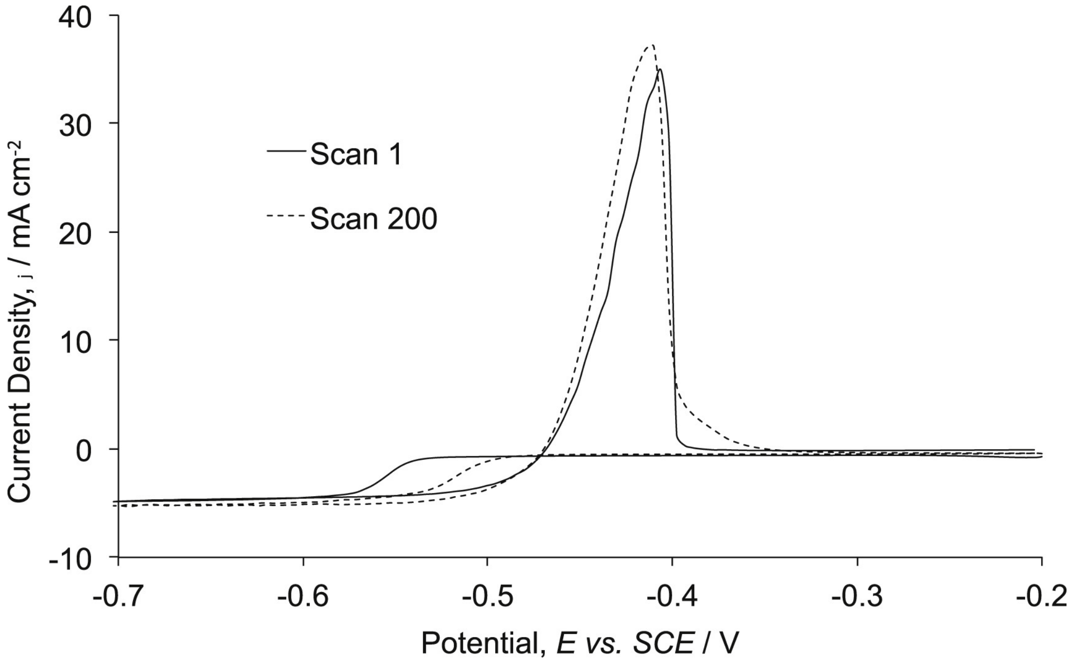

FIGURE 2.1: Cyclic voltammograms for the first and two hundredth cycle of the Pb^{2+}/Pb redox couple in 1.5 mol dm^{-3} MSA on a glassy carbon electrode. A temperature of 295 K was maintained and the initial Pb^{2+} concentration was 10 mol dm^{-3}. Reproduced with permission [78].

Pletcher et al. [79] conducted experiments on the effect of certain conditions on the quality of the lead deposit. A range of additives was used and their impact on deposit quality and coulombic efficiency were compared. Hexadecyltrimethylammonium hydroxide (HDTMA) was shown to be the most beneficial additive. However, in a larger system in a project funded by the Department of Trade and Industry, it is suggested that the effects of HDTMA do not continue to work at a larger scale. However, this is only mentioned briefly in the report and the authors do not suggest any reasons as to why this may occur [80]. This is discussed further in Section 2.4.

It is also suggested that the lead deposits are of the highest quality when the concentration of Pb^{2+} ions and MSA are low and the acid concentration is not above 2 mol dm^{-3}. Figure 2.2 shows SEM images of lead deposited from 0.5 mol dm^{-3} Pb^{2+}, 1.0 mol dm^{-3} MSA and 5 mmol dm^{-3} HDTMA ((a) and (b)) and 1.5 mol dm^{-3} Pb^{2+}, 1.0 mol dm^{-3} MSA and 5 mmol dm^{-3} HDTMA ((c) and (d)) at 25 mA cm^{-2} ((a) and (c)) and 50 mA cm^{-2} ((b) and (d)). Smoother deposit are seen at the lower current density and the lower Pb^{2+} concentration. Figure 2.3 shows SEM images of lead deposited from 0.3 mol dm^{-3} Pb^{2+}, 1.0 mol dm^{-3} MSA and 5 mmol dm^{-3} HDTMA ((a) and (b)) and 0.3 mol dm^{-3} Pb^{2+}, 2.4 mol dm^{-3} MSA and 5 mmol dm^{-3} HDTMA ((c) and (d)) at 25 mA cm^{-2} ((a) and (c)) and 50 mA cm^{-2} ((b) and (d)). Smoother deposit are seen at the lower current density and the lower H^{+} concentration. However, a low concentration of Pb^{2+} ions would adversely affect the capacity of the system. There must, therefore, be a compromise. The current density at the negative electrode can reach 100 mA cm^{-2} without significant adverse effects. Edge effects, i.e. failure occurring at the edge of the electrode more frequently than any other location, should be avoided by ensuring the cell design provides uniform mass transport and current density across the entire electrode surface [79].

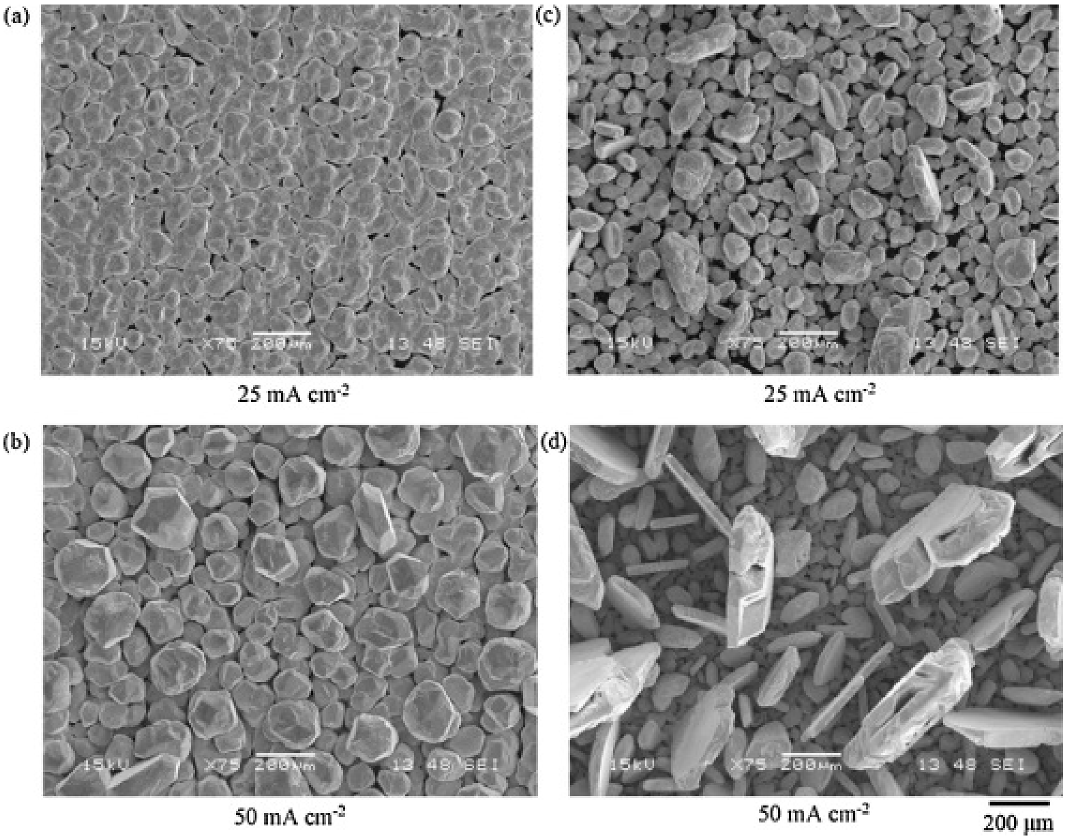

FIGURE 2.2: The effect of Pb^{2+} concentration on the morphology of Pb deposited at the negative electrode in an unstirred Hull cell. (a) and (b) show deposits from 0.5 mol dm^{-3} Pb^{2+}, 1.0 mol dm^{-3} MSA and 5 mmol dm^{-3} HDTMA. (c) and (d) show deposits from 1.5 mol dm^{-3} Pb^{2+}, 1.0 mol dm^{-3} MSA and 5 mmol dm^{-3} HDTMA. Reproduced with permission [79]

2.3.2 Lead Dioxide

Lead dioxide, lead (IV) oxide, has a molar mass of 239.19 g mol^{-1}. There are two forms of lead dioxide, α-PbO$_2$ and β-PbO$_2$. α-PbO$_2$ has a rhombic (columbite) crystalline form, a density of 9.80 g cm^{-3} at 20 °C and an electrical resistivity of 105 μΩ cm^{-1}. β-PbO$_2$ has a tetragonal (rutile) crystalline form, a density of 9.80 g cm^{-3} at 20 °C. PbO$_2$ is actually

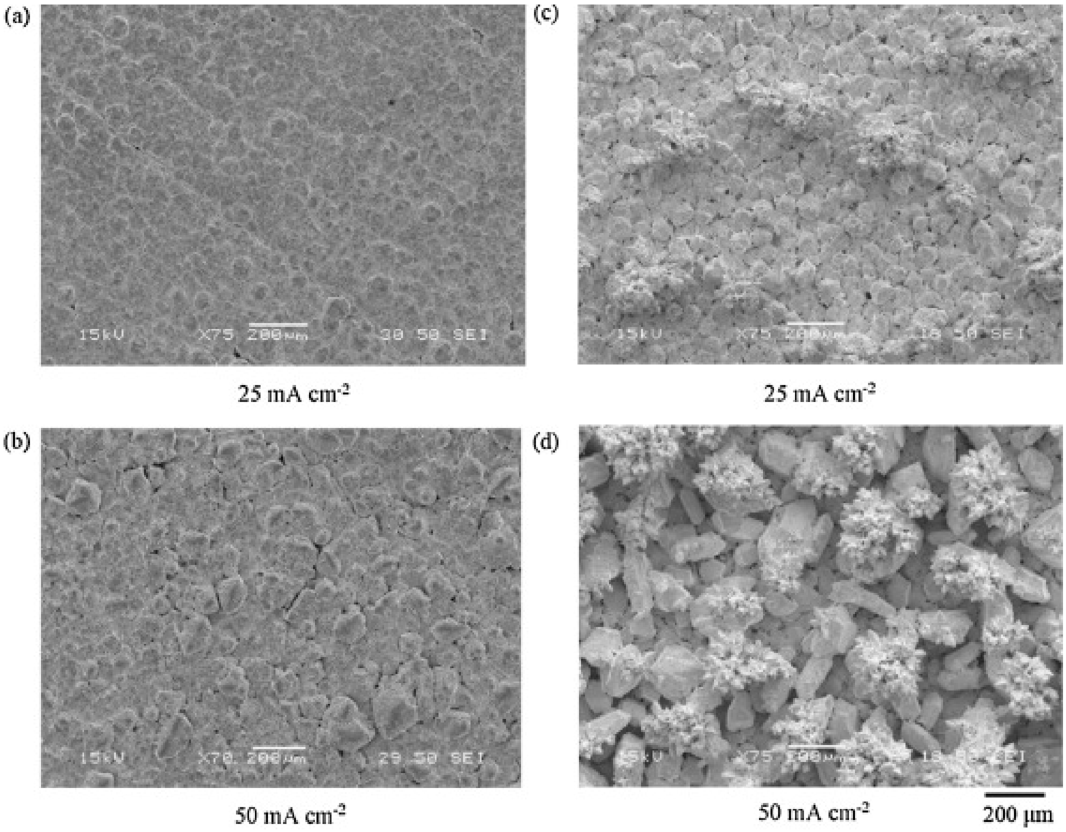

FIGURE 2.3: The effect of H$^+$ concentration on the morphology of Pb deposited at the negative electrode in an unstirred Hull cell for 2 hours. (a) and (b) show deposits from 0.3 mol dm^{-3} Pb^{2+}, 1.0 mol dm^{-3} MSA and 5 mmol dm^{-3} HDTMA. (c) and (d) show deposits from 0.3 mol dm^{-3} Pb^{2+}, 2.4 mol dm^{-3} MSA and 5 mmol dm^{-3} HDTMA. Reproduced with permission [79]

composed of PbO$_x$, where $x = 1.94$–2.03 for α-PbO$_2$ and $x = 1.87$–2.03 for β-PbO$_2$ [26]. In the lead acid battery, it is well known that the conditions and electrolyte composition affect the ratio of α-PbO$_2$ to β-PbO$_2$, with lower current favouring α-PbO$_2$ [81].

Wallis and Wills [78] also conducted cyclic voltammetry on the Pb^{2+}/PbO$_2$ redox couple, shown in Figure 2.4. The same experimental setup was used (described in Section 2.3.1). Significant differences in peak current density were seen and, by the 100th cycle, a decrease in peak current density was observed and the peak occurred over a broad range of potentials. It is shown that the positive redox reaction in the SLFB is far less reversible, the kinetics are far slower, overpotentials are high compared with the negative redox reaction and the reversibility of the reaction degrades significantly with cycling.

Pletcher et al. [82] show that high-quality deposits > 1 mm in thickness are possible over a wide range of Pb^{2+} and MSA concentrations up to a current density of 100 mA cm^{-2}.

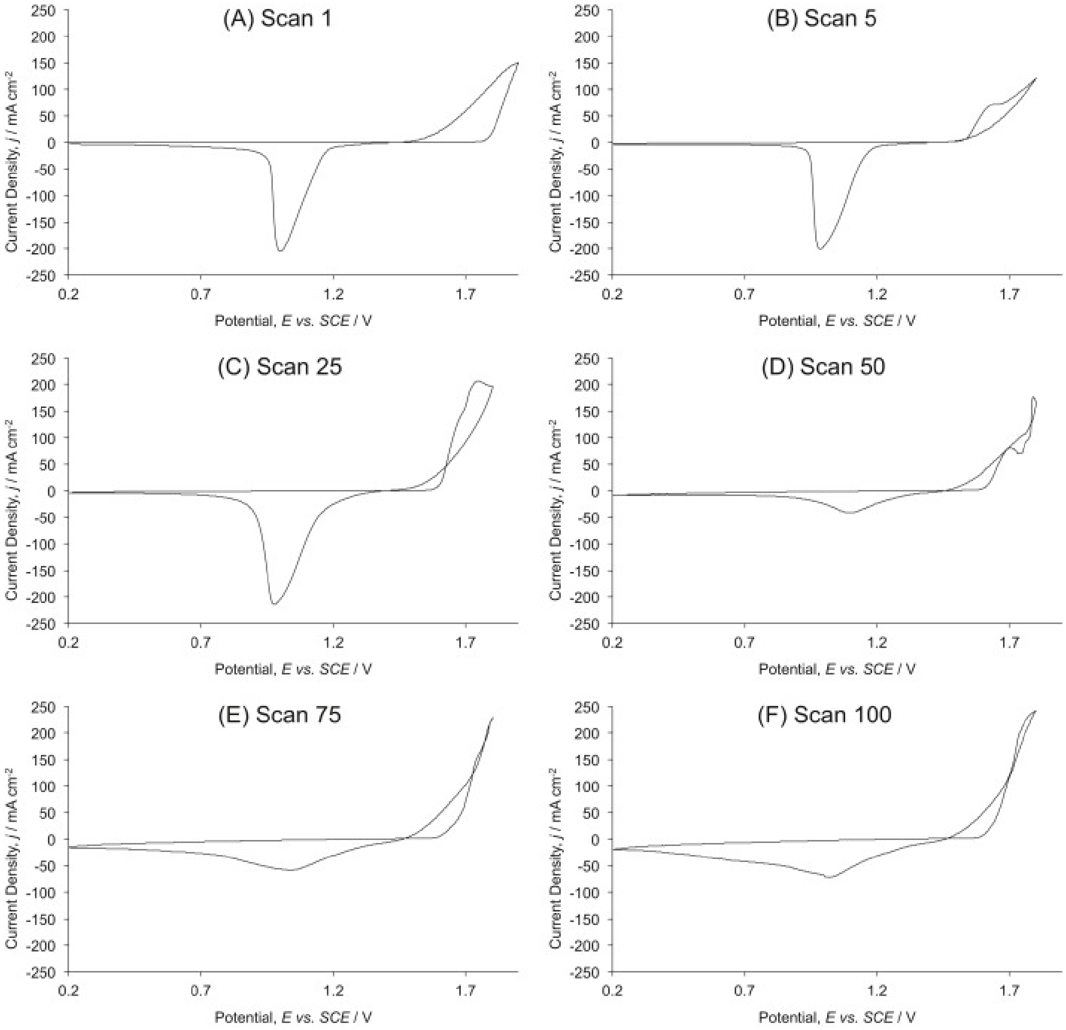

FIGURE 2.4: Cyclic voltammograms for the first (A), fifth (B), twenty fifth (C), fiftieth (D), seventy fifth (E) and hundredth (F) cycle of the $Pb^{2+}/Pb)_2$ redox couple in 1.5 mol dm^{-3} MSA and 0.5 mol dm^{-3} Pb^{2+} on a glassy carbon electrode. Reproduced with permission [78].

Figure 2.5 shows the morphology of PbO_2 deposited at current densities of 20 mA cm^{-2} ((a) and (c)) and 50 mA cm^{-2} ((b) and (d)) from an electrolyte of 1.5 mol dm^{-3} Pb^{2+}, 5 mmol dm^{-3} HDTMA and 0.15 mol dm^{-3} MSA ((a) and (b)), 1.5 mol dm^{-3} MSA ((c) and (d)). However, these deposits were formed by either a single charge or just 6 cycles. It is unclear if these conditions would be sustainable over a number of cycles. In practice, the current density is limited by oxygen evolution occurring at higher overpotentials. Oxygen evolution would decrease coulombic efficiency and Li et al. [83] show that coulombic efficiency of the positive electrode is further decreased when thick deposits are formed. In Pletcher et al.'s work [82], the main aspect that harmed deposit quality was stress within the deposited material. This stress was increased at high acid concentrations and high current densities. It is possible that with cycling these stresses occur more readily. However, further work on this aspect is required.

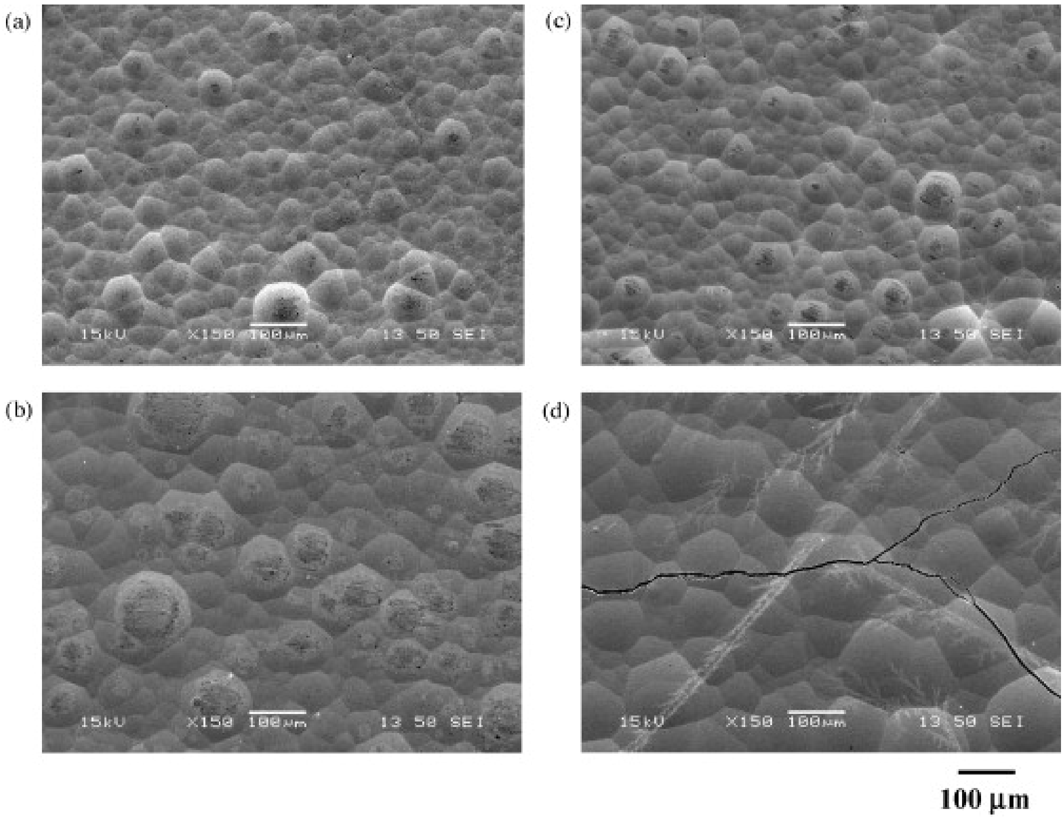

FIGURE 2.5: The effect of H^+ concentration on the morphology of PbO_2 deposited at the positive electrode in an unstirred Hull cell for 2 hours at current densities of 20 mA cm^{-2} ((a) and (c)) and 50 mA cm^{-2} ((b) and (d)). (a) and (b) show deposits from 1.5 mol dm^{-3} Pb^{2+}, 0.15 mol dm^{-3} MSA and 5 mmol dm^{-3} HDTMA. (c) and (d) show deposits from 1.5 mol dm^{-3} Pb^{2+}, 1.5 mol dm^{-3} MSA and 5 mmol dm^{-3} HDTMA. Reproduced with permission [82]

Work by Li et al. [83] and Sirés et al. [84] discuss the conditions required to form different ratios of α-PbO_2 and β-PbO_2. It is possible to form pure α-PbO_2 and pure β-PbO_2 or a mixture of the two. Conditions not only change the ratio of the different forms, but also the quality of the deposit. Both α-PbO_2 and β-PbO_2 can form high-quality deposits free from cracks and holes with a smooth compact morphology under optimal conditions. The reduction of PbO_2 is reported to be far less straightforward than its deposition and, frequently, there is a layer of PbO_2 remaining after discharge. This imbalance leads to material coming away from the positive electrode after cycling for long periods.

Wills et al. have discussed the formation of PbO_2 sludge that results from PbO_2 that is lost from the positive electrode [47]. This sludge can form as a film over the surface of the positive electrode, or it can settle in areas where the electrolyte flow rate is low and can cause a short circuit between the positive and negative electrodes. Edge effects, the growth of PbO_2 along non-conductive surfaces within the cell, were also discussed. Inlet manifolds, cell spacers and cell walls are areas that can allow growth of these deposits across the cell. The PbO_2 on these non-conducting surfaces is not easily removed during discharge, so material continues to grow across them.

2.4 Additives

Often, the right operating conditions in a battery will reduce the impact of problems that can arise within the system. However, this is not true in all cases. Sometimes, additives must be used to ensure good operation. In the SLFB, additives can be used for both negative and positive electrode reactions [78, 79, 85]. Any additive used must be soluble and stable within the electrolyte at any state of charge (SoC). Moreover, as the SLFB is designed to operate in an undivided manner, any additive must not adversely interfere with the reaction at either electrode. However, Krishna et al. [86] have shown that it is beneficial to operate the SLFB in a membrane-divided configuration to allow for electrode specific additives. Failure by shorting is also reduced.

2.4.1 Negative Electrode

The main concern with the deposition of lead at the negative electrode is that lead can deposit unevenly. Due to the high conductivity of lead and the electrolyte's decreased resistance as the inter-electrode gap decreases, any irregularities in the lead surface are intensified as charging continues. This leads to the formation of lead dendrites and subsequent shorting of the cell.

A levelling agent is, therefore, beneficial to lead deposition. Pletcher et al. [79] tested many additives with this aim; either a parallel plate flow cell (Figure 2.6(A)) or a parallel plate beaker cell with stirred electrolyte (Figure 2.6(B)) were used. Check tests were completed between the two different types of cell to ensure the results were comparable. The resulting deposit quality was observed using scanning electron microscopy (SEM) and was then categorised by performance into one of four categories.

Three additives from the highest quality deposit category achieved a coulombic efficiency of over 90 %, hexadecyltrimethylammonium hydroxide (HDTMA), sodium

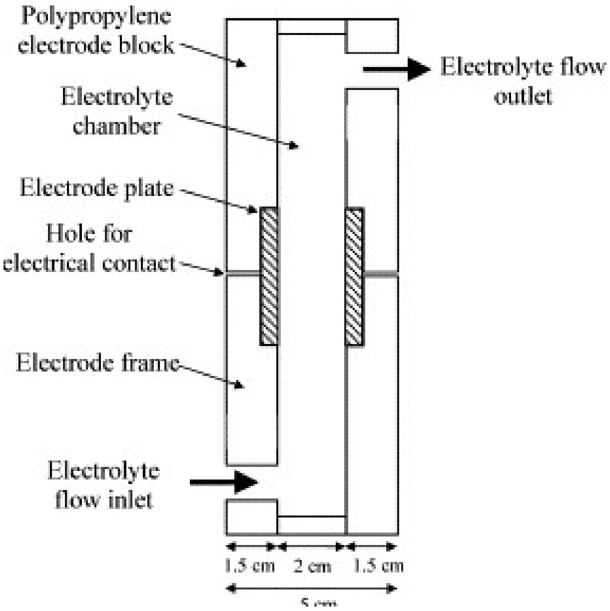

(A) Cross section of a laboratory parallel plate flow cell with 4 cm × 2 cm geometric area electrodes.

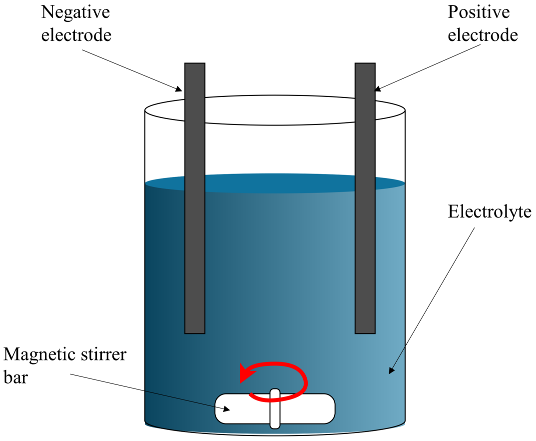

(B) Cross section of a parallel plate beaker cell with stirred electrolyte

FIGURE 2.6: Schematics of cells used by Pletcher et al. [79]. (A) is reproduced with permission.

ligninsulfonate, and Triton™ X100. Sodium ligninsulfonate and Triton™ X100 were both oxidised at the positive electrode. HDTMA was, therefore, the only candidate to maintain effectiveness over time. However, it has been reported that HDTMA is less effective when the system is scaled up [80].

Sodium ligninsulfonate was investigated in detail by Hazza et al. [85]. It was confirmed that the additive acted as a levelling agent for the deposition of lead at the negative electrode. Although it was found that the addition of the additive caused a decrease in charge efficiency and an increase in overpotential at the positive electrode, the quality of the PbO_2 deposit was found to be unaffected by the additive at low ligninsulfonate concentrations. At a concentration of 5 g dm^{-3}, crevices due to oxygen evolution were seen.

2.4.2 Positive Electrode

Slow kinetics are a significant issue for the reduction of PbO_2 in the SLFB. This issue leads to large overpotentials that negatively impact the efficiency of the battery. A catalyst would, therefore, be beneficial to the positive electrode reaction. Bismuth has been shown to be an effective additive at the positive electrode for the lead acid battery [87]. In the SLFB, Feng and Johnson show that Bi^{3+} ions improve the ability of a PbO_2 deposit to oxidise inorganic ions [88]. Wallis and Wills show that Bi^{3+} used in the SLFB improves the kinetics of the positive electrode reaction but report that bismuth preferentially deposits at the negative electrode over lead [78].

A similar surfactant to HDTMA may be beneficial at the positive electrode as well as the negative electrode. With hexadecyltrimethylammonium chloride and bromide, Low et al. [89] formed compact smooth PbO_2 deposits from methanesulfonic acid. However, the deposits were not assessed in the context of operation in the SLFB.

Fluoride has also been reported to improve the deposition of PbO_2. Cao et al. [90] show that F^- enhances the adhesion of PbO_2 to the electrode, while Amadelli et al. report that it also inhibits oxygen evolution at the positive electrode [91]. Lin et al. [92] show that the addition of 0.05 mol dm^{-3} sodium ethanoate significantly increases the cycle life of the SLFB due to the stabilisation of the PbO_2 deposit and the pH fluctuations at the interphase of the electrolyte and the PbO_2 deposit.

2.5 Performance

Research has been completed on the soluble lead system over a range of scales, from beaker cells [93], to 100 cm^2 flow cells [94], to a kW scale flow battery [80]. A range of electrolytes, operating conditions and electrode design and materials have been used. Pletcher and Wills have investigated the effect of conditions on battery performance [95].

Pletcher and Wills have produced an undivided single, parallel-plate flow cell with 1 cm × 2 cm electrodes using an electrolyte of 1.5 mol dm^{-3} lead methanesulfonate and 0.9 mol dm^{-3} MSA [95]. The cell was successfully cycled at current densities of 10-60 mA cm^{-2} achieving coulombic efficiencies typically between 80 % and 95 %. Individual energy efficiencies are not quoted. However, it is stated that the typical energy efficiency of the cells was approximately 65 %. This work was only completed over four cycles.

Oury et al. have produced a novel system that aims to reduce the issues caused by using a high current density at the positive electrode by using a honeycomb-shaped positive electrode [96]. This design uses two planer negative electrodes (6.5 cm × 6.5 cm) and a honeycomb, flow-through positive electrode. The electrolyte flowed in through the top of one cell, over the negative electrode, through the positive electrode into the next cell and out of the cell by flowing over a second negative electrode. Fluoride ions were used as an additive and approximately a hundred cycles with a 75 % energy efficiency were obtained. These cycles, however, were only to a lead-utilisation of 10 %. The flow-through nature of the positive electrode requires the entire plate to be positive. Hence the electrodes cannot be bipolar and the cells cannot be arranged in a bipolar stack. The benefits of which are well known [97].

A system using corrugated graphite sheet and reticulated vitreous carbon (RVC) as the positive and negative electrodes, respectively, had been produced by Banerjee et al. [98]. Various grades of RVC are compared for the negative electrode. The planar electrode area is 3.5 cm × 3.5 cm. Using a current density of 20 mA cm^{-2}, a coulombic efficiency of 95 % is achieved. The authors claim that 200 full charge-discharge cycles are completed with little effect on the cell's efficiency. However, this is achieved using short 10 minute cycles, utilising just 40 mAh of a theoretical 6800 mAh maximum capacity (calculated from the cell description in the article), giving a depth of discharge (DoD) of just 0.6 %.

Suman et al. [99] have determined that the decrease in coulombic efficiency of the SLFB is mainly due to oxygen evolution at the positive electrode. However, as highlighted by Collins et al. [94], as there is a build up of deposits at the electrodes and particles or sludge which comes away from the electrodes with cycling, there must be a decrease in Pb^{2+} concentration in the electrolyte with time and hence this must also be a source of decreased energy efficiency. Other studies have also highlighted that oxygen evolution is generally only observed at high current densities, when MSA concentration is high or when Pb^{2+} concentration is low [82, 100]. Luo et al. [101], however, suggest that at high overpotentials, and hence high current densities, deposition at the positive electrode is more likely to produce a deposit PbO_x with x close to 2.

Cycle life was consistently an issue in early SLFB studies. Using a flow cell with 100 cm × 100 cm electrodes, Collins et al. achieved just 164 cycles with a current density of 10 mA cm^{-2} before uneven deposit growth caused shorting across the electrodes. With increasing current density, the cycle life was further reduced to 40 cycles at 20 mA cm^{-2} and 19 cycles at 30 mA cm^{-2} [94]. However, additives (discussed in Section 2.4), control of potential [101] and maintenance cycles [63] have been shown to significantly increase the cycle life. In the latter case 7000 cycles were achieved [63].

The largest system produced to date is a 1000 cm^2 cell produced under a collaboration among the University of Southampton, C-Tech Innovation Ltd. and E.On. Funding was provided by the Department of Trade and Industry (DTI) [80]. A scale-up factor of 10 from previous work, [47], was chosen for the electrode area. This factor allowed for readily available carbon composite electrodes to be used whilst achieving near commercial scale. Details about cycling tests performed on this system are not well described. The system is described as a four-cell stack cycled at 50 mA cm^{-2} with a charging time of 'longer than 60 minutes'. Poor cycle life of just 10 cycles before shorting occurs is observed, which was attributed to a decrease in the effectiveness of HDTMA at this larger scale. The cycle life was able to be extended to 40 cycles with the addition of sodium lignosulfonate together with HDTMA. Further information about the construction and performance of the stack is limited. The University of Southampton has recently begun another project which aims to produce a battery of a similar scale [102].

2.6 Electrodes

Flow battery electrode research aims to find low-cost electrodes that are highly electrically conductive and highly stable in electrolytes. Carbon-based materials appear to meet these criteria and have found common use in the all-vanadium flow battery [39], the zinc-bromine flow battery [103] and the soluble lead flow battery.

Electrodes for the SLFB can be categorised into two-dimensional (2D) and three-dimensional (3D). 2D electrodes are flat planar electrodes that the electrolyte flows over. 3D electrodes are those which have features that extend away from this plane, such as those shown in Figure 2.7.

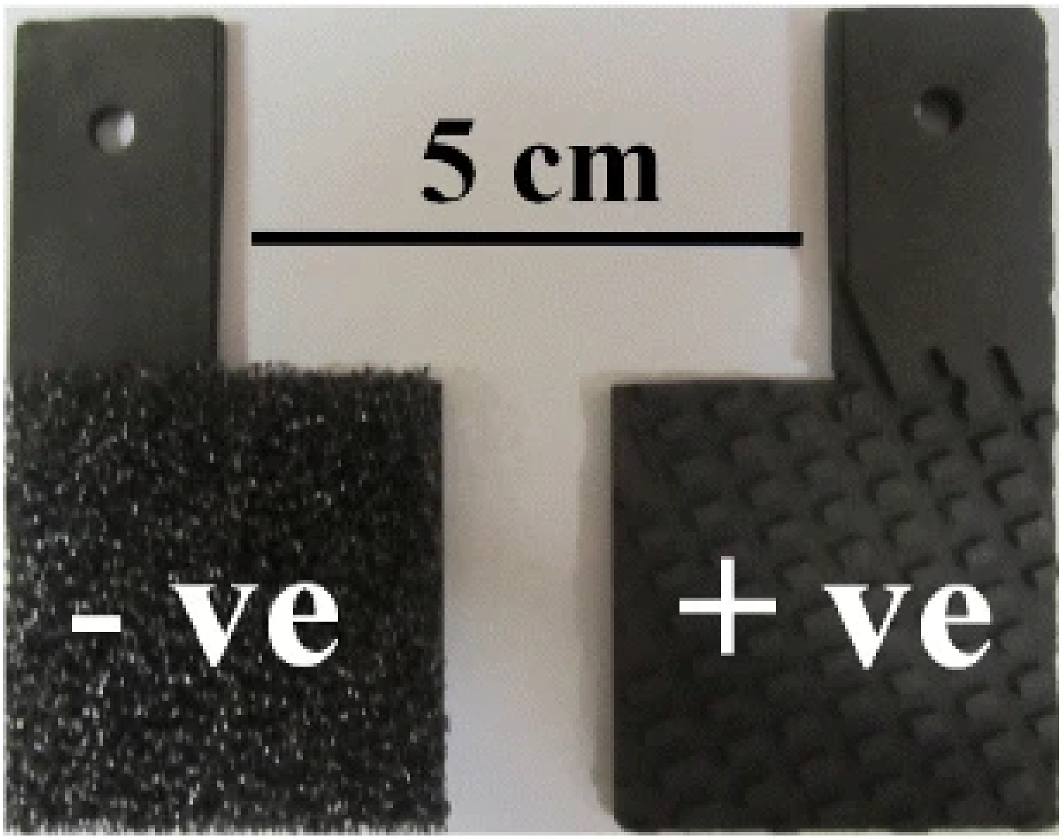

FIGURE 2.7: Example of 3D electrodes used by Banerjee et al. in the SLFB. The negative electrode shown is a 30 ppi reticulated vitreous carbon electrode and the positive electrode is a corrugated graphite plate. Reproduced with permission [98].

The first electrodes used in the SLFB were manufactured by pressing a mixture of carbon powder and high-density polyethene at 344 K with a pressure of 3-60 kg cm^{-2} [95]. This was used as a base for their electrodes:

1. Ni foam was pressed into the carbon polymer.
2. Reticulated vitreous carbon (RVC) pressed into the carbon polymer.
3. Type 2. electrode with scraped RVC.

The smooth plates were found to produce smooth, even deposits. However, solid material was found in the electrolyte after cycling. The type 3 electrodes produced much rougher deposits, but the deposits were found to cluster around the RVC fragments.

Gold has been identified as a possible electrode material for use in the SLFB [44]. However, at over £50,000 kg^{-1}, clearly the cost of gold as a solid electrode is prohibitive [104]. Preliminary work using a thin layer of gold on carbon-polymer electrodes in static electrolyte SLFBs is discussed in Appendix D.

RVC has been shown to have a number of useful properties for use as an electrode material. It has a high porosity, high permeability, large surface area, high thermal resistance and a rigid structure [105, 106]. Furthermore, it has been studied extensively as an electrode material for the recovery of heavy metals, including lead, from effluent streams [107].

2.7 Electrochemical Theory

Below, a summary of the fundamentals of electrochemical theory is presented. The model described in Chapter 4 builds on the theory presented here to develop the mathematical model used for simulations in later chapters.

2.7.1 Definition of terms

In its most basic form, an electrochemical system consists of at least an electrolyte, two electrodes and an external conductor. Newman and Balsara define an electrode as a material that contains electrons as the mobile species, which, as such, can be used to sense the electrons' potential. The electrolyte is defined as a material that conducts charge using ions as the mobile species, and electronic conduction is prevented [108]. At the interface between the electrodes and the electrolyte reduction and oxidation, or redox reactions occur.

An electrochemical reaction can be distinguished from a chemical redox reaction by the separation of reduction and oxidation. In an electrochemical reaction, reduction occurs at one electrode, the cathode, and oxidation takes place at the other electrode, the anode. In a chemical reaction, both reduction and oxidation take place at the same location. An electrochemical reaction is, therefore, divided into two half-reactions contained in their respective half-cells. Each half-reaction involves ions from the electrolyte and the transfer of electrons at the electrode.

Conservation of charge couples the rate of both half reactions. The rates of reaction of each half-cell are related to the current density by Faraday's law:

$$\dot{m} = \frac{IM}{Fz} \tag{2.1}$$

For example, consider an electrolyte containing an ionic species M^{+}. At the anode, the species is oxidised liberating an electron:

$$M^{+} \rightleftharpoons M^{2+} + e^{-} \tag{2.2}$$

At the cathode, the same species is reduced to the metallic form:

$$M^{+} + e^{-} \rightleftharpoons M^{0} \tag{2.3}$$

The half-cells do not have to contain the same electrolyte. In fact, in many electrochemical systems, each half-cell has its own electrolyte. In this case, take the following, more general example:

$$A^{n+1} + e^{-} \rightleftharpoons A^{(n-1)+} \tag{2.4}$$

$$B^{m+1} \rightleftharpoons B^{m+} + e^{-} \tag{2.5}$$

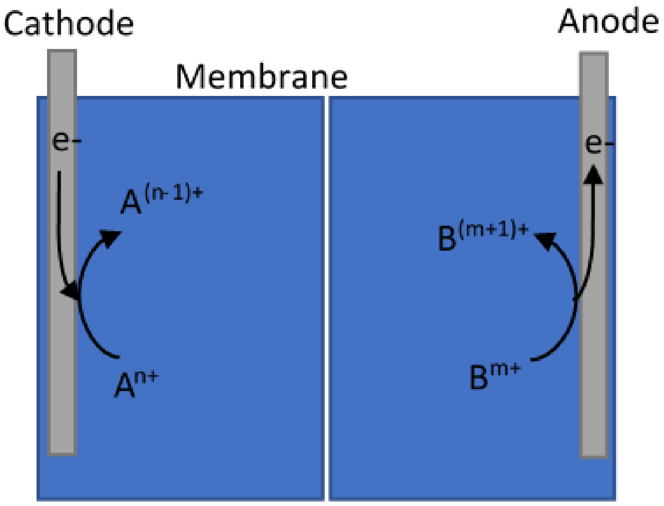

FIGURE 2.8: A typical electrochemical device. At the cathode, the active species A is reduced from a higher to a lower valence (n+ to (n-1)+) by the addition of an electron from the cathode. The active species B is oxidised to a higher valence (m+ to (m+1)+) liberating an electron which is collected by the anode.

Generally, to prevent a spontaneous reaction of the different active species, the electrolyte for each half-reaction must be separated in a way that allows some form of charge transfer but prevents mixing of the active species. This role is often fulfilled by an ion-exchange membrane.

2.7.2 Thermodynamics

Taking the example of an electrochemical device with the half-cells containing the reactions described in Equation 2.4 and Equation 2.5, it is the thermodynamic properties of the species which determines which reaction will tend to be a reduction reaction and which will tend to be an oxidation reaction. Specifically, the electrochemical potentials, which relate to the Gibbs free energy, G:

$$\Delta G = (\sum_i s_i \overline{\mu}_i)_1 - (\sum_i s_i \overline{\mu}_i)_2 \tag{2.6}$$

Where 1 arbitrarily represents one half-reaction and 2 represents the other, $\overline{\mu}_i$ is its electrochemical potential, s_i is the stoichiometric coefficient of species i defined by Equation 2.7.2:

$$\sum_i s_i X_i^{z_i} \rightleftharpoons ne^- \tag{2.7}$$

X_i is the chemical symbol for species i which has valence z_i and n electrons are transferred.

If the Gibbs free energy is negative, then the reactions will occur spontaneously. In the case where no current flows, the Gibbs free energy can be related to the potential difference of the electrodes by:

$$\Delta G = -nFE_{eq} \tag{2.8}$$

Where n is the number of electrons involved in the reaction and F is Faraday's constant. In this case, the potential is known as the equilibrium potential, E_eq, or open circuit potential.

2.7.3 Kinetics

For current to flow in an electrochemical system, there must be a deviation in electrode potential from the equilibrium potential. This deviation is known as the overpotential. The local current density can be related to the overpotential using the Butler-Volmer equation:

$$i = i_0 \left[e^{\frac{\alpha_a F}{RT}\eta} - e^{-\frac{\alpha_c F}{RT}\eta} \right] \tag{2.9}$$

Where I is the current density, i_0 is the exchange current density, which is equivalent to a rate constant in a chemical reaction [108], α_a and α_c are activity coefficients.

2.7.4 Mass transport

Mass transport in electrolytes is governed by three different mechanisms: diffusion, migration and convection.

Diffusion occurs when there is a difference in concentration within a solution. The rate of mass transport due to diffusion can be predicted by Fick's first law:

$$J_i = -D_i \left(\frac{\partial c_i}{\partial x} \right) \tag{2.10}$$

Where J_i is the mass transfer rate of species i, c_i is its concentration, x is distance in a given dimension, t is time, and D_i is the diffusion coefficient of the species in a certain solvent. Leading on from this, Fick's second law gives the rate of change of concentration:

$$\frac{\partial c_i}{\partial t} = D_i \left(\frac{\partial^2 c_i}{\partial x^2} \right) \tag{2.11}$$

Migration is the movement of charged ions due to a potential difference. In weak solutions, where charged particles are diffused enough that it can be assumed that there are no ion to ion interactions, migration can be defined by the simple linear relationship:

$$\frac{\partial c_i}{\partial t} = -u_m c_i \left(\frac{\partial \phi_l}{\partial x} \right) \tag{2.12}$$

Where ϕ_l is electrolyte potential and u_m is ionic mobility. In many modelling papers, mobility is defined as:

$$u_{m,i} = \frac{D_i}{RT} \tag{2.13}$$

Convection is the movement of the bulk fluid and can be driven by an applied pressure, or a buoyancy force due to differences in density. Fluid flow can be defined by a range of equations which are valid under different assumptions. For example, the Navier-Stokes equations describe viscous fluid flow:

$$\rho(\mathbf{u} \cdot \nabla)\mathbf{u} = \nabla \cdot [-p + \mu \nabla \mathbf{u}] \tag{2.14}$$

2.8 Modelling and Simulation

Modelling can be defined as the deliberate representation of a physical system or phenomenon. Models are used when they are lower-cost or easier to work with than the real system and are often useful tools in improving our understanding of it [109]. Models can be physical, conceptual or numerical. Indeed, many physical experiments may be defined as models [110].

However, the definition of modelling in this thesis will refer to numerical modelling, specifically computational modelling.

2.8.1 Battery modelling

Battery modelling can occur over a range of length scales. Figure 2.9 describes a variety of modelling techniques categorised by length scale. Generally, at smaller length scales, the model will provide results that are closer to the physical reality. However, modelling at smaller length scales is more computationally intensive. At larger length scales, models contain less physical detail but can include much larger systems for a given amount of computational resource. Battery modelling can broadly be categorised into the following sections [111, 112]:

- **Large scale modelling** For large scale models, the system is generally treated as a "black box" whereby empirical performance data over a range of operating conditions is used to predict how the overall system will perform with complex or realistic duty cycles. This can be to size a system for a required performance or to predict and optimise the economic use of a battery. Stochastic models such as

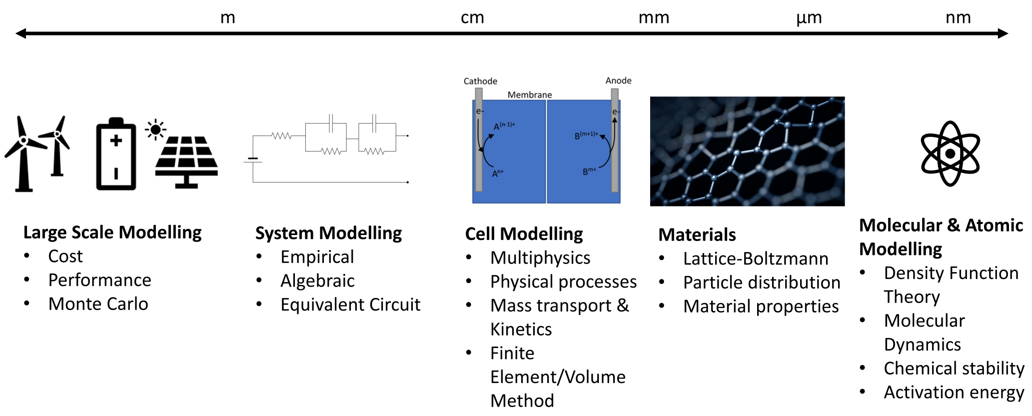

FIGURE 2.9: Classification of battery modelling over a range of length scales.

Monte Carlo simulations, which simulate numerous possible conditions to predict the likelihood of various outcomes, are included in this category. For example, Zhang et al. used Monte Carlo simulations to predict the remaining useful life of lithium-ion batteries [113].

- **System modelling** System modelling includes slightly more detail than large scale modelling. Often empirical data from single cells is used to build a simplified representation for a single cell, either by simplifying physics-based equations, by fitting cell performance to differential or algebraic equations or by using the data to build an equivalent circuit model. Systems modelled using equivalent electrical circuit models (EECs) are used to simulate the electrical performance of the battery by using common electrical components (resistors, capacitors and inductors) to describe the response of a battery system. Different configurations or sizes of cells and components can be quickly optimised using this form of modelling. Nejad et al. discuss a range of EECs for determining the condition of lithium-ion batteries [114].

- **Cell modelling** Multiphysics modelling is used to simulate physical processes within a battery. These models are generally based on conservation of mass, momentum, charge and energy. Equations such as Nernst-Planck and Butler-Volmer are used to simulate the mass transport and kinetics of the battery. Where there is movement of a fluid, for example flow of electrolyte in a flow battery, equations such as Navier-Stokes or, more generally, computational fluid dynamics (CFD) may be used. Simplifying assumptions are still made, including homogenisation of domains, such as porous electrodes, a reduction of spatial dimensions, e.g. creating a two dimensional model, excess electrolyte and electroneutrality. These equations can be solved using techniques such as finite element methods (FEM) or finite volume methods (FVM). For example, Al-Fetlawi et al. have produced a non-isothermal model using FEM for the all-vanadium redox flow battery [115].

- **Materials** Techniques such as the Lattice-Boltzmann method (LBM) are used to simulate the movement of particles at smaller length scales. With cell modelling local pressure, velocity and concentration distributions are modelled. The LBM uses fictitious microscopic particles to represent velocity, pressure and movement of ions within a domain. However, these particles are still assumed to have general material properties, such as mass, charge and volume. Qiu et al. use the LBM to model flow of electrolyte through pores in electrodes for the all-vanadium flow battery [116].

- **Molecular and atomic** At this length scale, individual molecules, atoms or ions are simulated using techniques such as molecular dynamics or density functional theory (DFT). Molecular dynamics simulates individual molecules as interacting particles using Newtonian equations of motion for each particle. This method is used to predict properties such as diffusion and thermodynamic properties. DFT uses quantum theory to investigate the arrangement of individual electrons and atomic nuclei within a molecule or ion to predict its properties, such as activation energy and chemical stability. Craig et al. have used DFT to explain the interaction between the active species and a poly(3,4-ethylenedioxythiophene) cathode for aluminium batteries [117].

2.8.2 Lead battery modelling

Given that lead-acid batteries are the oldest secondary battery, surprisingly little work has been completed to model lead-based batteries. This may, in part, be due to the complexity of modelling such batteries. In lead-acid batteries, as with redox flow batteries, the electrolyte contains active ions. Hence, as the SoC varies, the composition of the electrolyte changes. This has implications on the conductivity and voltage of the battery.

Numerical modelling has been used to understand aspects of the lead-acid battery since the late 1800s [118]. However, the complexity and nonlinearity of many aspects of this battery mean only recently, with the increasing availability of high-powered computational facilities, have attempts to model the whole system in detail been productive.

Unlike in a lithium ion battery capacitive or other intercalation reactions, lead acid battery electrode reaction kinetics cannot be modelled as a linear relationship and nonlinear Butler-Volmer kinetics are required. The overpotentials are also not equal in magnitude for charge and discharge, i.e. in the Butler-Volmer equation (Equation 2.9), $\alpha_c \neq \alpha_d$.

There are also significant changes in the physical properties of lead-based batteries during operation. For example, in a LAB, $PbSO_4$, an electrical insulator, is formed during discharge. At low fractions of $PbSO_4$, this causes only a slight change in electrical conductivity of the electrodes. However, as described by Euler et al. [119], for a two phase material consisting of a conductive phase and a non conductive phase, there is a critical limit for the volume fraction of nonconductive material, after which, the two phase material becomes nonconductive. The voltage drop which can occur in the LAB due to this critical limit being surpassed is known as Spannungsknie [118].

Simonsson and Ekdunge determine the electrode kinetics for porous lead dioxide [120], and porous lead [121], electrodes for the lead acid battery. They build a model to explain the current distribution in the positive electrode, showing that at high rates the current density both electrodes is greater at the surface. In the lead electrode, they go on to explain that this leads to a layer of lead sulphate covering the electrode surface which is the limiting factor during discharge at high currents.

Later Gu et al. developed a more complete model of the lead acid battery [122]. Their model incorporated transient charge/discharge behaviour, electrode kinetics, mass transport and convection of electrolyte due to density changes caused by acid stratification. Sauer et al. [123] develop a similar model for acid stratification and combine it with an equivalent circuit model; an efficient technique for estimating the battery current distribution, electrolyte concentration and state of charge of the electrodes, both spatially and temporally is developed.

2.8.3 Flow battery modelling

As with the lead-acid battery, numerical modelling has been used as a tool to understand flow batteries for almost as long as they have existed. Flow battery modelling has been an active area of research since the 1950s [112].

Ashraf Gandomi et al. [124] define a number of different design parameters for RFBs and link them to various loss mechanisms and thus how they affect commonly used performance metrics. The parameters are split into electrolyte, operating conditions (electrochemical and physical) and the electrochemical reactor (or stack). Within the electrolyte they define the following parameters:

- Concentration
- State of Charge
- Viscosity
- Conductivity
- Supporting electrolyte

The electrochemical operating conditions are current and voltage, and the physical operating conditions are flow rate and temerature.

The parameters in the stack are further broken down into the following categories:

- Electrolyte flow field
  - Channel geometry
  - Conductivity and porosity
- Electrode
  - Porosity
  - Surface area
  - Surface chemistry
  - conductivity

- Membrane
    - Thickness
    - Conductivity
    - Permeability
    - Ionic selectivity
- Manifold

The following sections provide an overview of efforts to model each of the relevant areas and how they affect the performance of RFBs via various losses. Ashraf Gandomi et al. describe these losses as polarisation losses (kinetic, ohmic and mass transport), coulombic losses (ion crossover, side reactions and shunt currents), and parasitic and pumping losses [124].

Zheng et al. categorise VFB modelling by the length scales, macro, micro and molecular/atomic methods with modelling applications of market, stack/system, cell and materials [111]. Chakrabarti et al. extrapolate these categories to include all RFB models [112]. In this section the frameworks defined by Gandomi et al. [124], Zheng et al. [111] and Chakrabarti et al. [112] will be used to provide an overview of the literature surrounding flow battery modelling.

2.8.3.1 Electrolyte flow

The flow of electrolyte in RFBs is an important area of research. The flow within the stack must balance achieving an optimum distribution of active species with a sufficient flow rate at the electrodes and maintaining acceptable parasitic pumping losses. Miyabashi et al. claim that a uniform distribution of electrolyte flow results in an increased energy efficiency [125].

Electrolyte flow is governed by convection, which is driven by a difference in pressure across the domain. The term convection covers both natural convection and forced convection. Natural convection occurs when there are differences in density within a solution, often due to a thermal gradient. However, in a reacting solution, this may also be due to differences in composition.

Forced convection occurs when there is a deliberate application of a force to the solution. This may be pumping, stirring or application of a pressure difference across the solution.

While there has been work to visualise the flow within RFB flow fields experimentally [126–130], precise data on flow distribution and the opportunity to optimise designs to achieve uniform flow mean numerical modelling is a powerful tool for understanding electrolyte flow in RFBs.

Escudero-González and López-Jiménez [131, 132] provide several parameters for quantitatively determining the uniformity of flow in different regions of the flow cell.

Flow fields in RFBs are generally either *flow by* fields which have planar or textured electrodes which the electrolyte flows over, or *flow through* electrodes which are porous electrodes through which the electrolyte flows.

Kok et al. have completed a series of studies investigating mass transport, including flow, in flow through porous flow battery electrodes using experimental techniques to measure permeability, and multiphysics simulations, including through domains generated from computed tomography scans [133–135].

2.8.3.2 Laminar flow between plates

For the flow by configuration, the flow field may be modelled as flow between two flat plates. The assumption here is that the plates are wide enough that the edges of the flow field do not have a significant influence on the flow of electrolyte. If the flow is assumed to be uniform in the streamwise direction, this case is known as Hele-Shaw flow [136].

$$\mathbf{u} = \frac{G_{ie}x - x^2}{2\mu}\nabla p \tag{2.15}$$

Where $\mathbf{u}$ is the electrolyte velocity. G_{ie} is the separation of the plates (interelectrode gap), x is the dimension normal to the surface of the plate, μ is dynamic viscosity and p is pressure.

This equations gives a parabolic velocity distribution.

2.8.3.3 Flow in porous media

Flow through electrodes are normally a porous conductive material. While calculating the flow explicitly through such domains is extremely computationally intensive, there are a number of simplifications which can be made. While on a micro-scale, the properties of the electrolyte flow in porous media are irregular, averaged over a macro-scale, these properties become much more regular spatially and temporally [137]. In this context, Darcy's Law is analogous to Stokes flow in a porous medium [138].

$$q = -\frac{K}{\mu}\nabla p \tag{2.16}$$

Where q is the flow rate through a porous medium and K is the porous medium's permeability. Permeability of a porous media may change with time if it is eroded or if there is contamination or a build-up of another substance.

Brinkman equations produce a relationship between permeability and porosity for a porous medium when assumed to consist of an array of spheres. This is valid for high porosities (>0.6) [139, 140].

$$\nabla p = -\frac{\mu}{K}\mathbf{u} + \mu\nabla^2\mathbf{u} \tag{2.17}$$

Forchheimer introduces a term for nonlinearities in fluid flow in porous media. This can occur even at low Reynold's numbers ($\sim$10) because of the high form drag due to the high surface area in porous media [137]. Equation 2.18 shows Darcy's Law modified with the Forchheimer term.

$$\nabla p = -\frac{\mu}{K} - c_F K^{-\frac{1}{2}}\rho|\mathbf{u}|\mathbf{u} \tag{2.18}$$

Where c_F is a form-drag coefficient and ρ is the fluid density.

Numerous studies have used these equations to simulate flow through porous electrodes in RFBs. It is also possible to model multiphase flow through porous media by slightly adapting these equations. Al-Fetlawi et al. used this technique as part of their simulations investigating gas evolution reactions in the VFB [115, 141].

2.8.3.4 Conductivity

In a flow battery, the electrolyte consists of dissociated anions and cations dissolved in a solvent. As the dissolved ions are charged, a current can flow, and the solution becomes conductive. Kohlrausch's law of independent movement of ions is useful for finding the conductivity of a solutions made up of multiple ions. This will apply to any real solution, consisting of at least a positive ion and a negative ion. It states that a solution's conductivity is equal to the sum of the conductivities of its constituent ions. This law assumes the electrolyte is wholly dissociated and that there is no interaction between the ions and so is only valid for infinitely dilute solutions [142].

$$\Lambda^0 = \sum_i \nu_i \lambda_i \tag{2.19}$$

Λ^0 is the limiting molar conductivity of the electrolyte, ν_i is the relative number of ions of species i (e.g. in H_2SO_4, $\nu_H = 2, \nu_{SO_4} = 1$) and λ_i is its molar ionic conductivity.

The molar conductivity, Λ is related to the electrolyte conductivity, σ in Equation 2.20.

$$\sigma = \Lambda c = F^2 \sum_i z_i^2 u_{m,i} c_i \tag{2.20}$$

Where $c = \frac{c_i}{\nu_i}$, F is Faraday's constant, z_i is the charge of ion i, $u_{m,i}$ is its mobility and c_i is its concentration.

The mobility, $u_{m,i}$, is given by the Nernst-Einstein equation.

$$u_{m,i} = \frac{D_i}{RT} \tag{2.21}$$

The Nernst-Einstein equation, however, is only valid at infinite dilution. Electrostatic interactions occur over a long range. Hence, even in dilute solutions these effects are important. The Nernst-Einstein equation can be modified to include the activity of the ions, Equation 2.22.

$$u_{m,i} = \frac{D_i}{RT} \gamma_{corr} \tag{2.22}$$

γ_{corr} can be related to the activity coefficient, γ_i:

$$\gamma_{corr} = \gamma_i^{\alpha},\ \alpha \approx \frac{\sqrt{I}}{|z_i|} \tag{2.23}$$

Peter Debye and Erich Hückel proposed a theory to explain why the activity of electrolyte deviates from that of an ideal solution in which the ions do not interact [143]. The Debye-Hückel law can be written as Equation 2.24.

$$log(\gamma_i) = \frac{-Az_i^2\sqrt{I}}{1 + Ba_0\sqrt{I}} \tag{2.24}$$

Where A and B are constants and a_0 is an empirically fitted function. I is the ionic strength which can be related to concentration, c, of species i, by:

$$I = \frac{1}{2}\sum_i z_i^2 c_i \tag{2.25}$$

Their limiting law (approaching infinite dilution) can be written as in Equation 2.26 [144], as I approaches zero, $1 + Ba_0\sqrt{I}$ tends to 1:

$$log(\gamma_i) = -Az_i^2\sqrt{I} \tag{2.26}$$

The theory only accounts for interactions between distant ions and is hence only applicable to dilute solutions. Some physical properties are still assumed to be those of the solvent. The following assumptions are still made:

- The solution is completely dissociated
- The ions are not polarised by the electric field and remain spherical
- The solvent simply provides a medium of constant permittivity.

Kohlrausch had previously described how conductivity varies from the limiting case in Equation 2.19. Onsager later built on Debye and Hückel's work to explain this law [145].

$$\Lambda = \Lambda^0 - K\sqrt{c} \tag{2.27}$$

Where Λ is molar conductivity, Λ_0 is molar conductivity at infinite dilution and K is a coefficient specific to the electrolyte.

2.8.3.5 Porous electrodes

The use of a porous material as an electrode has well known advantages. Firstly, a porous electrode provides a much greater surface area than a planar electrode which, as with other modelled approaches, can compensate for slow kinetics. The active species held in the electrolyte within the porous structure are inherently close to the electrode surface. Thus, electrolyte resistance and mass transport become less troublesome. In the case of deposition electrodes, such as the SLFB, the higher surface area also means, for the same amount of deposited material, the mechanical stress at the interface will be lower.

Tiedemann and Newman developed a one dimensional model for a porous separator and a macrohomogeneous porous electrode in contact with each other. They assume ohmic losses are dominant when compared to kinetic or concentration overpotentials [146].

2.8.3.6 Membranes

The membrane is a crucial component of most redox flow batteries. It ensures separations of the active species of each half-reaction. However, it is one of the most complex parts of a battery. Ion-exchange membranes consist of a porous matrix, which holds charged ions in place [147, 148].

There are several methods for modelling ion-exchange membranes. Each can include multiple ions crossing the membrane.

2.8.3.7 Nernst-Planck-Poisson

The Nernst-Planck-Poisson (NPP) method models the membrane as a porous medium with negative (positive) ions immobilised in a solid matrix for cationic (anionic) membranes. The pores are filled with electrolyte consisting of water and mobile ions. Poisson's equation relates the potential to the charge density:

$$\nabla \cdot (-\epsilon \nabla \phi_l) = \rho_c \tag{2.28}$$

Where ϵ is the permittivity in F m^{-1}, ϕ_l is the potential of the electrolyte in V and ρ_c is the charge density in C mol^{-3}. We can split ρ_c into the charge from the fixed ions and the charge from the mobile ions:

$$\rho_c = F \sum_i^N z_i c_i + z \rho_{c,fix} \tag{2.29}$$

Where F is Faraday's constant in C mol^{-1}, z_i is the valence of species i and c is its concentration in mol m^{-3}, which are summed over all N species. $\rho_{c,fix}$ is the charge density of the fixed ions in C mol^{-3}. Nernst-Planck equations describe the transport of species. As the membrane is a porous medium, effective diffusion coefficient and mobilities are used. Bruggeman assumptions, where a porous material is assumed to consist of two randomly distributed homogeneous, isotropic phases which are arranges as particles which are small compared to the sample size [149], are used to calculate the effective parameters.

$$\boldsymbol{J_i} = -d_{i,eff} \nabla c_i - z_i u_{m,i,eff} F c_i \nabla \phi_l + \boldsymbol{u} c_i \tag{2.30}$$

$$u_{m,i,eff} = \frac{D_{i,eff}}{RT} \tag{2.31}$$

$$D_{i,eff} = \varepsilon^{1.5} D_i \tag{2.32}$$

Where $\boldsymbol{J_i}$ is the flux of species i in mol m^{-2} s^{-1}, D_i is its diffusion coefficient in m^2 s^{-1}, $u_{m,i}$ is its mobility in s mol kg^{-1}, $\boldsymbol{u}$ is the electrolyte velocity in m s^{-1}, R is the gas constant in J K^{-1} mol^{-1}, T is the temperature of the electrolyte in K and ε is the membrane porosity. The subscript eff denotes an effective parameter in the porous media.

In the membrane, we can assume electrolyte velocity, $\boldsymbol{u} = 0$. As there is no production or consumption of ions and the electrolyte is stationary, we can state $\nabla \cdot \boldsymbol{J_i} = 0$.

2.8.3.8 Including Donnan potentials and electrolneutrality

The problem with the NPP method is when solving across the membrane-electrolyte boundary, the potential and concentration gradients are extremely steep. Hence, a large number of very fine elements is needed close to the boundary. We can rewrite the Nernst-Planck equation to include the electrochemical potential. Electrochemical potential, $\overline{\mu}_i$ (in J mol^{-1}) is expressed as:

$$\overline{\mu}_i = RT \ln\left(\frac{c_i}{c_{i,ref}}\right) + Fz_i\phi_l \tag{2.33}$$

Rewritten Nernst-Planck:

$$\boldsymbol{J_i} = -u_{m,i,eff} c_i \nabla \overline{\mu}_i \tag{2.34}$$

As we have stated $\nabla \cdot \boldsymbol{J_i} = 0$ and $u_{m,i,eff}$ is constant, we can say that for a sharp change in c_i, there will be a corresponding change in $\nabla \overline{\mu}_i$. However, as c_i will be neither close to 0 or ∞, we can say $\nabla \overline{\mu}_i$ will not be near vertical and therefore $\overline{\mu}_i$ will only have a small change on either side of the boundary. Therefore, we can assume [150]:

$$\overline{\mu}_{i,1} = \overline{\mu}_{i,2} \tag{2.35}$$

Where 1 denotes the electrolyte side of the boundary and 2 denotes the membrane side of the boundary. We can then apply this as a boundary condition at the internal boundary, known as the Donnan boundary condition:

$$\phi_{l,1} - \phi_{l,2} = \frac{RT}{z_i F} \ln\left(\frac{c_{i,1}}{c_{i,2}}\right) \tag{2.36}$$

Assuming electroneutrality replaces the Poisson equation with:

$$\rho_c = 0 \tag{2.37}$$

Therefore:

$$\nabla \cdot \sum_{i}^{N} z_i F \boldsymbol{J_i} = 0 \tag{2.38}$$

2.8.3.9 Fully selective membrane

This method only works if it can be assumed that the membrane allows only a single ion across it. This may be possible if modelling a perfect proton exchange membrane, but realistically this can only be assumed for an anionic exchange membrane where the only mobile ion is $CH_3SO_3^-$. If it is assumed there is only a single mobile ion and electroneutrality remains valid, the sum of the charge due to the fixed ion and the charge due to the mobile ion must be zero:

$$\rho_{c,fix} + \rho_{c,mob} = 0 \tag{2.39}$$

$$c_{mob} = -\frac{z_{fix} c_{fix}}{z_{mob}} \tag{2.40}$$

If the fixed charge (the charge of the membrane structure) is evenly distributed, we can assume:

$$\nabla c_{mob} = 0 \tag{2.41}$$

Therefore, the Nernst-Planck equation becomes:

$$\boldsymbol{J_i} = z_{mob} u_{m,mob,eff} F c_{mob} \nabla \phi_l \tag{2.42}$$

Or

$$\boldsymbol{J_i} = -\frac{\sigma_l}{z_{mob} F} \nabla \phi_l \tag{2.43}$$

Therefore

$$\boldsymbol{i_i} = -\sigma_l \nabla \phi_l \tag{2.44}$$

Where i is the current density in A m^{-2}, σ_l is the electrolyte conductivity and the subscript *mob* denotes the mobile ion. Assuming a fully selective membrane is advantageous because the only empirical inputs required are the conductivity of the membrane and the fixed charge distribution. As mentioned previously, however, it only works with a single charge carrier, which is a simplification even for the anionic membrane case.

NPP is impractical because of the need for permittivity and a very fine mesh (sub nm scale, increased solve times, and possible memory issues unless solved in 1D). Therefore for multiple mobile ions, using the method with Donnan potentials and electroneutrality is sensible. This method requires the diffusion coefficient for each ion in the membrane, which can be approximated using the Bruggeman correlation and the electrolyte diffusion coefficients, the method discussed in Section 2.8.3.7 using Equation 2.32. However, this requires knowing the porosity of the membrane and even then this is an approximation for tortuosity and does not account for the pore size being of a similar order to the molecule size. Krishna et al. [86], provide the conductivities of various separators at different concentrations, which may allow the effective diffusion coefficients for each ion to be calculated.

2.8.3.10 Deposition and dissolution

Electrochemical deposition and dissolution require a redox reaction whereby the oxidation state of a solvated species changes to form a solid during deposition. During dissolution, the oxidation state reverts to the original state and the solid species once again becomes solvated. In the case of metals, metal ions, M^{z+}, are reduced to a solid metal, M during deposition and during dissolution the metal is oxidised back to the soluble positive ions. In a metal deposition reaction the reaction in Equation 2.45 occurs at the interface between the electrode surface and the electrolyte in the left to right direction. Metal dissolution is described by the same equation but in the right to left direction. This reaction can occur via two types of process: electrodeposition and electroless deposition [151]. The difference is simply the source of electrons. Electrodeposition requires an external supply connected to the electrodes, whereas electroless deposition sources electrons from a reducing agent.

$$M^{z+} + ze^{-} \rightleftharpoons M \tag{2.45}$$

As is the case in the soluble lead flow battery, solvated metal ions may also be further oxidised to form a metal oxide. In this case, another element, such as oxygen is required to bind to the metal with a higher oxidation state. As an example of deposition from an aqueous solution, a metal ion, M^{z+}, is oxidised to form a solid metal oxide.

$$xM^{z+} + yH_2O \rightleftharpoons M_xO_y + ne^- + 2yH^+ \tag{2.46}$$

Where x, y and z satisfy conservation of charge.

2.8.3.11 Soluble lead flow battery modelling

It has been highlighted that the flow has a significant effect on the performance of the cell [152]. For the soluble lead chemistry to develop into a commercial system, the flow over the electrodes must be even and at an optimal speed.

There is also a need to design a flow field such that the electric path through the electrolyte is long enough to reduce the bypass, or shunt currents (currents that pass around the cell via the common electrolyte rather than through the bipolar electrodes) whilst still providing an adequately low-pressure loss [69]. This may require an electrolyte manifold that is external to the cell.

In recent years, the increase in computing power has made computational modelling and simulation easier, faster and more accessible. Multiphysics software, for example by COMSOL [153] or Asys [154], has led to the entire system for a flow battery to be modelled. This, combined with a growing amount of experimental data on the SLFB for model validation, has led to several models for the SLFB to be developed.

Shah et al. [155], Bates et al. [156], Oury et al. [157], and Nandanwar and Kumar [152, 158–160], have performed two dimensional, numerical simulations that consider the flow conditions as well as the kinetics of electrode reactions and the mass transport of Pb^{2+}, H^+ and a negative counter ion in an aqueous electrolyte. With the exception of Oury et al. [157], who simulated the steady-state of the system, all previous SLFB models have simulated the transient behaviour of the battery. Nandanwar and Kumar [152, 158–160], and Oury et al., [157], used the methanesulfonate ion, $CH_3SO_3^-$ as a counter ion. Shah et al., [155] also employed the methanesulfonate ion; however, in their methodology, the sulphuric acid anion, HSO_4^- is used. Bates et al., [156], also used HSO_4^- as the counterion. Pb^{2+} is insoluble in sulphuric acid and sulphuric acid is likely to dissociate further to SO_4^{2-} so it is unclear why this is used rather than $CH_3SO_3^-$.

Shah et al. produced the first SLFB model [155]. Their work focused on the effect of different current densities on the performance of the SLFB and shows that, as seen in experimental results, the coulombic efficiency (defined as the total charge drawn from the cell during discharge divided by the total charge applied to the cell during charge) of the system decreases as current density increases. They successfully simulated the two-step charging mechanism of the SLFB by including oxidation of the solid oxide deposit at the positive electrode.

Bates et al. [156] have produced a model of the SLFB and have run simulations to show the effect of different operating conditions on the performance of the SLFB. An increase in temperature is shown to increase the overpotential. However, the authors use several unrealistic conditions in the study, including simulations of the SLFB at 600 K. This temperature is significantly higher than the boiling point of the electrolyte and close to the melting point of lead. No phase change is included in the model. Furthermore, experimental data by Ji et al. [161] show that the overpotentials actually decrease with increasing temperature.

Oury et al. [157] proposed a novel honeycomb positive electrode design. Their proposed design provides an increase in the positive electrode's surface area compared with the negative electrode in an attempt to reduce the overpotentials associated with the positive reaction. This design consists of a positive-flow through electrode sandwiched between two planar negative electrodes and hence a stack of cells manufactured in such a way could not be arranged to form a bipolar stack. Significant further work would also be required to provide even flow of electrolyte over the electrodes.

Nandanwar and Kumar first investigated non-uniform current densities [152]. Then they studied the voltage spike/trough at the start of charges/discharges, which they termed the coup de fouet effect [158]. Most recently, they have incorporated free convection into their model. Free convection is the movement of the electrolyte due to its change in density. The authors compared two cases, forced convection, i.e. the flow is only due to pumping, and mixed convection, where both free and forced convection are considered. They concluded that at higher current densities (> 30 mA cm^{-2}) free convection becomes dominant and the system is able to run with a negligible applied flow rate [159].

Shah et al. [155], Nandanwar and Kumar [152, 158–160], and Bates et al. [156] have all considered a side reaction involving PbO, which leads to the characteristic two-step voltage profile during the second and all subsequent charges. Oury et al. [157] did not include side reactions and only simulated a cell at steady state, assuming constant concentration at the inlet.

All previous numerical models included a degree of experimental validation. For example, Shah et al. [155] validated numerical data over three different current densities, 10, 20 and 30 mA cm^{-2}, see Figure 2.10. Their model provides a close match in all cases. Nandanwar and Kumar [152] validated their model over two full charge-discharge cycles and obtained good agreement with the experimental data, see Figure 2.11. Bates et al. validated their numerical results over the first two charges and the first discharge at 15 mA cm^{-2} and found reasonable agreement with the experimental data [156], Figure 2.12. However, the two-step charging mechanism is more pronounced in simulated results than in their experimental validation.

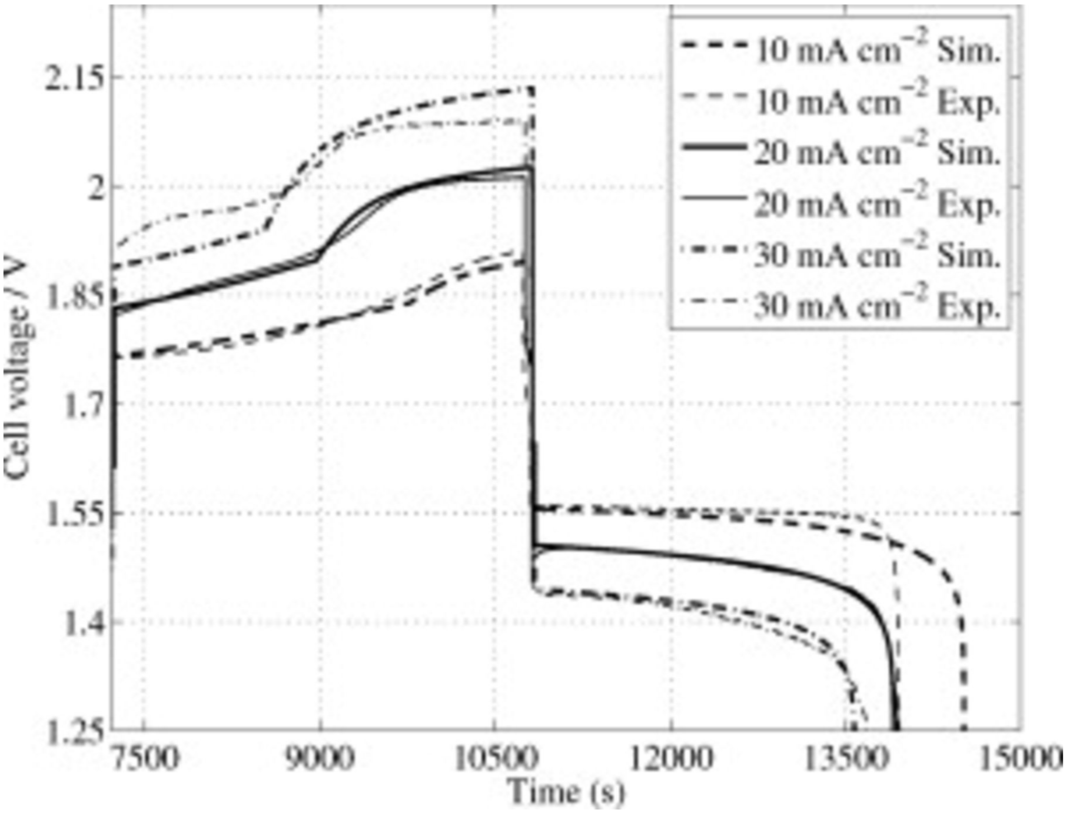

FIGURE 2.10: Validation of the numerical model by Shah et al. Experimental and simulated charge-discharge curves at varying current densities (10, 20 and 30 mA cm^{-2}. Reproduced with permission [155].

Oury et al. have validated numerical results with the experimental data over the first six cycles [157], Figure 2.13. However, they did not consider any side reactions in their calculation, so the voltage response does not apply to a large proportion of the

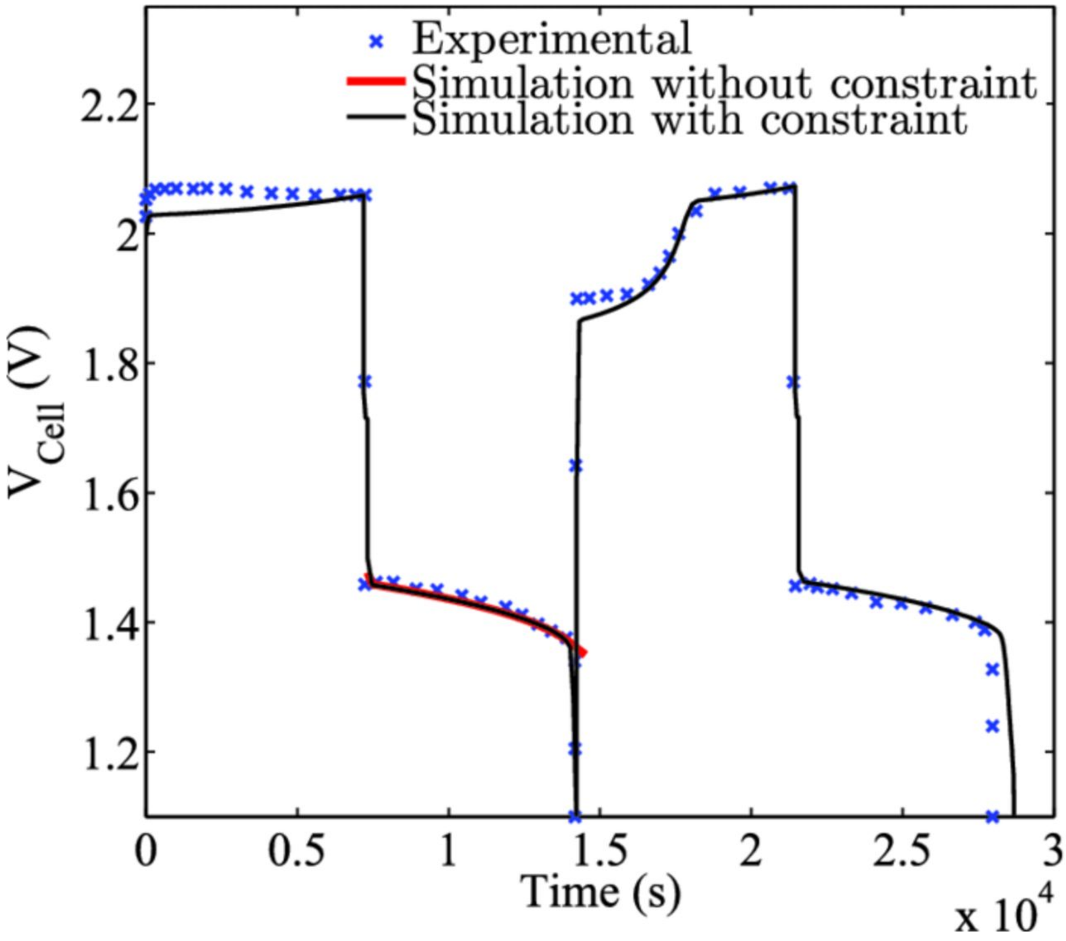

FIGURE 2.11: Validation of the numerical model by Nandanwar and Kumar. Experimental and simulated charge-discharge curves with and without a constraint on the availability of deposits at the electrodes. An average current density of 20 mA cm^{-2} was used. Reproduced with permission [152].

second and subsequent charges. Nevertheless, good agreement was found during discharge and for the later part of second and subsequent discharge cycles. A change in concentration due to incomplete discharges causes the voltage to increase with cycle number progressively. The model captures this.

In all previous SLFB models, Navier-Stokes equations were employed to simulate the flow of electrolyte. There are two approaches used in the literature to model the flow of electrolyte through the battery: the fluid equations can be solved at steady state before solving the rest of the model, or they can be solved transiently concurrently with the rest of the model. For example, Nandanwar and Kumar [152] and Bates et al. [156] performed steady-state simulations as constant fluid properties were assumed. Shah et al. carried out unsteady variable density simulations as the electrolyte density was not kept constant [155]. All studies assumed an incompressible fluid and, as such, kept the

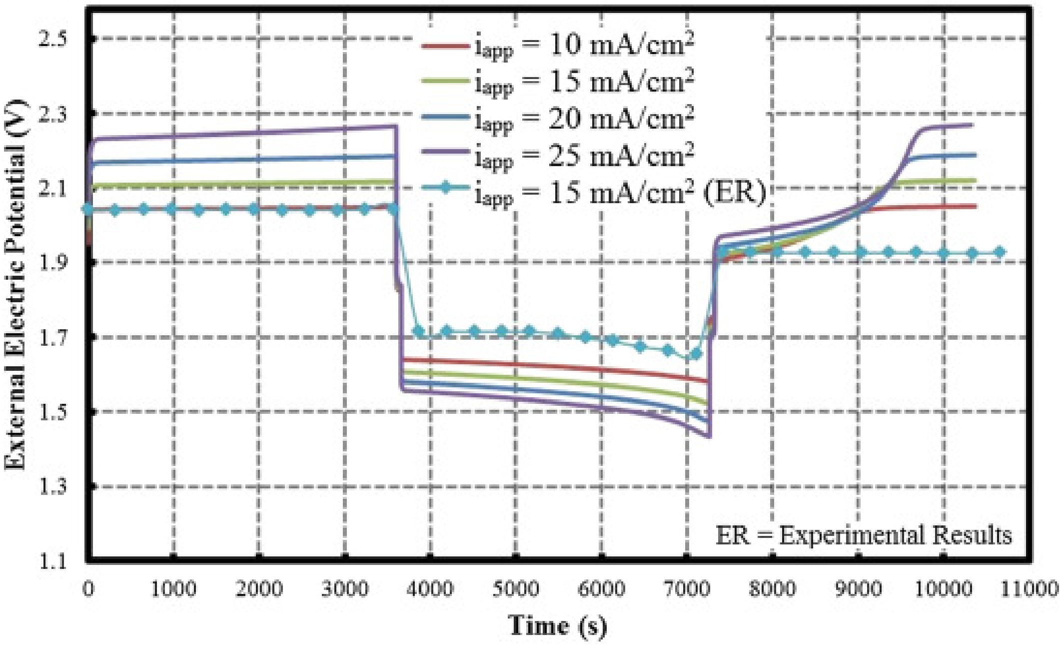

FIGURE 2.12: Validation of the numerical model by Bates et al. Experimental and simulated charge-discharge curves at a current density of 15 mA cm^{-2}. Simulated results at 10, 20 and 25 mA cm^{-2} are also included. Reproduced with permission [156].

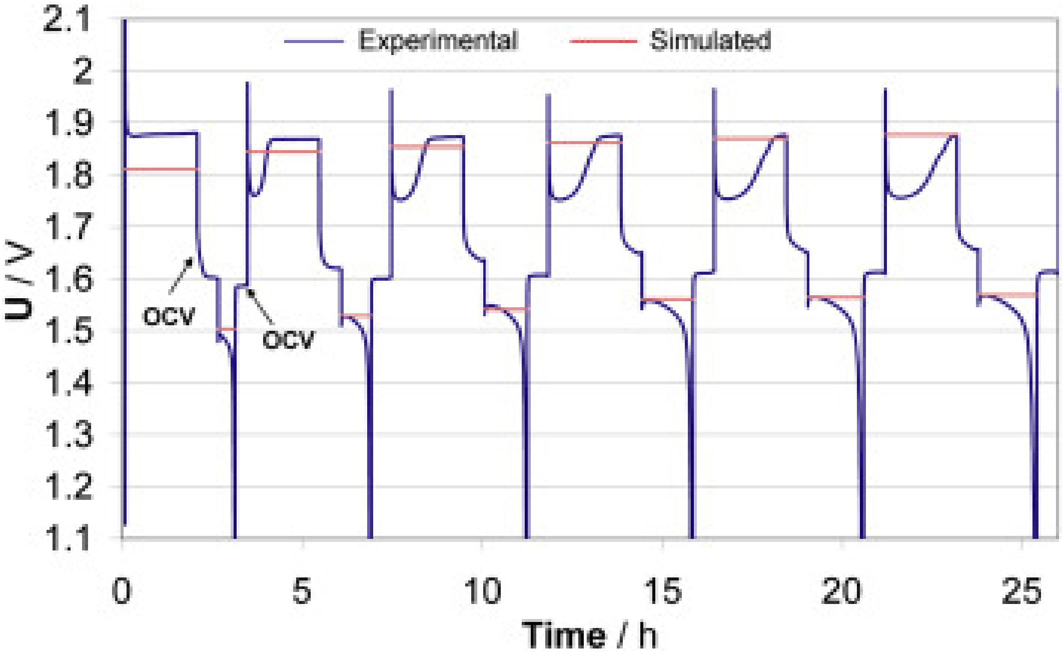

FIGURE 2.13: Validation of the numerical model by Oury et al. Experimental charge-discharge curves are compared with the simulation results over 6 cycles. An average current density of 10 mA cm^{-2} was used. Reproduced with permission [96].

viscosity constant.

Typically flow batteries operate at current densities ranging between 20 and 100 mA cm^{-2} [36, 162, 163] and a report on the SLFB has suggested a target of 50 mA cm^{-2} or higher for commercial operation [80]. As additional capacity is generally lower cost than additional power in RFBs, a higher ratio of energy to power will make them more competitive. In the SLFB, at these current densities, a large capacity to power ratio would lead to thicker deposits than the maximum thickness of 1 mm suggested by Pletcher et al., [79], for efficient operation with a long cycle life. The effect of these thick deposits must be understood for optimal cell performance. A comprehensive review of the SLFB by Krishna et al. also highlighted the lack of understanding of the effect of the change in geometry of the deposits during operation [5]. This is the basis for the work presented in Chapter 5 and [2].

Krishna et al. [86] show that by dividing the SLFB, the cycle life and coulombic efficiency (with electrode specific additives) can be increased. All previous modelling of the SLFB was completed with an undivided configuration. However, numerical modelling can form a useful tool in determining the properties required for a successful membrane in the SLFB. This is developed into Chapter 7.

The majority of the work discussed in this section modelled the SLFB with flat planar electrodes. However, the benefit of reducing the local current density by increasing the electrode surface area, especially of the positive electrode have been made clear computationally by Nandanwar and Kumar [152] and Oury et al. [157], and experimentally using RVC electrodes in the SLFB by Banerjee et al. [98] and Pletcher et al.@[95]. These works are discussed in Section 2.5, Section 2.6 and Section 2.8.3.5 and form the motivation for Chapter 8 and [4].

2.9 Engineering and Scale-up

Even after decades of research on redox flow batteries, engineering aspects across the whole sector remain largely neglected, even for commercially successful systems. The large amount of work acknowledges engineering issues exist but fails to draw upon existing electrochemical engineering knowledge. Most significantly is the need to reduce capital and running costs of such systems. There is established literature on filter-press cells, electrolysers and alkaline fuel cells, for example, which addresses many of the shared issues also faced with RFBs.

It could be argued that, as many proposed RFBs are some way off becoming commercialised, these engineering aspects are less important than the work that is being carried out. However, the author believes more progress in the field could be made by emphasising the engineering aspects of RFBs, as many of these aspects can be applied to the whole field.

Arenas et al. [164] define six fundamental engineering aspects of an RFB:

- Cell and stack design requires input from several different disciplines, including knowledge from chemical, materials and mechanical engineering, as well as knowledge from chemical and electrochemical disciplines.
- The reaction environment has requirements for the electrolyte flow through the cell, including flow rate and direction as well as the current and potential distribution over the electrodes.
- Monitoring and diagnostics of the system. Many battery systems require a battery management system (BMS) to ensure safe and efficient operation of the system and to identify any faults in the system. RFBs are no exception. A system to monitor potential, temperature and flow conditions in each cell in the stack can be coupled with a management and diagnostics system to ensure the battery remains balanced and identify any problems that need to be addressed.
- Figures of merit are quantities relating to the performance of a battery allowing for comparison between different systems and chemistries, such as capacity, energy density and energy efficiency.
- Dimensionless correlations are represented by dimensionless numbers, such as the Sherwood number ($Sh = \frac{convective mass transfer rate}{Diffusion rate} = \frac{hL_c}{D}$ h is the mass transfer coefficient, L_c is the characteristic length and D is the diffusion coefficient) or the Reynolds number($Re = \frac{Inertial forces}{Viscous forces} = \frac{\rho u L_c}{\mu}$ ρ is fluid density, u is velocity and μ is dynamic viscosity). These quantities define certain qualities of a cell or a stack to allow for that specific parameter to be compared between different systems.
- Scale-up and construction of RFBs form the process of developing a system from fundamental electrochemistry via laboratory work to an electrochemical cell before further work on pilot-scale, then prototype devices, to form a commercial device.

A periodic maintenance cycle will be required for the SLFB to dissolve the built-up layer on the positive electrode and any sludge material back into the electrolyte. The current method discussed in the literature is to add hydrogen peroxide to the solution. Collins et al. [71] show that periodic addition of 0.86 mol dm^{-3} H_2O_2 quickly dissolves any PbO_2 and, at a lower rate, Pb, back into solution. This process successfully extends the cycle life of the flow cell. However, the efficiency of the system decreases with the addition of H_2O_2 and the conclusion was drawn that the process is unlikely to be an economical method of maintenance at a commercial level. Further work in this area is required. Lanfranconi et al. [63] also include a periodic maintenance cycle. They periodically discharge the battery to 0 V, which appears to significantly improve the cycle life of the SLFB. However, as there is no direct comparison between cycling the battery with and without the maintenance cycle, further work is required to determine its exact effect.

The electrodes within a flow battery must perform well electrochemically and be stable both chemically and mechanically within the electrolyte. Nikiforidis et al. have compared a range of novel and commercial materials for use in the negative half-cell of the zinc-cerium flow battery [165]. However, many of the commercial materials are no longer available. Chemical resistance, electrical conductivity, compactness and mechanical strength are defined as key properties by the authors.

A cost model for the VFB has been developed by Viswanathan et al. [166]. This study uses three models to describe the system: an electrochemical model, a flow model and a model of shunt currents to estimate parasitic losses from pumping and bypass currents. Installation costs were neglected due to the high variability between projects. Material and component costs were found in the literature and by contacting vendors. The resulting simulation gives costs for the system in present, near-term and optimistic cases and provides a breakdown of the cost of each component of the system.

ARPA-e (Advanced Research Projects Agency-energy) has set a target for capital cost of \$100 kWh^{-1} for grid-scale energy storage [167], an ambitious target, especially when compared to the target of \$250 kWh^{-1} for electric vehicle (EV) batteries [168]. However, Mellentine et al. concluded that, based on simulations of a 2 MW 10-year flow battery system, flow batteries with installation costs of less than \$500 kWh^{-1} could be profitable [169].

While an attractive benefit of RFBs is relatively simple control and management systems compared to conventional batteries, because the cells do not require balancing in the same manner, there is still a need for a BMS [69]. This BMS is required to prevent overcharge and discharge, which can lead to hydrogen and oxygen evolution, unbalanced cells or, in the case of the SLFB, locally reversing the polarity of the electrodes, causing Pb and PbO_2 to be deposited on the positive and negative electrodes respectively. The BMS is also responsible for ensuring the battery is operating within the allowed thermal limits. Further work is required to determine these exact limits, but in studies which vary the operating temperature of the SLFB, peak energy efficiency is seen between 298 K [170] and 313 K [161].

To be successful, RFBs should combine low installation costs with low maintenance costs, a long cycle life, low downtime, the ability to source all the required components and chemicals sustainably and a low risk of contamination or environmental damage from operating, maintaining and decommissioning the system. These operations should also be able to be performed safely. It should also have a high energy efficiency with low parasitic losses from pumps, power electronics and other associated systems.

2.10 Summary

The soluble lead flow battery is able to operate in an undivided manner due to Pb^{2+} being common to both redox couples. Thus, it may lead to significant reductions in the amount of apparatus required for storing and pumping the electrolyte and cost savings due to the lack of requirement of a separator. Many of the battery materials, including lead, are presently commercially available and an electrolyte formed of the relatively non-aggressive methanesulfonic acid means a wide range of materials are available for use in the battery.

An important area that is lacking in SLFB development is a cost-effective maintenance cycle to allow for extended operation of the system. Addition of hydrogen peroxide has been explored as an option. However, this method is expensive and alternatives have not been extensively explored. An up-to-date cost analysis of the SLFB is also lacking.

There has been substantial work on the understanding of the mechanisms of lead and lead dioxide formation and stripping at the electrodes. Conditions that allow for smooth, even deposition have been discussed, including the use of additives to achieve the desired deposit quality.

There is, however, a significant amount of work to be completed for the SLFB to move towards becoming a commercial technology. Little work on the effect of real operating conditions has been explored. This includes the effect of leaving the system in a charged, or partially charged, state over extended periods of time. There has been a limited amount of work on the engineering aspects of flow cells in general. For the SLFB, there have been only a few studies on modelling the system. A full 3D model should be developed and validated. It should includes the change in geometry and electrolyte composition during operation and that can be easily adapted for different systems including different electrode material, cell geometry and whether the cell is undivided, semi-divided or fully divided. There is also significant space for testing and development of electrode materials and form factors. Some specific electrode materials and morphologies have been explored, but there is not a comprehensive comparison of electrodes and how they perform in lab-based cells or how they are expected to perform over extended operation in a commercial system. These areas form the basis of the work presented in the following chapters.

Chapter 3

Experimental setup

Two flow cells were used in the validation of the modelling presented in this thesis, a 100 cm^2 cell and a 10 cm^2 cell. Both flow cells were connected to a flow circuit consisting of a Cole-Parmer Masterflex L/S digital drive peristaltic pump, Masterflex Norprene flexible tubing and barb connectors with jubilee clips to ensure a firm connection where appropriate. The peristaltic pumps were calibrated for a volumetric flow rate by measuring the time to fill a 500 cm^3 measuring cylinder.

The electrolyte consisted of an aqueous solution of 0.5 mol dm^{-3} methanesulfonic acid (CH_3SO_3H) and 0.7 mol dm^{-3} lead methanesulfonate ($Pb(CH_3SO_3)_2$). The commercially available solutions used to produce this electrolyte are listed in Table 3.1.

TABLE 3.1: Summary of chemicals used to produce electrolyte for experimental work.

Chemical	**Formula**	**Concentration**	**Supplier**
Lead Methanesulfonate	$Pb(CH_3SO_3)_2$	50 wt. % in H_2O	Sigma Aldrich
Methanesulfonic Acid	CH_3SO_3H	70 wt. % in H_2O	Sigma Aldrich

The electrode material used in each cell differed and is explained in the relevant subsequent sections. Before each experiment, the electrodes were prepared by rubbing with fine silicon carbide paper to remove any excess polymer binder, deposits from previous experiments or other residue. A wash with distilled water then acetone followed to remove any loose material from the abrasion process.

An MTI 8-channel battery analyser was used to control and measure the cell potential and supply and draw constant currents during charge and discharge. The battery analyser was connected to a computer and testing plans were implemented in TC 5.3 software which also logged the cycling data and provided voltage limits for safe operation of the cell.

3.1 100 cm^2 cell

Experimental validation was carried out using a cell that was previously designed and made by Southampton and CTech Innovation ltd as part of the Department of Energy and Climate Change (DECC) Energy Storage Component Research & Feasibility Study Scheme – A soluble lead redox flow battery demonstrator (PBatt) [80]. The cell consisted of two polyether ether ketone (PEEK) flow frames (34 cm × 22 cm), used to distribute the flow over the electrodes and hold the electrodes in place with an inter-electrode gap of 1.2 cm (Figure 3.1). This configuration allowed for the use of a separator if desired. Two further PEEK blocks housed the current collectors. Copper foam was placed between the brass current collectors and the electrodes to ensure a good electrical contact. The cell was compressed by two stainless steel end plates (34 cm × 22 cm) fixed with 12 bolts. To ensure good sealing and an even compression, the bolts were tightened with an equal torque of 15 N m, providing even pressure over the gaskets.

Both electrodes were Entegris carbon polymer (polyvinyl ester) plates. The electrode housing limited the exposed area of each electrode to 10 cm × 10 cm. The cell was sealed using Viton gaskets. 1000 cm^3 of electrolyte was circulated through the cell. The pump was set to a constant speed so that the volumetric flow rate was 27.6 $\mathrm{cm}^3\,\mathrm{s}^{-1}$, corresponding to a mean linear velocity over the electrodes of 2.3 $\mathrm{cm\,s}^{-1}$ when no deposit was present.

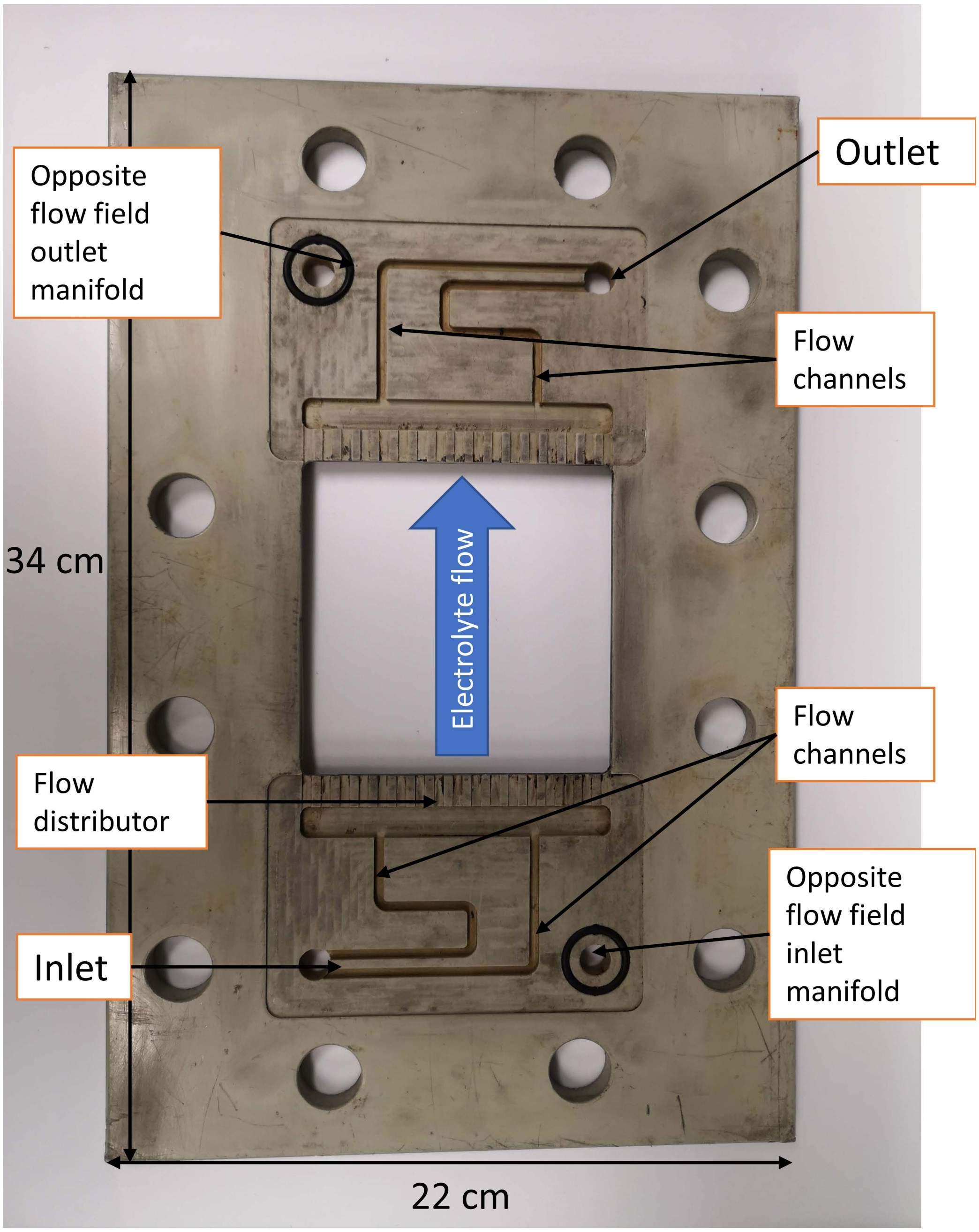

FIGURE 3.1: Flow field of 100 cm^2 flow cell. Electrolyte flows in via the inlet at the bottom of the frame, then from bottom to top of the electrode area and out via the outlet at the top of the frame. Manifolds allow electrolyte to pass through to the opposite flow field.

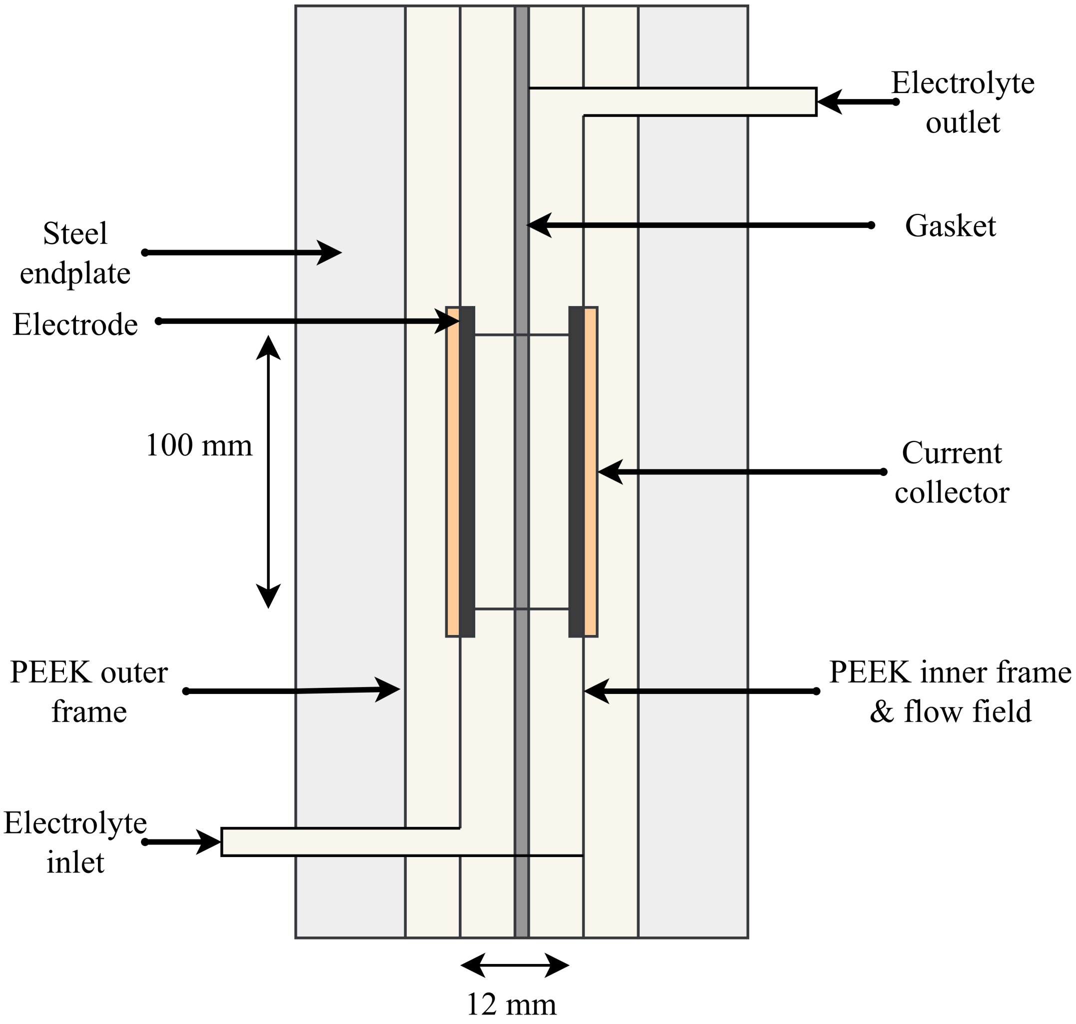

FIGURE 3.2: Schematic showing a cross-section of the 100 cm^2 flow cell. components from outside to centre: Steel endplates, PEEK outer frames, current collectors, electrodes, PEEK inner frames, gasket.

3.2 10 cm^2 cell

A smaller 10 cm^2 cell was also used for some cycling experiments. This cell consisted of acrylic flow frames, 1.5 mm (uncompressed) silicone foam gaskets, SGL carbon sigracell bipolar plates [171], copper foil current collectors, an insulating layer of hard norprene and 10 mm thick stainless steel endplates. The cell was held together with four M8 bolts, one in each corner. 400 cm^3 of electrolyte was circulated at a volumetric flow rate of 7 cm^3 s^{-1}, which corresponds to an average electrolyte velocity of approximately 2.3 cm s^{-1} over plain bipolar pates.

The active area of the bipolar plates was 2.5 cm × 4 cm.

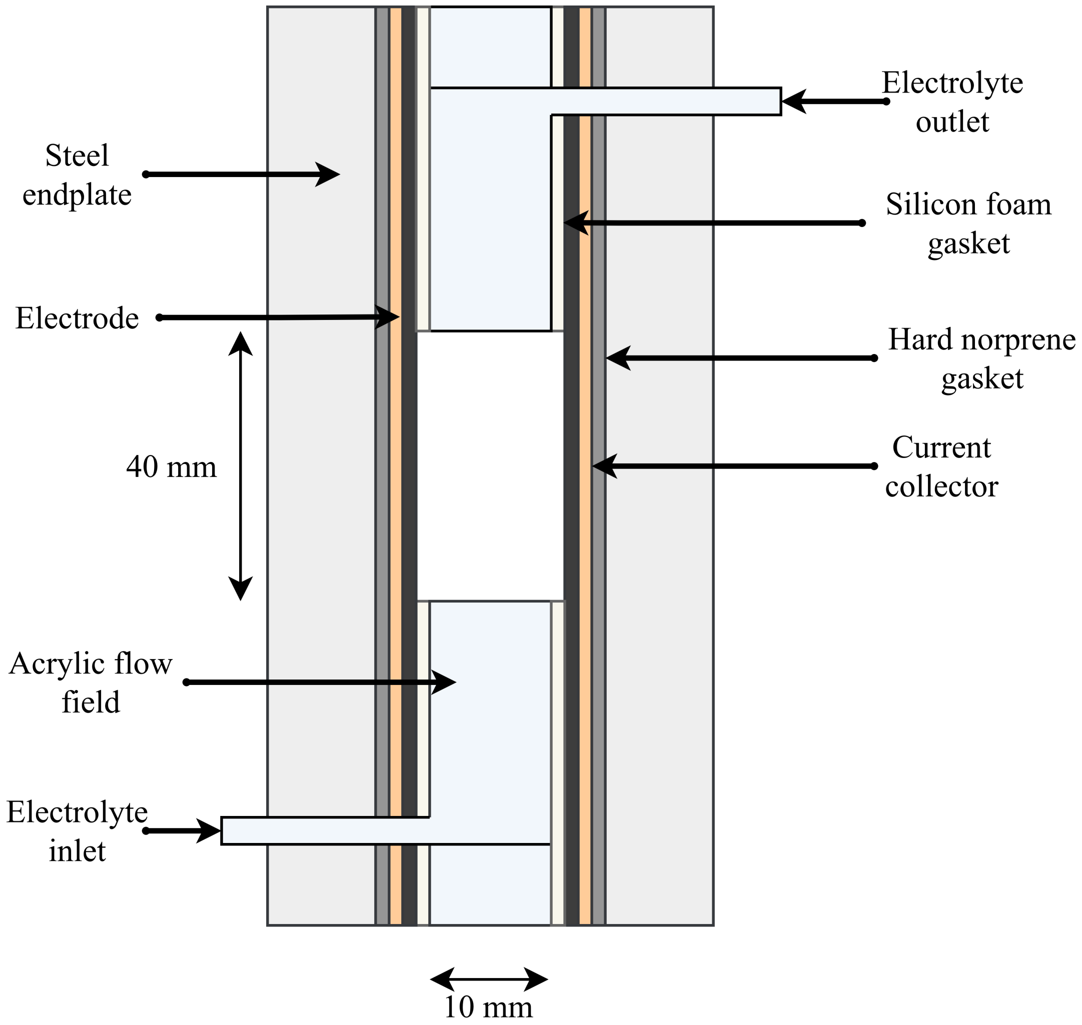

FIGURE 3.3: Schematic showing a cross-section of the 10 cm^2 flow cell. Components from outside to centre: Steel endplates, hard norprene insulating gaskets, current collectors, electrodes, silicone gaskets, acrylic flow field.

Where reticulated vitreous carbon (RVC) was used, cell compression was used to maintain a good contact between the bipolar plate and the RVC. In this setup, an AmerSil FF60 microporous separator was used to divide the negative and positive half cells, as shown in Figure 3.4.

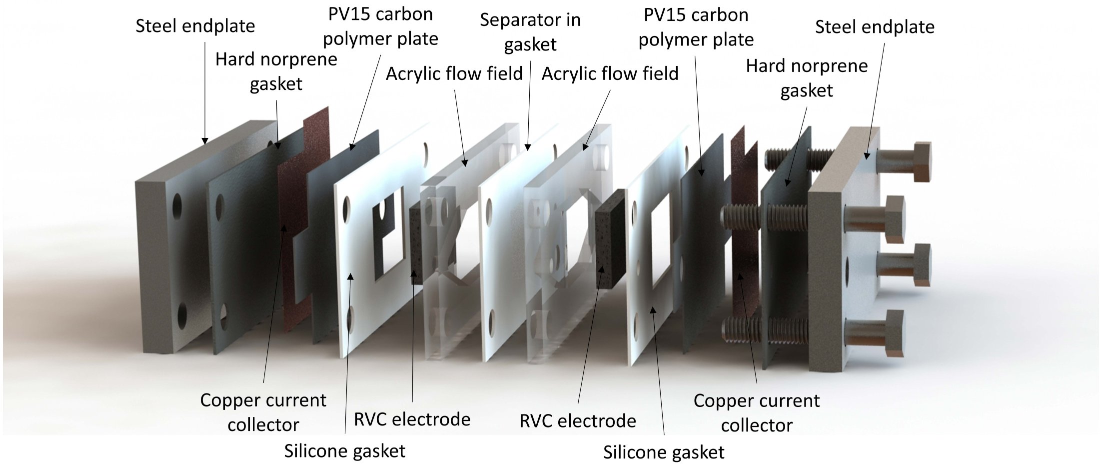

FIGURE 3.4: Exploded view of 10 cm^2 flow cell.

Chapter 4

Model setup

This chapter describes the methodology for producing a basic model of the soluble lead flow battery. Subsequent chapters develop this model into more sophisticated versions from which results are generated and presented.

A two-dimensional, transient model simulating the operation of a single-cell soluble lead flow battery has been produced using COMSOL Multipyhsics® which uses the finite element method (FEM). FEM is the default method for COMSOL Multipyhsics® and is frequently used when modelling the SLFB, including the following models the presented model is adapted from [152, 155, 157–160]. However, methods such as the finite volume method (FVM) have been used for flow battery modelling, but typically at a smaller length scale when a high degree of detail is required or when the flow is the major focus of the simulation [116].

The model incorporates a simulation of the electrolyte including conservation of mass and momentum based on the Navier-Stokes equations. The model also includes a simulation of the concentration of the following soluble species: H^+, Pb^{2+}, $CH_3SO_3^-$ based on the Nernst-Planck equation as well as equations for kinetics of the electrode reactions.

In this thesis, the work presented builds on this general model to provide the first modelling approach to the following SLFB aspects:

- Using a moving mesh technique to include the effects of the increase in deposit thickness and hence decrease in interelectrode gap with SoC.

- A non-linear approach to modelling the mobility of ions in the electrolyte vs SoC. This gives a significantly closer match with experimental conductivity measurements of the electrolyte than previous models.
- Using a semi-divided (porous separator – single electrolyte) and fully divided (ion-exchange membrane – separate positive and negative electrolytes) configuration of the SLFB.
- A SLFB with porous foam electrodes (reticulated vitreous carbon)
  - Using open source software OpenImpala to provide homogenised electrode parameters from CT scans of different RVC grades.
  - Dilating binary images from CT scans to estimate the 3D structure of RVC electrodes with different volumes of deposited Pb and PbO_2.
- A representation of the positive and negative deposits on planar electrodes.

When the SLFB is charged to a high capacity, the deposits at each electrode become significant in size which affect the resistance of the cell and the flow conditions within the battery. The conductivity of Pb should be consistent assuming compact even deposits. Lead has a conductivity of 5×10^4 S cm^{-1} [172]. However, PbO_2 has a conductivity ranging from 10^3 - 10^4 S cm^{-1} for α-PbO_2 and β-PbO_2, respectively [173]. Any other leady oxides present further complicate the issue [158]. As the electrolyte conductivity is normally less than 1 S cm^{-1} [49], the difference to the overall cell resistance is likely to be dominated by this.

All previous SLFB models have used a Nernst-Einstein equation for ionic mobility which gives a simple, linear relationship between ion concentration and electrolyte conductivity. As Krishna et al. [49] have shown experimentally, this is a poor representation of the SLFB electrolyte conductivity, a significantly improved, semi-empirical representation of electrolyte conductivity is developed.

Experimental work on laboratory flow cells by Krishna et al. [86] showed that including a separator in the SLFB allows for electrode specific additives and improved cycle lifetime of the battery. This model is developed to allow for inclusion of simple porous separators and both anionic and cationic exchange membranes in the SLFB.

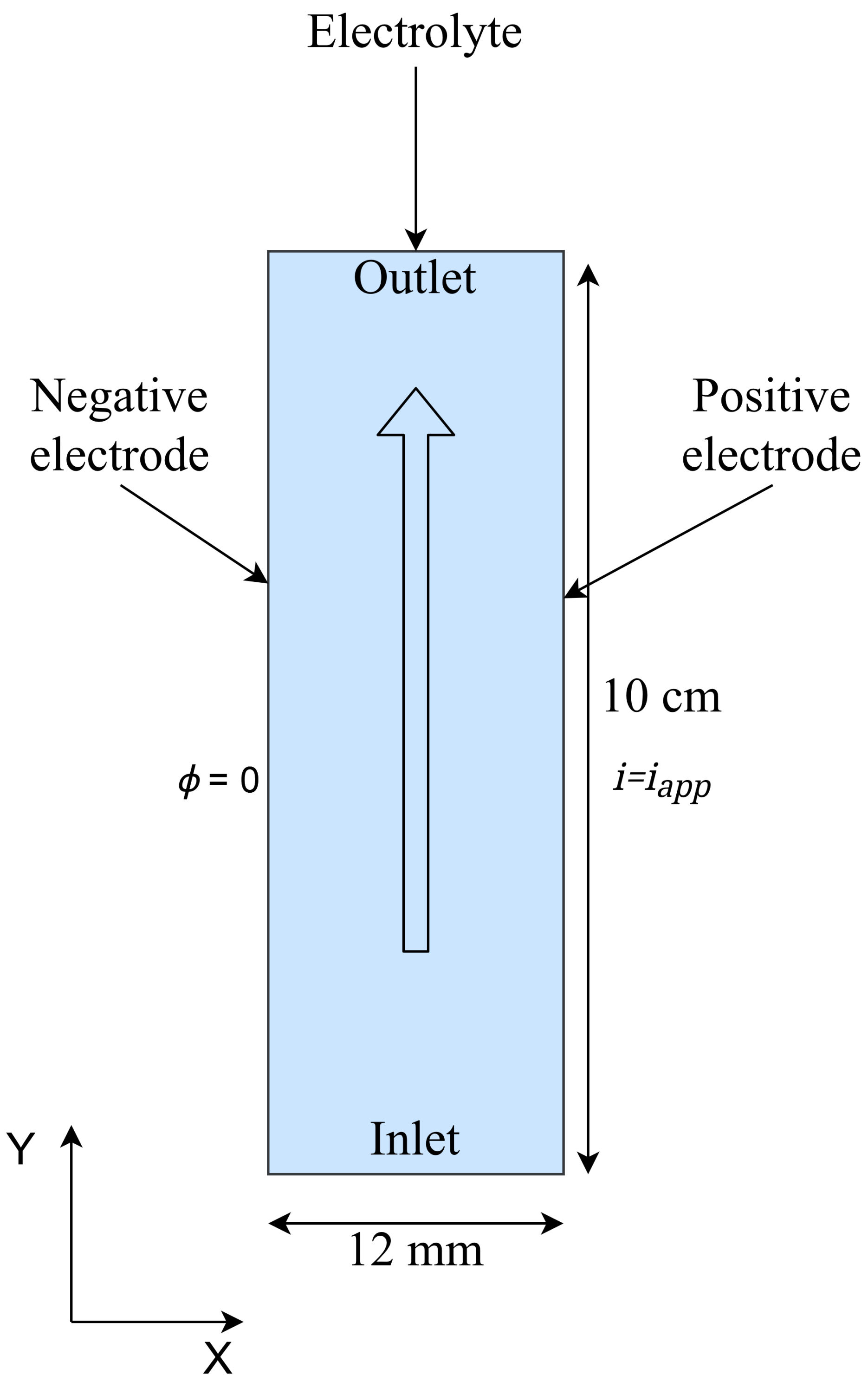

FIGURE 4.1: Schematic showing the general geometry, including domains and boundaries used in simulations. Where electrode domains are included, these are described in the relevant chapter.

To address the imbalance between fast kinetics at the negative electrode and slower kinetics at the positive electrode, various geometries have been proposed to increase the effective surface area of the positive electrode. Concentric cylindrical electrodes [152] and a flow through honeycomb electrode between planar negative electrodes [96, 157] have both shown an improvement in performance for a single unit cell. However, neither can be arranged in a bipolar stack, somewhat mitigating the increase in applied current by increasing the complexity, volume and mass of a multi-cell system. Cylindrical electrodes are impractical to arrange in a bipolar stack as with each cell arranged further from the centre of the cylinder, the surface area would increase and hence the current density would decrease. The total current would be limited by the current density of the innermost cell, so the stack would require more electrode area than an equivalent stack with parallel electrodes. For the honeycomb arrangement, the current changes direction in each cell, flowing from the outer negative electrodes to the central positive electrode during discharge or vice versa during charge and so current must be collected via an external connection at each cell.

In this thesis, reticulated vitreous carbon (RVC) electrodes on a bipolar carbon plate are modelled to produce design recommendations for a cell with electrodes with unequal surface area while maintaining the ability to be arranged in a bipolar stack. The model developed in this thesis consists of, as a minimum, two solid domains, one for each of the positive and negative electrodes respectively, divided by a fluid domain through which the electrolyte flows. The model does not include the external flow circuitry or the electrolyte reservoir. The exact mechanism of the positive electrode reaction is not well understood, and it is known that gas evolution can occur at both electrodes in the SLFB. The literature describes that the main side reaction at the positive electrode forms non-stoichiometric PbO_x compounds from PbO_2, where x is between 1 and 2. Lead hydroxides may also be present [155, 174]. However, this model includes just one side reaction at the positive electrode where it is assumed that some PbO_2 is reduced to solid PbO rather than soluble Pb^{2+}. Hence the following reactions are used to describe the SLFB:

$$\textit{Positive} \qquad Pb^{2+} + 2H_2O \rightleftharpoons PbO_2 + 4H^+ + 2e^- \qquad E^0 = +1.46\ \text{V}\ \textit{vs SHE} \tag{4.1}$$

$$\textit{Negative} \qquad Pb^{2+} + 2e^- \rightleftharpoons Pb \qquad E^0 = -0.13\ \text{V}\ \textit{vs SHE} \tag{4.2}$$

$$\textit{Cell} \qquad 2Pb^{2+} + 2H_2O \rightleftharpoons Pb + PbO_2 + 4H^+ \qquad E^0_{cell} = +1.59\ \text{V} \tag{4.3}$$

$$\textit{Positive side reaction} \qquad PbO + H_2O \rightleftharpoons PbO_2 + 2H^+ + 2e^- \qquad E^0 = +0.28\ \text{V}\ \textit{vs SHE} \tag{4.4}$$

The side reaction is only present during the second and any subsequent charges. This is illustrated in the voltage profile of the SLFB where a two-step charging mechanism is observed in these steps with a lower voltage initially before returning to a higher voltage at the end of the charging step.

4.1 Assumptions

To define the scope of the problem to be solved, the model is simplified using several assumptions to allow the model to be run efficiently at the scale of a 100 cm^2 cell.

- The dilute solution assumption is used [175], and the electrolyte is assumed to consist only of Pb^{2+}, H^+, CH_3SO_3^- and water. All species other than water are assumed to be completely dissociated.
- Electrolyte flow is considered to be laminar and incompressible. However, the electrolyte density does change with concentration of ionic species. A low Reynold's number of approximately 500 suggests laminar flow is a reasonable assumption. The velocity is assumed to be fully developed at the inlet, manifold effects are not considered.
  - As $Re = \frac{\rho u L_c}{\mu}$, the maximum values for ρ, u and L_c and the minimum value for μ will give the maximum feasible Re. $\rho_{max} = 1.25\ \text{g}\,\text{cm}^{-3}$, $u_{max} = 2.3\ \text{cm}\,\text{s}^{-1}$, $L_{c,max} = 2$ cm and $\mu_{min} = 0.96$ mPa s. Hence $Re_{max} \approx 500$.

  - Constant inlet velocity is assumed so *Re* does not increase beyond this and the flow regime remains laminar.

- Deposits are assumed to be fully dense and form with smooth surfaces. For deposits in porous electrodes, the surface area and porosity are calculated assuming deposits form evenly normal to the electrode surface.
  - This allows reasonable simulation of deposits without the need to mesh down to µm scales to incorporate surface features on the deposits.

- Only the chemical reactions defined in the previous section are present.

- Movement of water across the membrane is neglected in the ion-exchange membrane divided configuration. The volume of each electrolyte is therefore considered to remain constant.

- Perfect, instantaneous mixing in the electrolyte reservoir is assumed to occur.
  - This removes the need to model fluid mixing in an external reservoir and the associated pumping circuit.

- The electrolyte is defined by the electroneutrality condition:
  - $\sum_i z_i c_i = 0$

- Temperature remains constant
  - This removes the need to model heat fluxes in and out of the cell and associated pumping circuit. As a flow battery has electrolyte flowing through it, if the electrolyte is able to cool sufficiently in the external reservoir, the electrolyte will keep the stack at a relatively constant temperature.

Where z_i is the valence of species i and c_i is its concentration.

4.2 Governing Equations

Each model defines the domains which are included at the start of the chapter. For clarity, here each set of governing equations is defined for each domain type used in this thesis: solid electrode/deposit, electrolyte, porous electrode, and membrane. In general, for all domains, this model is governed by conservation of mass, momentum and charge.

4.2.1 Free Electrolyte

The flow of electrolyte is described by the Navier-Stokes and continuity equations. Using a maximum electrolyte density of 1.25 g cm^{-3} at 0.7 mol dm^{-3} Pb^{2+} and 1 mol dm^{-3} MSA, a minimum viscosity of 1.0 mPa at 0.5 mol dm^{-3} MSA and 0 moldm^{-3} Pb^{2+}, a characteristic length of 2.0 cm for a 1 cm inter-electrode gap and a fluid velocity of 2.3 cm s^{-1}, the maximum Reynolds number for the system is calculated to be ∼550. As Re $\ll$ 2000 the laminar form of the Navier-Stokes and Continuity equations are used.

$$\rho(\mathbf{u} \cdot \nabla)\mathbf{u} = \nabla \cdot [-p + \mu \nabla \mathbf{u}] \tag{4.5}$$

$$\rho \nabla \cdot \mathbf{u} = 0 \tag{4.6}$$

Where $\mathbf{u}$ is the liquid velocity in m s^{-1}, p is the pressure in Pa and μ is the dynamic viscosity in Pa s.

The concentrations and transport of species in the electrolyte are described using the Nernst-Planck equations.

$$\mathbf{N_i} = -D_i \nabla c_i - z_i u_{m,i} F c_i \nabla \phi_{l,i} + \mathbf{u} c_i \tag{4.7}$$

$$u_{m,i} = \frac{D_i}{RT} \tag{4.8}$$

$$\mathbf{j} = F \sum_i z_i \mathbf{N_i} \tag{4.9}$$

Where $\mathbf{N_i}$ is the flux of the species i (H^+, Pb^{2+}, $CH_3SO_3^-$) in mol m^{-2} s^{-1}, D_i is its diffusion coefficient in m^2 s^{-1}, c_i is its concentration in mol m^{-3}, z_i is its valence, $u_{m,i}$ is its mobility in s mol kg^{-1}, $\phi_{l,i}$ is the potential of the electrolyte in V, F is Faraday's constant in C mol^{-1}, R is the gas constant in J K^{-1} mol^{-1}, T is the temperature of the electrolyte in K and $\mathbf{j}$ is current density in A m^{-2}.

4.2.1.1 Density

The electrolyte density has a linear relationship with both [Pb^{2+}] and [H^+]. As the electrolyte is water based, the relationship is offset by the density of water:

$$\rho_l = \rho_{H_2O} + a_{\rho 1} c_{Pb^{2+}} + a_{\rho 2} c_{H^+} \tag{4.10}$$

Where $a_{\rho 1}$ and $a_{\rho 2}$ are constants empirically validated using experimental data collected by Krishna et al. [49].

4.2.1.2 Viscosity

Viscosity has a more complex relationship with electrolyte concentration than density. Viscous forces are determined by intermolecular forces and hydrodynamic forces [176]. However, data collected by Krishna et al. suggests a linear increase with [H^+] and a quadratic relationship with [Pb^{2+}] [49].

$$\mu = a_{\mu 1} + a_{\mu 2} c_{Pb^{2+}} + a_{\mu 3} c_{Pb^{2+}}^2 + a_{\mu 4} c_{H^+} \tag{4.11}$$

Where $a_{\mu 1}$, $a_{\mu 2}$, $a_{\mu 3}$ and $a_{\mu 4}$ are constants empirically validated using experimental data collected by Krishna et al. [49].

4.2.2 Solid Electrode

The solid electrode is assumed to consist of only a carbon polymer electrode material initially. Once deposition occurs, Faraday's law and deposit material density is used to calculate the volume of deposit material. This is discussed further in Chapter 5. The only physics modelled in the solid electrode domains is electrical conductance. This is governed by Ohm's law:

$$\sigma_s \nabla^2 \phi_s = \nabla \cdot j \tag{4.12}$$

Where σ_s is conductivity of electrode, s, ϕ is the potential across the electrode and j is current density.

4.2.3 Porous Electrode

A porous electrode domain is modelled by homogenising the solid phases and electrolyte phase. This significantly reduces the complexity of the problem by reducing a complex three-dimensional problem with two phases to a single domain for which electrolyte and electrode equations can be solved by approximating the tortuosity, permeability, volume fraction and surface area of each phase. The volume fractions of the solid phase and liquid phase must satisfy a conservation of volume:

$$\varepsilon_l + \varepsilon_s = 1 \tag{4.13}$$

Maintaining conservation of charge, the total current entering the solid phase at the boundary, which is equal to the total current within the solid phase and the ionic current in the electrolyte.

$$\nabla \cdot j_s + \nabla \cdot j_l = 0 \tag{4.14}$$

The current transferred from the electrode to the electrolyte is linked to the rate of reaction by multiplying the reaction rate by the change of valence of the reactant and Faraday's constant.

4.2.3.1 Electrolyte

In the electrolyte phase, the fluid flow is described using the Brinkman equations. These are an extension of Darcy's law which include dissipation of energy due to viscous shear forces, in a similar manner to Navier-Stokes but in porous media. The Brinkman equations become relevant at higher flow rates. It is valid at high porosity [137].

$$\frac{1}{\varepsilon}\rho\frac{d\mathbf{u}}{dt} + \frac{1}{\varepsilon}\rho(\mathbf{u}\cdot\nabla)\mathbf{u}\frac{1}{\varepsilon} = \nabla\cdot[-p + \mu\frac{1}{\varepsilon}\nabla\mathbf{u} - \frac{2}{3}\mu\frac{1}{\varepsilon}\nabla\cdot\mathbf{u}] - \frac{\mu}{\kappa}\mathbf{u} \tag{4.15}$$

Where ε is the porosity of the porous domain and κ is the permeability of the domain in m^4. Porosity is the ratio of electrolyte volume, V_l to electrode volume, V_s.

$$\varepsilon = \frac{V_l}{V_s} \tag{4.16}$$

Backegberg et al., [114], define permeability as a function of tortuosity using:

$$\kappa = \frac{\varepsilon^3}{K\tau^2 S^2} \tag{4.17}$$

Where K is the Kozeny constant, which is dependent on the pore shape, ε_l is the volume fraction of the electrolyte and τ_l is its tortuosity and S is the specific surface area of the porous structure. The surface area is approximated by:

$$S = \frac{2(1-\varepsilon)}{r_p} \tag{4.18}$$

Where the domain is approximated to consist of an array of cylinders and r_p is the mean radius of the cylinders.

As in the electrolyte domain, Nernst-Planck govern the transport of species in the electrolyte. However, effective parameters for diffusion and mobility are required to account for the tortuosity and non-unity volume fraction of electrolyte in a porous medium.

$$\mathbf{N_i} = -D_{i,eff}\nabla c_i - z_i u_{m,i,eff} F c_i \nabla \phi + \mathbf{u} c_i \tag{4.19}$$

Where subscript eff denotes an effective parameter calculated from tortuosity and volume fraction. Tortuosity here refers to effecitve tortuosity rather than geodesic tortuosity and is related to the effective diffusion coefficient by a steady-state Fickian diffusion equation, Equation 4.20:

$$D_{i,eff} = \frac{\varepsilon_l}{\tau_l} D_i \tag{4.20}$$

$$u_{m,i,eff} = \frac{\varepsilon_l}{\tau_l} u_{m,i} \tag{4.21}$$

4.2.3.2 Electrode

The solid phase is again governed by Ohm's law. However, again to correct for the porosity and tortuosity of the domain, an effective value is required for conductivity.

$$\sigma_{s,eff}\nabla^2\phi_s = \nabla \cdot \mathbf{j} \tag{4.22}$$

$$\sigma_{s,eff} = \frac{\varepsilon_s}{\tau_s}\sigma_s \tag{4.23}$$

Here σ_s is the conductivity of a two-phase solid, the carbon of the RVC and the deposit material. To calculate the total conductivity of the solid, effective medium theory is used [177].

$$\varepsilon_1 \frac{\sigma_1 - \sigma_s}{\sigma_1 + 2\sigma_s} + \varepsilon_2 \frac{\sigma_2 - \sigma_s}{\sigma_2 + 2\sigma_s} = 0 \tag{4.24}$$

Where subscripts 1 and 2 denote the different phases.

4.2.4 Membrane

As the SLFB can be operated undivided, divided by a microporous separator, or divided by an ion exchange membrane, the model must be able to include all three configurations. Microporous separators, as the name would suggest, have very small pore sizes and hence a high surface area. The hydraulic permeability through the separators is therefore high. Compared to the free electrolyte or the relatively highly permeable RVC electrodes, the flow within a microporous separator can be assumed to be negligible. The separator can either be modelled with the Nernst-Planck equation for porous media neglecting the convection term, or by simplifying the domain so the concentration of ions is not explicitly modelled. In the latter case, the domain is simply defined by an ionic conductivity. The ion-exchange membrane is more complex. However, there are a number of simplifying assumptions which can make modelling the domain more reasonable. The membrane domain is a porous medium, so the effective diffusion coefficient is lower than in the free electrolyte. Using the Bruggeman correlation the effective diffusion coefficients can be calculated from the porosity, ε:

$$D_{i,eff} = \varepsilon^{1.5} D_i \tag{4.25}$$

Again, the Nernst-Planck equation for porous media from equation 4.19 is used.

4.3 Boundary Conditions

4.3.1 Inlet and Outlet

The velocity of the electrolyte at the inlet is set to be constant with a Gaussian distribution. At the outlet, diffusive fluxes and current are equal to zero normal to the outlet boundary. The pressure at the outlet is also set to zero (gauge):

$$-D_i \nabla c_i \cdot \mathbf{n} = 0,\ i \cdot \mathbf{n} = 0,\ p = 0 \tag{4.26}$$

The concentrations of the species at the inlet were calculated using an equation assuming perfect mixing in the reservoir. The concentration at the outlet was taken and volumetrically averaged with the concentration of the reservoir at the previous time step.

$$\frac{d}{dt} c_{in,i} = \frac{L}{V} \left(\int_{outlet} \mathbf{N_i} \cdot \mathbf{n} dS - \int_{inlet} \mathbf{N_i} \cdot \mathbf{n} dS \right) \tag{4.27}$$

Where V is the electrolyte reservoir volume and L is the depth of the domain normal to the 2D plane.

4.3.2 Kinetics

The electrode reaction kinetics are described using the Butler-Volmer equation. To account for the availability of solid species in the reaction kinetics, the equation was modified so that when the solid surface concentration approached 0 during discharge, the exchange current density (equal to $Fk_0, Pbc_{Pb^{2+}}$ and $Fk_0, PbO_2 c_{Pb^{2+}} \frac{c_{H^+}}{c_{H_0^+}}$ for the negative and positive electrodes respectively) also tended to 0.

Negative electrode:

$$i_{loc,Pb} = Fk_{0,Pb} c_{Pb^{2+}} \left(e^{\left(\frac{\alpha_{o,neg} F \eta_{neg}}{RT} \right)} - e^{\left(-\frac{\alpha_{r,neg} F \eta_{neg}}{RT} \right)} \right) \tag{4.28}$$

Positive electrode:

$$i_{loc,PbO_2} = Fk_{0,PbO_2} c_{Pb^{2+}} \frac{c_{H^+}}{c_{H^+,ref}} \left(e^{\left(\frac{\alpha_{o,pos} F \eta_{pos}}{RT} \right)} - e^{\left(-\frac{\alpha_{r,pos} F \eta_{pos}}{RT} \right)} \right) \tag{4.29}$$

If the cell is discharging and $c_i = 0$, where $i = Pb$ for the negative electrode and PbO_2 for the positive electrode:

$$i_{loc,Pb} = i_{loc,PbO_2} = 0 \tag{4.30}$$

For all other cases, equations 4.28 & 4.29 are valid. Where i_{loc} is the local current density in A m^{-2}, $k_{0,Pb}$ and k_{0,PbO_2} are the rate constants for the negative and positive reactions respectively in m s^{-1}, α is the transfer coefficient with subscripts o and r for the anodic and cathodic reactions and pos and neg for the positive and negative reactions respectively and the subscript 0 represents an initial condition. η is the overpotential in V and is given by:

$$\eta = E_{ext} - \phi - E_{eq} \tag{4.31}$$

Where E_{ext} is the external potential, ϕ is the local ionic potential and E_{eq} is the equilibrium potential at each electrode in V. The values for E_{eq} are calculated using the Nernst equation:

Negative

$$E_{eq} = E_0 + \frac{RT}{zF} \ln c_{Pb} \tag{4.32}$$

Positive

$$E_{eq} = E_0 - \frac{RT}{zF} \ln \frac{c_{Pb}}{c_{H^+}} \tag{4.33}$$

Where E_0 is the standard reduction potential in V, R is the universal gas constant in J K^{-1} mol^{-1}, T is the temperature in K, z is the valence of the reaction and c is the concentration of the species in subscript. The kinetics of the side reaction were described using:

$$i_{loc} = F \left(k_{f,PbO} c_{PbO}^2 e^{\left(\frac{F\eta_{pos}}{RT}\right)} - c_{H^+} c_{PbO_2} k_{b,PbO} e^{\left(-\frac{F\eta_{pos}}{RT}\right)} \right) \tag{4.34}$$

Where $k_{f,PbO}$ is the forward rate constant for the side reaction, and $k_{b,PbO}$ is the backward rate constant for the side reaction.

4.3.3 Electrodes

No slip wall conditions were employed with velocity set to zero $\mathrm{m\,s^{-1}}$ at each electrode surface. The x and y components of velocity, u and v are therefore set to zero:

$$u = 0,\ v = 0 \tag{4.35}$$

An average current density was applied at the positive electrode surface, eq(5.2). The negative electrode potential was set to zero, eq(5.1).

$$\phi = 0 \tag{4.36}$$

$$\int_0^Y j dy = y j_{app} \tag{4.37}$$

Where j is the current density, j_{app} is the average applied current density at the positive electrode and y is the height of the electrode in the y-direction.

4.3.4 Membrane

As there are significant changes of concentration and potential on either side of the membrane, Donnan potentials may be used. This gives two values for concentration and electrolyte potential at the membrane-electrolyte interface – one approaching from the electrolyte domain and another approaching from within the membrane, denoted by subscripts 1 and 2 respectively. To do this, the electrochemical potentials for both conditions are set to be equal, Equation 4.38. Then the equation relating concentrations and electrolyte potential to electrochemical potential, Equation 4.39, can be substituted into Equation 4.38 to calculate the Donnan potential, Equation 4.40.

$$\overline{\mu_{i,1}} = \overline{\mu_{i,2}} \tag{4.38}$$

$$\overline{\mu_i} = RT \ln\left(\frac{c_i}{c_{i,ref}}\right) + F z_i \phi_l \tag{4.39}$$

$$\phi_{l,1} - \phi_{l,2} = -\frac{RT}{z_i F} \ln\left(\frac{c_{i,1}}{c_{i,2}}\right) \tag{4.40}$$

Where $\overline{\mu_i}$ is the electrochemical potential and $c_{i,ref}$ is an arbitrary reference concentration.

4.4 Mesh Sensitivity

As with any finite element analysis (FEA) study, a mesh sensitivity study, is required to ensure the results are valid. A finer mesh usually leads to a more accurate solution but requires more processing power and memory to solve. A mesh sensitivity study aims to find the point where any further increase in the number of elements does not significantly improve the quality of the solution. This can be done for the global mesh size, but can also be done locally, at areas of interest or regions with particularly high rates of change of dependent variables.

Further to this, the tolerance of the solver used to decide when the solution is converged and the order of the elements in the mesh must also be checked.

For each variation of the model described in this thesis, a mesh sensitivity study was completed. In the interest of brevity, the mesh sensitivity analysis for a single model is presented here. However, the same method was repeated for each of the other models. Further information on these models is shown in Appendix C.

The mesh is described by several parameters: the number of elements vertically, the number of elements horizontally, the number of boundary layer elements and the growth factor for the elements in each direction. The growth factor is the amount a boundary layer element increases in size with each element with distance from the boundary. Applying this allows for finer elements near the boundaries and larger elements in the bulk domain. For models with electrode and/or membrane regions, the horizontal elements can be divided into separate parameters for each domain.

Maximum current density over the entire simulated period was chosen as the parameter for determining if the mesh was sufficiently fine. Current density is linked to all other variables of interest (species concentration, overpotential and hence cell potential), so was an appropriate choice.

Figure 4.2 shows the variation of maximum current density magnitude during the first charge and the computation time for each simulation verses number of elements in each direction for the divided SLFB with RVC electrodes model. In this case, the number of elements beyond which give diminishing returns for model accuracy were: 150, 30, 5 and 7 elements in the vertical direction, horizontal direction in electrodes, horizontal direction in the membrane and boundary layer elements respectively. Note that with fewer than 150 elements in the vertical direction the solution did not consistently converge.

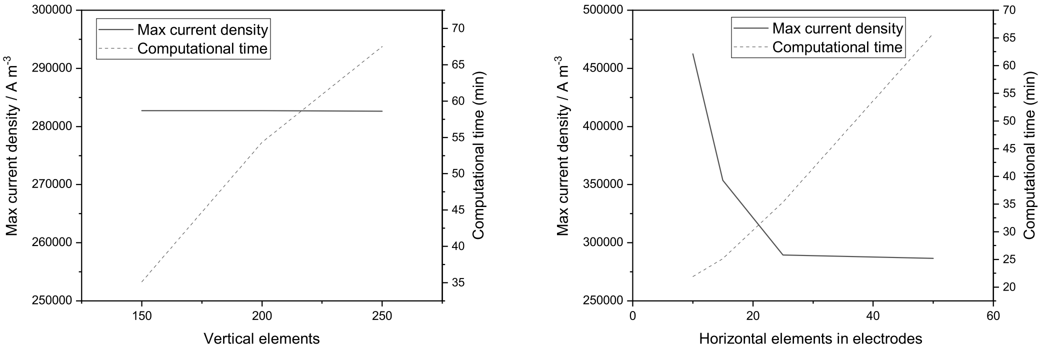

(A) Number of elements in the y-direction (vertical) (B) Number of elements in the x-direction (horizontal) in the electrode domains

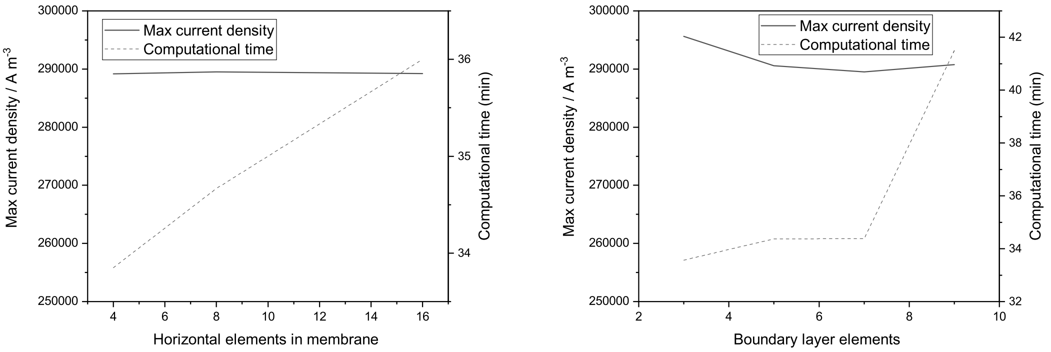

(C) Number of elements in the x-direction (horizontal) in the membrane domain

(D) Number of boundary layer elements

FIGURE 4.2: Maximum local current density magnitude (solid lines) and computational time (dashed lines) recorded with when number of elements are varied for the divided SLFB with RVC electrodes model.

Chapter 5

Moving Mesh

The effects of deposit growth on the SLFB are investigated using the modelling framework described in Chapter 4. The model is set up with only solid and electrolyte domains. A novel approach to simulate deposit growth and dissolution by reforming the geometry at each time step is used to investigate the effect of this change in geometry due to the formation and dissolution of deposits at high capacity and applied current density on the cell resistance, voltage response and electrolyte concentration distribution. In order to observe significant changes in electrode deposit thickness, long charge times are required. A charge time of 24 hours at 20 mA cm^{-2} leads to a lead deposit of approximately 2 mm thick. This is calculated using Faraday's Law Equation 1.1.

The geometry for the model initially consists of a fluid domain representing the electrolyte and two solid domains at either side of it. One for the negative electrode and one for the positive electrode. Initially, the solid domains are both 1 mm thick, a nominal value chosen to represent the thickness of clean carbon electrodes, and the fluid domain and hence the inter-electrode gap is 12 mm thick. This gap is typical in the literature [94] and is also the inter-electrode gap in the experimental cell used for validating the study, see Section 3.1. As the cell is charged the sizes of the solid domains grow and the fluid domain decreases in size correspondingly. The opposite occurs during discharge.

Two techniques are available to mesh the system as the geometry changes: a moving mesh and an adaptive mesh. In the moving mesh technique, the number of elements remains constant. Whereas, in an adaptive mesh technique, the geometry is re-meshed at certain intervals to reduce the computational cost. In this study, a moving mesh is applied to capture the change in deposit geometry with state of charge. This is because the areas of interest are close to the electrode boundaries, which require multiple boundary layer elements. In this study, the number and size of the boundary elements remain constant. Therefore, only a marginal benefit could be gained by using an adaptive mesh. This small advantage may be lost due to the additional computational effort of re-meshing. This was confirmed with a significant increase in computational time with an initial comparison of the two methods which is discussed in more detail in Appendix B. The simpler moving mesh technique is therefore chosen.

The size of the electrodes is calculated simply using Faraday's law, Equation 1.1, and typical values of density for Pb, PbO_2 and PbO, as described in Chapter 1. Equation 5.1 shows the equation used to calculate the electrode thickness.

$$d_e = d_{e,0} + \sum_i \frac{\int I_i dt}{Fz_i \rho A - e} \tag{5.1}$$

Where d_e is the thickness of the electrode, e, A_e is the electrode area and I_i is the local reaction current density for each respective species, i, averaged over the respective electrode surface, e.

Because the geometry is changing as the model moves, the mesh needs to adapt accordingly. Figure 5.1 shows the change in the model geometry as the cell is charged and discharged. Initially, $d_e p$ and $d_e n$ represent only the positive and negative carbon polymer electrode material respectively. After charging the values for d increase and therefore G_{ie} decreases. When the cell discharges, d_{en} returns to very close to $d_{en,0}$. However, due to the formation of some PbO, $d_{ep,d}$ is larger than $d_{ep,0}$.

The mesh used in this study is shown in Figure 5.2. A rectangular mesh is used with 30 elements distributed across the width of the liquid domain and 60 along the length of the cell. A further 15 boundary layer elements are added at each electrode surface on the liquid side of the electrode. In total, there are 3600 elements. The mesh sensitivity was assessed using the method discussed in Section 4.4.

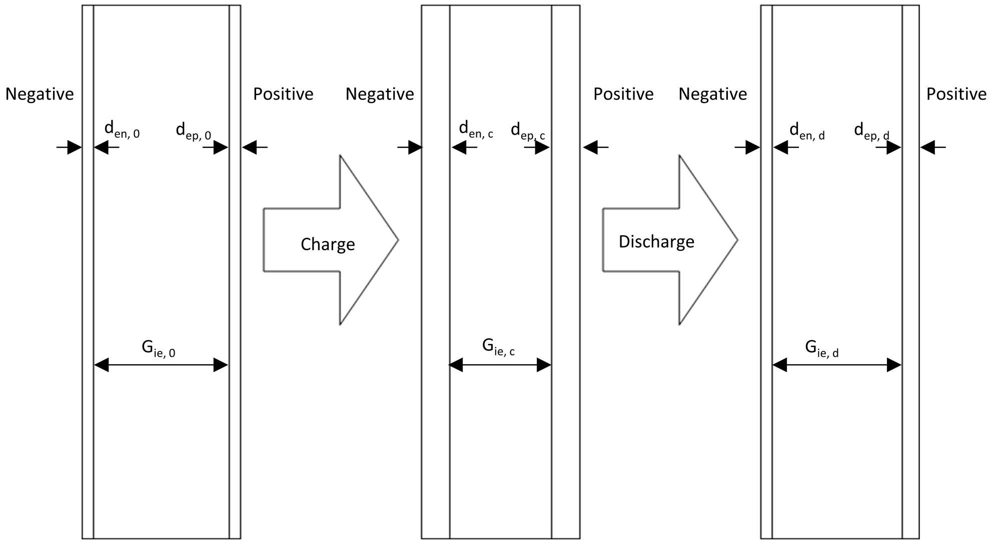

FIGURE 5.1: Geometry as it changes from clean electrodes (left) to electrodes with deposits combined into a single solid domain at each electrode (right). G_{ie} is the inter-electrode gap, d_{ep} and d_{en} are the positive and negative solid domain thicknesses respectively. Subscript 0 represents before cycling, c represents after charging and d after discharging.

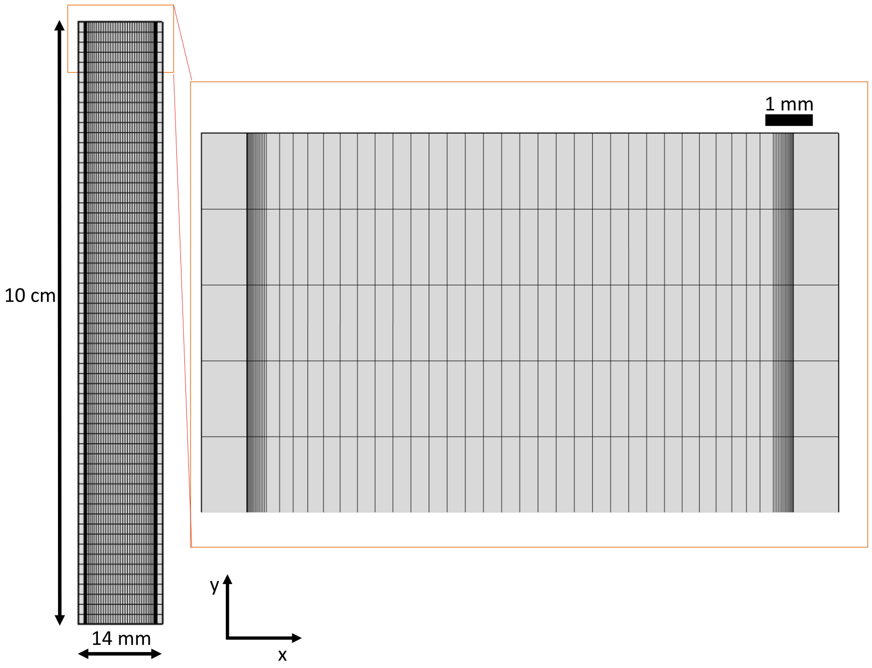

FIGURE 5.2: A snapshot of the mesh used for all simulations. The full mesh is shown on the left and a zoomed section is shown on the right. The mesh shown is at t = 0

5.1 Density, Conductivity and Viscosity

Because the electrolyte significantly changes composition with varying SoC, the density, conductivity and viscosity of the electrolyte also change accordingly. Similarly, as the deposits grow at each electrode, the conductivity of the solid domains also changes.

Using data from Krishna et al., [49], the density, conductivity and viscosity of the electrolyte can be calculated from the concentrations of Pb^{2+} and H^+. This data was measured using solutions with a range of Pb^{2+} and H^+ concentrations. An equation was drawn that described the line of best fit through the data points. The line was then used as a reference for the values of density and viscosity in the model. The conductivity, however, was calculated in the model using the diffusion coefficients. These values were taken from previous models in the literature but, as described in the Chapter 6, these proved to be inaccurate and so adjustments were made for subsequent simulations.

Both solid domains consist of 1 mm of carbon polymer electrode, with the remaining thickness, where applicable, consisting of lead at the negative electrode and lead dioxide and lead oxide at the positive electrode.

5.2 Parameters and Variables

5.2.1 Initial values

Initial values for variables used in the numerical model are highlighted in Table 5.1. The velocity, concentrations and interelectrode gap $\mathbf{u}$, C_{H^+}, G_{ie} from Collins et al. [94] were taken to be reasonable conditions. However, the Pb^{2+} concentration, C_{PbII}, was increased to 1000 mol dm^{-3} to accommodate the high capacity required for this work. Temperature was room temperature and electrodes were nominally 1 mm thick. To ensure local concentrations remained positive and so mass transport limitations did not occur, the electrolyte volume was chosen to be double that required for a 24 hour charge at 20 mA cm^{-2}.

TABLE 5.1: Initial values of parameters used in the model.

Symbol	Parameter	Value
u	Average inlet velocity	$2.3\ \mathrm{m\,s^{-1}}$
C_{PbII}	Pb^{2+} concentration	$1000\ \mathrm{mol\,dm^{-3}}$
C_{H^+}	H^+ concentration	$500\ \mathrm{mol\,dm^{-3}}$
T	Temperature	298 K
V	Volume of electrolyte reservoir	$3.6\ \mathrm{dm^3}$
G_{ie}	Interelectrode gap	12 mm
d_e	Electrode thickness	1 mm

5.2.2 Parameters

The values for parameters that were kept constant for each simulation are summarised in Table 5.2. The symbol used and a description of each parameter is included.

TABLE 5.2: Summary of parameters used in all simulations.

Symbol	Parameter	Value	Reference
D_{PbII}	Pb^{2+} diffusion coefficient	$7.0 \times 10^{-10}\ \mathrm{m^2\,s^{-1}}$	[156]
D_H	H^+ diffusion coefficient	$9.3 \times 10^{-9}\ \mathrm{m^2\,s^{-1}}$	[156, 157]
$D_{CH_3SO_3^-}$	$CH_3SO_3^-$ diffusion coefficient	$1.33 \times 10^{-9}\ \mathrm{m^2\,s^{-1}}$	[156, 157]
$k_{0,Pb}$	Pb/Pb^{2+} reaction rate constant	$2.1 \times 10^{-7}\ \mathrm{m\,s^{-1}}$	[155]
k_{0,PbO_2}	PbO_2/Pb^{2+} reaction rate constant	$2.5 \times 10^{-7}\ \mathrm{m\,s^{-1}}$	[155]
$k_{0,b,PbO}$	Backward side reaction rate constant	$4.5 \times 10^{-7}\ \mathrm{mol\,m^{-2}\,s^{-1}}$	[155]
L	Vertical cell length	0.1 m	
M_{Pb}	Molar mass of lead	$207.21\ \mathrm{g\,mol^{-1}}$	[26]
M_{Pb}	Molar mass of lead dioxide	$239.2\ \mathrm{g\,mol^{-1}}$	[26]
M_{Pb}	Molar mass of lead oxide	$223.2\ \mathrm{g\,mol^{-1}}$	[26]
ρ_{Pb}	Density of lead	$11.337\ \mathrm{g\,cm^{-3}}$	[26]
ρ_{Pb}	Density of lead dioxide	$9.65\ \mathrm{g\,cm^{-3}}$	[26]
ρ_{Pb}	Density of lead oxide	$9.53\ \mathrm{g\,cm^{-3}}$	[26]
t	Rest period	120 s	

5.3 Solver

Each simulation used the same solver setup. The time-stepping the solver used was a backward differentiation formula (BDF) method for time-stepping as it is known for its stability. The BDF method uses solutions from previous time steps to approximate the derivative of an equation. A non-linear controller is used for further stability.

The solver used is a multifrontal massively parallel sparse direct solver (MUMPS) and the default COMSOL values are used. Figure 5.3 depicts a simplified version of the process the solver undergoes. The MUMPS solver solves the equations using using an initial guess U^{i0}, a Newton-Raphson method is used to refine U^{i0} to U^{i+1}, if the difference between the two values is less than a prescribed relative error the solver has converged on a solution. If the difference is larger than the relative error, U^{i+1} becomes the new guess and the process is repeated. When the solver has converged for a time, t, a value Δt is added and the process is repeated for the next time step. The BDF method used aims to keep the difference between U^i and U^{i+1} close to the relative error by increasing or decreasing Δt within certain bounds.

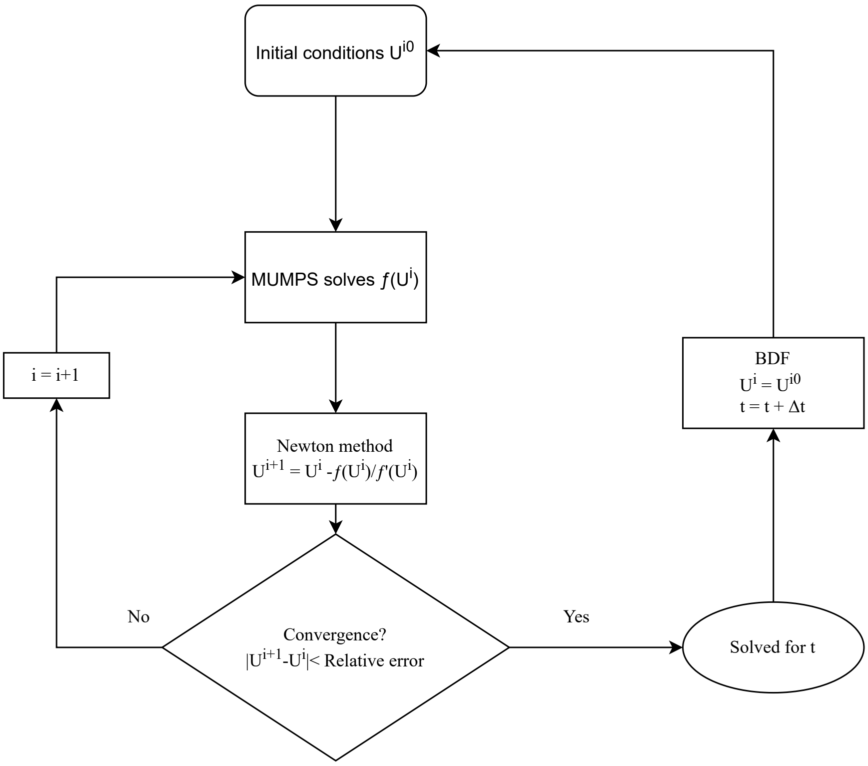

FIGURE 5.3: A simple flowchart describing the process taken by the solver, where U^i is the dependent variable for each equation $f(U^i)$ for iteration i at time t.

5.4 Rate constant

The kinetics of the main reactions were relatively consistent in the literature. Therefore, values from literature were used for these parameters. However, for the side reaction, values were inconsistent for the forward rate constant. Therefore, a parametric sweep varying $K_{0f,PbO}$ was completed. The voltage vs time curve for the second 24 hour charge of the cell is shown in Figure 5.5. Cycling a physical cell is required to validate the value chosen and to ensure the other rate constants are valid for cycling with 24 hour charges. However, a value of 0.002 for $k_{0f,PbO}$ gave a reasonable response and was within the range used in the literature and was therefore chosen, see Figure 5.4.

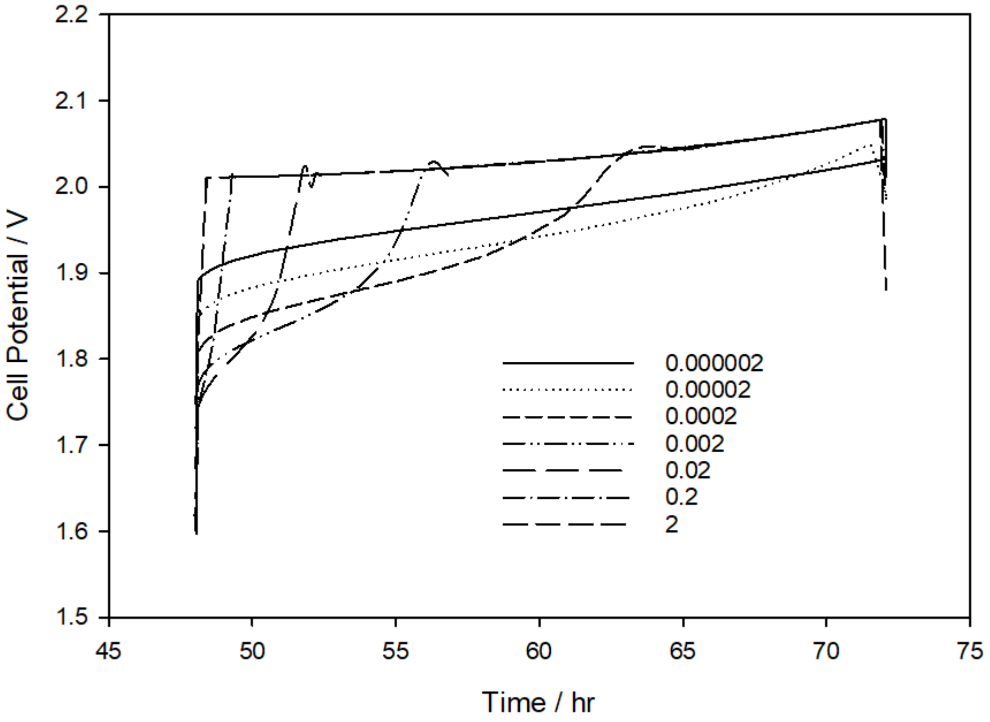

FIGURE 5.4: Simulated cell potential vs time of the second charged cycle at 20 mA cm^{-2} with a varied forward rate constant, $k_{0f,PbO}$, for the side reaction from 2 to 2 × 10^{-6} mol m^{2} s^{-1}.

Using this value for the rate constant, the modelled cell was cycled for two charge-discharge cycles at constant currents of 20 mA cm^{-2} and 30 mA cm^{-2}.

5.5 Simulated cycling regime

With each current density, the simulated cell was charged to a constant Pb utilisation, so the cell charged at a higher rate was charged for a correspondingly shorter time. The simulated cell was charged at a constant current until an average capacity of 480 mAh cm^{-2} was reached. At a current density of 20 mA cm^{-2} this corresponded to a 24 hour charge. The model was set to open-circuit (no applied current) for 120 s, before discharging until the cell voltage reached 1.2 V with a current density of 20 mA cm^{-2}. After another 120 s period at open-circuit, the charge-discharge cycle was repeated.

It can be seen in Figure 5.6 that the model charged at a higher rate also had greater overpotentials, as expected. It can also be seen that the overpotential of the cells with the moving mesh are marginally smaller than those with no change in geometry, due to the net change in resistance over all domains. As the deposits grow, there is increasing ohmic resistance, particularly from the PbO_2, while the inter-electrode gap diminishes and the electrolyte conductivity varies as a function of SoC speciation.

During the first charge period in the simulation, the voltage starts at circa 2.0 V and steadily rises to 2.1 V due to consumption of Pb^{2+} from the electrolyte and increasing electrode deposits. On simulating discharge, the voltage decreases from 1.7 V to circa 1.55 V before a rapid decrease in voltage to 1.2 V due to a decreasing mass of electrode deposits available for the discharge reaction. On the second charge in the simulation, there is initially a lower charge voltage as PbO is converted to PbO_2 at the positive electrode. Once the PbO is consumed by the reaction, the main reaction becomes dominant again and the voltage rises to a voltage comparable to that seen in the first charge. This is consistent with experimental results previously reported [170].

When a moving mesh is applied to the model over the first cycle, it is seen that the overpotential is lower than when a static mesh is used, Figure 5.6. At both 20 mA cm^{-2} and 30 mA cm^{-2}, when charge is simulated, the cell potential is lower and during discharge, it is higher when a moving mesh is implemented which shows the effect of electrolyte resistance on cell potential, i.e. there is a smaller difference in cell potential between charge and discharge due to the deposits, or active electrode surfaces, getting closer to each other, therefore reducing the interelectrode gap. In both cases, in the charging step of the simulation, this difference in cell voltage increases with time. By

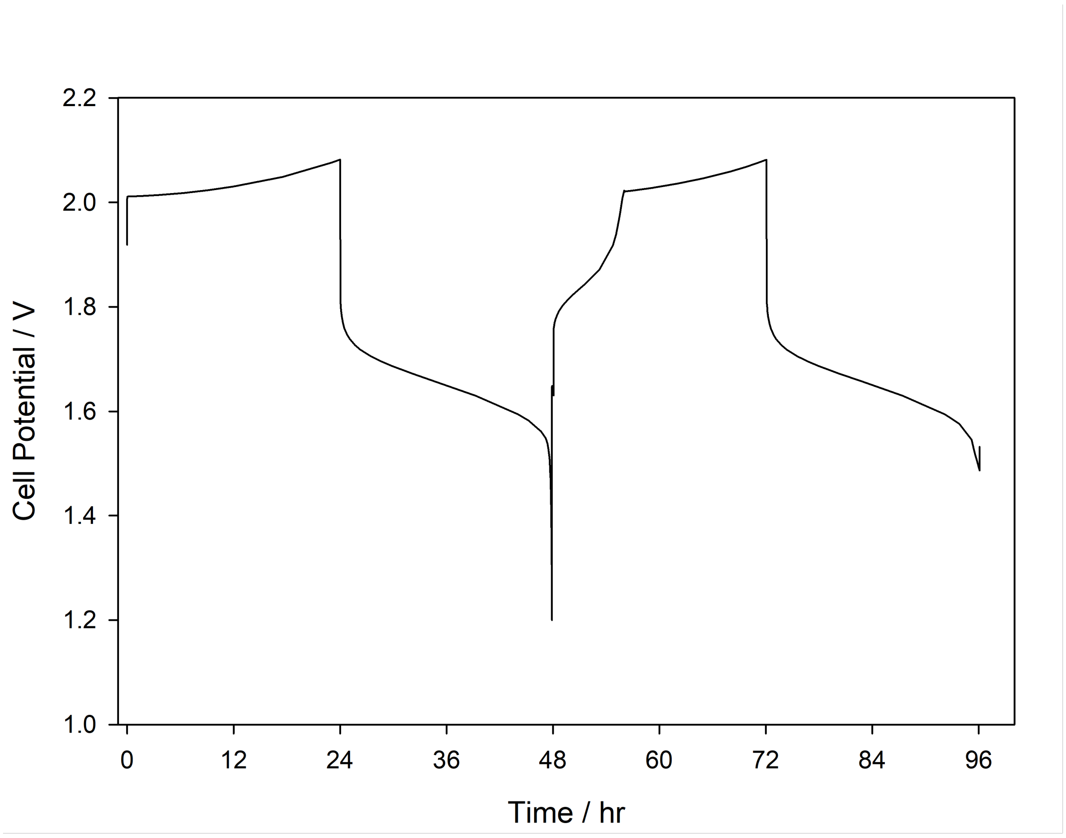

FIGURE 5.5: A simulated cell voltage vs time at 20 mA cm^{-2} using a moving mesh. Two charge-discharge cycles are simulated each with a 24 hour charge, a 2 minute rest at open circuit and a discharge to 1.2 V. The two-step charging mechanism is included in the second charge.

the end of charging, at 20 mA cm^{-2}, the static mesh voltage is 2.11 V compared to 2.08 V for the moving mesh. At 30 mA cm^{-2}, the difference increases, with cell potentials of 2.25 V and 2.17 V for the static and moving mesh results respectively. During discharge, the difference in both cases is minor. The difference is greatest when the higher current density is applied. An overpotential which increases with time and with current density suggests this could be primarily due to a change in resistance of the cell. If only a static mesh is used, a higher potential will be predicted, which would lead to an overestimate of SoC in a real system.

As the deposits form on the electrodes in the model, the resistance of the electrodes changes due to the change in geometry. Furthermore, as the electrolyte domain reduces in size with the formation of deposits, the concentrations of species in the electrolyte also change with SoC. Hence, the resistance of the electrolyte domain changes further.

The method used to calculate the resistance of the deposits assumes uniform conductivity. In this study, it is assumed that the deposits are uniform and compact. As such, the

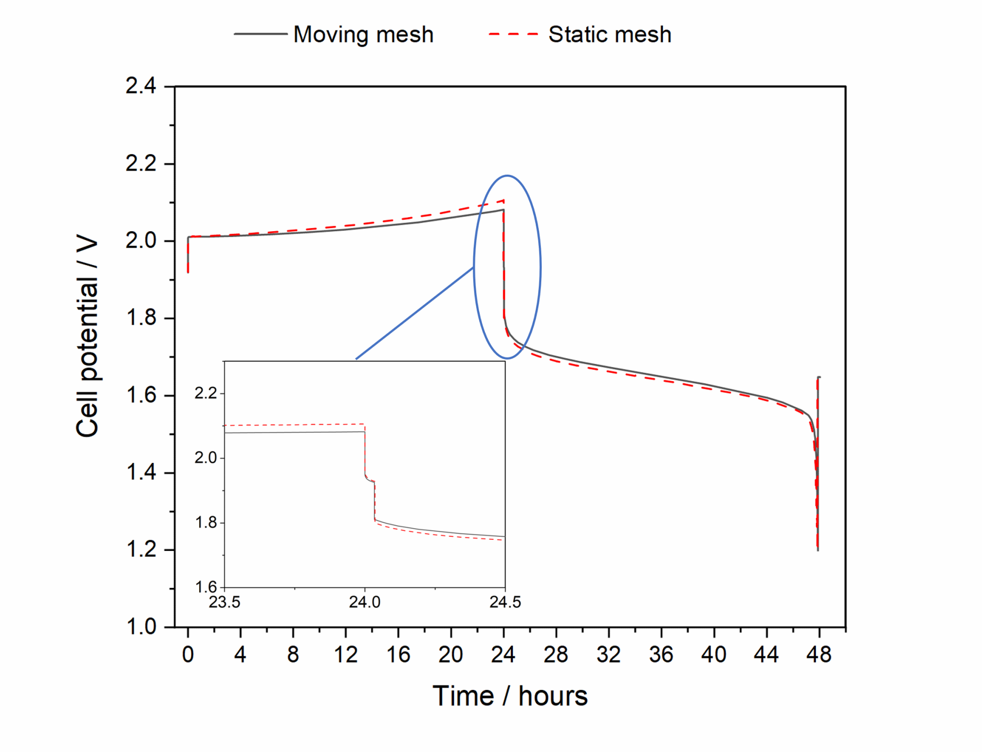

(A) 20 mA cm^{-2}

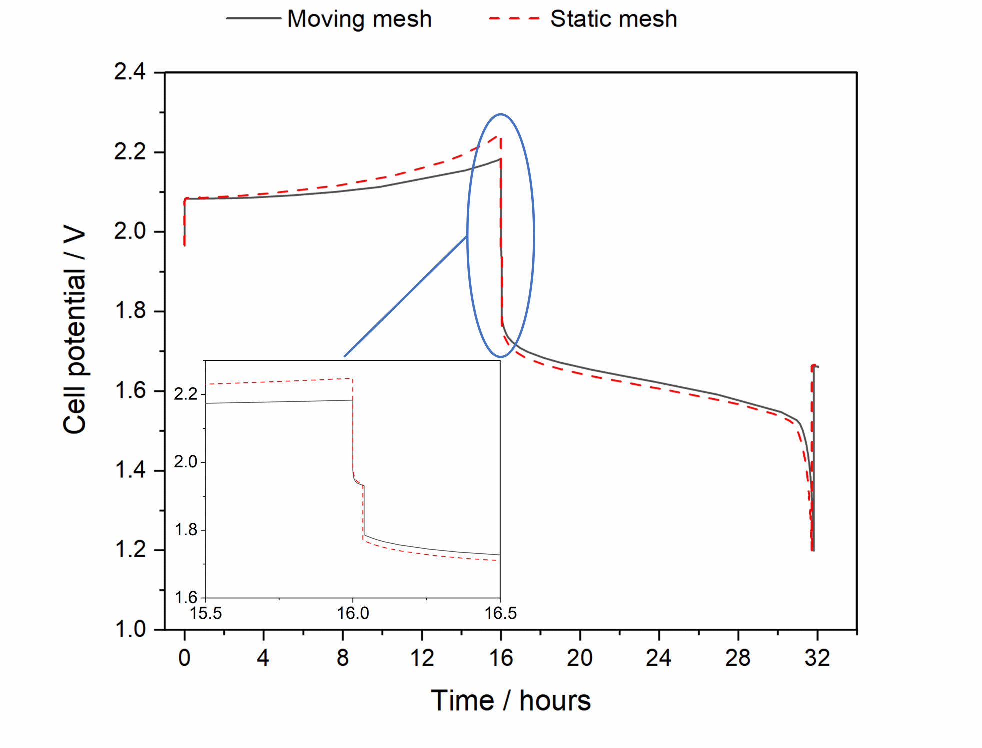

(B) 30 mA cm^{-2}

FIGURE 5.6: Simulated cell voltage vs time for one cycle a for static (red dashed line) and moving (black solid line) meshes at 20 (A) and 30 (B) mA cm^{-2}. Inset is zoomed into the region at the end of charge.

conductivity values for bulk Pb and PbO_2 species are used. While flat two-dimensional electrode deposits are difficult to achieve in reality, this is the target for SLFB design and it is still possible to extract meaningful trends in cell resistance and flow rate using this technique. The value used for the conductivity of the lead deposit at the negative electrode is 50000 $S\,cm^{-1}$ [172]. At the positive electrode, as the morphology as well as the mass of any PbO in the deposit would affect the conductivity, and the extent to which this would occur is beyond the scope of this model, the deposit conductivity was assumed to be entirely that of PbO_2. The conductivity of PbO_2 ranges from 10^3 - 10^4 $S\,cm^{-1}$ for α-PbO_2 and β-PbO_2, respectively [173]. A mixture of the two forms was assumed and a value of 5000 $S\,cm^{-1}$ was used for the conductivity of the positive electrode.

The value used for the resistivity of the carbon polymer electrodes was 0.0006 $\Omega\,cm$ and was taken from the datasheet for SGL Sigracell PV15, which has been previously used in SLFB development [171].

Figure 5.7 describes the change in simulated cell resistance, measured across the inlet of the electrolyte domain over two full cycles, each consisting of a 24 hour charge and a discharge to 1.2 V. The cell resistance is seen to change by a factor of three between solid domains simulating clean electrodes and fully formed deposits. The majority of the cell resistance is due to the electrolyte domain, with just 1.6×10^{-6} Ω due to the solid domains at the maximum deposit thickness, a negligible amount compared to the 10^{-2} Ω of the electrolyte domain. Due to the change in the inter-electrode gap when a moving mesh is used, there is a significant change in the resistance of the electrolyte when compared to the static mesh. The cell resistance after the charge step of the simulation is 33 % lower in the moving mesh when compared to the static mesh simulation with resistances of 0.0116 Ω and 0.0172 Ω, respectively. This difference is reduced to 9 % after discharge when the moving mesh gives 0.0230 Ω and the static mesh gives 0.0250 Ω.

This fluctuation in resistance is likely to be an underestimate due to neglecting the presence of an insoluble discharge product, PbO, a compound which has a much higher resistance than PbO_2, and the calculated resistance of the electrolyte which is significantly lower than the conductivity measurements by Krishna et al. would suggest [49]. This discrepancy is addressed in Chapter 6. The diffusion coefficient will change as

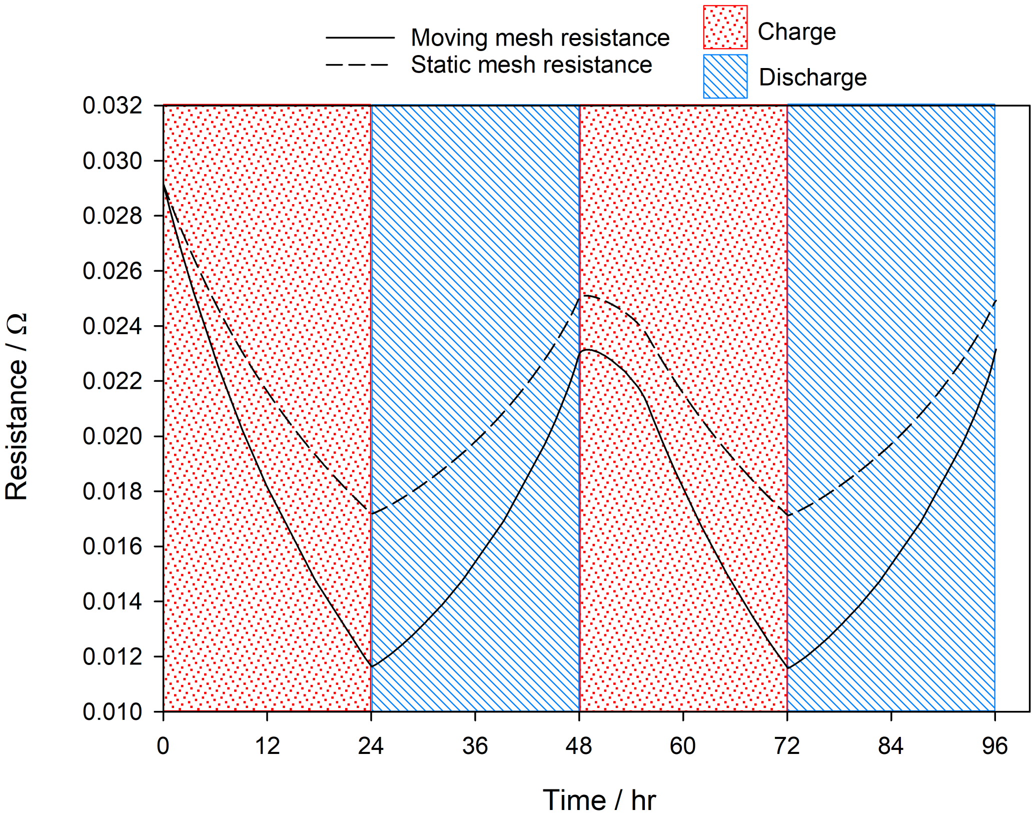

FIGURE 5.7: Cell and electrolyte resistance vs time for static and moving mesh simulations. The cell resistance includes the resistance of the electrolyte deposits and the carbon electrode. Both resistances are measured across the electrolyte inlet. The cell was run at 20 mA cm^{-2}. Charging is shown with a red dotted background and discharge with a blue striped background.

a function of electrolyte composition, which would be consistent with the conductivity measurements by Krishna et al. In this simulation, the electrodes have a minimal effect on the resistance of the cell. The variation in resistance due to the deposits is 0.5 μΩ.

Figure 5.8 shows the Pb^{2+} concentration profiles of a section of the cell comparing the simulation run with a moving mesh and without the moving mesh at 20 mA cm^{-2}. Generally, a similar concentration profile is seen when comparing the two methods and the bulk concentration is almost identical in both cases. However, the change in geometry leads to a shallower gradient close to the positive electrode. With a more sophisticated understanding of mechanisms, this difference in concentration close to the electrode may be significant.

When charging to 480 mA h cm^{-2}, the deposit size can vary significantly. To account for this in the model, the moving mesh adapts to the change in geometry. This is shown in Figure 5.9. The cell initially has clean electrodes. As a charge is simulated, Pb and PbO_2

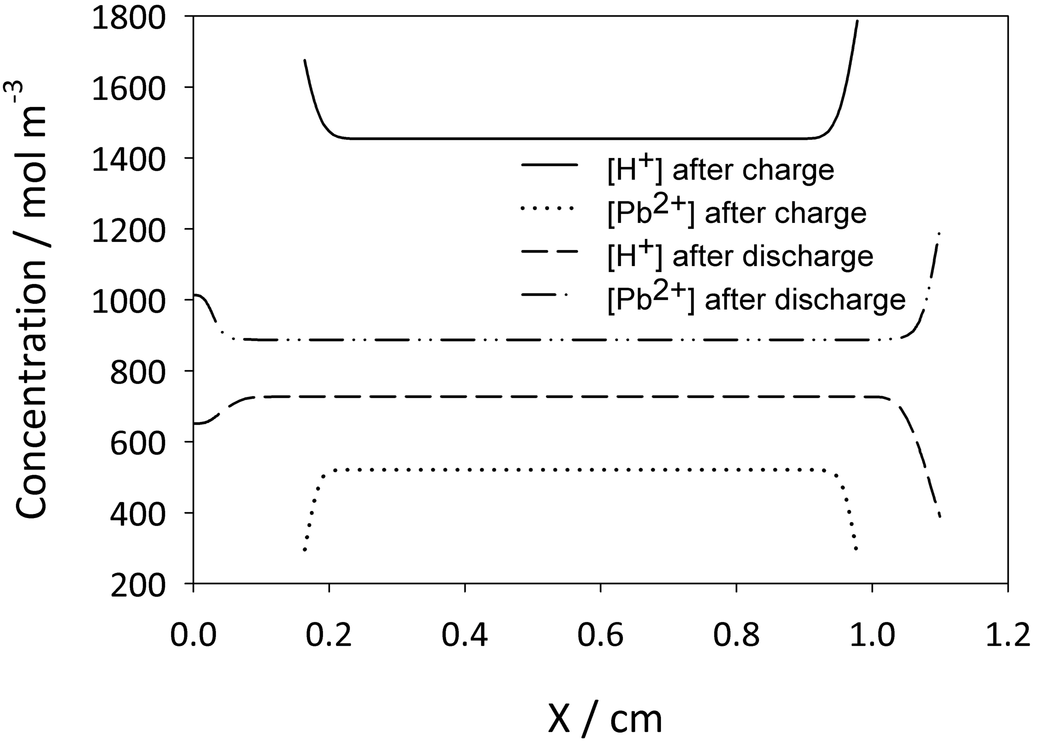

(A) With a simulated change in geometry

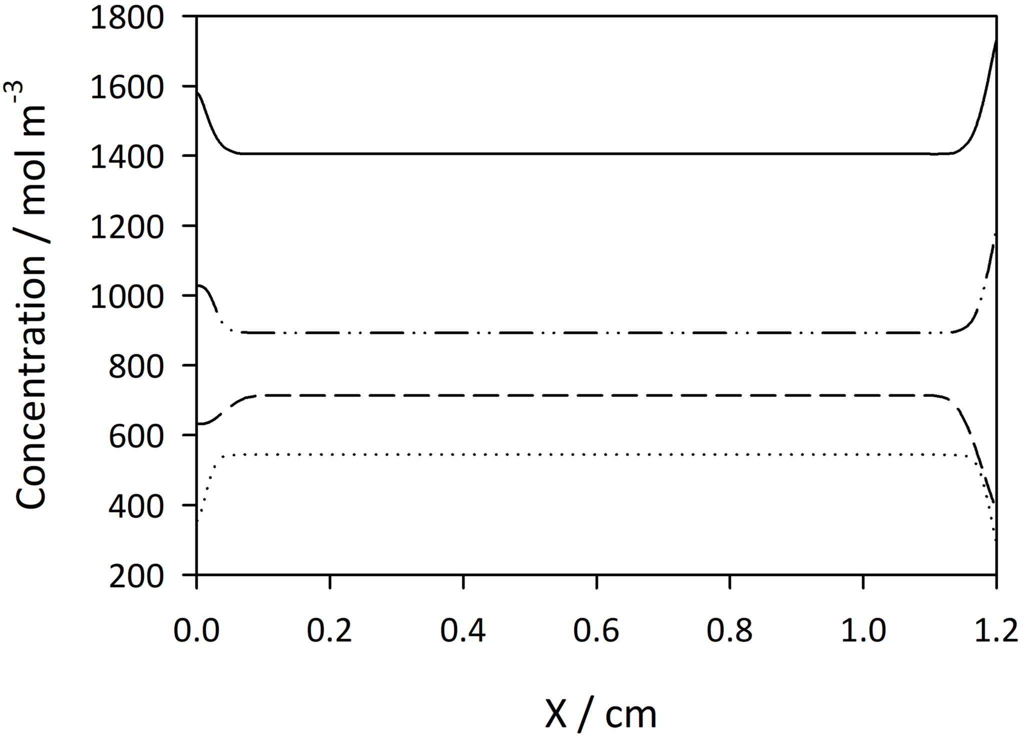

(B) Without a simulated change in geometry

FIGURE 5.8: Concentration profiles of the SLFB with and without a simulated change in geometry. A current density of 20 mA cm^{-2} is used.

form on the negative and positive electrodes respectively. When discharge is simulated, these deposits are stripped from the electrode surface. However, PbO forms at the positive electrode. During subsequent charges, PbO is converted to PbO_2 alongside the PbO_2 that forms from Pb^{2+} in solution. In Figure 5.9, the electrodes are initially just the carbon polymer bipolar plates (a). When the charge is simulated, both electrodes grow in size (b) before reducing again as discharged is simulated (c). (c) shows the negative electrode domain is virtually clean again after discharge. However, at the positive electrode, PbO is still deposited. The process is repeated for the subsequent charge (d) and discharge (e).

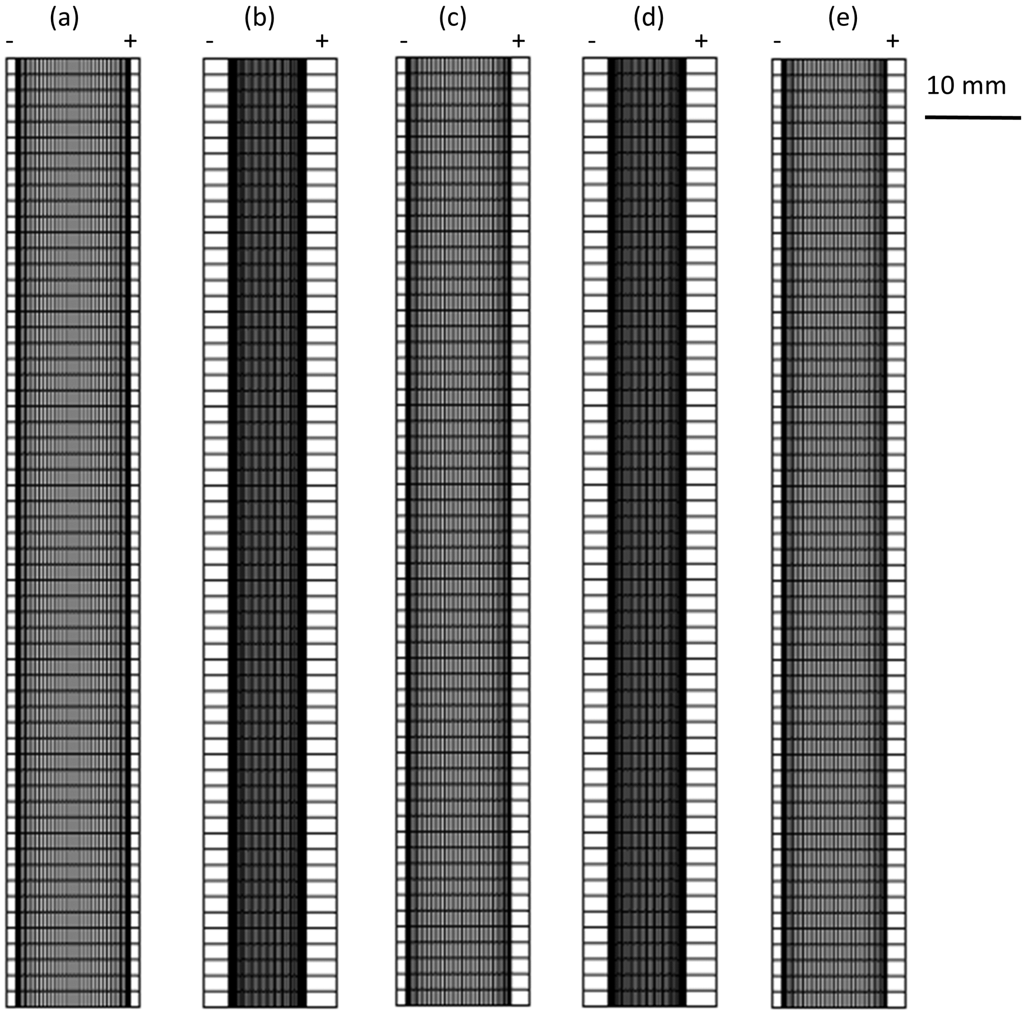

FIGURE 5.9: Progression of the moving mesh from clean electrodes (a) to 1 charge (b) then 1 discharge (c), 2 charges (d) and 2 discharges (e). The negative electrode is on the left side of each cell and the positive electrode is on the right.

As discussed at the beginning of the chapter, the mesh is not adaptive. Therefore, the number of elements remains constant. Only the dimensions of the elements change as the geometry changes.

Figure 5.10 shows the volumetric flow rate of the electrolyte as the cell is cycled during the moving mesh and static mesh simulations. In this model, to ensure the laminar flow regime remains valid, the applied electrolyte velocity was fixed as a boundary condition. As expected, the static mesh shows a constant flow rate as both the geometry and the velocity were both constant. The moving mesh simulation, however, shows a significant difference in flow rate ranging from 27.8 cm^3 s^{-1} to 18.6 cm^3 s^{-1}. In order to cycle a physical cell effectively, a battery management system for the flow cell would need to take this variation into account for control of the pump.

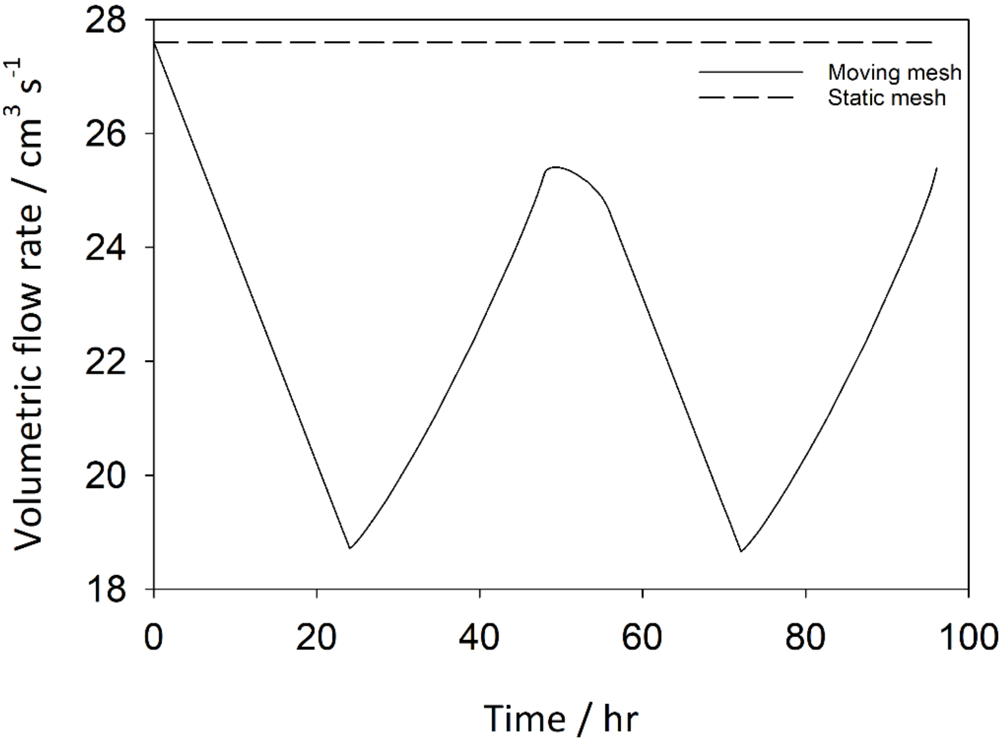

FIGURE 5.10: Simulated volumetric flow rate vs time of the cell cycled at 20 mA cm^{-3} for both the static mesh (dashed line) and the moving mesh (solid line).

Figure 5.11 shows the simulated electrolyte velocity profile over the liquid domain, (a), and the distribution of the y-component of velocity over a line drawn across the centre of the electrolyte domain, (b). The y-component (vertical) of the velocity dominates while flow in the x-direction (horizontal) is negligible. As explained in Chapter 4, the average velocity is constant. Therefore, as shown in Figure 5.11, the volumetric flow rate varies

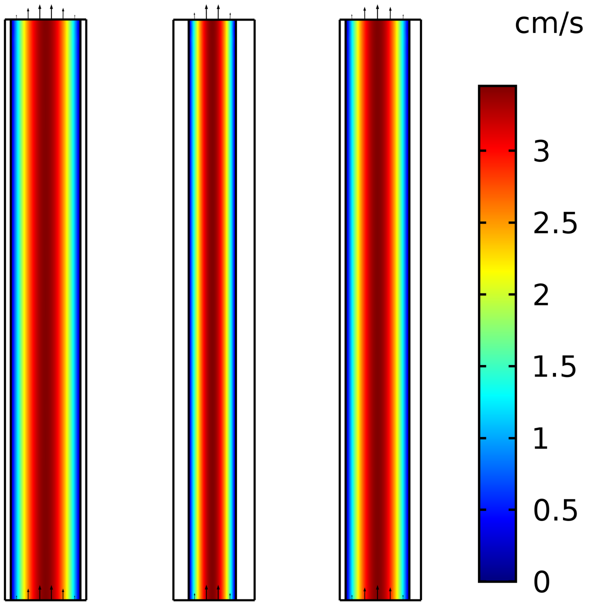

(A) Velocity distribution over the entire 2D domain, from left to right, at time = 0, after the charging and after discharging.

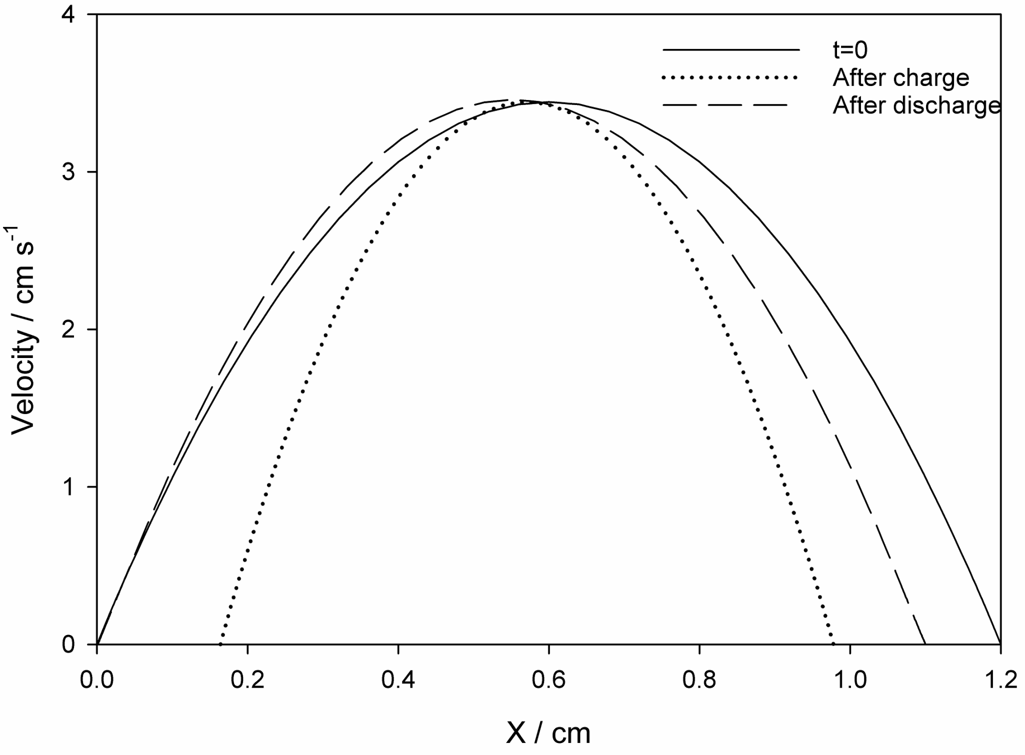

(B) Velocity distribution at the mid-height of the electrodes at time = 0 (solid line), after charging (dotted line) and after discharging (dashed line).

FIGURE 5.11: Simulated velocity profile of the electrolyte before the first charge, after the first charge and after the first discharge.

as the liquid domain changes size with SoC. The flow remains parabolic throughout the simulation, with a maximum velocity of 3.46 cm s^{-1} at the centre of the inter-electrode gap. The velocity is zero at the boundaries, in line with the no-slip boundary condition at the electrode surfaces. A parabolic velocity profile is applied at the inlet and so the velocity profile is consistent along the length of the electrolyte domain.

5.6 Current distribution

Although the assumption made here is that the deposit grows evenly across the surface of the electrode, the current density suggests there would be a greater deposit growth near the inlet. The simulated local current density sharply increases as the inlet is approached. Figure 5.12 shows the current distribution along the boundary of each electrode domain. When comparing this with the simulated overpotential Figure 5.14, concentration Figure 5.15, electrolyte potential and equilibrium potential Figure 5.13 calculated using the Nernst equation, the reasons become clear.

As the electrolyte flows along the electrode boundaries, it follows that the Pb^{2+} concentration will decrease with distance from the inlet during charge and increase during discharge, sharply, initially as the electrode reactions form a concentration gradient, Figure 5.15. Both the electrolyte potential and the equilibrium potential depend on concentration. Figure 5.13 shows that the simulate equilibrium potential decreases gradually as the inlet in approached but the equilibrium potential decreases dramatically close to the inlet. As overpotential is defined by the external potential minus the electrolyte potential and the equilibrium potential, it is expected that the simulated overpotential will increase dramatically near the inlet. Figure 5.14 shows that this is indeed the case, and hence, the current density follows the same trend.

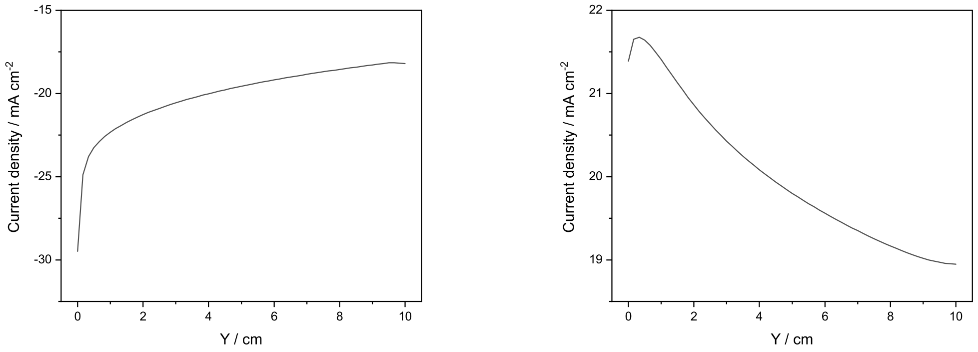

(A) Negative electrode during charge

(B) Negative electrode during discharge

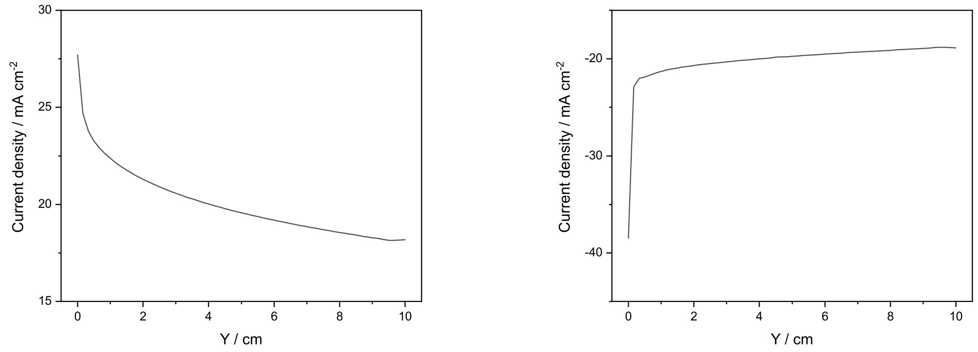

(C) Positive electrode during charge

(D) Positive electrode during discharge

FIGURE 5.12: Simulated current density along the y-direction of the electrodes. Y=0 is at the inlet.

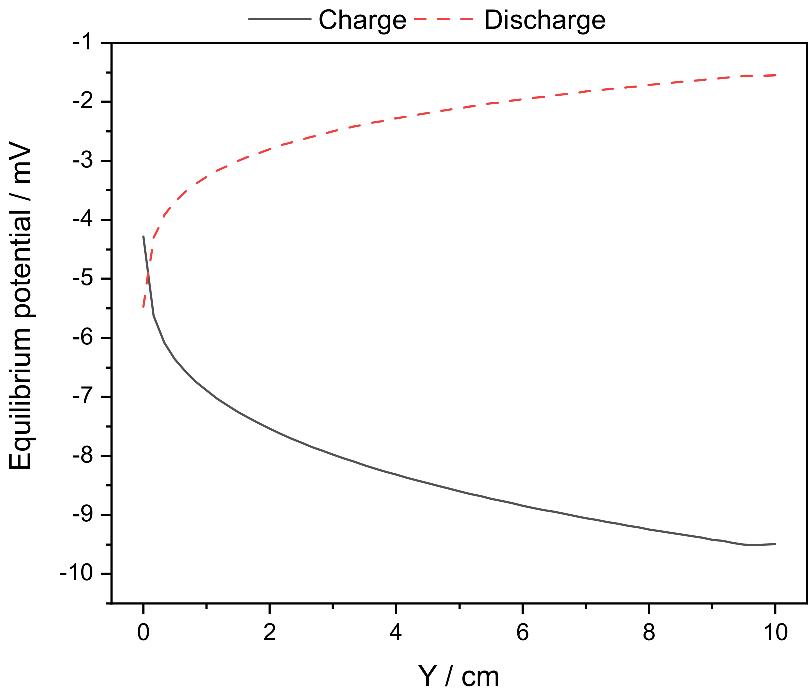

(A) Negative electrode

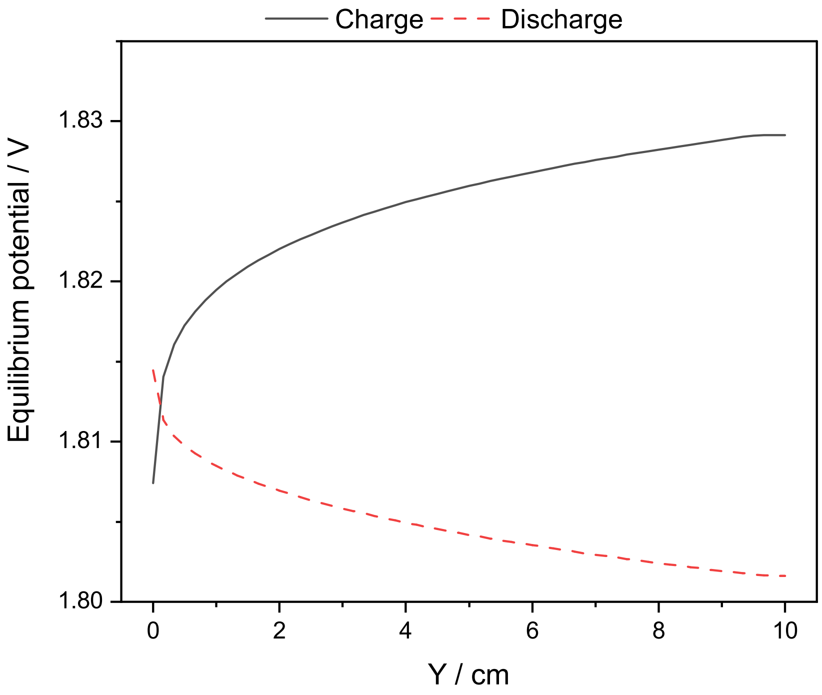

(B) Positive electrode

FIGURE 5.13: Simulated equilibrium potential during charge (solid black line) and discharge (dashed red line) along the y-direction of the electrodes. Y=0 is at the inlet.

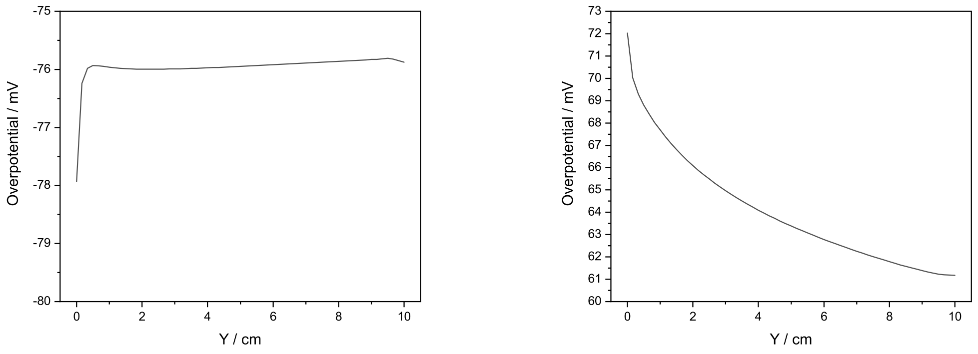

(A) Negative electrode during charge

(B) Negative electrode during discharge

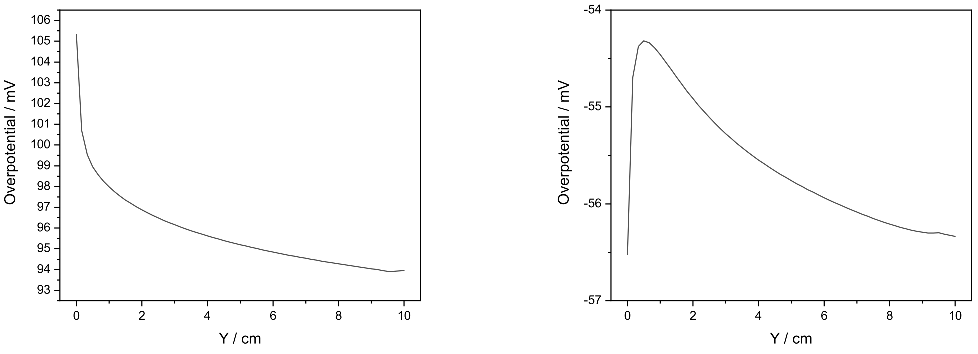

(C) Positive electrode during charge

(D) Positive electrode during discharge

FIGURE 5.14: Simulated overpotential along the y-direction of the electrodes. Y=0 is at the inlet.

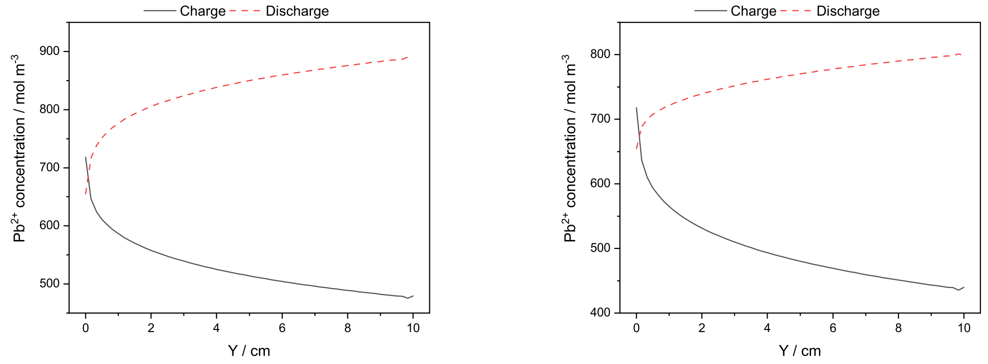

(A) Pb^{2+} concentration at negative electrode

(B) Pb^{2+} concentration at positive electrode

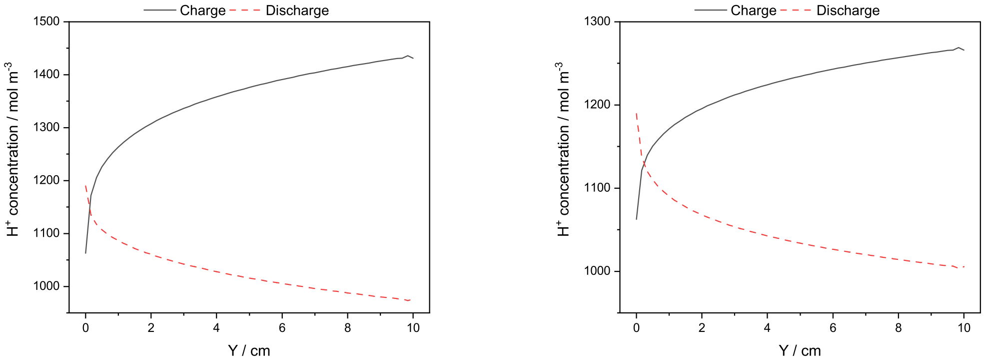

(C) H^{+} concentration at negative electrode

(D) H^{+} concentration at positive electrode

FIGURE 5.15: Simulated concentration in the y-direction of the electrodes during charge (solid black line) and discharge (red dashed line). Y=0 is at the inlet.

5.7 Comparison with experimental results

As the majority of experimental charge-discharge cycling of the SLFB has been with charges of between 1 and 2 hours, in order to validate the simulations against these results, the model was run again over using a simulated 1 hour charge cycle. Reducing the charge time to 1-hour also made a direct experimental comparison more straightforward and reduced the cost of materials for the electrolyte. Results from literature, [94, 95, 152, 155], have been used to validate the model when run over a 1 hour charge alongside experimental data measured by the author. The cell potentials seen during the second charge and subsequent discharge in studies where a current density of 20 mA cm^{-2} was used have been compiled and the average values are plotted against the simulated and experimental cell potential in Figure 5.16. The simulated voltage profile is 1.85 V at the beginning of the charge. It then steadily rises to circa 2.00 V by 3000 s with a maximum gradient at circa 2000 s. The static mesh and moving mesh simulations give virtually identical results over a 1 hour charge as only $\approx$ 80 µm deposits are formed. Hence, only the moving mesh simulation results are shown in Figure 5.16.

In the physical cell, the resistance between the electrode surface and the tab on the current collector, measured using a Fluke BT510 portable battery analyser, was found to be approximately 30 mΩ at each electrode. This resistance is not included in the simulations and hence the experimental voltage profile has been adjusted to compensate accordingly. The simulated voltage profile broadly matches the experimental curve. However, the change between the voltages of the characteristic two-step charging mechanism is less sudden in the simulated result and the cell potential during the first step occurs at circa 70 mV lower in the experimental result. The literature cell potentials are taken at the beginning and end of the charge with the point of maximum gradient used as the point of transition. The average initial and final literature potentials are 1.86 V and 2.02 V, respectively. The turning point occurs at 1620 s, a reasonable match with the simulated and experimental results from this work. However, there is also significant variability between the potentials of these two steps in the literature results.

In the literature, while the potential during the second step is consistent, the potential of the first step varies significantly between studies. The difference between cell potentials during these two steps ranges from 100 mV to 200 mV. These factors support the evidence that the mechanism of the two-step charging is more complex than the simple

PbO side reaction included here and elsewhere. A better understanding of this area is therefore required. Furthermore, Verde et al. suggest that the PbO_2 nucleation, particle size and phase (α- and β-) have a significant effect on the first step potential and timing [93]. These aspects are not included in the model.

There is a moderate discrepancy between the simulated and experimental cell voltage during discharge; the simulated cell voltage is approximately 1.6 V compared with the experimental value of 1.55 V and the literature value of 1.48 V. The literature values are from a range of systems with different inter-electrode gaps, starting Pb^{2+} and free acid concentrations and different total volumes of electrolyte. The PbO_2 properties discussed by Verde et al. [93] also affect the discharge potential.

The cell potential at the end of the charge, where it is assumed only the main electrode reactions take place match closely between simulated, experimental and data from the literature. Other variables that may contribute to a change in resistance, such as the contact resistances in the cell are also not included in the model. The change in resistance due to these factors is likely to contribute to the difference in cell potential seen during discharge.

However, with a full experimental parameterisation study including producing Tafel plots for the kinetics to accurately determine the rate constants, it is expected a closer match with experimental results would be observed. This should be an area of future work for modelling the SLFB.

It should be noted that the work in this chapter aims to implement a moving mesh to take account of Pb and PbO_2 deposit formation/dissolution to simulate the SLFB system better. During both charge and discharge, the voltages derived using a moving mesh are closer to the observed experimental values than for the static mesh. On the timescale of one-hour charge/discharge periods, the difference is small ($<$10 mV); however, as shown in Figure 5.6, over more typical operational periods for the SLFB ($>$1 hr), the difference can be over 100 mV. This demonstrates a significant improvement in simulation for the moving mesh approach. Over sequential charge/discharge cycling, the voltage and SoC are more accurately simulated.

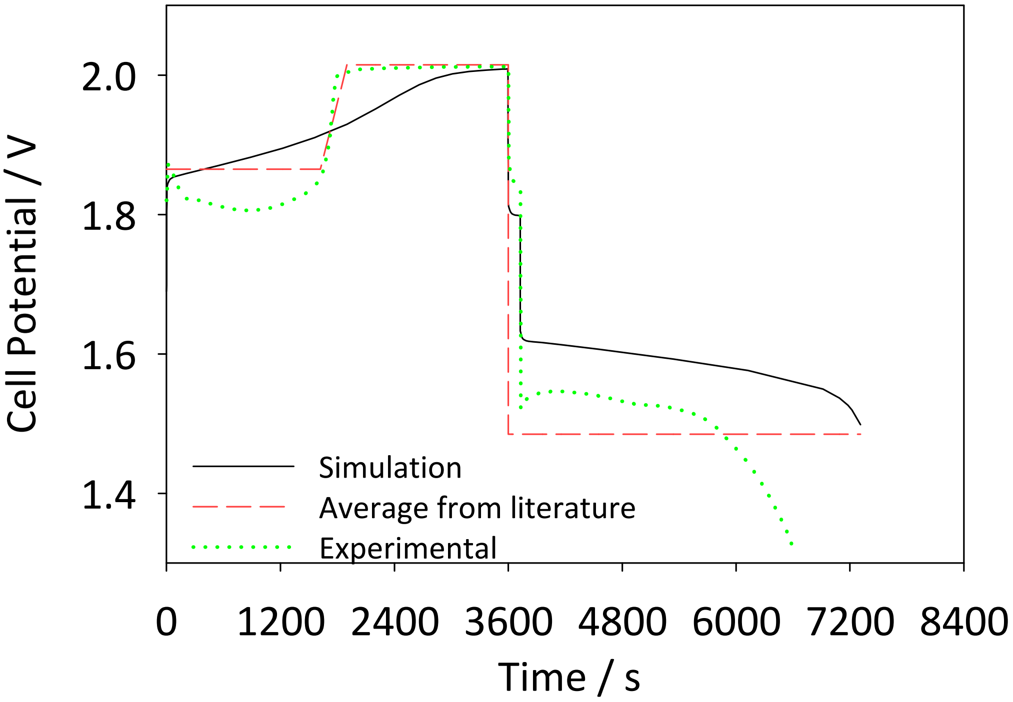

FIGURE 5.16: A comparison of simulated cell potential (solid black line) using a moving mesh during the second charge with average values seen in the literature (dashed red line) and experimentally measured cell potential (dotted green line) for the second charge-discharge cycle at a constant current density of 20 mA cm^{-2}.

5.8 Micro-Computed Tomography

Preliminary micro-computed tomography (μ-CT) scans were completed on a static electrolyte divided cell of 2 cm^2. As an aid to visualise the deposition of Pb/PbO$_2$ during in-situ cycling.

The cell was cycled to failure inside a custom 150 kVp / 225 kVp Hutch micro-CT scanner. The cell was cycled at a constant current of 100 mA during the first charge and discharge cycle followed by 200 mA for each remaining charge and discharge cycle. Cut off voltages of 2.5 V and 0.1 V were used for charge and discharge respectively.

The cell was scanned continuously using the micro-CT scanner, throughout cycling. Each scan took approximately 17 minutes. Due to the time take for each scan, the rest periods between charge and discharge and vice-versa were 30 minutes. This way, a full scan could be completed before each charge and each discharge without the deposits at each electrode changing over the time taken to scan the cell.

Figure 5.17 shows the progression of Pb and PbO_2 deposits as the cell is cycled. Each image is separated by either a charge or a discharge step. Figure 5.18 displays the voltage-time curve. After cycle 3, the cell potential begins to reach the charge cut-off voltage leading to a reduction in charge time. Comparing Figure 5.17 (A) with Figure 5.17 (C), the reason for this can clearly be seen. The Pb deposit is largely detached from the negative electrode in Figure 5.19 by the following step (Figure 5.17 (D)), the majority of the deposit has collapsed and has collected at the base of the negative half of the cell. This led to a large capacity loss and hence the large overpotential after a reduced period of time during charging. There is, therefore, a need for a better electrode-deposit interface. One way of improving this would be to use improved electrode materials.

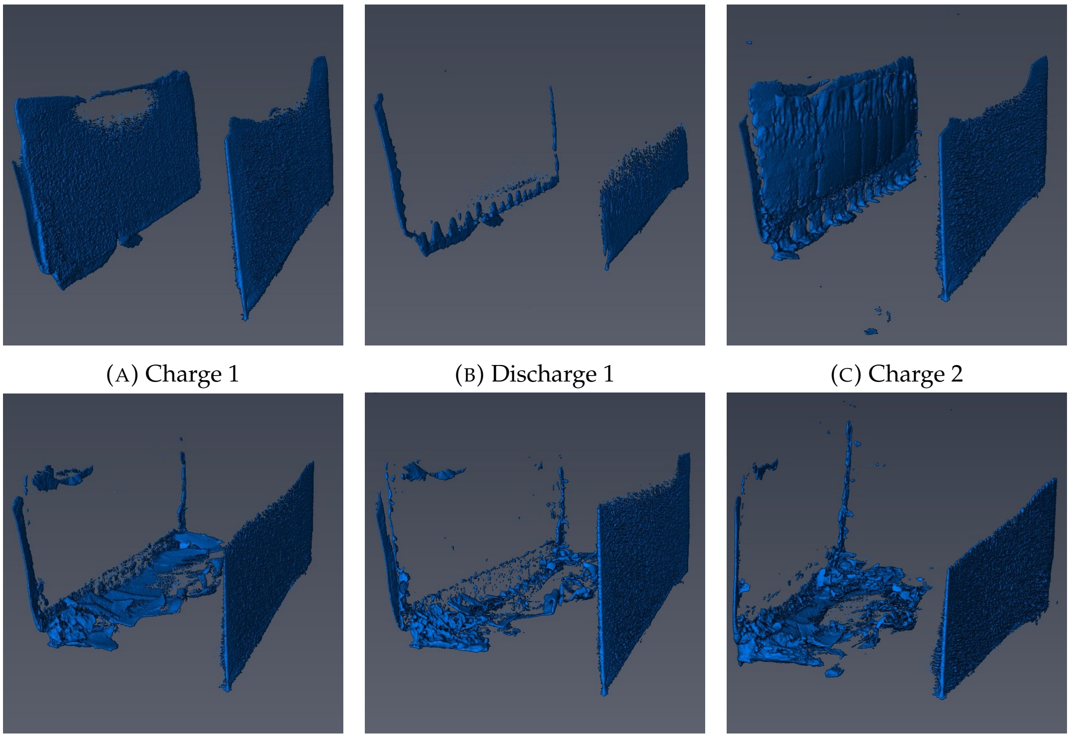
(A) Charge 1 (B) Discharge 1 (C) Charge 2

(D) Discharge 2 (E) Charge 3 (F) Discharge 3

FIGURE 5.17: Reconstructions of CT scans of deposits over the first three cycles in a static electrolyte cell with 2 cm × 4 cm electrodes.

While the performance of the static electrolyte cell was poor, μ-CT is shown to work well for visualising Pb and PbO_2 deposits in the SLFB. Hence a good opportunity has arisen for further work incorporating μ-CT scans into the development and validation of models such as the moving mesh model discussed in this chapter.

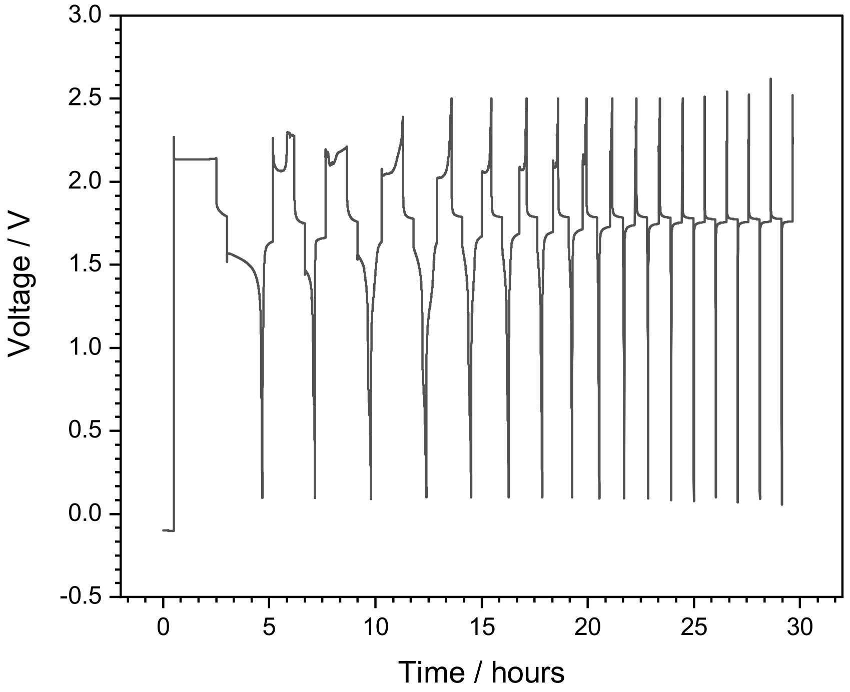

FIGURE 5.18: Voltage time curve of the divided static electrolyte cell.

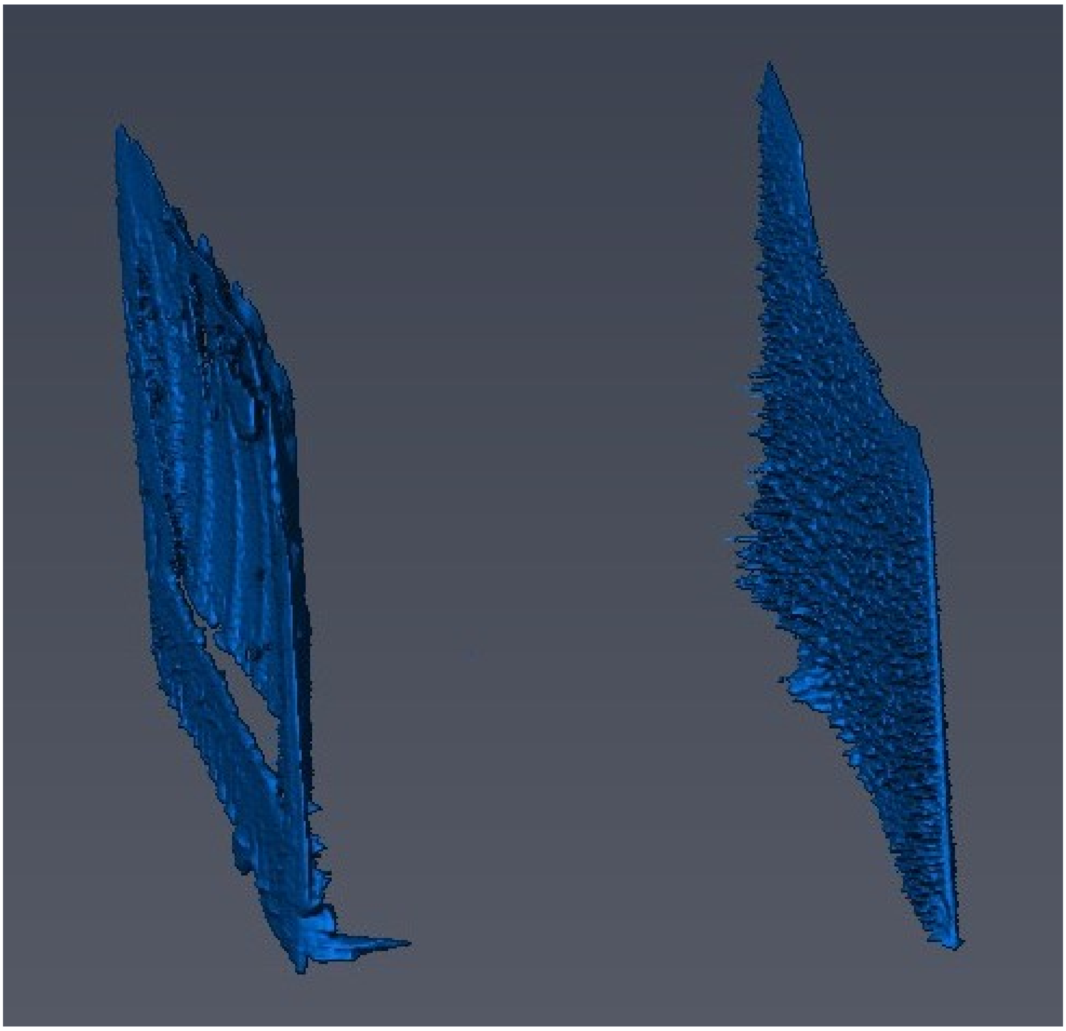

FIGURE 5.19: Reconstruction of the CT scan after the second charge. The left deposit (negative electrode) has largely separated from the electrode surface.

5.9 Conclusions

A two-dimensional time-dependent numerical model has been produced to simulate the operation of the SLFB. A moving mesh technique has been deployed to simulate the deposition of solid Pb and PbO_2 at the negative and positive electrodes respectively and accounts for the change in geometry that results from these deposits. The change in geometry results in a greater resistance of the solid domains due to an increase in thickness but, more significantly, accounts for the overall decrease in electrolyte resistance as the cell increases in SoC. The change in geometry also allows for a higher value for the concentration of acid species locally to the electrodes after charging. The significance of implementing this moving mesh model is the ability to model flow battery systems involving a solid/liquid phase change and hence the varying reaction chamber geometry as a function of state of charge. This has direct implications for other systems such as the Zn-Br, Zn-air, Zn-Ce, etc. With proof of concept of this modelling approach demonstrated in this chapter, future work can be carried out to refine the electrochemical and thermodynamic problems.

This chapter shows the importance of the electrolyte conductivity on the performance of the SLFB. Hence, a more detailed model which closely represents the experimentally measured electrolyte conductivity over a range of concentrations is required. This work is developed in Chapter 6.

Furthermore, while planar electrodes represent the bulk of work completed on the SLFB, it has been shown that the SLFB operates more favourably at lower current densities, particularly at the positive electrode [82, 152]. Therefore, in order to maximise power density and keep current density low, three-dimensional electrodes must be considered. Chapter 8 expands on the work completed in this chapter to include a novel approach to modelling the use of three-dimensional electrodes in the soluble lead flow battery.

Chapter 6

Electrolyte Conductivity

The simple Nernst-Einstein relation, Equation 6.1, is commonly used to calculate the mobility, $u_{m,i}$ of mobile ions, i, in electrolytes. However, this gives a linear relationship for conductivity vs concentration for each of the constituent cations, H^+ and Pb^{2+}.

$$u_{m,i} = \frac{D_i}{RT} \tag{6.1}$$

Krishna et al. have shown that this relationship is non-linear [49]. For the SLFB, this is true to such an extent that there is a positive correlation between conductivity and concentration at low H^+ and Pb^{2+} concentrations, but a negative correlation at higher concentrations. By using Equation 6.2 in place of the mobility in the Nernst-Einstein equation, a much closer fit is achieved.

Using a correction factor for the mobility, γ_{corr}, derived from Kohlrausch's square-root law, mobility is defined as:

$$u_{m,i} = \frac{D_i}{RT}\gamma_{corr} \tag{6.2}$$

γ_{corr} can be related to the activity coefficient, γ_i with a correction exponent, α:

$$\gamma_{corr} = \gamma_i^{\alpha},\ \alpha \approx \frac{\sqrt{I}}{|z_i|} \tag{6.3}$$

γ_i is calculated using a variation on the Debye-Hückel equations, [108]:

$$\log_{10} \gamma_i = -\frac{A z_i^2 \sqrt{I}}{1 + B a_0 \sqrt{I}} \tag{6.4}$$

Where A and B are constants, a_0 is an empirically fitted function with constants δ_i, and I is the ionic strength:

$$a_0 = (\delta_i c_i)^{-\frac{1}{3}} \tag{6.5}$$

$$I = \frac{1}{2} \sum_i z_i^2 c_i \tag{6.6}$$

The Nernst-Einstein equation is only strictly valid at infinite dilution, which is appropriate given the greater deviation between experimental values and those predicted by the Nernst-Einstein equation at higher concentrations. At non-zero concentrations, neither the diffusion coefficient, nor the mobility can be easily defined by a single value. Due to the empirical nature of the coefficients in Equation 6.2, and so as not to over complicate the model, the diffusion coefficient is assumed to be constant at all concentrations and the difference in mass transport is defined as being only due to the varying mobility.

A simple, one-dimensional model was developed, consisting only of an electrolyte domain. A potential difference of 0.1 V was applied across the domain. The current density was measured and used to calculate the electrolyte conductivity.

6.1 Parameters

Values for fixed parameters for the conductivity simulations are defined in Table 6.1. These parameters are empirically fitted to agree with the data presented by Krishna et al. [49]. Conductivity data has also been presented by Hazza et al. [44] at a lower temperature of 292 K. This data is not presented. However, this does highlight a need for further work to develop the method presented in this chapter.

TABLE 6.1: Parameters for conductivity simulations

Symbol	Parameter	Value
$D_{Pb^{2+}}$	Pb^{2+} diffusion coefficient	$4 \times 10^{-9}\ m^2\,s^{-1}$
D_{H^+}	H^+ diffusion coefficient	$1.05 \times 10^{-8}\ m^2\,s^{-1}$
$D_{CH_3SO_3^-}$	$CH_3SO_3^-$ diffusion coefficient	$1.5 \times 10^{-9}\ m^2\,s^{-1}$
$z_{Pb^{2+}}$	Pb^{2+} valance	+2
z_{H^+}	H^+ valance	+1
$z_{CH_3SO_3^-}$	$CH_3SO_3^-$ valance	-1
$\delta_{Pb^{2+}}$	Pb^{2+} constant	3.52243
δ_{H^+}	H^+ constant	0.94331
$\delta_{CH_3SO_3^-}$	$CH_3SO_3^-$ constant	0.18444
A	Constant	$0.51\ dm^{1.5}\,mol^{-0.5}$
B	Constant	$3.29\ dm^{1.5}\,mol^{-0.5}$
T	Temperature	298 K

6.2 Conductivity Results

The Nernst-Einstein equation assumes there is no interaction between ions and hence is only valid for infinitely dilute solutions. There are numerous methods for compensating for interactions between particles ion a solution. While even these calculations are only accurate for solutions up to $mmol\,dm^{-3}$ concentrations, semi-empirical models can predict conductivity as a function of concentration at higher values.

The simulated conductivity calculated using the Nernst-Einstein equation (Equation 6.1) as the mobility int he model is shown in Figure 6.1(A). The relationship between simulated conductivity and both $[H^+]$ and $[Pb^{2+}]$ has a positive linear correlation. The simulated conductivity vs concentration of H^+, Pb^{2+} and $CH_3SO_3^-$ is shown against the experimental data gathered by Krishna et al. [49] in Figure 6.1 (B). Here, while there is a positive correlation between $[H^+]$ and experimental conductivity at all Pb^{2+} concentrations, interactions between ions cause a deviation from the linear Nernst-Einstein prediction and at high $[Pb^{2+}]$, $[H^+]$ has a smaller effect on conductivity. With an increasing Pb^{2+} concentration, the conductivity increases at low $[H^+]$, while at high $[H^+]$, the conductivity decreases. The model successfully predicts this complex, non-linear relationship between Pb^{2+} ion concentration and conductivity of the electrolyte as a function of free acid concentration. The model closely matches the experimental data, with a maximum deviation of 22 $mS\,cm^{-1}$. Over the range of concentrations shown in Figure 6.1 (0 to 1.5 $mol\,dm^{-3}$ $[H^+]$ and 0 to 1.5 $mol\,dm^{-3}$ $[Pb^{2+}]$), a value of R^2 is calculated to be 0.985 for the novel approach and just 0.189 for the simple Nernst-Einstein equation.

This is a significant difference. At a [Pb^{2+}] of 1.5 mol dm^{-3} and a [H^+] of 1.5 mol dm^{-3}, there is a difference between the experimental conductivity and the previously used Nernst-Einstein numerical method of a factor of 4.

While this complex relationship between concentration and electrolyte conductivity is required to accurately model the local conductivity and mobility of ions within the electrolyte, by taking an average value of expected concentration there is an approximately linear relationship between SoC and electrolyte conductivity, see Figure 6.2. The linear relationship in not appropriate for use in the Multiphysics models used in this thesis, due to local concentration gradients near planar electrodes or within porous electrodes. While these effects cause a deviation from the linear conductivity relationship, it is still important to consider these local differences in concentrations in Multiphysics models due to their effect on electrode kinetics. However, the linear simplification would be an appropriate tool to improve the conductivity model of higher-level models, such as those using equivalent electrical circuits or in models including only the bulk electrolyte concentration.

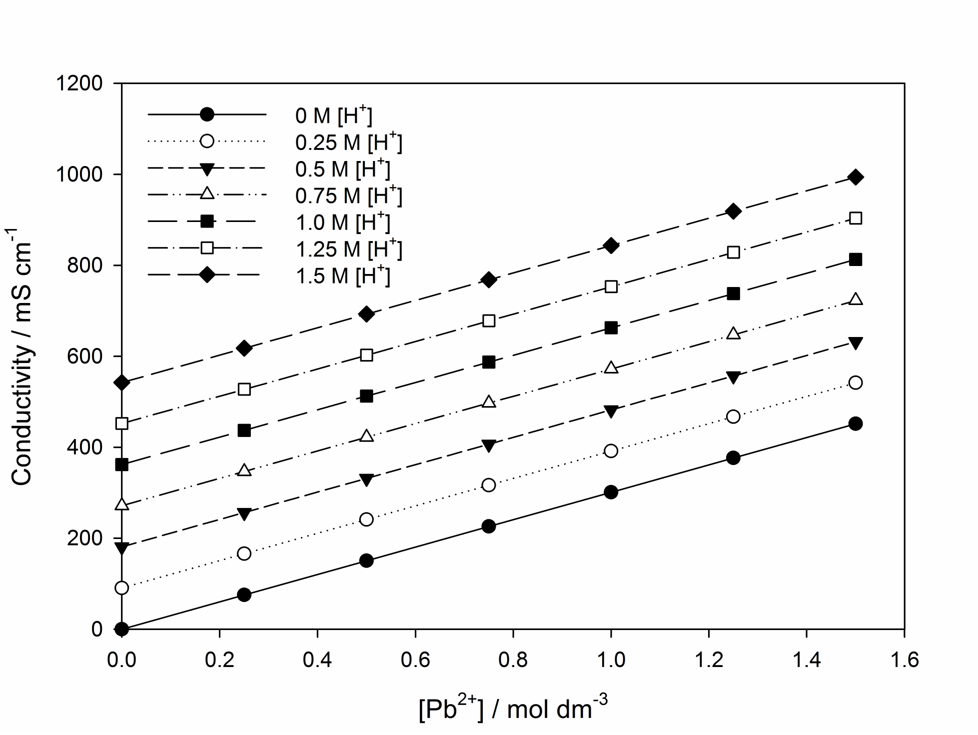

(A) Conductivity using the simple Nernst-Einstein equation

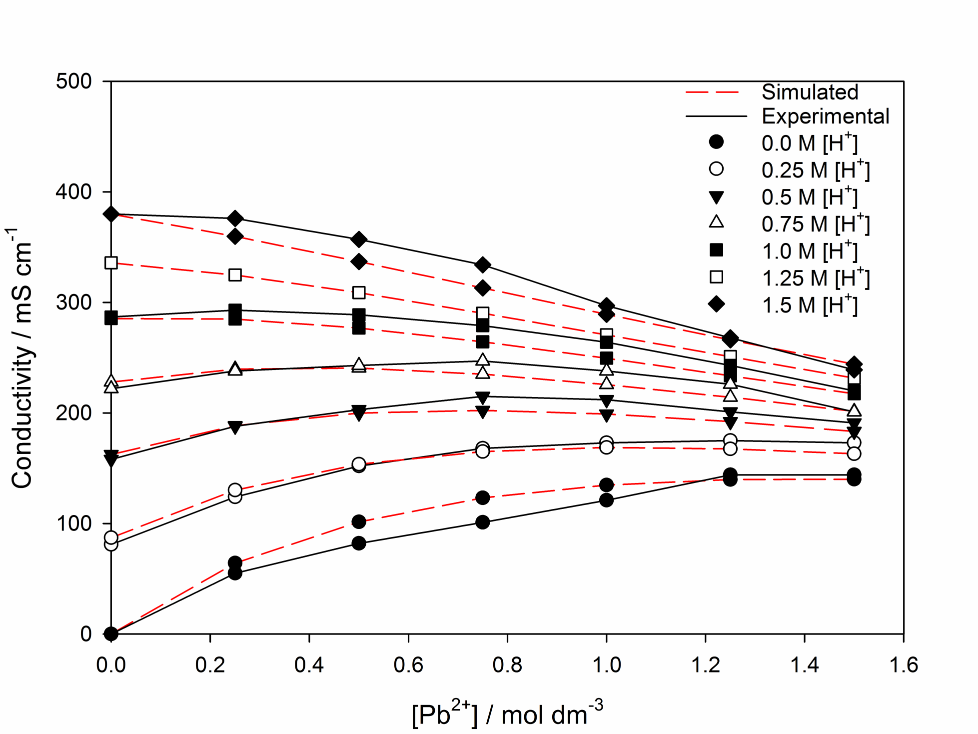

(B) Experimental conductivity (solid black line) and simulated conductivity calculated using the modified equation for mobility (red dashed line)

FIGURE 6.1: Simulated (red dashed line) and experimental (solid black line) electrolyte conductivity vs concentration of Pb^{2+} and H^+ ions. Experimental data from [49].

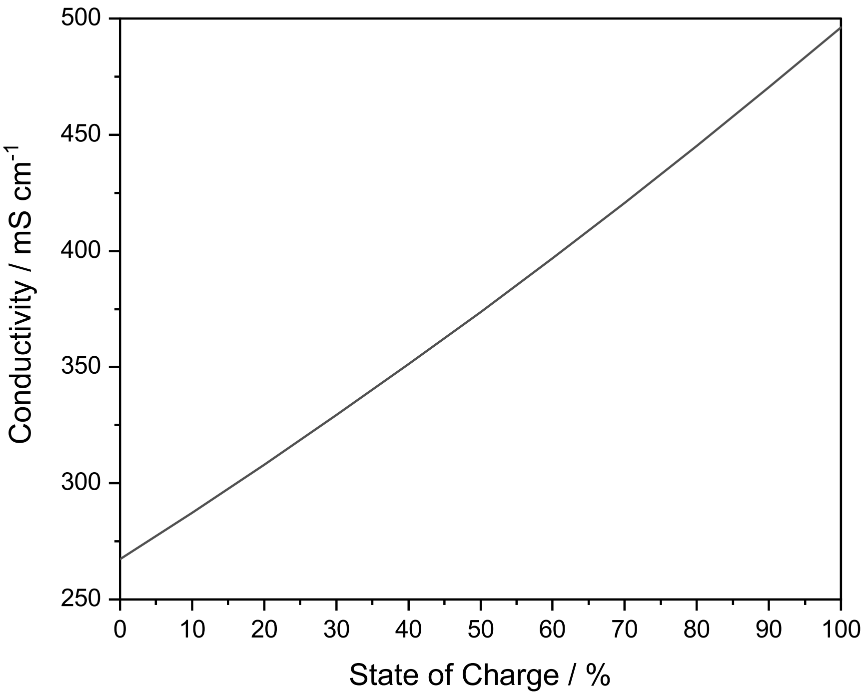

FIGURE 6.2: Bulk conductivity calculated using the modified method vs electrolyte state of charge. The starting concentrations are 0.7 mol dm^{-3} Pb^{2+} and 1.0 mol dm^{-3} H^+.

6.3 Summary

An improved method for calculating conductivity from electrolyte concentration, which is novel in its application to the SLFB, is presented. This method calculates the conductivity of the SLFB electrolyte with a significantly closer fit to experimental measurements than any previously used methods, with an increase in R^2 from 0.189 to 0.985. It shows that while there is a complex relationship between electrolyte species concentration and conductivity, over the operating range of the SLFB, the average conductivity of the electrolyte varies approximately linearly with electrolyte state of charge. The improved method of calculating conductivity allows for the development of novel modelling approaches which require accurate electrolyte conductivity values. This is essential in the development of the divided SLFB model, described in Chapter 7 and gives a greater degree of confidence in the design suggestions provided for three dimensional RVC electrodes described in Chapter 8.

Chapter 7

Modelling the divided soluble lead flow battery

The soluble lead flow battery is able to operate in an undivided manner with only a single electrolyte. This negates the need for electrolyte balancing and means only a single pump and flow circuit are required, reducing the complexity of the battery. Despite the advantages of a single electrolyte and simplified reaction chamber, dividing the cell can be advantageous and can mitigate some of the issues with SLFBs. First Wallis and Wills [78] increased the cycle life of the SLFB in a static electrolyte cell by including a membrane, then Krishna et al. [86] showed dividing the cell with either a simple porous separator or with an ion-exchange membrane also improved the cycle life in a flow battery. In this configuration, the separator acts as a physical barrier to prevent failure by electrical shorting of uneven deposit growths and, when an ion exchange membrane is used, electrode specific additives may be included in the electrolytes.

Several studies have modelled the SLFB [152, 155–160]. However, all these studies model the SLFB in an undivided configuration. There is, however, extensive modelling of ion-exchange membranes in other flow batteries, such as the vanadium redox flow battery [111, 115, 178]. In this chapter, a model for a divided SLFB is developed and validated using experimental results from the literature [86].

Two variants of the model are used. The first is a simple one-dimensional, steady-state model used to validate the potential drop measured across the membrane and to quickly screen a wide range of parameters for porous separators, anion and cation exchange membranes. This model consistes of three domains: a membrane/separator domain dividing two electrolyte domains.

The second variant implements a membrane domain within a two-dimensional transient model. This model also consists of two electrolyte domains and a membrane/separator domain.

7.1 Membrane

The membrane domain is a porous medium, so the effective diffusion coefficient is lower than in the free electrolyte. Using the Bruggeman correlation the effective diffusion coefficients can be calculated from the porosity, ε:

$$D_{i,eff} = \varepsilon^{1.5} D_i \tag{7.1}$$

$$u_{m,i,eff} = \varepsilon^{1.5} u_{m,i} \tag{7.2}$$

Where $D_{i,eff}$ is the effective diffusion coefficient. Where $D_{i,eff}$ is used to calculate mobility, $u_{m,i}$ becomes $u_{m,i,eff}$. In the ion exchange membrane, it is assumed there is a negligible flow. The Nernst-Planck equation therefore becomes:

$$\mathbf{N_i} = -D_{i,eff}\nabla c_i - z_i u_{m,i,eff} F c_i \nabla \phi \tag{7.3}$$

7.2 Two-dimensional model

The two-dimensional, transient model also includes Navier-Stokes and Continuity equations to describe the flow of electrolyte and a transient term to describe the flux of ions in all domains.

$$\rho\frac{\partial \mathbf{u}}{\partial t} + \rho(\mathbf{u}\cdot\nabla)\mathbf{u} = \nabla\cdot[-p + \mu\nabla\mathbf{u}] \tag{7.4}$$

$$\nabla\cdot\mathbf{u} = 0 \tag{7.5}$$

Where ρ is the electrolyte density, $\mathbf{u}$ is its velocity, t is time, p is the pressure and μ is the electrolyte viscosity.

$$\frac{\partial c_i}{\partial t} = -\nabla \cdot \mathbf{N_i} \tag{7.6}$$

By using this method for calculating mobility in both the electrolyte and the membrane, it is possible to calculate the potential drop across the membrane.

During simulations in the two-dimensional model, the cell was cycled by charging for 1 hour and fully discharging for two cycles with each step separated by a rest of 120 s.

7.3 Parameters

Default values for parameters used in the simulations in this chapter are highlighted in Table 7.1. The majority of these values are used to match experimental work by Krishna et al. [49].

TABLE 7.1: Default values for parameters used in the simulations of the divided soluble lead flow battery

Symbol	Parameter	Value
i_{app}	Applied current density	171 mA $\mathrm{cm^{-2}}$
ε_{Nafion}	Nafion 115 porosity	0.12
ε_{FAP450}	FAP-450 porosity	0.2
ε_{FF60}	FF60 porosity	0.5
$c_{fix,Nafion}$	Nafion 115 fixed charge distribution	115 C $\mathrm{cm^{-3}}$
$c_{fix,FAP450}$	FAP-450 fixed charge distribution	165 C $\mathrm{cm^{-3}}$
d_{Nafion}	Nafion 115 membrane thickness	100 µm
d_{FAP450}	FAP-450 membrane thickness	50 µm
d_{FF60}	FF60 separator thickness	650 µm
D_{PbII}	7×10^{-10}	$\mathrm{m^2\,s^{-1}}$
D_H	9.3×10^{-9}	$\mathrm{m^2\,s^{-1}}$
$D_{CH_3SO_3}$	1.33×10^{-9}	$\mathrm{m^2\,s^{-1}}$
d	Separator/Membrane thickness	100 µm

7.4 Microporous separator

In the SLFB, microporous separators are simple physical barriers to prevent shorting across the cell via deposit growth. Intuitively, the potential drop across these separators will decrease with decreased thickness and increased porosity. Hence an optimisation based on potential drop alone will suggest a fully porous separator with zero thickness. However, the simulated increased potential drop with the addition of separators with varying thickness and porosity is presented at a range of simulated current densities to aid with making informed design decisions.

The simulated potential drop across the separator is determined by three main factors: the conductivity of the electrolyte, which is linked to the concentration of species in the electrolyte as described in Chapter 6, the porosity of the membrane, and its thickness.

The methods for simulating anion-exchange membranes is validated against data from [86]. Figure 7.1 shows this experimental data with two simulation techniques: first measuring the potential drop across the membrane boundaries directly and secondly by simulating the experimental technique used, by measuring the difference across 2 mm either side of the membrane and subtracting the potential difference across the same region with no membrane present.

There is a significant difference between the two simulated techniques, with the direct measurement showing an increased potential drop of approximately 50 %. This is mainly due to the thickness of the separator (0.65 mm). The experimental technique subtracts the potential drop caused by the electrolyte that would occupy the thickness of the separator. However, the experimental values are entirely within the bounds of the two simulated methods.

In this section, the one-dimensional model is used to simulate the porous separator performance. In the remainder of the chapter, in the figures, the SoC is denoted by the [Pb^{2+}] at that SoC. The starting conditions are 700 mol m^{-3} Pb^{2+} and 1000 mol m^{-3} H^+. The concentrations at each simulated SoC are described in Table 7.2.

TABLE 7.2: Concentrations at simulated states of charge.

[Pb^{2+}]/ mol m^3	**[H^+]**/ mol m^3	**[$CH_3SO_3^-$]**/ mol m^3
1	2398	2400
230	1940	2400
460	1480	2400
700	1000	2400

In this model, the porosity is linked to the transport parameters (diffusion coefficient and mobility) in the separator by the Bruggeman equation, Equation 7.1. As expected this

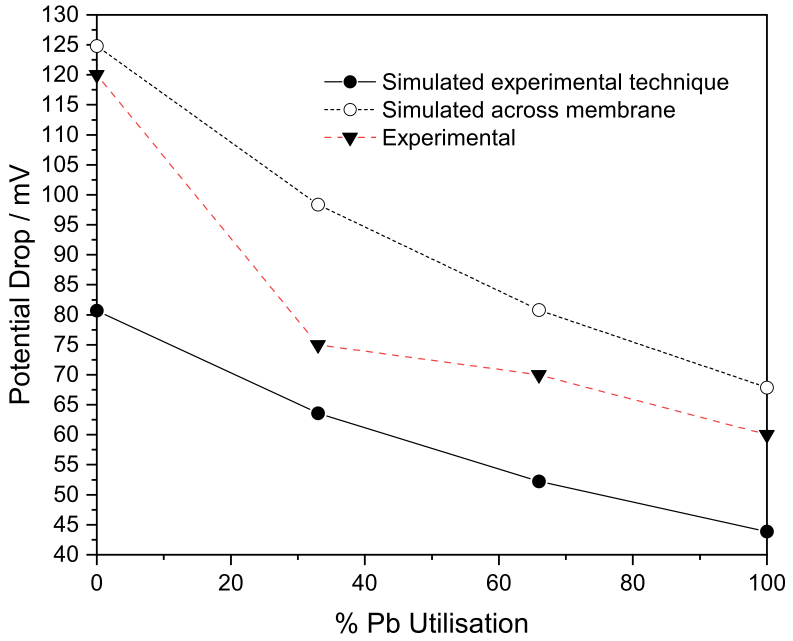

FIGURE 7.1: Experimental (red dashed line) and simulated potential drop mimicking the experimental technique (black solid line) an simulated potential drop measured directly (black dotted line) across an FF60 microporous separator. A current density of 171 mA cm^{-2} is used. Experimental data from [86].

gives an exponential relationship between potential drop and porosity, see Figure 7.2. With varying porosity, the potential drop ranges from ∞ at zero porosity to close to no potential drop at a porosity of 1 (a non-zero value would be presented because the electrolyte that occupies the thickness of the separator still has a resistance). The difference in simulated potential drop across the membrane due to SoC (i.e. at fixed porosity) is approximately linear, as expected extrapolating from Figure 6.2. However, the gradient of this linear relationship is larger at lower porosities due to the increased tortuosity. The transport parameters in the separator may be determined by other factors, such as pore size or tortuosity. However, these factors are not considered in this simple model.

Varying the thickness of the separator gives a linear relationship with simulated potential drop which follows Ohm's Law, see Figure 7.3. In a completely charged state ([Pb^{2+}] = 1 mol m^{-3}), the simulated potential drop varies from 30 mV with a thickness of 0.25 mm to over 150 mV at a thickness of 1.25 mm. In a fully discharged state ([Pb^{2+}] = 700 mol m^{-3}), the potential drop ranges from 56 mV to over 280 mV. This is a significant potential drop.

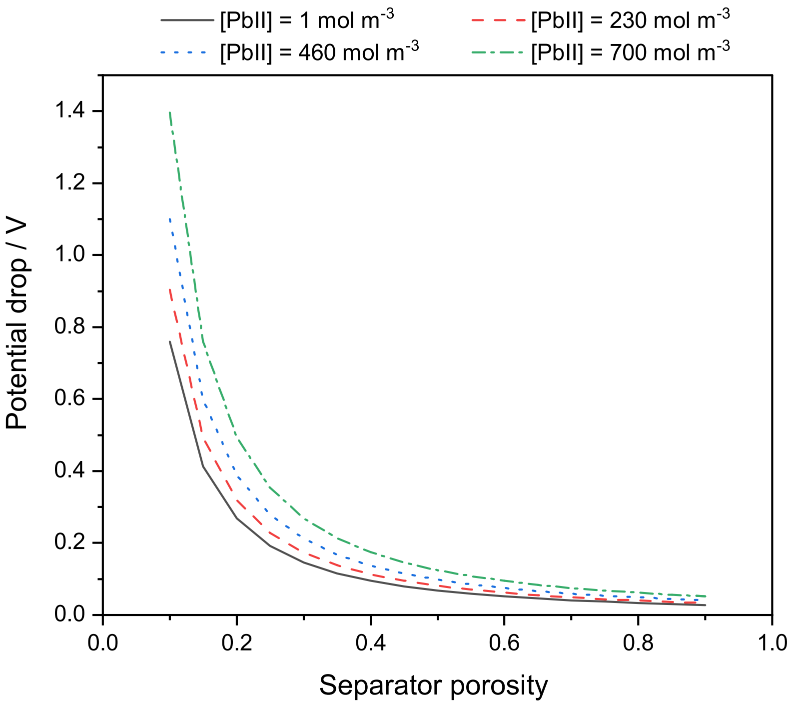

FIGURE 7.2: Simulated potential drop across a porous separator with varied porosity at different simulated electrolyte states of charge: $[Pb^{2+}]$=1 mol m^{-3} & $[H^+]$ = 2398 mol m^{-3} (black solid line), $[Pb^{2+}]$ = 230 mol m^{-3} & $[H^+]$ = 1940 mol m^{-3} (red dashed line), $[Pb^{2+}]$ = 460 mol m^{-3} & $[H^+]$ = 1480 mol m^{-3} (blue dotted line) and $[Pb^{2+}]$ = 700 mol m^{-3} & $[H^+]$ = 1000 mol m^{-3} (green dot-dashed line).

Even assuming infinitely fast kinetics and no other resistive losses, only accounting for losses due to the separator for a battery with an open circuit potential of 1.7 V, the voltage efficiency would be 72 %.

Given the potential drop across the separator follows these two simple laws, a porous separator can be modelled as a resistive domain, with the conductivity calculated from the porosity and the electrolyte concentrations at the boundaries. Flux across the membrane can be implemented as boundary conditions for the electrolyte domains on either side of the separator. These boundary conditions require one ion to have a fixed concentration within the separator. However, the $CH_3SO_3^-$ ion concentration is constant across the domain and at all simulated states of charge. Therefore, a constant counter ion concentration is a reasonable assumption. Using this method requires fewer elements in the separator, so will reduce the computational effort required to solve.

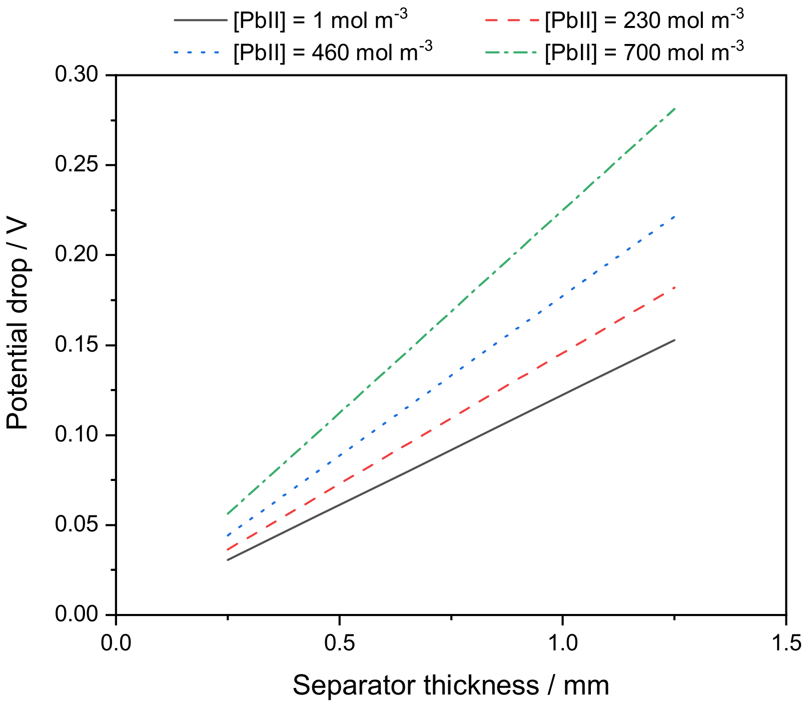

FIGURE 7.3: Simulated potential drop across a porous separator with varied thickness at different simulated electrolyte states of charge: $[Pb^{2+}] = 1$ mol m^{-3} & $[H^+] = 2398$ mol m^{-3} (black solid line), $[Pb^{2+}] = 230$ mol m^{-3} & $[H^+] = 1940$ mol m^{-3} (red dashed line), $[Pb^{2+}] = 460$ mol m^{-3} & $[H^+] = 1480$ mol m^{-3} (blue dotted line) and $[Pb^{2+}] = 700$ mol m^{-3} & $[H^+] = 1000$ mol m^{-3} (green dot-dashed line).

7.5 Anion-exchange membrane

An anion exchange membrane (AEM) is one which allows negatively charged anions to pass through, while inhibiting the movement of positive cations. Physically, AEMs are formed of polymer chains with covalently bound positively charged chemical groups [147]. An AEM is modelled as a porous domain with a fixed positive charge distributed throughout the domain. In this section, the effects of applied current density, membrane porosity and distribution of the fixed positive charge are simulated using a 1D model.

Again, the model is validated against data from [86]. Figure 7.4 shows the experimental data with the same two simulation techniques described in Section 7.4. In this case the simulated values are far closer together than for the porous separator. This is in part due to the thickness of the membrane (here, just 0.05 mm) and partly due to the difference in concentration in the non-membrane domains, with increases in both $[H^+]$ and $[Pb^{2+}]$ on the positive side of the membrane decreases in both on the negative side.

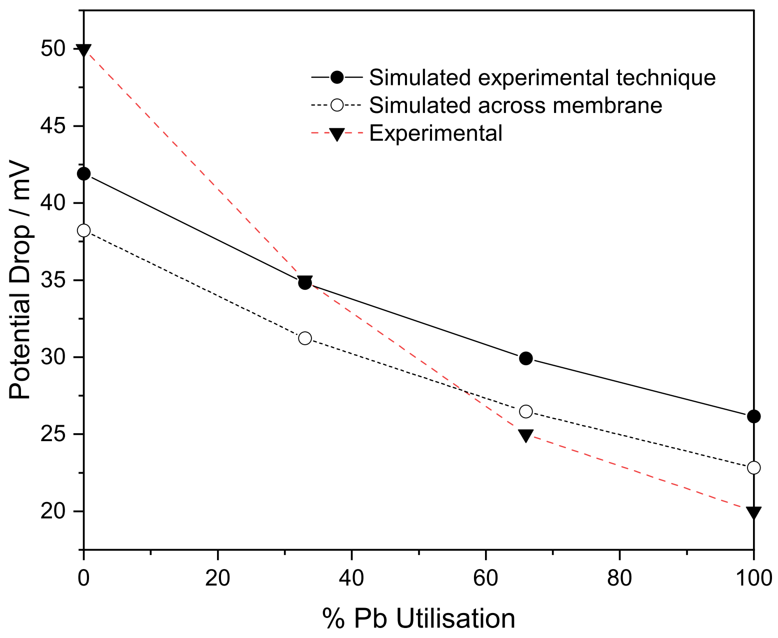

FIGURE 7.4: Experimental (red dashed line) and simulated potential drop mimicking the experimental technique (black solid line) an simulated potential drop measured directly (black dotted line) across an FAP-450 anion-exchange membrane. A current density of 171 mA cm^{-2} is used. Experimental data from [86].

The following sections describe the effect of varying the current density, membrane porosity and fixed charge distribution on the performance of an anion-exchange membrane simulated using the one-dimensional model. The default values for these parameters are included in Table 7.3.

TABLE 7.3: Default values of parameters used in for simulating an anion exchange membrane.

Parameter	Value	Units
Current density, i	171	mA cm^{-2}
Membrane porosity, ε	0.12	-
Fixed charge distribution, C_{fix}	115	C cm^{-3}

The potential drop across ion-exchange membranes is primarily determined by two factors: the ohmic resistance or conductivity of the material and the Donnan potentials, the potential difference due to a sharp change in ion concentrations at the membrane boundaries, see Section 4.2.4. The methods of calculating the conductivity of the membranes are similar to that of the simple porous separator. However, because of the fixed charge in the membrane, calculating the mobile ion concentrations is more complex than using those at the electrolyte boundaries.

7.5.1 Effect of current density

Applied current density was varied from 10 mA cm^{-2} to 210 mA cm^{-2} at four different simulated states of charge of the electrolyte as described in Table 7.2.

As is shown in Figure 7.5, the simulated potential drop across the membrane increases linearly with current density at all concentrations. Therefore, with a constant concentration, the simulated anion exchange membranes have a constant resistance over a range of current densities. This suggests either Donnan potentials are very small compared to the ohmic drop across the membrane or they are equal on either side of the membrane.

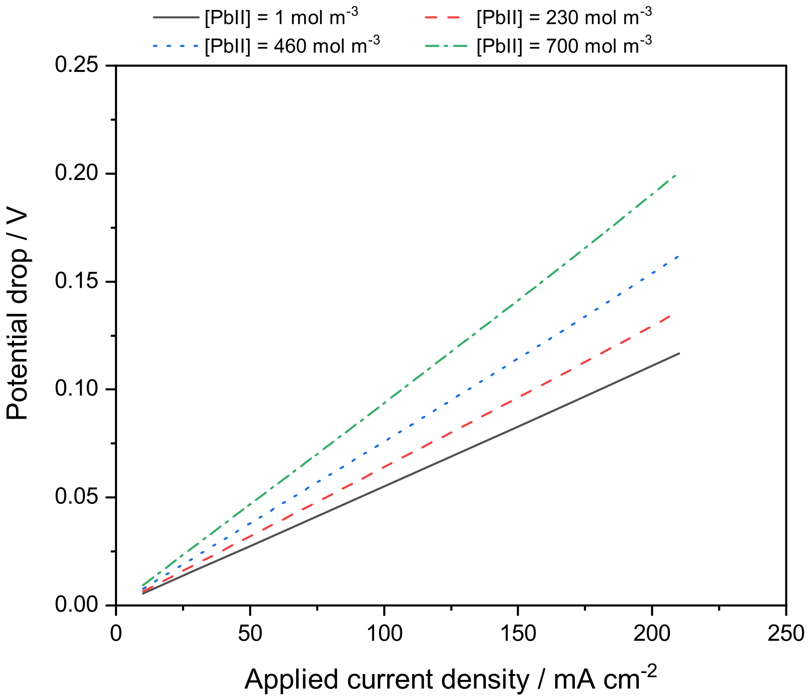

FIGURE 7.5: Simulated potential drop across an anion-exchange membrane with varied current density at different simulated electrolyte states of charge: [Pb^{2+}] = 1 mol m^{-3} & [H^{+}] = 2398 mol m^{-3} (black solid line), [Pb^{2+}] = 230 mol m^{-3} & [H^{+}] = 1940 mol m^{-3} (red dashed line), [Pb^{2+}] = 460 mol m^{-3} & [H^{+}] = 1480 mol m^{-3} (blue dotted line) and [Pb^{2+}] = 700 mol m^{-3} & [H^{+}] = 1000 mol m^{-3} (green dot-dashed line).

To put these values into context, at 100 mA cm^{-2}, the potential drop across the electrolyte with an interelectrode gap of 1 cm is 375 mV at 0.7 mol dm^{-3} Pb^{2+} and 1.0 mol dm^{-3} H^{+}. At 20 mA cm^{-2}, but otherwise the same conditions, a 72 mV drop is expected.

The membrane in the model here adds an extra 93 mV at 100 mA cm^{-2} and 18 mV at 20 mA cm^{-2}, approximately a 25 % increase. At 20 mA cm^{-2}, a typical charging potential might be 2.0 V and a discharge potential of 1.6 V, providing an 80 % voltage efficiency. With the extra 18 mV potential drop (charging at 2.018 V and discharging at 1.582 V) the simulated voltage efficiency drops to 78 %.

7.5.2 Effect of porosity

The effect of porosity on potential drop across the membrane is determined by the effective diffusion parameters within the membrane. Here, the relationship is determined by the Bruggeman equation, see Equation 7.1.

As expected, the simulated potential drop decays exponentially with increasing porosity. At 5 % porosity, the potential drop is large, between 300 and 600 mV. However, this drops to below 100 mV by 20 % porosity, and by 60 % porosity, the potential drop is below 20 mV. At this point there is only a small impact on the total potential drop across the cell. Again, there is no obvious deviation from the exponential fit defined by the Bruggeman equation, so simulated Donnan potentials must remain small.

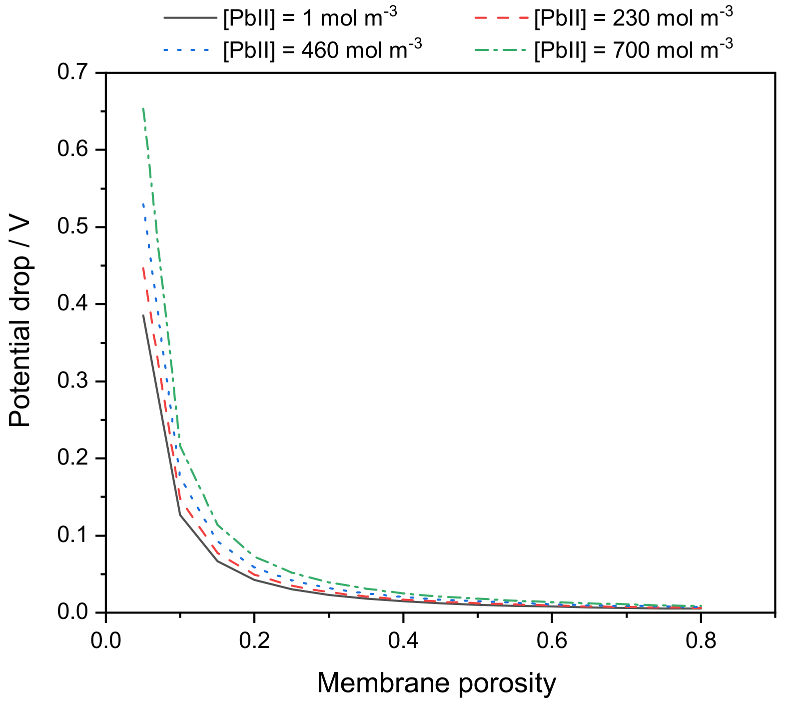

(A) Full range

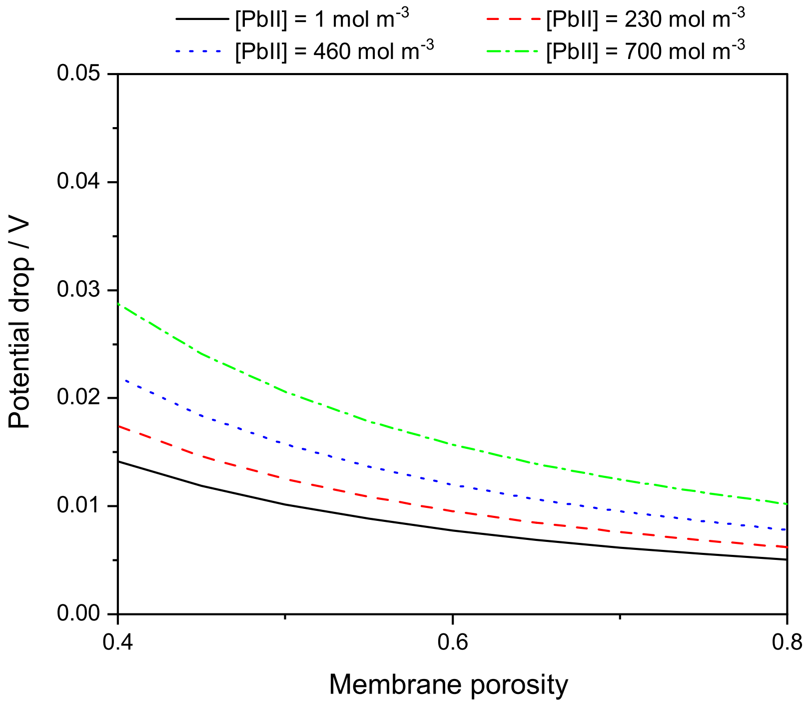

(B) Zoomed in

FIGURE 7.6: Simulated potential drop across an anion-exchange membrane with varied membrane porosity at different simulated electrolyte states of charge: $[Pb^{2+}] = 1\ \mathrm{mol\,m^{-3}}$ & $[H^{+}] = 2398\ \mathrm{mol\,m^{-3}}$ (black solid line), $[Pb^{2+}] = 230\ \mathrm{mol\,m^{-3}}$ & $[H^{+}] = 1940\ \mathrm{mol\,m^{-3}}$ (red dashed line), $[Pb^{2+}] = 460\ \mathrm{mol\,m^{-3}}$ & $[H^{+}] = 1480\ \mathrm{mol\,m^{-3}}$ (blue dotted line) and $[Pb^{2+}] = 700\ \mathrm{mol\,m^{-3}}$ & $[H^{+}] = 1000\ \mathrm{mol\,m^{-3}}$ (green dot-dashed line).

7.5.3 Effect of charge distribution

The fixed charge distributed in the anion exchange membrane is positive. With an increasing charge concentration, there is an increase in potential drop across the modelled anion exchange membrane, see Figure 7.7. However, this increase is modest. For a ten fold increase in fixed charge concentration, there is less than 10 mV (∼10 %) increase in potential drop at high SoC and 3 mV (∼2 %) at high SoC. This appears small. However, it can be explained by the high concentrations of ions in the electrolyte compared to the charge concentration combined with the roughly equal electrolyte concentrations on either side of the membrane. There are, therefore, no significant Donnan potentials and so a negligible difference in simulated potential drop with varying charge concentration.

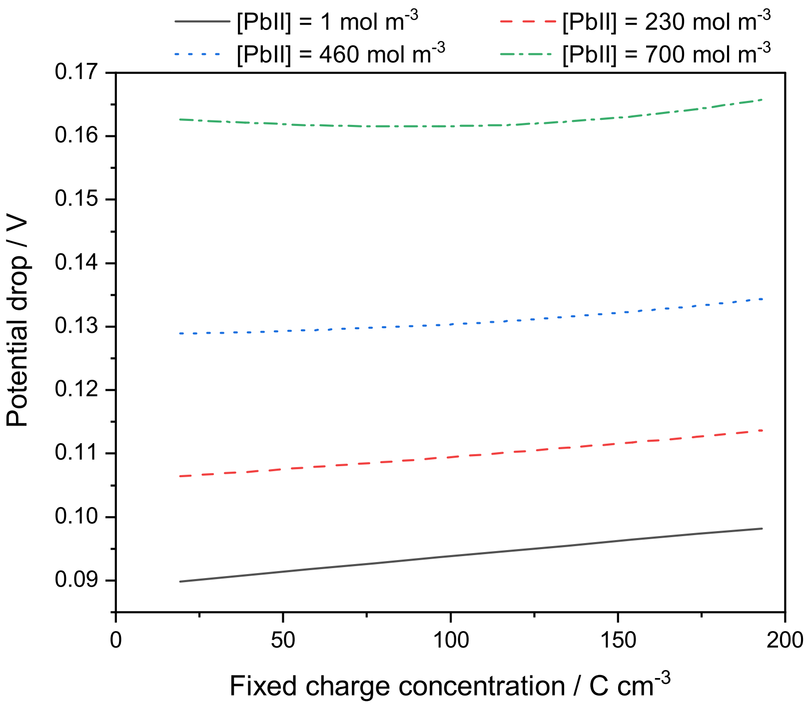

FIGURE 7.7: Simulated potential drop across an anion-exchange membrane with varied fixed charge concentration at different simulated electrolyte states of charge: $[Pb^{2+}] = 1$ mol m^{-3} & $[H^+] = 2398$ mol m^{-3} (black solid line), $[Pb^{2+}] = 230$ mol m^{-3} & $[H^+] = 1940$ mol m^{-3} (red dashed line), $[Pb^{2+}] = 460$ mol m^{-3} & $[H^+] = 1480$ mol m^{-3} (blue dotted line) and $[Pb^{2+}] = 700$ mol m^{-3} & $[H^+] = 1000$ mol m^{-3} (green dot-dashed line).

7.6 Cation-exchange membrane

For validating the cation-exchange membrane, a Nafion 115 ion exchange membrane, was chosen. Figure 7.8 shows the experimental results gathered by Krishna et al. [86], and the results from the same two simulation techniques described in Section 7.4 for this membrane. The potential drop of this membrane is much higher than that of the AEM ranging between 50-200 mV. However, the membrane is much thicker (0.1 mm) and it is less porous. The fit with experimental data is reasonable. Differences are likely to arise because Nafion 115 is also selective based on ion size. This is not included in this model.

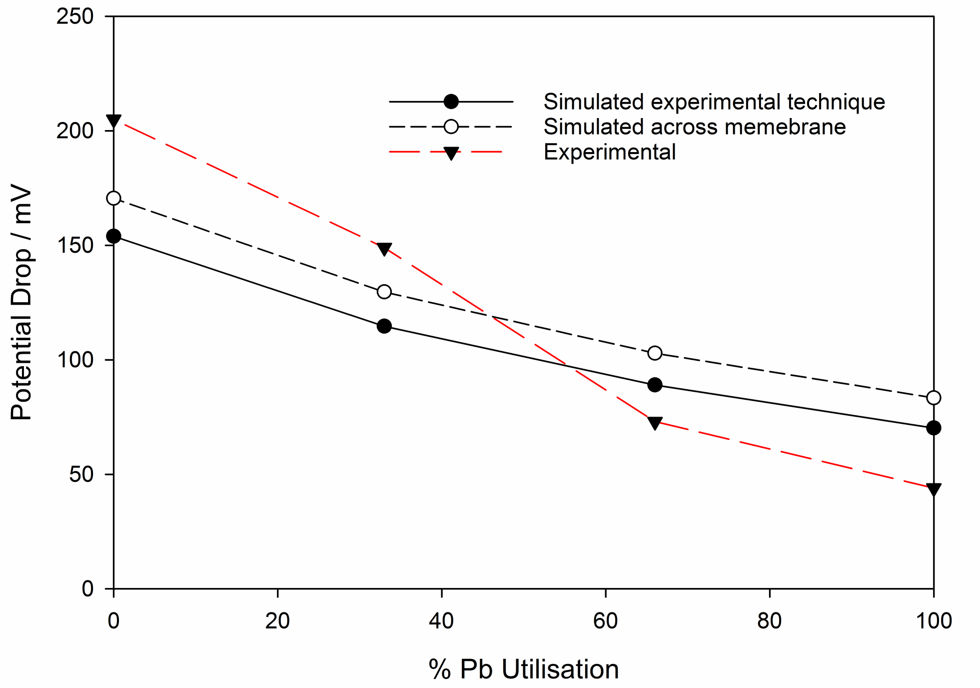

FIGURE 7.8: Experimental (red dashed line) and simulated potential drop mimicking the experimental technique (black solid line) an simulated potential drop measured directly (black dotted line) across a Nafion 115 membrane. A current density of 171 mA cm^{-2} is used. Experimental data from [86].

The simulated potential distribution across a membrane domain and an electrolyte domain which extends 2 mm to either side of the membrane, displayed in Figure 7.9, show the majority of the potential drop across the membrane is due to the resistance of the membrane. While there are clearly Donnan potentials present in the simulation (vertical changes in potential at the boundaries X = 0.002 m & X = 0.0021 m), they are much smaller than the overall drop across the membrane. Because these potentials are related to the logarithm of the ratio of concentrations across the membrane boundary, see Equation 4.40, and the fixed concentration within the membrane is of the same order as the electrolyte concentrations, the Donnan potentials at each boundary are small. Furthermore, because the added potential drop is the difference between the Donnan potentials, if there is little difference in concentration on either side of the membrane, the added potential drop will be further reduced.

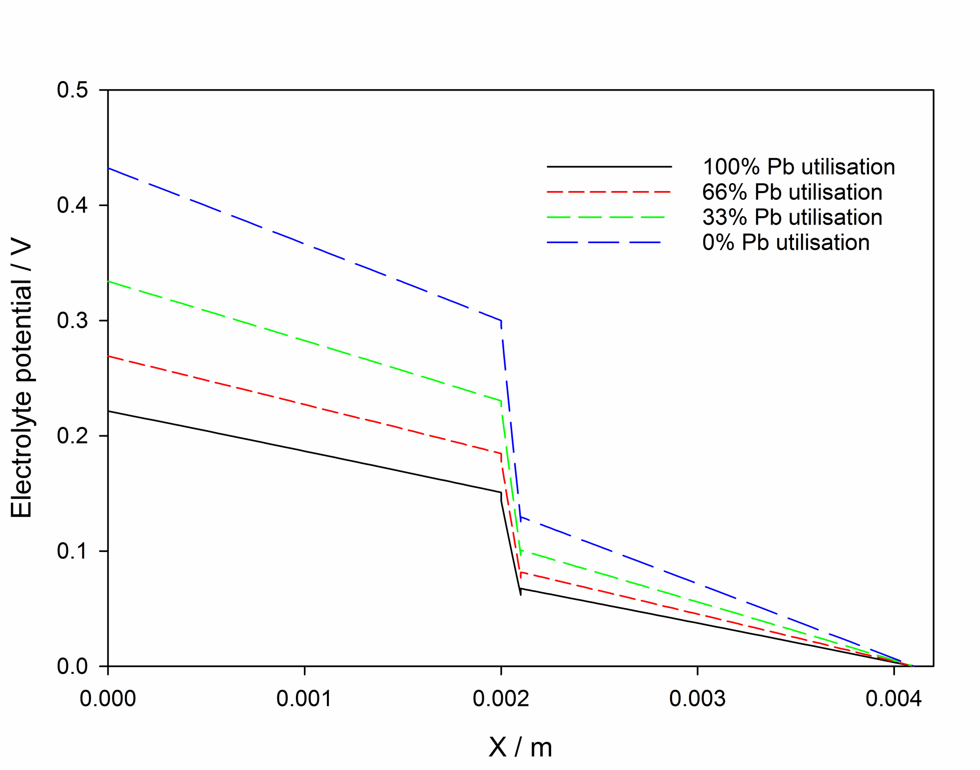

FIGURE 7.9: Simulated electrolyte potential using a reference of 0 V at the maximum value for X. Values for electrolyte simulating 100 % (solid black line), 66 % (red short dashed line), 33 % (green dashed line) and 0 % (blue long dashed line) Pb^{2+} utilisation are included.

7.6.1 Effect of current density

A very similar relationship is seen for simulated potential drop against current density with the cation-exchange membrane and the anion exchange membrane, see Figure 7.10. Again a linear relationship suggests the membrane closely aligns with Ohm's Law. However, the electrolyte concentration has a greater effect on the cation exchange membrane, with an increased potential drop at low states of charge ($[Pb^{2+}] = 700$ mol m^{-3}) and a decreased drop at high states of charge ($[Pb^{2+}] = 1$ mol m^{-3}) in the simulation when compared to the anion exchange membrane. This is logical. As the cation exchange membrane allows cations to pass across more readily, in this case more H^+ and Pb^{2+}

than the counter ion, as the proportion of cations shifts to more H^+ and fewer Pb^{2+} ions and the H^+ is more conductive the resistance of the membrane should decrease, as it does. Conversely, as there is only a single counter ion, and the flow of cations is resisted in an anion exchange membrane, the higher abundance of the more conductive H^+ has a smaller effect.

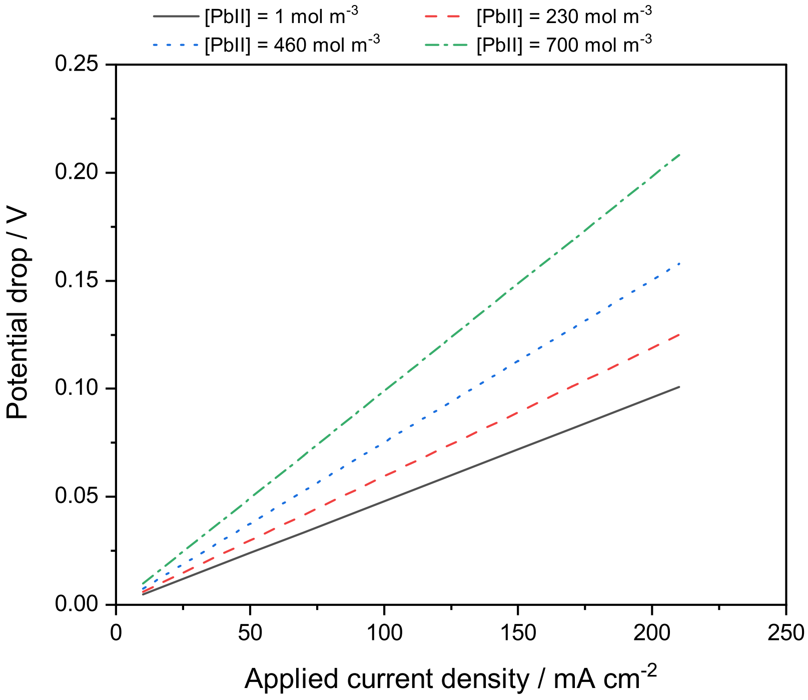

FIGURE 7.10: Simulated potential drop across an cation-exchange membrane with varied current density at different simulated electrolyte states of charge: $[Pb^{2+}]$ = 1 mol m^{-3} & $[H^+]$ = 2398 mol m^{-3} (black solid line), $[Pb^{2+}]$ = 230 mol m^{-3} & $[H^+]$ = 1940 mol m^{-3} (red dashed line), $[Pb^{2+}]$ = 460 mol m^{-3} & $[H^+]$ = 1480 mol m^{-3} (blue dotted line) and $[Pb^{2+}]$ = 700 mol m^{-3} & $[H^+]$ = 1000 mol m^{-3} (green dot-dashed line).

7.6.2 Effect of porosity

The effect of porosity on the simulated potential drop across the membrane is again very similar between the cation and anion exchange membrane, see Figure 7.11. The spread of potential drop across the different simulated electrolyte concentrations is again smaller in the cation exchange membrane. This is more noticeable at the high potential drops of a low porosity membrane.

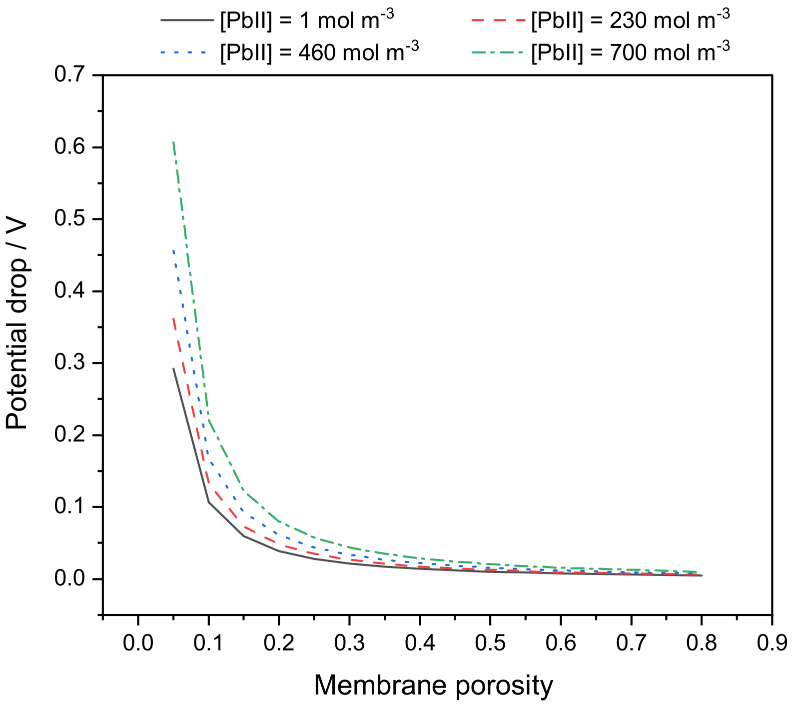

FIGURE 7.11: Simulated potential drop across an anion-exchange membrane with varied membrane porosity at different simulated electrolyte states of charge: [Pb^{2+}] = 1 mol m^{-3} & [H^+] = 2398 mol m^{-3} (black solid line), [Pb^{2+}] = 230 mol m^{-3} & [H^+] = 1940 mol m^{-3} (red dashed line), [Pb^{2+}] = 460 mol m^{-3} & [H^+] = 1480 mol m^{-3} (blue dotted line) and [Pb^{2+}] = 700 mol m^{-3} & [H^+] = 1000 mol m^{-3} (green dot-dashed line).

7.6.3 Effect of charge distribution

As the simulated concentration of the negative charge in the cation exchange membrane increases, the potential drop increases at low SoC, but decreases at a high SoC. This suggests the cation exchange membrane has an inhibiting effect on Pb^{2+} ions, while H^+ ions are able to pass through the membrane in the model more easily at a higher charge concentration. As the fixed negative charge concentration in the model increases, the concentration of the free cations will increase to maintain electroneutrality. By looking at Figure 6.1 in the previous chapter, it can be seen that with increasing Pb^{2+} concentration, the conductivity decreases if the H^+ is high enough. Yet, the conductivity increases with increasing H^+ concentration. Hence, if the cations increasing in concentration within the membrane are mostly Pb^{2+}, it follows that the conductivity of the membrane will decrease leading to a higher potential drop. However if the cations are mostly H^+, the conductivity of the membrane will increase causing a lower potential drop.

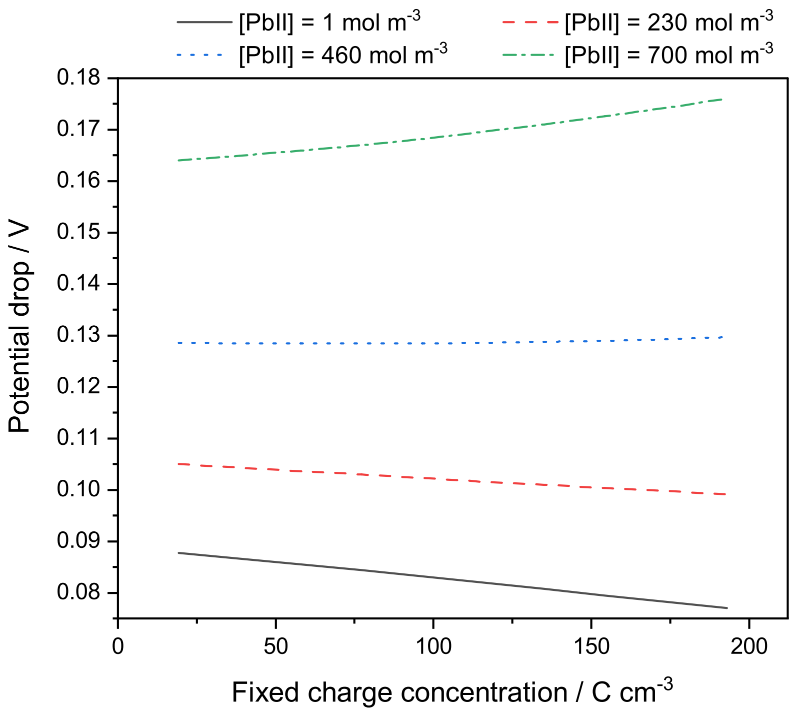

FIGURE 7.12: Simulated potential drop across an anion-exchange membrane with varied fixed charge concentration at different simulated electrolyte states of charge: $[Pb^{2+}] = 1\ mol\,m^{-3}$ & $[H^+] = 2398\ mol\,m^{-3}$ (black solid line), $[Pb^{2+}] = 230\ mol\,m^{-3}$ & $[H^+] = 1940\ mol\,m^{-3}$ (red dashed line), $[Pb^{2+}] = 460\ mol\,m^{-3}$ & $[H^+] = 1480\ mol\,m^{-3}$ (blue dotted line) and $[Pb^{2+}] = 700\ mol\,m^{-3}$ & $[H^+] = 1000\ mol\,m^{-3}$ (green dot-dashed line).

7.7 Additive crossover

One of the main advantages of using an ion exchange membrane in the SLFB is it facilitates the use of electrode specific additives [5]. A perfect membrane would allow an additive which is beneficial at one electrode but detrimental at the other by preventing crossover of the additive. As membranes are not perfectly selective, here additives with different charges, diffusion coefficients and concentrations are modelled to determine the selectivity of membranes with different properties on these simulated additives.

There are a range of additives which have been tested in the SLFB [5, 85], the most common of which are discussed in Section 2.4. At the negative electrode, levelling agents, such as hexadecyltrimethyl ammonium hydroxide (HDTMA, $CH_3((CH_2)_{15}N(CH_3)_3)^+$) and ligninsulfonate (long organic chain, single negative charge ion) are beneficial to deposition of Pb. However, ligninsulfonate, in particular, is oxidised at the positive electrode which reduced coulombic efficiency of the battery and removes the beneficial additive from the electrolyte. Pletcher at al. have conducted preliminary tests on 35 additives for the negative electrode [79]. The mechanisms for the benefit of each is not discussed. However, additives such as benzethonium hydroxide, glycolic acid ethoxylate 4-nonylphenyl ether and Tyloxapol™ were shown to produce excellent Pb deposits but the effects on the positive electrode were not discussed and the additives have not been further discussed in the literature. This highlights the possibility of many potentially beneficial additives for use in the SLFB.

At the positive electrode, slow kinetics can be improved with a catalyst additive. Bismuth (Bi^{3+}) has been shown to improve kinetics at the positive electrode [78, 88]. However, it is preferentially deposited before Pb at the negative electrode.

The work in this section is intended to aid in choosing a suitable membrane for testing potential additives while while limiting crossover.

Table 7.4 shows the default values of parameters used in these simulations unless otherwise stated. The default additive valence was nominally chosen to be +1, while the diffusion coefficient was chosen as a value similar to that of Bi^{3+} [179–181] (a common SLFB additive), Pb^{2+} and $CH_3SO_3^-$. A typical additive concentration was chosen [79, 85] and the fixed charge concentration fitted against validation data for Nafion 115 was used as the default, see Section 7.5.

To provide some context of the fluxes described in this section, at a continuous flux of 1×10^{-5} mol m^{-2} s^{-1} an additive with a concentration of 5 mmol dm^{-3} in 1 dm^3 of electrolyte would take just 7 hours for the concentration to be equal on both sides of the membrane. Accordingly a flux of 1×10^{-9} would take 70000 hours.

TABLE 7.4: Default values of parameters used in for simulating additive crossover in a membrane divided SLFB.

Parameter	Value	Units
Additive Valence, z_{add}	+1	-
Additive diffusion coefficient, D_{add}	1×10^{-9}	m^2 s^{-1}
Additive concentration, c_{add}	5	mmol dm^{-3}
Membrane charge distribution, C_{fix}	+115	C cm^{-3}
Current density, i	171	mA cm^{-2}

7.7.1 Effect of additive valence

In the model, the valence of the additive was varied between -3 and +3 and the flux of the additive was measured at the membrane boundary. The additive crossover flux was simulated for cases with the additive present on either side of the cell.

The case with the additive on the positive side of the cell is shown in Figure 7.13 (A). In this case the membrane was significantly more effective when the additive had a negative charge.

When the additive is applied to the negative side of the cell, a similar profile is seen, but with the modelled membrane being most effective when the additive has a positive charge. However, as shown in Figure 7.13 (B), while the shape is similar the flux is almost doubled.

It should be noted that when referring to the positive or negative side of the cell, this is with respect to the simulated electrolyte potential. So, during charge, the more positive electrolyte potential is next to the positive electrode, while during discharge, the positive electrolyte potential is next to the negative electrode. Hence, for any charged additive, it will undergo a higher rate of flux during either charge or discharge depending on its valence.

The large difference in simulated flux between a cation additive and an anion additive is likely due to the effect of migration, with cations moving with a higher flux away from the positive side of the cell and anions moving with a higher flux from the negative side of the cell.

An anion exchange membrane was used in these simulations, hence the reduced flux of the cation positive electrode additive compared to the flux of the anion negative electrode additive.

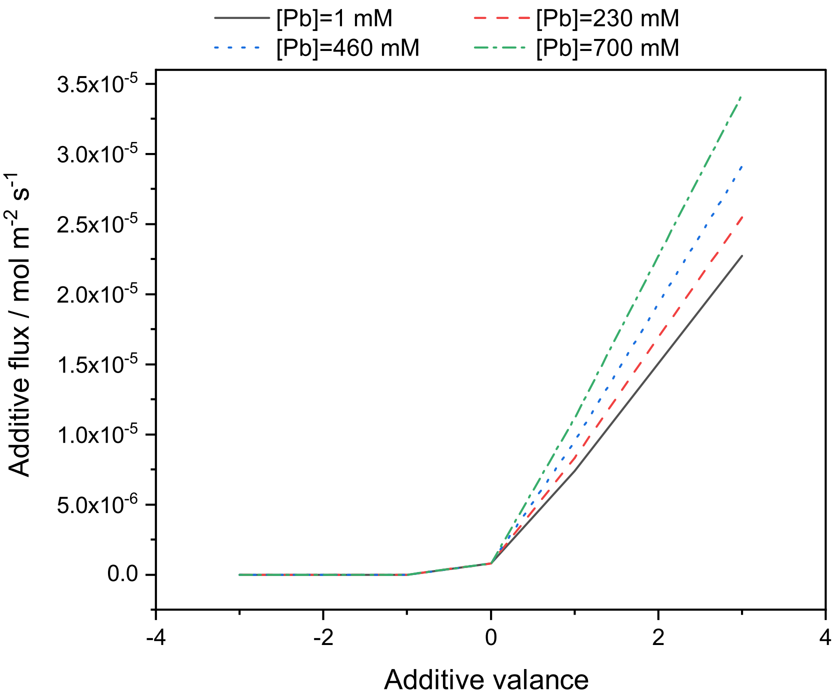

(A) Positive electrode additive

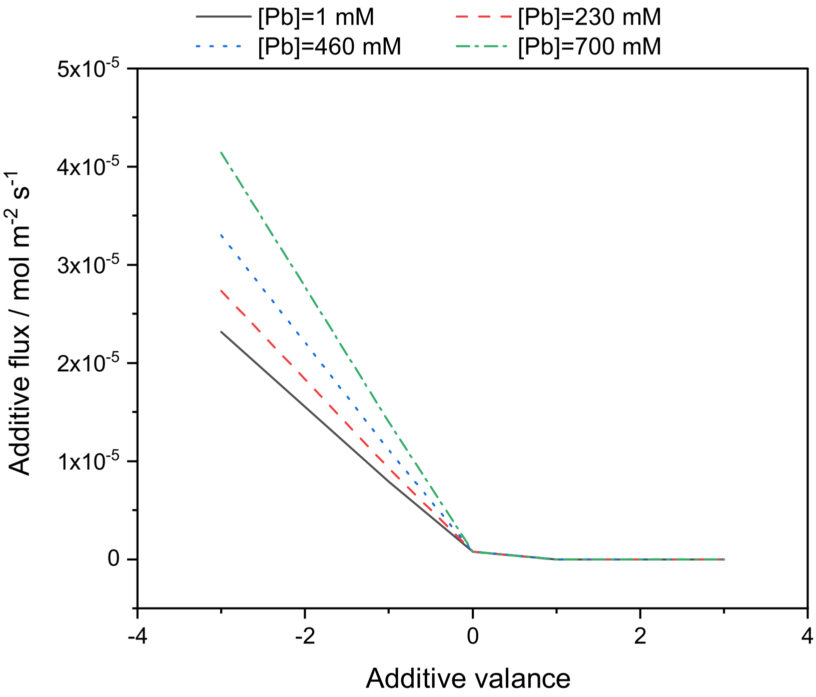

(B) Negative electrode additive

FIGURE 7.13: Simulated flux of additive through the membrane vs valence of the additive ion at different simulated stated of charge: $[Pb^{2+}]$ = 1 mol m^{-3} & $[H^+]$ = 2398 mol m^{-3} (black solid line), $[Pb^{2+}]$ = 230 mol m^{-3} & $[H^+]$ = 1940 mol m^{-3} (red dashed line), $[Pb^{2+}]$ = 460 mol m^{-3} & $[H^+]$ = 1480 mol m^{-3} (blue dotted line) and $[Pb^{2+}]$ = 700 mol m^{-3} & $[H^+]$ = 1000 mol m^{-3} (green dot-dashed line).

7.7.2 Effect of additive diffusion coefficient

As there are many additives which have been or may be considered for use in the SLFB, the effect of a wide range of diffusion coefficients is considered. For cases where the diffusion coefficient is not varied, a value of 1×10^{-9} m^2s^{-1} was chosen. This is similar to the value used for Pb^{2+} and $CH_3SO_3^-$ in the simulations and is also roughly equivalent to the diffusion coefficient of Bi^{3+} [179–181], an additive used at the positive electrode of the SLFB [78, 85].

Figure 7.14 shows the effect of varying the diffusion coefficient of the modelled additive. Additives with a higher diffusion coefficient clearly have a higher flux across the membrane, with a linear relationship in all cases presented.

When an anion additive is added to the electrolyte with a more negative potential, the simulated flux also increases with lead concentration, Figure 7.14 (A). For a cation additive added to the more negative side of the modelled cell, the simulated flux decreases with increased lead concentration , Figure 7.14 (B). When added to the electrolyte with a more positive potential, the flux of an anion additive decreases with lead concentration, Figure 7.14 (C), and the flux of a cation additive increases with lead concentration, Figure 7.14 (D).

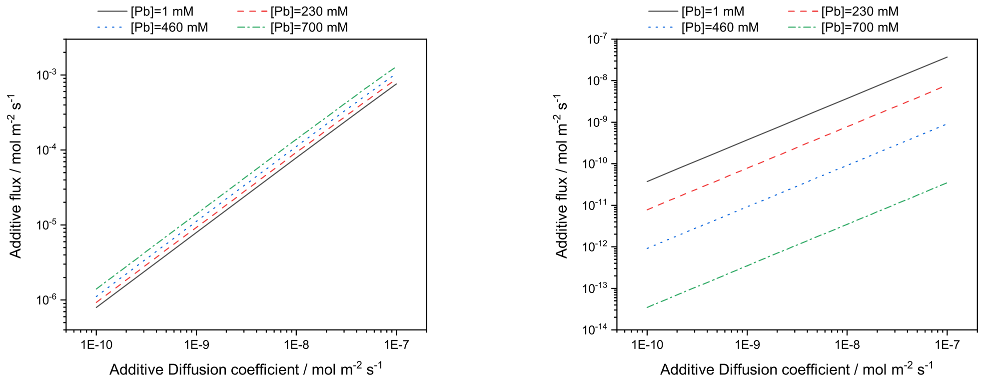

(A) Negative electrode anion additive

(B) Negative electrode cation additive

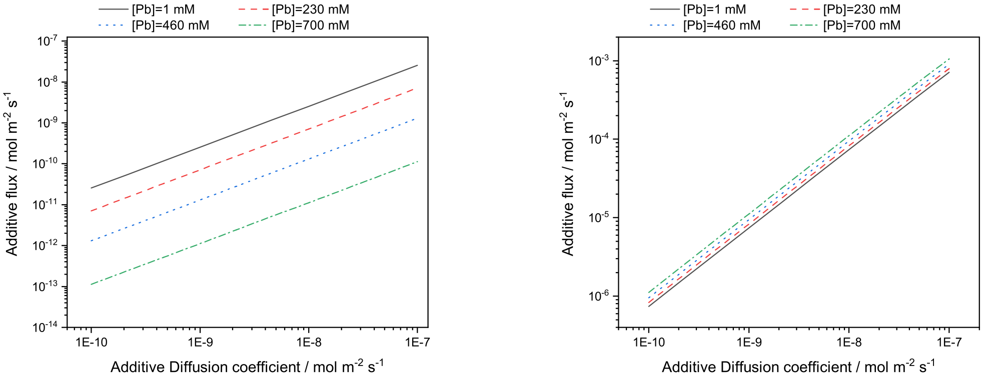

(C) Positive electrode anion additive

(D) Positive electrode cation additive

FIGURE 7.14: Simulated flux of additive through the membrane vs diffusion coefficient of the additive ion at different simulated stated of charge: $[Pb^{2+}]$ = 1 mol m^{-3} & $[H^+]$ = 2398 mol m^{-3} (black solid line), $[Pb^{2+}]$ = 230 mol m^{-3} & $[H^+]$ = 1940 mol m^{-3} (red dashed line), $[Pb^{2+}]$ = 460 mol m^{-3} & $[H^+]$ = 1480 mol m^{-3} (blue dotted line) and $[Pb^{2+}]$ = 700 mol m^{-3} & $[H^+]$ = 1000 mol m^{-3} (green dot-dashed line).

7.7.3 Effect of additive concentration

Additive concentrations are generally in the region of mmol dm^{-3} [79, 85]. Higher additive concentrations may have a beneficial effect on the deposit quality and cycle life, but may decrease efficiency. Figure 7.15 shows that the flux across the membrane increases linearly with a concentration of the additive for both anion and cation additives and for additives on both sides of the cell.

The simulated additive concentration was varied from 5 to 50 mmol dm^{-3}, the flux of the additive across the membrane is shown in Figure 7.15. When added to the electrolyte with a more positive potential, the flux of an anion additive decreases with lead concentration, Figure 7.15 (A), and the flux of a cation additive increases with lead concentration, Figure 7.15 (B) and when added to the electrolyte with a more positive potential, the flux of an anion additive decreases with lead concentration, Figure 7.15 (C), and the flux of a cation additive increases with lead concentration, Figure 7.15 (D). This corresponds to the scenarios shown in Figure 7.13.

While membranes are generally more selective for species at low concentrations [182], the high overall concentration and low difference in concentration of the electrolyte across the membrane and hence the low Donnan potentials result in a linearly increasing relationship in the model with additive concentration.

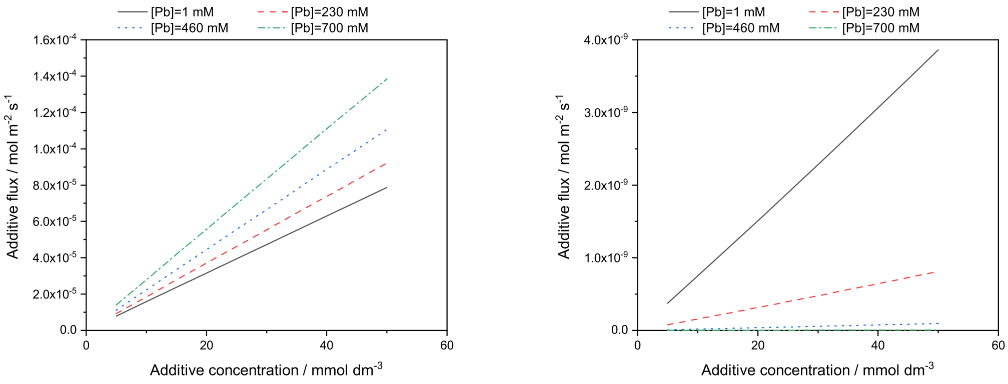

(A) Negative electrode anion additive (B) Negative electrode cation additive

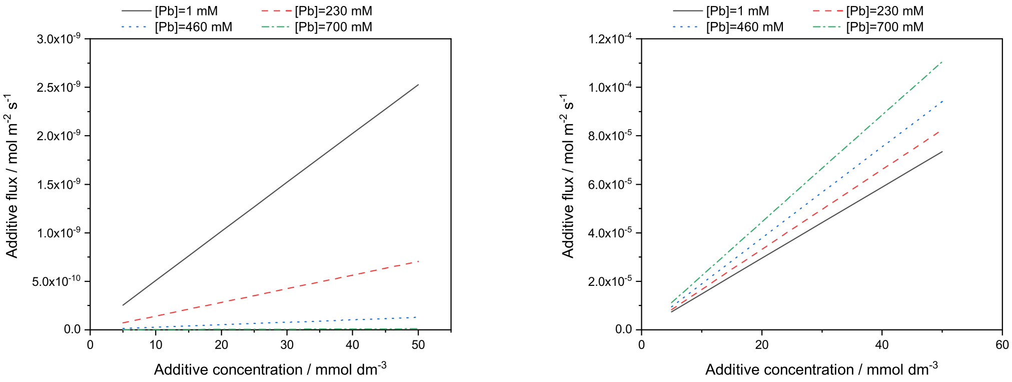

(C) Positive electrode anion additive (D) Positive electrode cation additive

FIGURE 7.15: Simulated flux of additive through the membrane vs concentration of the additive ion at different simulated states of charge: $[Pb^{2+}] = 1\ mol\,m^{-3}$ & $[H^+] = 2398\ mol\,m^{-3}$ (black solid line), $[Pb^{2+}] = 230\ mol\,m^{-3}$ & $[H^+] = 1940\ mol\,m^{-3}$ (red dashed line), $[Pb^{2+}] = 460\ mol\,m^{-3}$ & $[H^+] = 1480\ mol\,m^{-3}$ (blue dotted line) and $[Pb^{2+}] = 700\ mol\,m^{-3}$ & $[H^+] = 1000\ mol\,m^{-3}$ (green dot-dashed line).

7.7.4 Effect of membrane charge distribution

The fixed charge in the modelled membrane has a significant impact on selectivity of certain ions. When modelling a cation exchange membrane there is a negative fixed charge and in an anion exchange membrane there is a positive fixed charge. Figure 7.16 shows that while there is a significant difference in simulated flux depending on the fixed charge concentration, the trend between flux and concentration is determined by the position and charge of the ion with respect to the electrolyte potential.

When modelling a cation additive at the more negative electrolyte potential, Figure 7.16 (B) and an anion additive at the more positive electrolyte potential Figure 7.16 (C), the additive flux is significantly lower when an anion exchange membrane is used. In both, the simulated flux decreased with an increased lead concentration. The trend is reversed when the ions are moved to the opposite electrolyte potential. However, the difference in flux is less pronounced.

This suggests the motion of ions may be more closely linked to the movement of the other ions across the membrane.

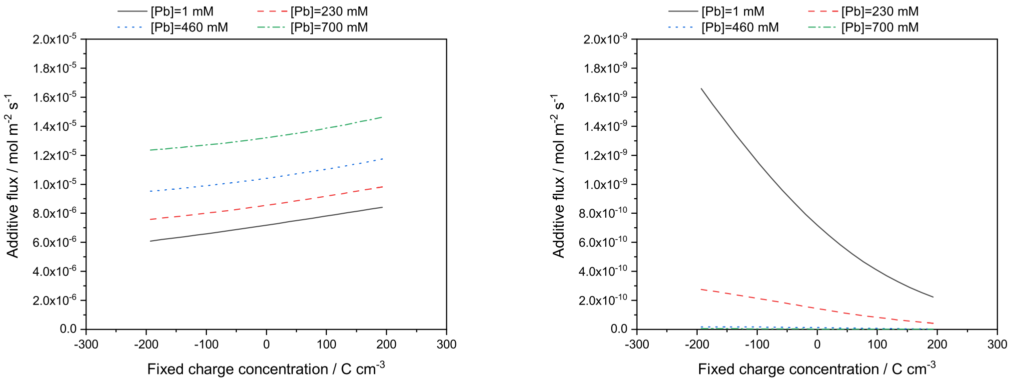

(A) Negative electrode anion additive

(B) Negative electrode cation additive

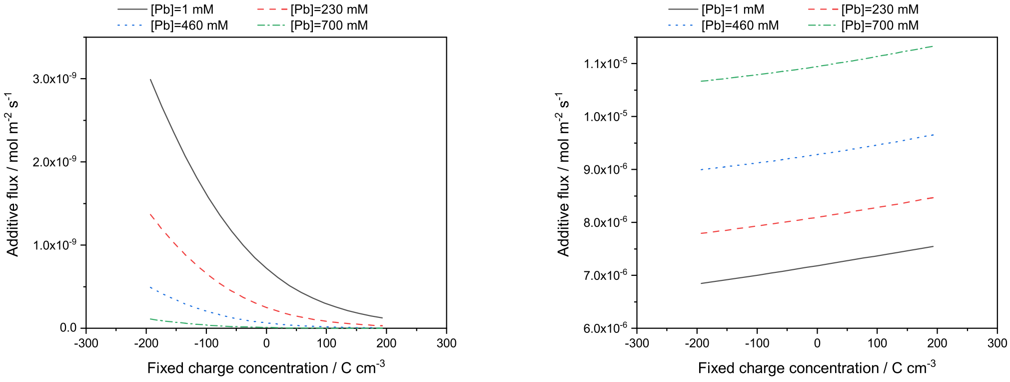

(C) Positive electrode anion additive

(D) Positive electrode cation additive

FIGURE 7.16: Simulated flux of additive through the membrane vs fixed charge concentration in the membrane at different simulate states of charge: $[Pb^{2+}] = 1\ mol\,m^{-3}$ & $[H^{+}] = 2398\ mol\,m^{-3}$ (black solid line), $[Pb^{2+}] = 230\ mol\,m^{-3}$ & $[H^{+}] = 1940\ mol\,m^{-3}$ (red dashed line), $[Pb^{2+}] = 460\ mol\,m^{-3}$ & $[H^{+}] = 1480\ mol\,m^{-3}$ (blue dotted line) and $[Pb^{2+}] = 700\ mol\,m^{-3}$ & $[H^{+}] = 1000\ mol\,m^{-3}$ (green dot-dashed line). A negative fixed charge represents a cation exchange membrane and a positive fixed charge represents an anion exchange membrane.

7.8 Divided cell two-dimensional model

Here the same membrane properties as those described for validating the cation-exchange membrane as described in Section 7.6 are used. Data presented for charge and discharge are taken during charge are at t = 3200 s and during discharge at t = 7200 s.

The two-dimensional model incorporates flow of electrolyte and uneven distribution of current in the y-direction of the electrodes. Both these factors affect the concentration distribution. The mesh is fixed. Figure 7.17 shows the simulated concentration across the width of the cell along a line between the midpoint of the height of the electrodes. Duringa simulated charge, the Pb^{2+} concentration is even across the bulk of the electrolyte. However, in the closest 1.5 mm to both electrodes, as Pb^{2+} is consumed in the electrode reactions, the concentration drops from $\sim$390 mol m^{-3} in the bulk to $\sim$230 mol m^{-3} at the negative electrode surface and $\sim$180 mol m^{-3} at the positive electrode surface. The simulated H^+ concentration is also consistent in the bulk at $\sim$1620 mol m^{-3} and, increases in the nearest 1.5 mm to both electrodes. As H^+ is a product of the positive electrode reaction during charge, the increase in concentration to over 2000 mol m^{-3} is expected. At the negative electrode, there is an increase in concentration to 1800 mol m^{-3}, which maintains electroneutrality.

The simulated concentration of each species also varies on either side of the membrane, leading to an increase in Donnan potential drop. This is exacerbated with an increase in current density. The mesh selection and sensitivity study are described in Appendix C.

However, Figure 7.18, which shows the simulated potential distribution over a 2D simulated flow cell when the cell is run at currents of 10, 20, 30 and 50 mA cm^{-2} shows the simulated potential drop within the membrane, also increases. In the electrolyte domain, the potential increases almost linearly with distance through the electrolyte. At the boundary between the membrane and the electrolyte domains, however, there are significant changes in the modelled electrolyte – as expected from the concentration profile. Table 7.5 displays the total potential difference across the membrane, the potential difference due to Donnan potentials and the potential difference within the membrane due to its conductivity in the simulation. This shows that the membrane conductivity dominates the potential drop across the membrane both during charge and discharge. However, as current density is increased in the simulation, the ratio of membrane conductivity to Donnan drop decreases.

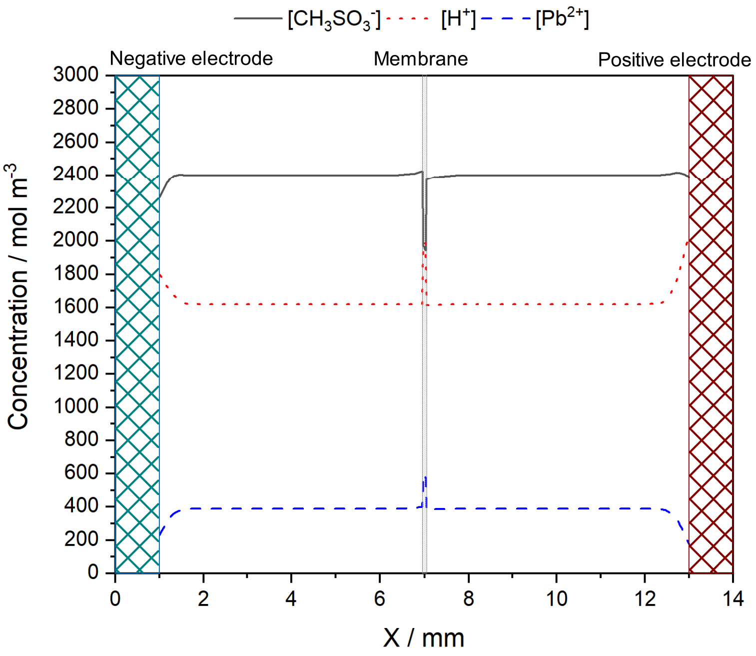

(A) Charge

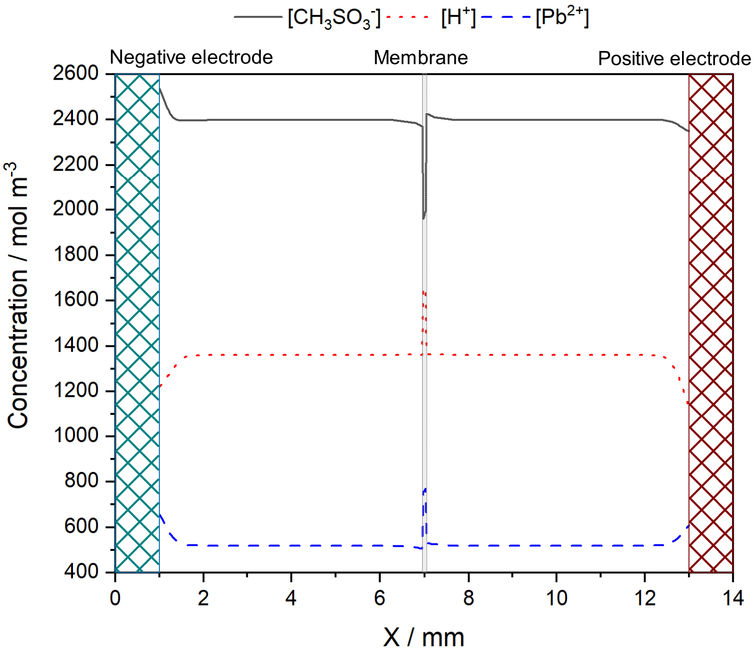

(B) Discharge

FIGURE 7.17: Simulated concentration profiles for each species, $CH_3SO_3^-$ (black solid line), H^+ (red dotted line) and Pb^{2+} (blue dashed line), over the width of the cell with an applied current density of 50 mA cm^{-2}. A spike/trough in each of the species is seen in the membrane. The negative electrode region is shaded in blue, the positive electrode region is shaded in red and the membrane is shaded in grey.

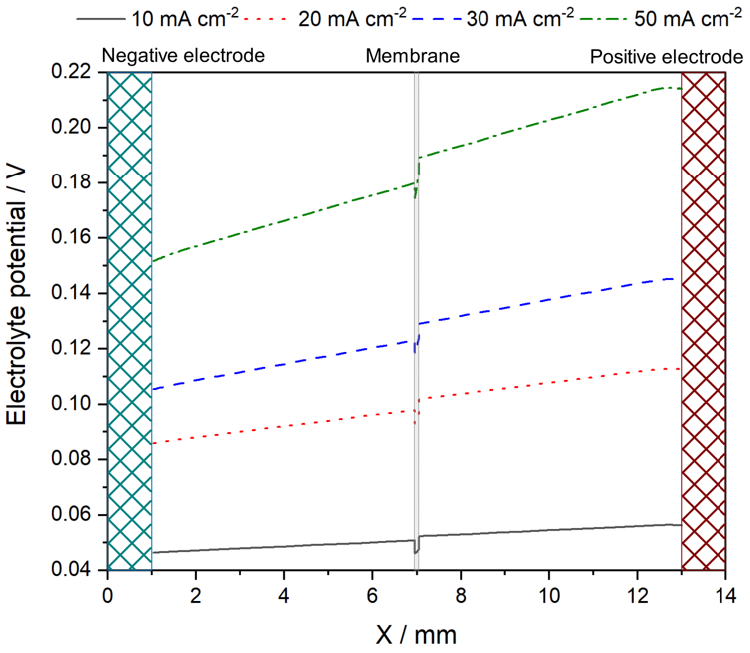

(A) Charge

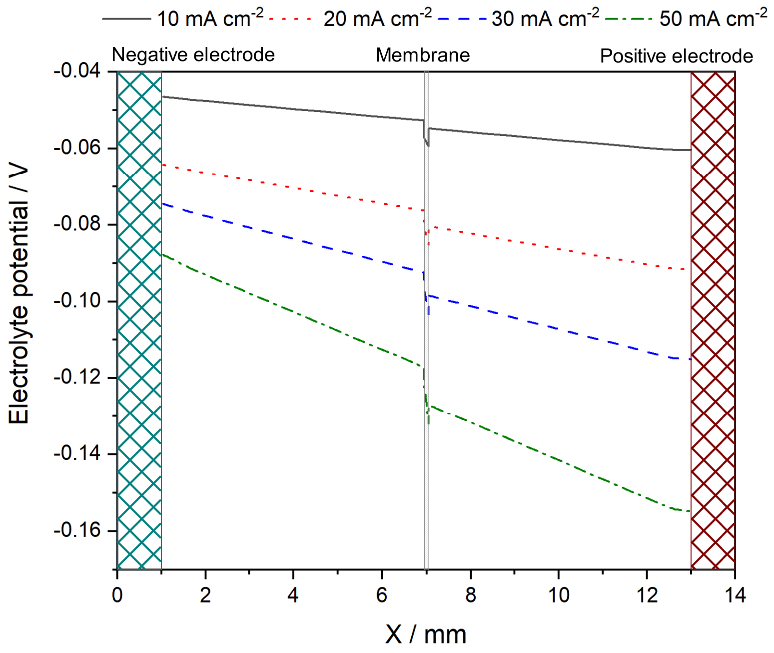

(B) Discharge

FIGURE 7.18: Simulated electrolyte potential distribution across the midpoint of the cell at 10 mA cm^{-2} (solid black line), 20 mA cm^{-2} (dotted red line), 30 mA cm^{-2} (dashed blue line), and 50 mA cm^{-2} (dot-dashed green line). The negative electrode region is shaded in blue, the positive electrode region is shaded in red and the membrane is shaded in grey.

TABLE 7.5: Breakdown of potential drop across the membrane during charge and discharge. Current densities of 10, 20, 30 and 50 mA cm^{-2} are used.

	Potential during charge (mV)			**Potential during discharge** (mV)		
Current Density (mA cm^{-2})	**Donnan** (ϕ_D)	**Conductivity** (ϕ_C)	**Ratio** $\left(\frac{\phi_C}{\phi_D}\right)$	**Donnan** (ϕ_D)	**Conductivity** (ϕ_C)	**Ratio** $\left(\frac{\phi_C}{\phi_D}\right)$
10	0.0149	1.48	84	0.0230	2.04	89
20	0.0487	3.99	82	0.0473	4.02	85
30	0.0753	5.89	78	0.0728	5.94	82
50	0.131	9.34	71	0.134	9.79	73

7.9 Summary

A one-dimensional model was used to screen a wide array of variables to simulate porous separators and ion exchange membranes in a single cell SLFB. The potential drop across each membrane was investigated and the selectivity of ion exchange membranes for a range of hypothetical additives was simulated.

The simulated potential drop across ion exchange membranes was almost entirely attributed to ohmic losses. Donnan potentials were present in the simulations, increasingly so at higher current densities. However, these were two orders of magnitude smaller than the ohmic drop across the membrane.

In the SLFB model, both anion and cation exchange membranes are more selective against cation additives when they are added at the negative electrode and anion additives when they are added at the positive electrode. Additive concentration had very little effect on the time it takes for a given proportion of the additive to cross the membrane in the simulations and ions with a low diffusion coefficient (and hence low mobility) cross the membrane less easily.

The high overall concentrations of the electrolyte and hence low Donnan potentials at the boundaries were found to reduce the selectivity of the ion exchange membranes to a range of simulated additives.

Porous separators were found to be easily modelled using just porosity and the concentration of the electrolyte species at the boundary. This technique was employed in the model for the divided cells described in Chapter 8.

Chapter 8

Image based modelling of porous RVC electrodes

As the kinetics of the positive electrode reactions are far slower than the Pb^{2+}/Pb reaction at the negative electrode [82, 94], to achieve the best performance of the SLFB, having a lower current density at the positive electrode than at the negative electrode is advantageous. The obvious approach to this is to have a positive electrode with a larger surface area than the negative electrode.

Several approaches to this problem have been discussed previously. Oury et al. suggest using a 3D honeycomb flow through positive electrode arranged between two flat planar negative electrodes [96, 157]. While Nandanwar and Kumar [152], suggest a concentric arrangement of cylindrical electrodes with the annular electrolyte flow. The positive electrode in this arrangement is the outer electrode and the negative the inner.

Both these approaches achieve a higher surface area at the positive electrode. However, while both achieve improved performance when compared to standard planar electrodes, when considering their arrangement into a stack neither approach is able to make use of bipolar electrodes and hence do not make efficient use of materials or, in the case of the concentric arrangement, space. Furthermore, increasing the surface area of both electrodes is likely to be advantageous as the Pb morphology is also improved at lower current densities [79].

In the series of papers that introduced the SLFB, Pletcher et al. [95] introduced the use of foam materials as three-dimensional electrodes. Using such materials adhered to the surface of planar bipolar plates allows for customisation of electrode properties (thickness, porosity, pore density, material) for each electrode while maintaining the use of a bipolar stack.

Reticulated vitreous carbon (RVC) was one material highlighted for use in the SLFB. Pletcher et al. described a battery using RVC at the positive electrode and nickel foam at the positive electrode [95]. Both porous materials were adhered to a bipolar plate. While nickel electrodes have been shown to dissolve into the electrolyte, causing negative effects on the performance of the battery, RVC has received further use as an electrode with lead compounds, particularly in the wastewater treatment industry. RVC has also seen extensive use as an electrode material with other flow battery chemistries.

Chapter 5 assesses the effect of deposits at different states of charge on the SLFB with flat planar electrodes. In this chapter, a similar approach is taken for the SLFB when 3D, porous RVC electrodes are used. However, in this study, we employed a fixed geometry because RVC electrodes can be modelled as a single porous domain with changing porosity, tortuosity and permeability with state of charge. Previously published micro-CT scans of RVC [183] are reanalysed using an open-source software, OpenImpala [184].

8.1 Initial conditions

Initial values for parameters used in the simulations are displayed in Table 8.1. Concentrations similar to those in the literature, [5], were chosen with corresponding values for density and viscosity. The remaining initial values were selected to ensure consistency with the boundary conditions. To ensure non-conflicting boundary and initial conditions, several initial values were set to 0. The boundary conditions were then applied with a smoothed Heaviside smoothing function, which uses a piecewise 5th degree polynomial equation, applied over the first 1.5 s of the simulation.

TABLE 8.1: Initial conditions used for modelling three dimensional electrodes

Variable	Initial Value	Unit
u	0	m s^{-1}
v	0	m s^{-1}
p	0	Pa
c_{PbII0}	700	mol m^{-3}
c_{H0}	1000	mol m^{-3}
ϕ_l	0	V
ϕ_s	0	V
$\phi_{s,+}$	0	V
$a_{v,10}$	620	m^{-1}
$a_{v,30}$	1400	m^{-1}
$a_{v,45}$	1450	m^{-1}
$a_{v,80}$	1700	m^{-1}
$a_{v,100}$	1450	m^{-1}
ε	0.97	-
μ_{e0}	1.6762	mPa s
ρ_{e0}	1.727	kg dm^{-3}

8.2 Parameters

Values for parameters used in the simulations in this chapter are displayed in Table 8.2.

TABLE 8.2: Parameters used for modelling three dimensional electrodes

Parameter	Value	Unit	Reference
A	0.51	$\mathrm{dm^3\,mol^{-1}}$	Chapter 6
B	3.29	$\mathrm{dm^3\,mol^{-1}}$	Chapter 6
b_1	3.52243	$\mathrm{dm^3\,mol^{-1}}$	Chapter 6
b_2	0.94331	$\mathrm{dm^3\,mol^{-1}}$	Chapter 6
b_3	0.18444	$\mathrm{dm^3\,mol^{-1}}$	Chapter 6
D_{PbII}	7×10^{-10}	$\mathrm{m^2\,s^{-1}}$	Chapter 5
D_H	9.3×10^{-9}	$\mathrm{m^2\,s^{-1}}$	Chapter 5
$D_{CH_3SO_3}$	1.33×10^{-9}	$\mathrm{m^2\,s^{-1}}$	Chapter 6
k_{0Pb}	2.1×10^{-7}	$\mathrm{m\,s^{-1}}$	Chapter 5
k_{0PbO_2}	2.5×10^{-7}	$\mathrm{m\,s^{-1}}$	Chapter 5
k_{0b}	4.5×10^{-7}	$\mathrm{mol\,m^{-2}\,s^{-1}}$	Chapter 5
k_{0f}	0.002	$\mathrm{mol\,m^{-2}\,s^{-1}}$	Chapter 5
K	11.25	-	
ρ_{Pb}	11.337	$\mathrm{kg\,dm^{-3}}$	[185]
ρ_{PbO_2}	9.65	$\mathrm{kg\,dm^{-3}}$	[185]
ρ_{PbO}	9.53	$\mathrm{kg\,dm^{-3}}$	[185]
σ_{Pb}	4.69×10^6	$\mathrm{S\,m^{-1}}$	[186]
σ_{PbO_2}	8000*	$\mathrm{S\,m^{-1}}$	[187]
σ_{RVC}	330	$\mathrm{S\,m^{-1}}$	[183]
T	300	K	
z_{PbII}	2	-	
z_{H^+}	1	-	
$z_{CH_3SO_3^-}$	-1	-	

*Approximated constant value based on a mixture of α- and β- phases.

8.3 Input data (computed tomography)

The raw CT data was obtained from work by Arenas et al. [183] which used a Nikon/X-Tek XTH 225 instrument, with an isotropic resolution of 9.6 µm per voxel and a detector size of 2000 x 2000 pixels. The data for scans of 20, 30, 45, 80 and 100 ppi(pores per inch) was binarised and cropped into a cuboid domain.

For each grade of RVC, the morphology of the porous electrodes was virtually modified [188] by voxel dilation of the solid domain of the RVC CT dataset in the open-source software ImageJ [189]. Each dataset was dilated by a single voxel and then further dilated until the following specified total solid volume fractions were reached: 0.1, 0.2, 0.3, 0.5 and 0.8. Both the original and new dilated datasets were multiplied by 0.5. As the data was 8-bit, this resulted in an pore (electrolyte) phase with a value of 0 and a solid phase with a value of 127. The original dataset was then added to each of the

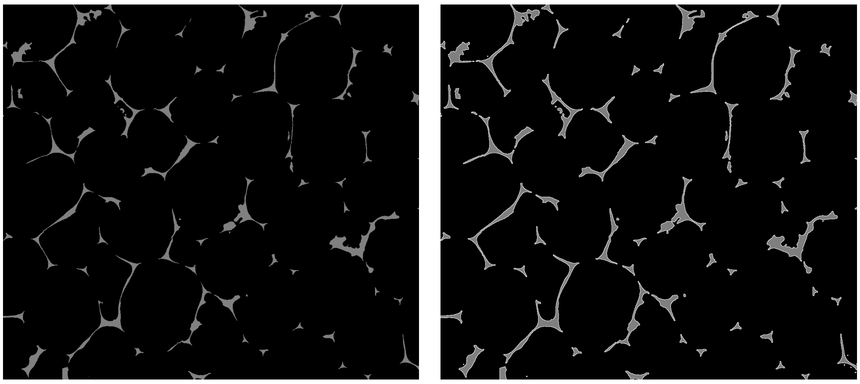

(A) RVC only (B) 1 voxel dilation

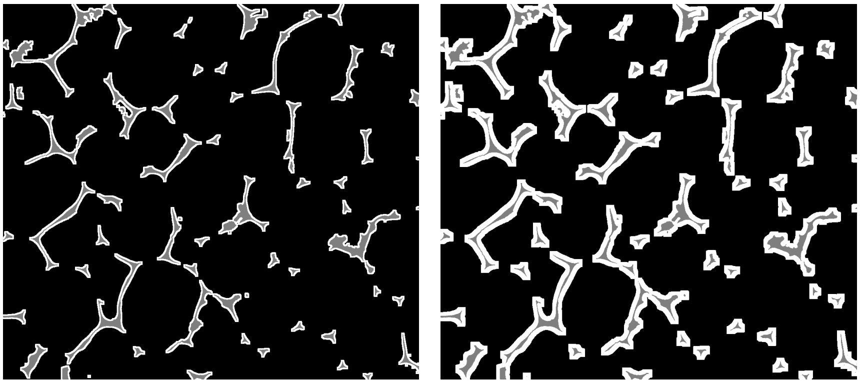

(C) Dilated to $\varepsilon_s \approx 10$ % (D) Dilated to $\varepsilon_s \approx 20$ %

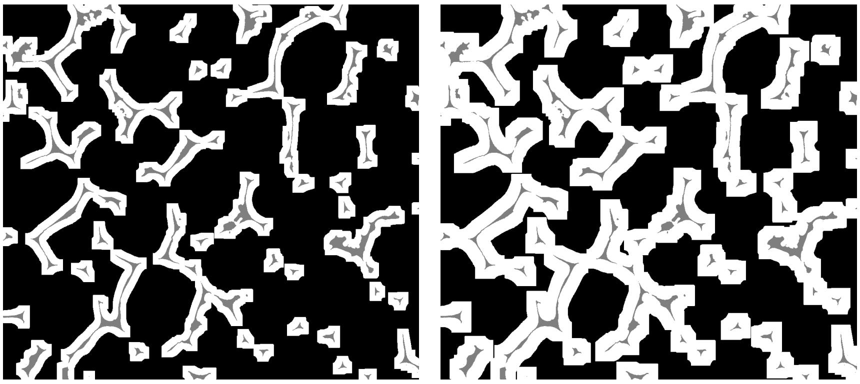

(E) Dilated to $\varepsilon_s \approx 30$ % (F) Dilated to $\varepsilon_s \approx 50$ %

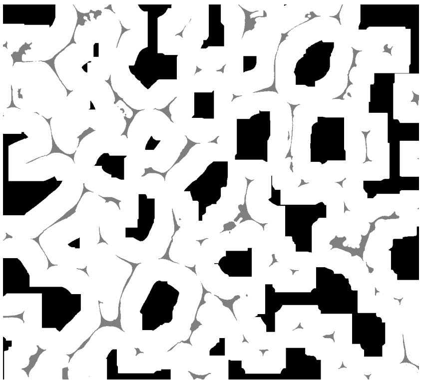

(G) Dilated to $\varepsilon_s \approx 80$ %

FIGURE 8.1: Images from CT data of 30 ppi RVC, thresholded into RVC and electrolyte, with further voxel dilation to form artificial deposit phases. The original RVC dataset is dilated by 1 voxel, then to a total solid volume fraction of 10 %, 20 %, 30 %, 50 % and 80 %. Pore space (electrolyte) is shown in black, RVC in grey and deposit in white.

dilated datasets to achieve a three-phase segmented dataset with RVC holding a value of 255, the artificial electrode deposit 127 and the electrolyte 0. A slice of each resulting dataset for the 30 ppi grade of RVC is shown in Figure 8.1 with pore space shown in black, RVC in grey and simulated deposit in white. For each dataset, a value for porosity and tortuosity was obtained using the open-source software OpenImpala, [184]. Here, tortuosity refers to effective tortuosity, not geodesic tortuosity [190]. A similar approach has been used to design the microstructure of lithium ion electrodes [191].

The surface area for each dataset was calculated using the Surface area analysis in the ImageJ plugin BoneJ [192]. This approximates the surface area of the dataset by creating a surface mesh from the raster dataset and then calculates the surface area of the mesh.

There are a number of different techniques for approximating the surface area for a porous domain with varying porosity. As with other aspects of porous domain approximations, it is common to assume the domain consists of either solid spheres or cylinders in an electrolyte matrix or vice versa. The best choice of approximate geometry depends on the morphology of the porous domain being modelled. As displayed graphically in Figure 8.2, while these approximations hold for certain ranges of porosities, they fail to capture the surface area over the full range of 0 to 1.

Taking the simple example of a cylinder of electrolyte in a solid matrix, which is easily visualised in 2D, the domain can be represented as an array of equally spaced cylinders with radius r and distance between centres d. The specific surface area is then:

$$a_v = \frac{2\pi r}{d^2} \tag{8.1}$$

Porosity is:

$$\varepsilon = \frac{\pi r^2}{d^2} \tag{8.2}$$

So, in terms of porosity, if d is fixed, specific surface area is:

$$a_v = \frac{2\sqrt{\pi\varepsilon}}{d} \tag{8.3}$$

Conversely if r is fixed instead:

$$a_v = \frac{2\varepsilon}{r} \tag{8.4}$$

Other methods include using a solid cylinder in an electrolyte matrix, with fixed d, Equation 8.5:

$$a_v = \frac{2\sqrt{\pi(1-\varepsilon)}}{d} \tag{8.5}$$

A solid cylinder in an electrolyte matrix, with fixed r, Equation 8.6:

$$a_v = \frac{2(1-\varepsilon)}{r} \tag{8.6}$$

An electrolyte sphere in a solid matrix, with fixed d, Equation 8.7:

$$a_v = \frac{\sqrt[3]{36\pi\varepsilon^2}}{d} \tag{8.7}$$

An electrolyte sphere in a solid matrix, with fixed r, Equation 8.8:

$$a_v = \frac{3\varepsilon}{r} \tag{8.8}$$

A solid sphere in an electrolyte matrix, with fixed d, Equation 8.9:

$$a_v = \frac{\sqrt[3]{36\pi(1-\varepsilon)^2}}{d} \tag{8.9}$$

A solid sphere in an electrolyte matrix, with fixed r, Equation 8.10:

$$a_v = \frac{3(1-\varepsilon)}{r} \tag{8.10}$$

This approach gives a reasonable assumption for surface area if $2r < d$. However, when $2r > d$, this approach assumes a_v continues to increase with increasing r. In reality, a_v decreases. Figure 8.2 shows how specific surface area varies with porosity for all combinations of the following relationships: fixed distance between particle centres fixed particle size varied distance between particles, solid particles in a liquid matrix, liquid particles in a solid matrix, cylindrical particles and spherical particles.

With a fixed r, the surface area varies linearly with porosity with liquid volumes in a solid matrix increasing with increasing porosity and solid volumes in a liquid matrix decreasing with increasing porosity, spheres give a steeper gradient for the same radius in both cases. This method may be appropriate if modelling a system with only a small change in porosity close to either 0 (using liquid volumes in a solid matrix) or 1 (using solid volumes in a liquid matrix). However, over a large range or using a porosity close to 0.5, this method cannot give a consistently good approximation.

With a fixed d, liquid volumes in a solid matrix still increase with increasing porosity and vice versa for solid volumes in a liquid matrix. However, clearly from Equation 8.7, Equation 8.3, Equation 8.9 and Equation 8.5, the relationship is no longer linear. This approach will yield a better match for a larger range of porosities. However, each case would only be applicable for at most half the porosity range with 0 to 0.5 using liquid volumes in a solid matrix and 0.5 to 1 using solid volumes in a liquid matrix. It would therefore be possible to produce a two case method changing the matrix from liquid to solid at a porosity of 0.5 to give a reasonable approximation.

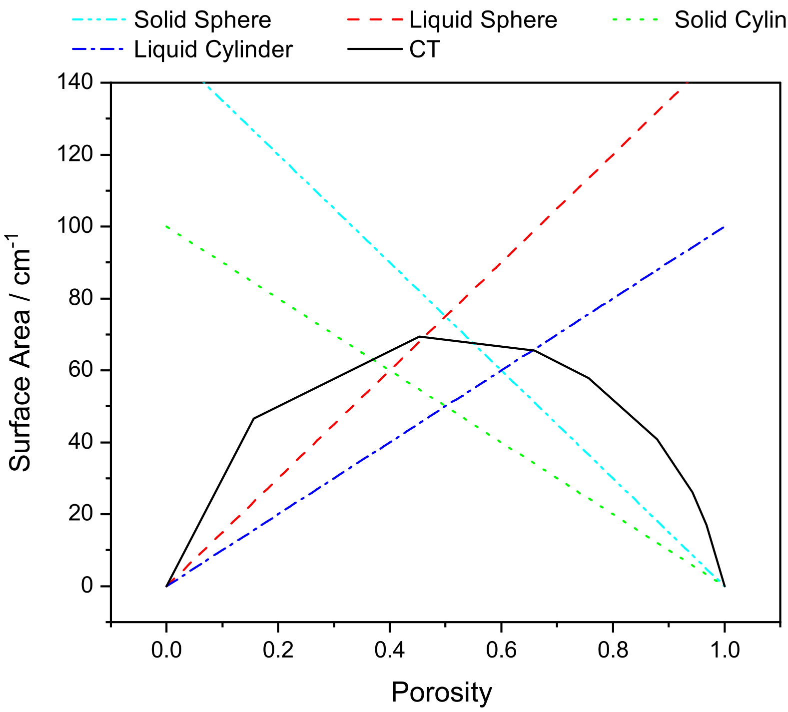

(A) Fixed r = 0.02 cm

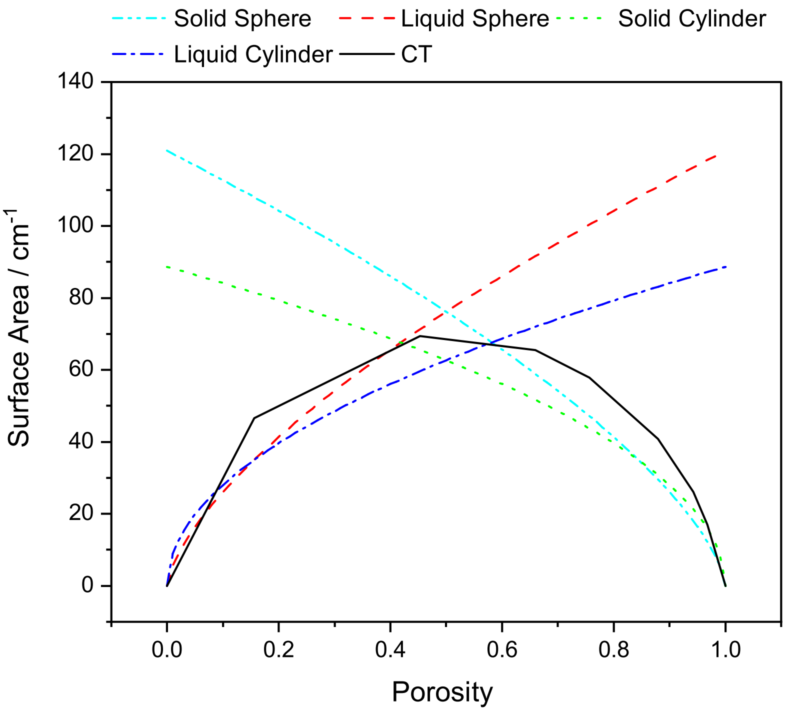

(B) Fixed d = 0.04 cm

FIGURE 8.2: A comparison of different methods for estimating a porous electrode surface area: A solid sphere in a liquid matrix (blue dot-dot-dashed line), a liquid sphere in a solid matrix (red dashed line), a solid cylinder in a liquid matrix (green dotted line), a liquid cylinder in a solid matrix (dark blue dot dashed line) and a CT estimate based on a scan of 80 ppi RVC (black solid line).

8.4 Results and Discussion

The COMSOL model described in Chapter 4 is configured for for the domains shown in Figure 8.3. Figure 1.5 (A) shows the undivided configuration which consists of three domains, a porous positive electrode, a free electrolyte domain and a porous negative electrode. The electrolyte flows in the y-direction from bottom to top. Figure 8.3 (B) shows the divided configuration. This is the same as the undivided configuration but with the free electrolyte domain replaced by a microporous separator domain.

8.4.1 Undivided cell

Initially, the cell in the model was set up with 3 mm RVC domains at the positive and negative electrodes, separated by a 6 mm electrolyte domain. The total gap between current collectors was 12 mm. For each grade of RVC described, an applied current density of 20, 30 and 50 mA cm^{-2} was applied to the model at the positive current collector boundary for a duration of 1 hour. A discharge step was then simulated with the same applied current density until the cell voltage dropped to 1.3 V.

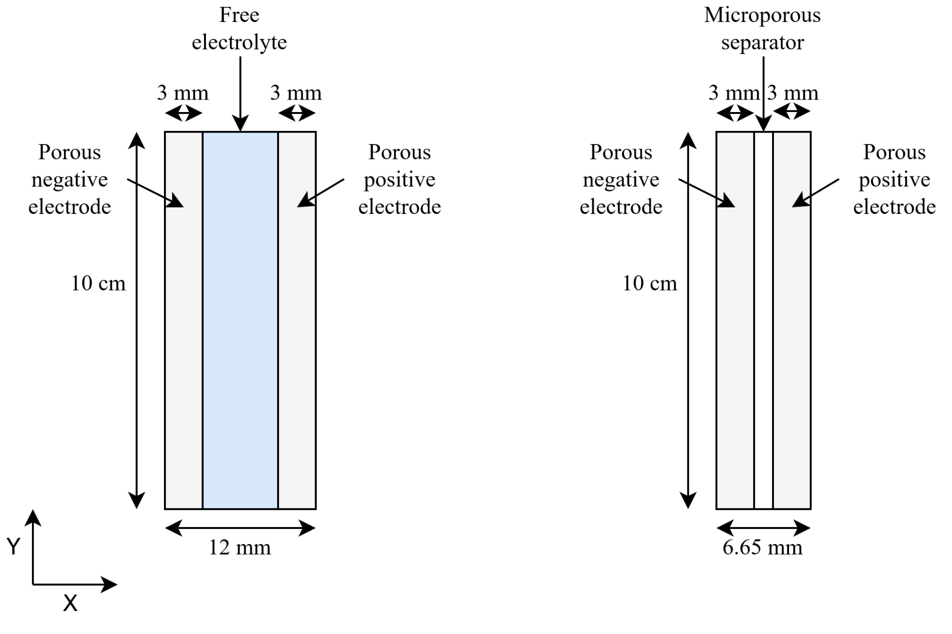

(A) Undivided with free electrolyte domain.

(B) Divided by a microporous separator.

FIGURE 8.3: Schematic showing the geometries used to model the SLFB with porous electrodes.

A value of 1.3 V was chosen as the discharge cut-off voltage because, after this point, the cell potential drops very sharply. While a lower cut-off voltage does not change the discharge time significantly, it added a significant amount of computational time due to the very short time-stepping required to calculate the period of rapid potential change. For brevity, general trends from the simulation results are discussed using the 10 ppi case as a representative example. Other grades of RVC are included where relevant comparisons are made.

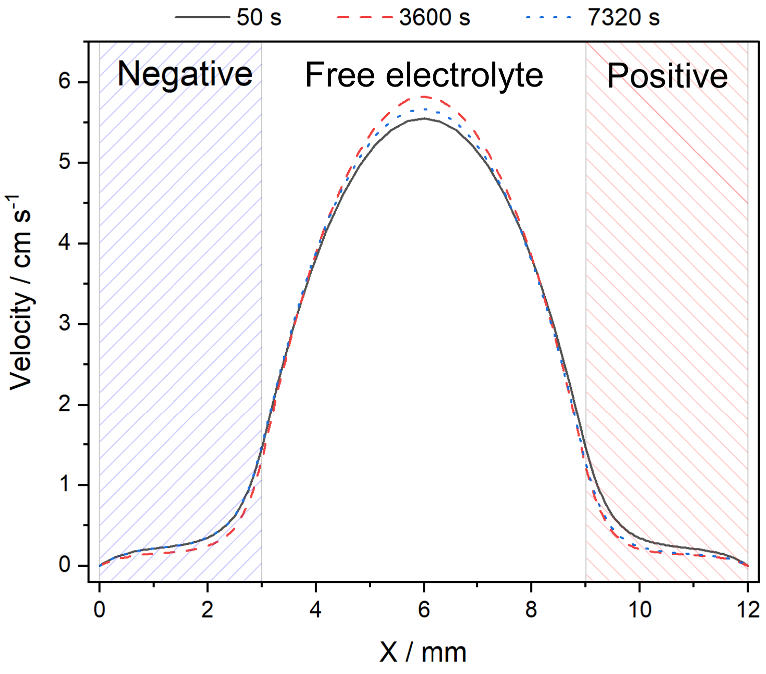

FIGURE 8.4: Simulated velocity profile across the mid-height of the electrodes of the undivided cell using 10 ppi RVC and an applied current density of 20 mA cm^{-2} at time=50 s(solid black line), time=3600 s (red dashed line) and time=7320 s (blue dotted line). The negative (left, blue) and positive (right, red) electrodes domains are highlighted.

Figure 8.4 shows the velocity profile across the modelled cell, where the 0-3 mm corresponds to the negative electrode domain, 3-9 mm corresponds to the electrolyte domain and 8-12 mm corresponds to the positive electrode domain. The three simulated velocity profiles shown correspond to just after the start of the first charge (t = 50 s), the end of the first charge period (t = 3600 s) and the end of the first discharge period (t = 7320 s). In this configuration, as seen in Figure 8.4, the simulated electrolyte velocity is considerably lower in the porous electrode domains than in the free electrolyte domain, even at initial conditions and for the RVC grade with the largest pore size (10 ppi). It can be seen that by the end of the first simulated charge period, the velocity within both positive and negative electrode domains decreases, corresponding to the increase in tortuosity caused by the build-up of deposits. By the end of the first simulated discharge period, the velocity profile in the negative electrode domain is broadly similar to that of the starting state, while the velocity in the positive electrode domain remains lower than the starting state, indicating a build-up of insoluble leady oxides. Figure 8.4 shows that after the first charge period applied to the model, when the velocity distribution changes by a similar magnitude, the velocity in the positive electrode domain remains very low during the remaining cycles, irrespective of SoC. However, in the negative electrode domain, the velocity alternates between its initial value and a lower rate at the end of discharge. This is due to the side reaction at the positive electrode meaning solid PbO remains even after discharge. Therefore, the permeability of the positive electrode domain remains higher than that of the negative electrode domain, which returns to close to its initial value after discharge. The peak velocity in the middle of the electrolyte domain increases as deposits are built up within the electrodes during the simulation. More electrolyte is forced through the lower resistance, free electrolyte domain.

The simulated current density in the porous electrode domains varied spatially in both x and y directions. Figure 8.5 shows the simulated current distribution in the x-direction at regular intervals during each charge and discharge. The first charge is from 0-3600 s, the first discharge from 3720-7320 s, the second charge from 7440-10740 s and the second discharge from 11160-14760 s. For each grade of RVC and at all simulated current densities, the current was initially highest near the current collector boundaries. As the model was charged, the current density became more evenly distributed in the x-direction.

In this configuration, the current density was highest at the bottom of both electrode domains, near the inlet throughout both charge and discharge. Figure 8.6 shows the current distribution in the y-direction at the midpoint of both porous electrode domains. There was a substantial (between 12 and 55 $\mathrm{mA\,cm^{-3}}$ increase in simulated current density in both electrodes in the closest 1 cm to the inlet.

As such, with continued charging in the simulation, the higher rate of deposition reduced the porosity near the inlet. The electrolyte flow was therefore further diverted around the electrode domains. As shown in Figure 8.7, which shows the simulated electrolyte

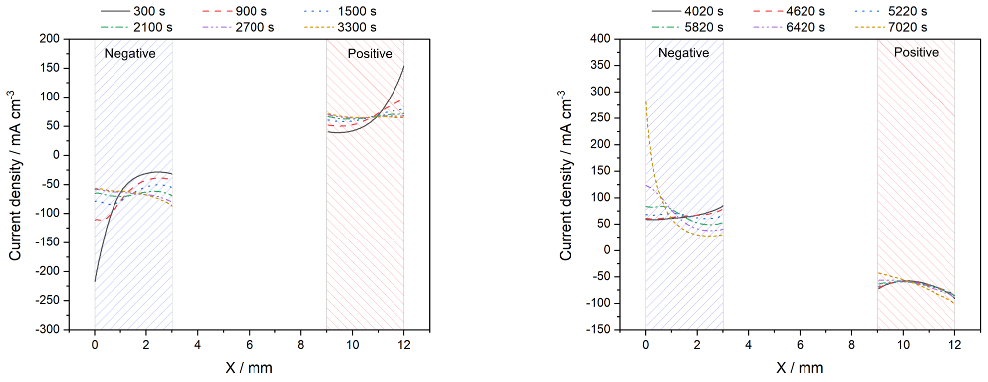

(A) Charge 1 (B) Discharge 1

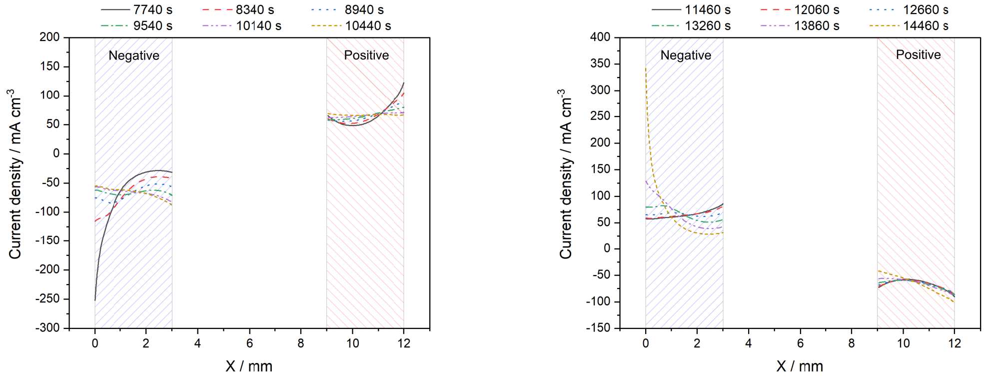

(C) Charge 2 (D) Discharge 2

FIGURE 8.5: Simulated current distribution in the x-direction at the mid height of the electrodes for the undivided configuration of the 10 ppi electrodes with an applied current density of 20 mA cm^{-2}. The negative (left, blue) and positive (right, red) electrodes domains are highlighted.

velocity distribution in the y-direction with the midpoints of both electrode domains, the electrolyte velocity distribution is uneven in the y-direction as the charge cycle continues. Throughout cycling, the simulated electrolyte velocity decreases sharply in the first few cm of the electrodes. By the end of the first charge, the flow in the top 6 cm of both electrode domains drops to below 2 mm s^{-1}, less than 10 % of the bulk velocity. Figure 8.8 shows the simulated concentration distribution after 3550 s, shortly before the end of the first charge of the simulation. Here it is seen that with the reduced electrolyte flow, the Pb^{2+} concentration within the electrode domains was not readily replenished. Near the outlet, the Pb^{2+} concentration in both electrode domainss drops to below 0.1 mol dm^{-3}.

Figure 8.9 shows the concentration distribution across the model at the midpoint of the electrode domains at varying times and current densities for each RVC grade. At higher rates of charge and grades of RVC with a larger number of pores, the simulated concentration gradients are larger and for all models at 50 mA cm^{-2} near end of charge,

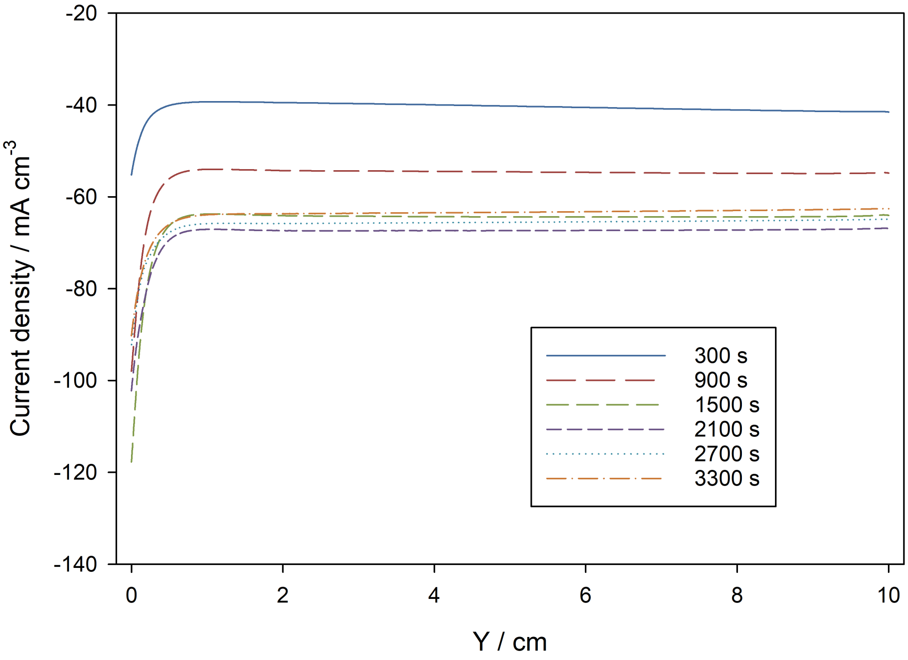

(A) Negative electrode

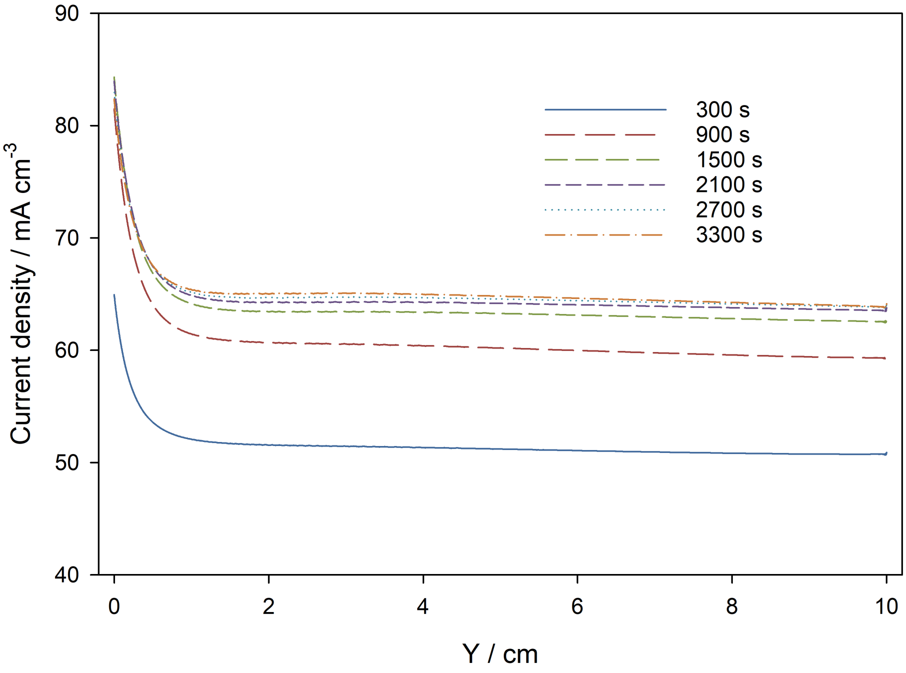

(B) Positive electrode

FIGURE 8.6: Simulated current distribution in the y-direction taken as a slice at the midpoint of the electrode domains for the 10 ppi electrodes. y=0 is at the inlet at the bottom of the cell. In both electrodes there is a significantly increased current density in the first 1 cm of the domain. Current density varies with time as the current is not even in the x-direction.

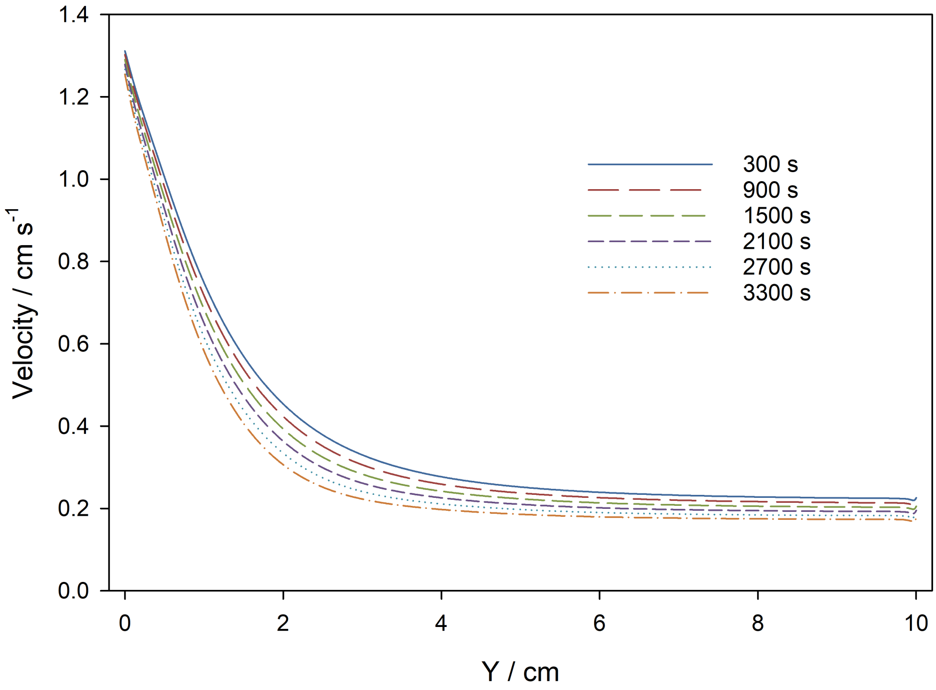

(A) Negative electrode

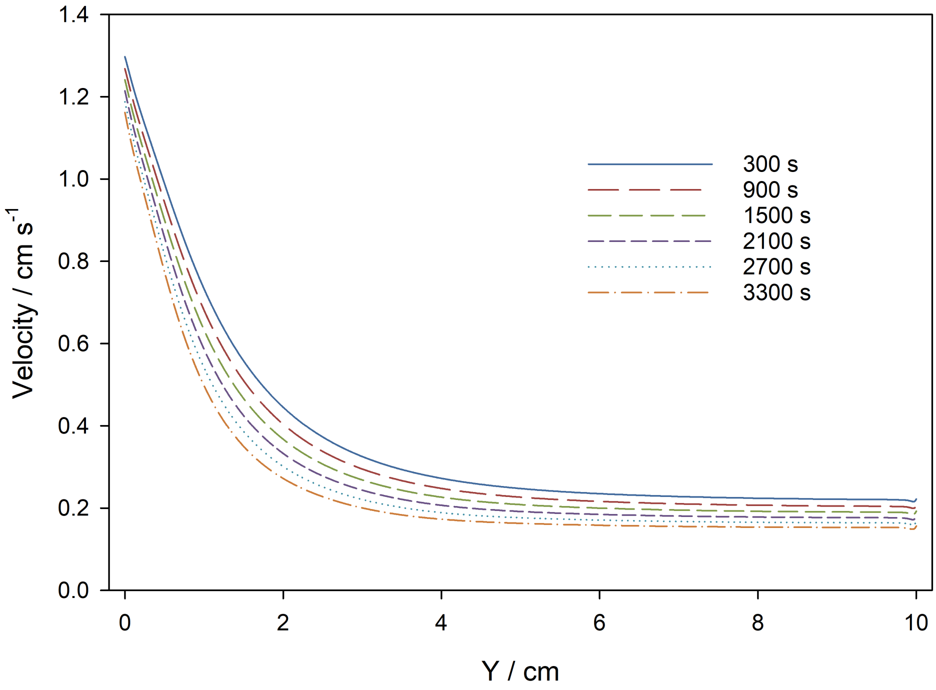

(B) Positive electrode

FIGURE 8.7: Simulated velocity distribution in the y-direction at the midpoint of the 10 ppi electrodes. The velocity begins at over 1 cm s^{-1} near the inlet in both electrodes, but rapidly reduces with increased distance from the inlet. The change in velocity levels off after approximately 4 cm and remains relatively constant between 1.5 and 3 mm s^{-1} in both electrodes.

the Pb^{2+} concentration drops to below 0.1 mol dm^{-3} compared to a bulk concentration of 0.22 mol dm^{-3}, see Figure 8.5. This indicates that the flow of electrolyte and diffusion of Pb^{2+} is inadequate to maintain a high current within the electrodes near the current collector boundary when lead utilisation in the bulk electrolyte is high. The reduced Pb^{2+} concentration leads to a higher overpotential required to maintain a current density and hence in areas with a lower Pb^{2+} concentration, the simulated current density is decreased. A higher current density is therefore seen close to the boundary with the bulk electrolyte domain. In physical cells, this may lead to Pb being deposited at the interface between the porous electrode domain and the electrolyte domain, as is described by Iacovangelo and Will during zinc deposition on porous carbon electrodes [193], negating the advantage of a lower local current density from a porous electrode.

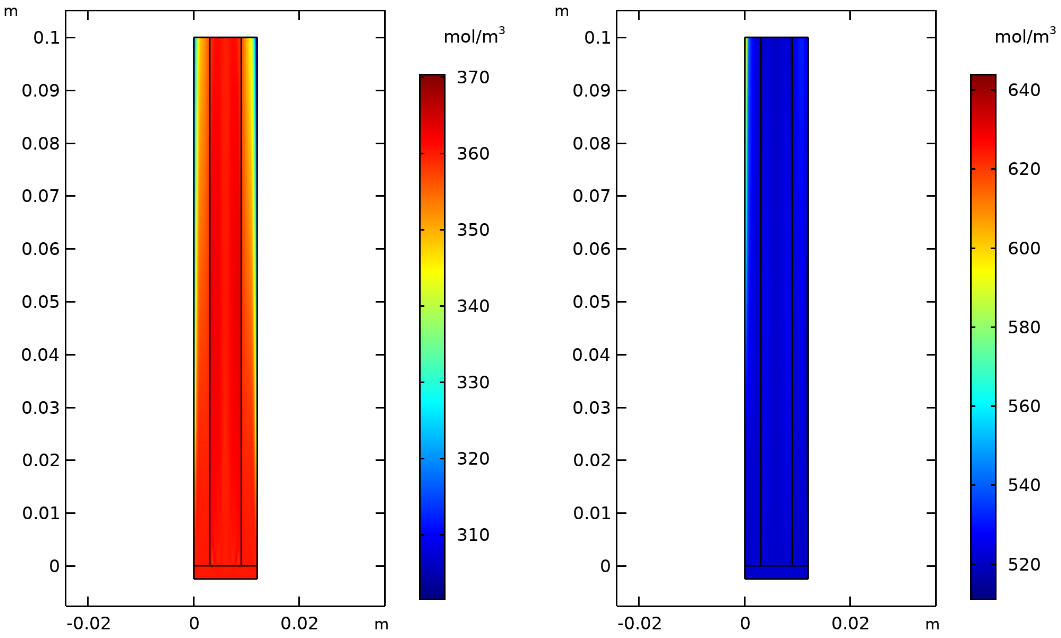

(A) Charge 1 (B) Discharge 1

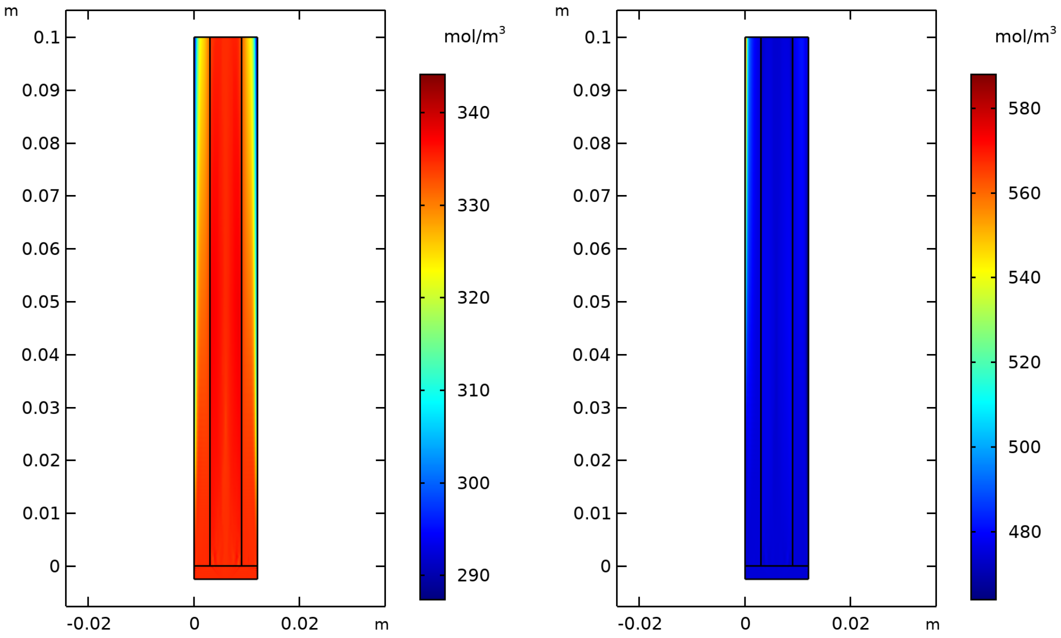

(C) Charge 2 (D) Discharge 2

FIGURE 8.8: Simulated Pb^{2+} concentration distribution near the end of the first charge for the 50 mA cm^{-2} cell using 10 ppi electrodes. The entire simulated domain (x-y plane) is shown. Red shows a higher concentration and blue shows a low concentration.

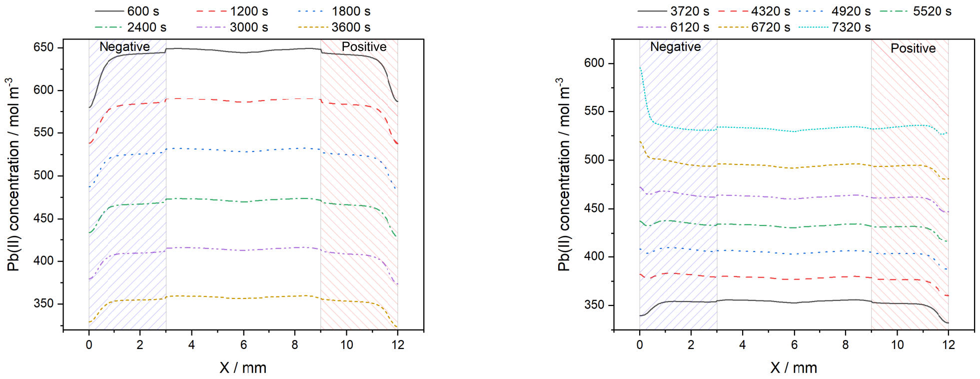

(A) Charge 1 (B) Discharge 1

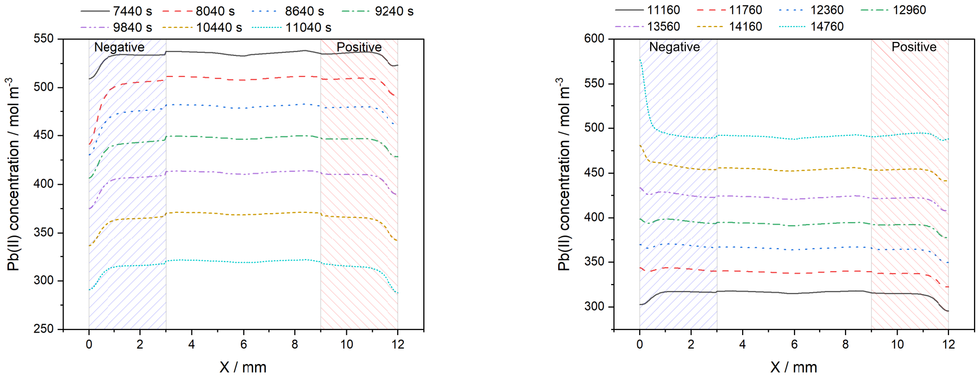

(C) Charge 2 (D) Discharge 2

FIGURE 8.9: Simulated distribution of Pb^{2+} concentration in the x-direction at the mid height of the electrodes for the undivided configuration of the 10 ppi electrodes with an applied current density of 20 mA cm^{-2}. The negative (left, blue) and positive (right, red) electrodes domains are highlighted.

8.4.2 Divided cell

To encourage a higher flow within the electrode domains and to overcome this reduction in Pb^{2+} concentration, the free electrolyte domain was removed from the model. Clearly, the electrodes cannot be touching, and in a real cell, dendrites are common and can grow between the electrodes [5]. Hence, a non-conducting porous separator domain was placed between the electrode domains to prevent short circuiting, but to allow the transfer of ions. Polyethylene microporous separators are commonly used in Zn-Br RFBs [194].

The same 1 hour charge cycle was applied to this divided model, with 20, 30 and 50 mA cm^{-2} applied to each grade of RVC. Figure 8.11 shows the current distribution in the x-direction for the divided model. The distribution of current within the electrode domains is very similar to that in the undivided model. The simulated current density starts off highest closest to the current collector at the start of charge. By the end of the 1 hour charge step in the simulation, while there is a slight increase in current at the outer edge of both electrode domains, the current distribution is far more even. The current density near the inlet is also substantially less pronounced. The current density averaged across the inlet is approximately 71 mA cm^{-3} at the positive electrode and 69 mA cm^{-3} in the negative electrode, compared to the average in the electrode domains of 67 mA cm^{-3}. Figure 8.10 shows that while there is some variation in simulated current density vs y, which is to be expected due to the increased concentration overpotential with increased distance from the inlet, there is not the sharp increase near the inlet as seen with the undivided model.

As the electrolyte is forced through the electrode domains, the concentration of soluble species remains far more constant. There is also a virtually flat concentration profile in the x-direction other than close to the separator boundary. These effects are in agreement with work by Masliy et al. who describe the expected current density distribution for a generalised redox reaction in porous electrodes [195]. In the negative electrode domain, there is a decrease in both Pb^{2+} and H^+ concentration as the separator boundary is approached during charge, while in the positive electrode domain the concentration of both species increases. The opposite is true during discharge.

Comparing different grades of RVC in Figure 8.13, there is little difference in the current distribution of the divided models. However, in general, the grades of RVC with a larger pore size gave a more even simulated current distribution in the x-direction. During the charge step of the simulations, the current distribution initially changes rapidly. However, with further charging, the simulated current distribution stabilises. When the model is run at 20 mA cm^{-2}, this occurs after approximately 2700 s, at 30 mA cm^{-2} by 2100 s, and at 50 mA cm^{-2} by 1500 s. At 50 mA cm^{-2}, this stable current distribution varies from circa 0.16 A cm^{-3} at the current collector to 0.13 A cm^{-3} at its lowest near the centre and 0.34 A cm^{-3} near the membrane in the negative electrode domain at 100 ppi. In the negative electrode domain at 10 ppi, simulated current density varies from 0.14 A cm^{-3} to 0.15 A cm^{-3} to 0.30 A cm^{-3}. A similar trend is seen in the positive electrode domains.

The most striking difference between simulations using different grades of RVC is the overpotential. This is to be expected, as while the starting porosity is roughly equivalent across the different grades, the surface area varies significantly. A higher

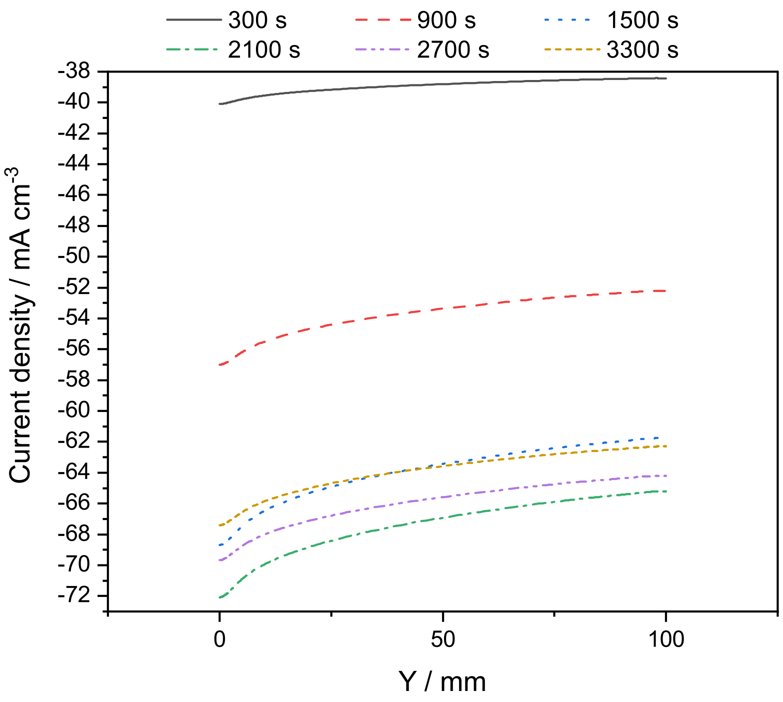

(A) Negative electrode

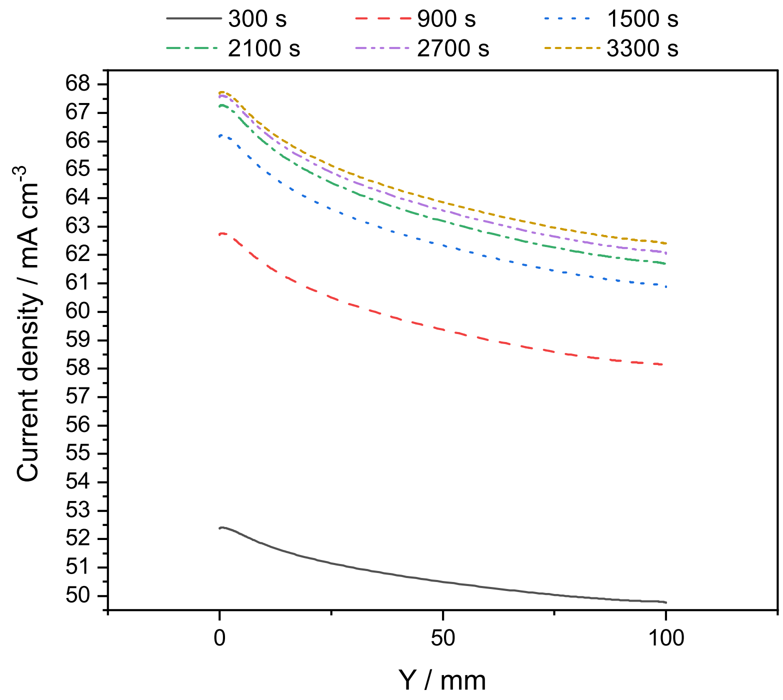

(B) Positive electrode

FIGURE 8.10: Simulated current density distribution in the y-direction at the midpoint of the electrodes of the divided cell during the first charge.

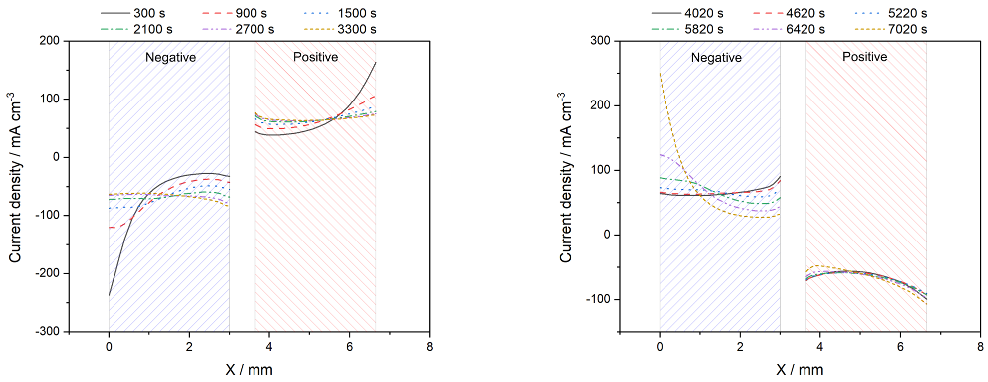

(A) Charge 1 (B) Discharge 1

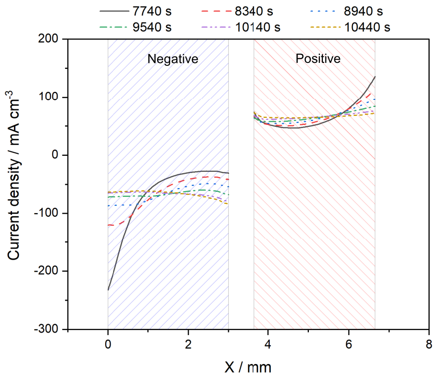

(C) Charge 2

FIGURE 8.11: Simulated current distribution in the x-direction at the mid height of the electrodes for the divided configuration of the 10 ppi electrodes with an applied current density of 20 mA cm^{-2}. The negative (left, blue) and positive (right, red) electrodes domains are highlighted.

surface area leads to a lower local current density and by inspecting the Butler-Volmer equations, Equation 2.9, it can be determined that this leads to a lower overpotential. Accordingly, the 100 ppi electrode domains, which have smaller pores and hence a larger surface area, have a greatly reduced overpotential during both charge and discharge steps in the simulations than the lower ppi electrodes. When compared to the 10 ppi electrodes, the simulated overpotential is reduced by approximately 100 mV.

Current density appears to have a much greater impact on variation in current distribution in the simulations. While the general trend of decreasing current near the current collectors and increasing near the membrane boundary is true for all the simulated applied current densities, at 20 mA cm^{-2} in the 10 ppi electrode domains, the current remains approximately even throughout the electrode once it has settled. However, as the current density is increased, the current near the separator boundary increases

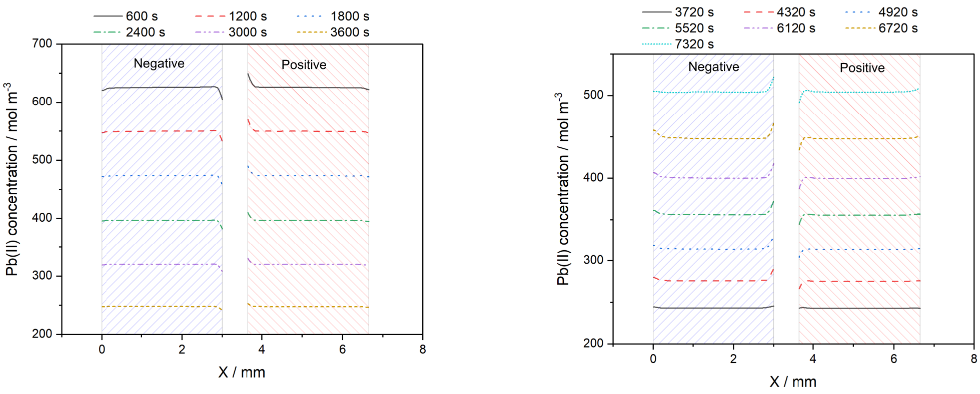

(A) Charge 1 (B) Discharge 1

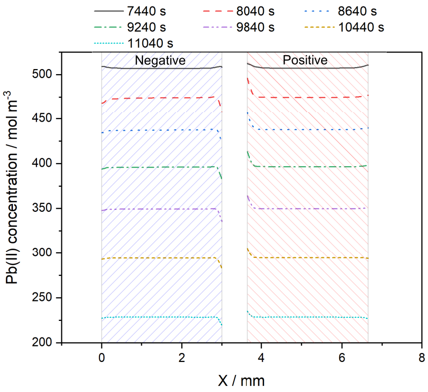

(C) Charge 2

FIGURE 8.12: Simulated Pb^{2+} concentration distribution in the x-direction at the mid height of the electrodes for the divided configuration of the 10 ppi electrodes with an applied current density of 20 mA cm^{-2}. The negative (left, blue) and positive (right, red) electrodes domains are highlighted.

more than in the remainder of the electrodes. This is true for both the positive and the negative electrode domains.

One method to decrease the variability in current density within the electrodes would be to combine grades of RVC to form a graduated electrode. A similar method is used with lithium ion batteries [196]. While it appears that there would be little benefit in this method at lower current densities, at higher currents, the region close to the separator boundary would benefit from a relative reduction in current density. This could be achieved by using a larger pore size close to the centre of the cell than for the bulk electrode. Only a small region would require this increased pore size, allowing the remainder of the electrode to take advantage of the lower overpotential and hence increased efficiency gained from using RVC with smaller pores.

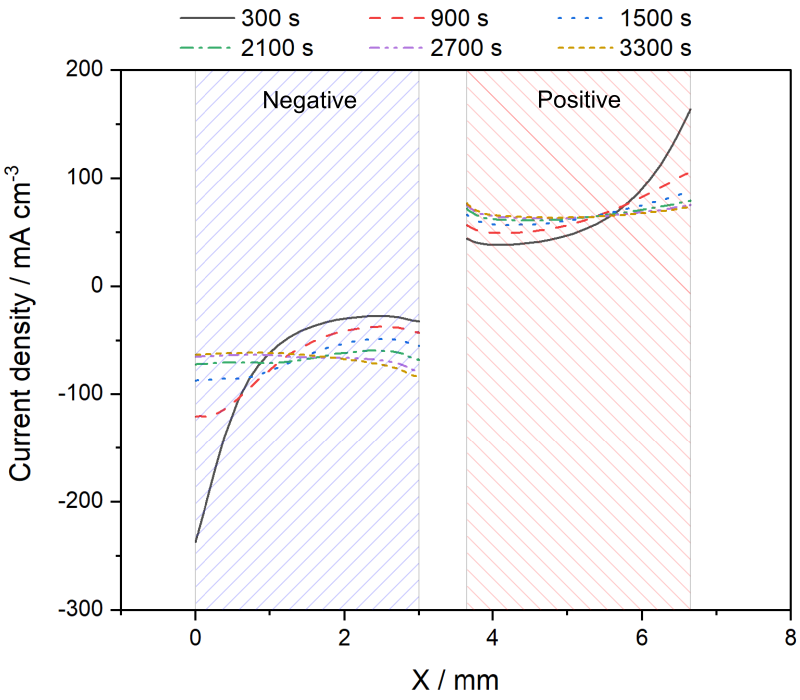

(A) 10 ppi

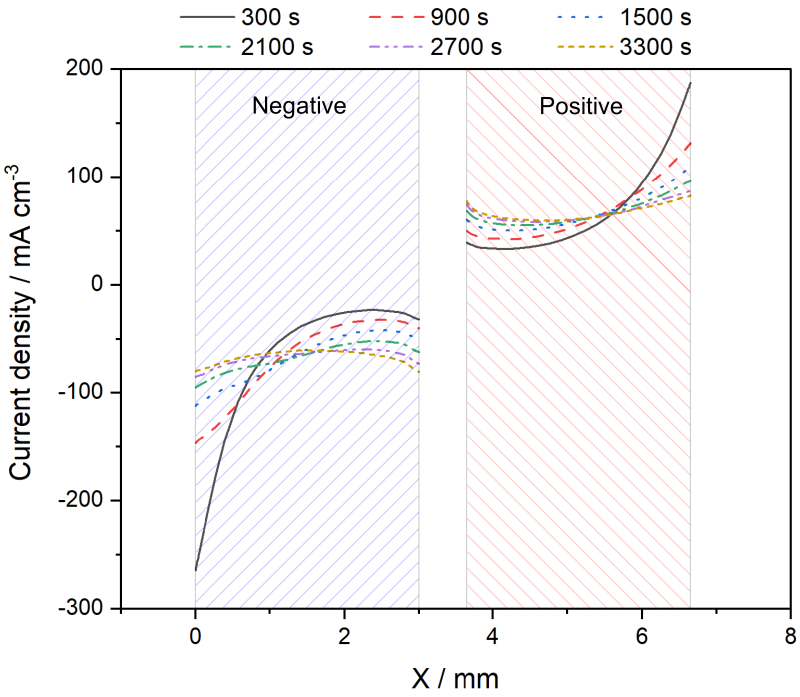

(B) 100 ppi

FIGURE 8.13: Simulated current distribution in the x-direction at the mid height of the electrodes for the divided configuration with an applied current density of 20 mA cm^{-2}. The negative (left, blue) and positive (right, red) electrodes domains are highlighted.

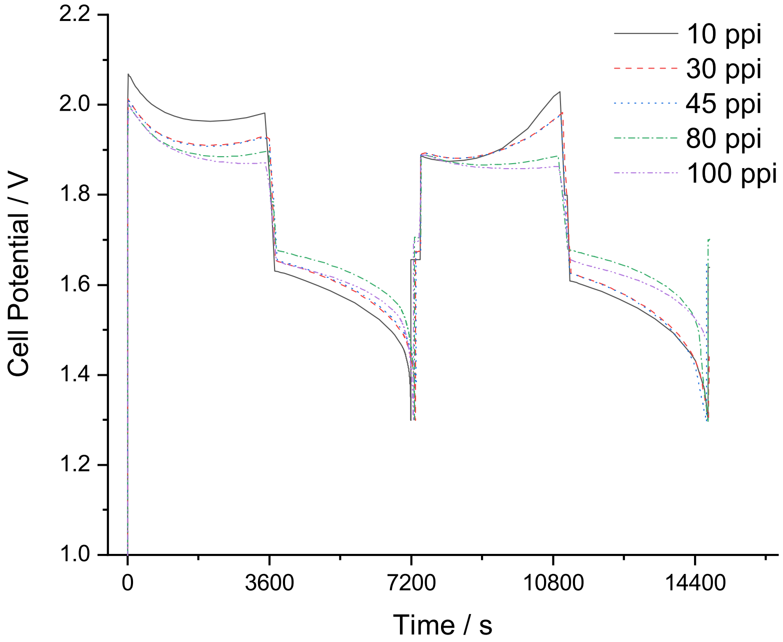

FIGURE 8.14: Simulated cell potential vs time for different grades of RVC with an applied current density of 20 mA cm^{-2}.

8.5 Validation

A comparison between experimental and simulated cell potential of a cell cycled at 20 mA cm^{-2}using 80 ppi RVC electrodes is shown in Figure 8.15. The experimental cell described in Section 3.2 was used. A 400 cm^{-3} volume of electrolyte containing 700 mol m^{-3} Pb^{2+} and 1000 mol m^{-3} H^+ was circulated through the cell. The model setup was modified to match the dimensions of the experimental cell. The first cycle is omitted. The simulated potential closely matches the experimental at the start of both the charge and discharge steps. At the end of the charge, the experimental cell potential rises to approximately 2.05 V. However, the simulated voltage remains at approximately 1.85 V. This suggests that the kinetics of the reactions at the positive electrode could be improved and the side reaction in this model is simplified. Further work is required to fully understand this reaction. During discharge, while the coulombic efficiency of the experimental cell is lower, the cell potential of the simulated cell is closely matched to that of the experimental cell. Verde at al. [93] show that the particle morphology, size and phase (α or β) of the deposited PbO_2 affect when the potential rises during charging and substantially affect the coulombic efficiency. These PbO_2 properties are not included in this model and could partially or entirely account for the differences seen between the simulated and experimental curves.

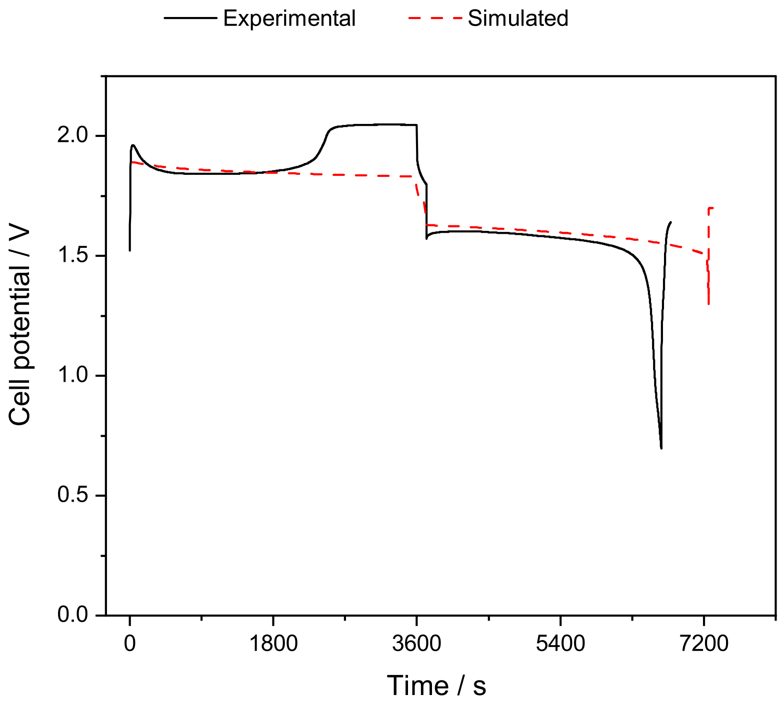

FIGURE 8.15: Cell potential from the experimental and simulated 10 cm^{-2} cells. The cells were divided and used 80 ppi RVC electrodes.

Future work to provide further validation could include μ-CT imaging deposits from a physical cell on RVC electrodes at various states of charge. The flow of electrolyte could also be validated by injecting dye into the electrolyte of a transparent cell at various states of charge.

8.6 Conclusions

Computed tomography images of plain RVC were manipulated using a voxel dilation technique to simulate the properties of RVC electrodes with deposited Pb and PbO_2 for use in the SLFB. Open source software OpenImpala was used to convert these manipulated datasets into homogeneous domains with standardised parameters for porosity, tortuosity and hydraulic permeability. These parameters were then used as properties for homogeneous RVC electrode domains in a novel two-dimensional transient, numerical model for investigating three-dimensional electrodes in the soluble lead flow battery.

The model highlights the benefits of using reticulated vitreous carbon as an electrode material at both electrodes. The model highlights the issues with using thin layers of RVC divided by a region of free electrolyte as has been used in previous experimental studies of RVC in the SLFB. Even with the high permeability of RVC, there is a significant reduction in simulated electrolyte velocity within the electrodes. A high current density is predicted near the inlet which causes a build-up of deposit in this area, further diverting the electrolyte out of the electrode domains. Forcing the electrolyte through the RVC electrode domains by replacing the free electrolyte domain with a microporous separator domain significantly improved the simulated current distribution in the y-direction. The concentration distribution is also substantially smoother in both x and y directions.

The higher surface area of RVC with smaller pores leads to a reduction in simulated overpotential. Comparing the 100 ppi model with the 10 ppi RVC model, there is a reduction in overpotential of over 100 mV when cycled with a simulated current density of 50 mA cm^{-2}. While using a single grade of RVC for each electrode still gives an uneven current distribution, in future, by taking advantage of their different overpotentials, it may be possible to combine different grades of RVC to provide an optimal current distribution for a specific application.

The work in the chapter is validated by comparison to experimental results. A good agreement is seen between simulated and experimental results.

Chapter 9

Conclusions

Numerical modelling allows for the investigation of qualities which are difficult to measure, are time consuming or are expensive to investigate using physical experimentation. While no model of any nature is completely accurate, the trends and approximate values obtained from models are often useful. Validation against experimental work gives further confidence in the validity of the results.

A two-dimensional, transient model for the soluble lead flow battery has been developed based on conservation of mass, momentum, charge and energy, combined with expressions for kinetics of electrode reactions. This model has been further developed to investigate specific aspects and configurations of the SLFB.

A moving mesh technique which allowed the simulation of the change in geometry due to the formation of the electrode deposits, Pb and PbO_2, at the electrode surfaces. The model captured the resulting increase in thickness of the solid domains and decrease of in thickness of the liquid electrolyte domain. While an increase in resistance of the solid domain was observed, the reduction in resistance of the less conductive electrolyte domain was more significant leading to a reduction in overall resistance of approximately one third when compared to static mesh simulations. Furthermore, at high states of charge, there is a substantial change in the flow rate of the electrolyte, which shows advanced pumping control may be necessary if an even velocity over the electrode surfaces is desired. The moving mesh technique is also directly applicable to any other flow battery technologies in which one or both electrode reactions contain a change of phase between liquid and solid. A notable example is the zinc electrode in the Zn-Br battery.

The electrolyte conductivity was shown to have a significant impact on predicting the potential drop across the cell and hence on the predicted voltage efficiencies. However, the Nernst-Einstein method typically used to predict the conductivity of the electrolyte was shown to be highly inaccurate, especially at low states of charge.

An adapted Debye-Huckel method of calculating the electrolyte conductivity was employed. While strictly only applicable to low concentrations, a good match was found with experimental data from the literature was found at all concentrations.

The updated conductivity model also allowed for more accurate modelling of the ion-exchange membranes and porous separators in the SLFB. A wide range of parameters, including applied current density, separator geometry and porosity, and the fixed charge distribution within ion exchange membranes were varied and used as inputs for simulations in a simplified steady state, one-dimensional model of the SLFB.

Computed tomography images of reticulated vitreous carbon electrodes were manipulated using a voxel dilation technique to simulate different states of charge of porous electrode in the SLFB. Open-source software OpenImpala was used to sproduce macro-homogeneous parameters from these datasets. These parameters were used as inputs in porous electrode domainsin a two-dimensional transient model.

The model highlights several issues with using RVC electrodes separated by a free electrolyte domain, as has been previously used experimentally in the literature. It predicts uneven current distribution in both x- and y- directions. A high current density at the inlet caused a buildup of deposit diverting the flow around the outside of the porous electrodes. Replacing the free electrolyte domain with a porous separator led to a far more even current distribution in both x- and y- directions within the porous electrode domains. The higher surface area of RVC electrode with smaller pores led to a reduction in overpotential. At 50 mA cm^{-3}, 100 ppi electrodes had an overpotential of 100 mV less than 10 ppi electrodes.

Chapter 10

Future work

While there are still numerous challenges to overcome for optimal operation of the soluble lead flow battery, the work presented in this thesis has shown that the soluble lead flow battery

To continue the work presented in this thesis, the recommended next steps are in the following areas:

- **Integrating with lead acid battery recycling** Work presented in the literature has shown that the SLFB can operate and may actually benefit from operating using electrolyte recovered from spent lead acid batteries. Chapter A described how SFLB electrolyte could be produced as a standard part of electrochemical secondary lead recovery. Significant further work is required to develop this system. In the interim, material from the existing process can be used to produce the electrolyte with and unused parts of the battery recirculated into the recycling stream.
- **Improving the moving mesh** Further work to develop the model to capture the effects of uneven current distribution on the deposit geometry. Combining this with modelling the flow of electrolyte through a three dimensional domain would allow for an interesting topology optimisation of the flow circuit and electrodes.
- **Experimental work validating choice of membrane and additives** The results presented in Chapter 7 provide useful information for making choices regarding membrane choice for specific additive parameters. However, experimental work detailing the effectiveness of specific membranes with specific additives is lacking.

A study detailing the effect of additive crossover during operation of the SLFB would be a valuable addition to the literature. Preliminary work showing the effectiveness of in-situ CT-scanning is shown in Section 5.8. This technique is able to image the deposits to give an indication of failure mechanisms, but it would also be a useful validation technique for changing geometry on both planar and porous/structured electrodes.

- **Graduated RVC electrodes** The overpotential in the RVC electrodes described in Chapter 8 varied significantly between different grades of RVC. By intentionally varying the pore size in the electrodes and their dimensions, a bespoke design for each electrode could be designed for optimal current distribution.
- **Gold electrodes** Initial work showing gold coated electrodes may improve the cycle life in static electrolyte cells is presented in Appendix D. Building on this work, a systematic study to determine the best method of gold plating, optimal mass loading and the mechanism by which gold extends the cycle life would be beneficial to the field.
- **Scale up** Scaling up from a lab scale system to a commercially viable system requires consideration of many aspects beyond the stack, including power electronics, pumping requirements, material use, safety systems and a battery management system, among other aspects. However, the tools and models developed in this thesis could be modified to provide information on the operation of individual cells when combined into a multi-cell stack and when the electrode dimensions are dramatically increased.
- **Economic considerations** A particular consideration of the SLFB is that power and energy are only partially decoupled, so the cost of electrode materials must be considered for the post per kWh and per kW. Using gold or RVC electrodes may improve the performance of the SLFB, but it is critical that these improvements outweigh the added costs of these materials. A parameterised economic model to allow for cost-benefit analysis of each design choice would be a very useful tool.

Appendix A

Justification of the soluble lead flow battery based on an existing lead supply chain

A.1 Lead Recycling

The majority of secondary lead production is done by smelting. In smelting, a reducing agent and heat are applied to an ore or impure waste metal stream to remove impurities through flue gases and the production of slag [197]. This process is a highly mature technology and, with the addition of desulfurisation processes can be designed to produce low emissions. Smelting, however, requires high temperatures to operate and is, therefore, a highly energy-intensive process [53]. Heat is typically supplied using natural gas. As the price of gas per kWh is low, the cost of recovering lead using a thermal process is difficult to compete with. However, even with the higher cost of electricity when compared to gas, highly efficient electrochemical processes are emerging which may be able to compete.

In this chapter, H. J. Enthoven's Darley Dale smelter is used as a case study for conversion to an electrochemical secondary lead recovery method. Such a process would complement the development of the SLFB as a system with readily available recycled materials and a route for recycling at end of life.

A.1.1 Existing Process

An overview of the existing process at the Darley Dale smelter is described here. To recycle waste lead-acid batteries, they must first be broken up and separated into various streams for treatment. The sulfuric acid is first drained from the batteries. The remainder of the battery is then put through a battery breaker. From the output of the battery breaker, the paste containing lead oxides and lead sulfate is screened off. The polypropylene casing is floated off and the remaining metallics and waste plastic are recovered, dried and then fed into the required furnace.

A.1.1.1 Paste

This process focuses on the paste from the battery. The wet paste from the battery breaker is first dried via a two-stage process. The majority of the moisture is removed using a vacuum belt which reduces the paste to a 15 % wet paste. The remainder of the paste is recombined with the metallics and waste case and is dried using a rotary drier.

The dried material is fed into a reverberatory furnace which produces lead a high antimony and tin sinter and a sulfur-rich fume.

A.1.1.2 Sulfuric acid from lead-acid batteries

The sulfuric acid that comes directly from waste lead-acid batteries contains a high level of impurities and is at approximately 15 % concentration. In the existing process that is considered here, the waste sulfuric acid is combined with lime (CaO) to produce gypsum ($CaSO_4$). The gypsum is then washed with clean 50 % sulfuric acid to remove impurities. The impurity containing acidic liquid is then sent to the effluent treatment plant.

A.1.1.3 Effluent Treatment

Large quantities of water containing lead and other impurities are produced in the existing process. These materials must be reduced to far lower levels before the water is able to leave the site. Any acidic effluent must be neutralised.

A.2 Proposed Process

A process for electrochemically recovering lead while also providing a source of electrolyte is proposed to fit into the existing plant. Figure A.1 shows a brief overview of the existing process, the proposed process and how the two would be connected. The links between the two processes are shown by dashed arrows.

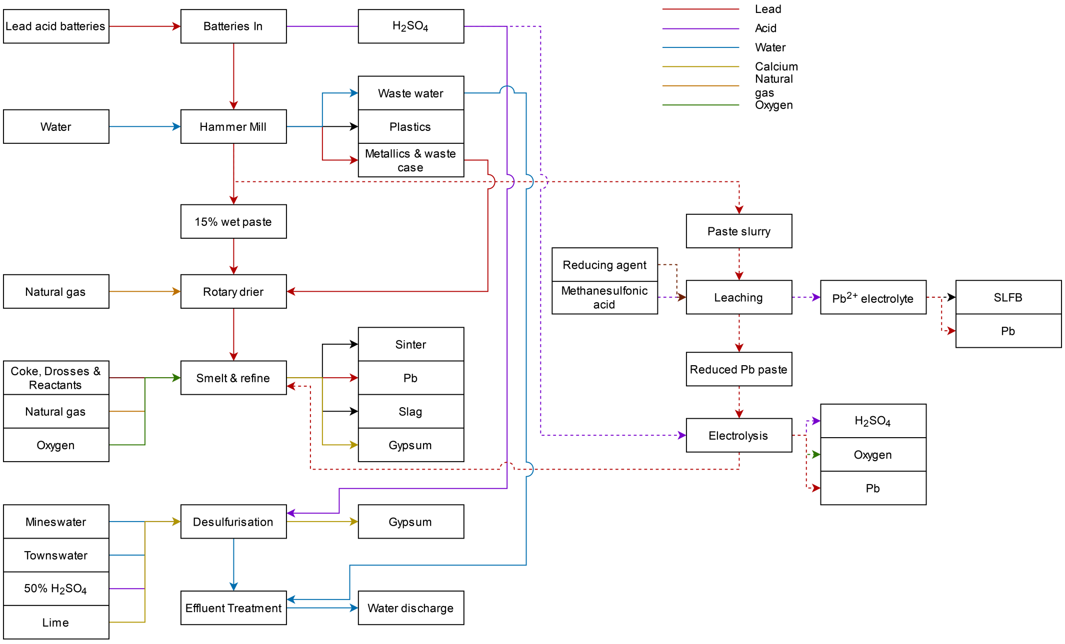

FIGURE A.1: Proposed process for electrochemically recovering lead from spent lead acid batteries.

A.3 Sulfate plant

The proposed process for dealing with the lead sulfate in the paste is based on the process described by Spijkerman and Groenen [74] which converts all lead compounds to lead sulfate before electrochemically recovering lead metal from a fluidised bed of the lead sulfate. The process is explained in more detail in Section 2.2.2. However, in the proposed process, there is no need to convert the lead oxides to lead sulfate. The entire paste is circulated as a slurry through the cell. The lead sulfate is converted to lead metal and is plated onto the lead particles that are fed into the system.

The sulfuric acid from the waste lead-acid batteries can also be added to the cathode side of this cell. The sulfuric acid would dissociate to sulfate ions and H^+ ions. At the cathode, the H^+ ions would be converted to H_2 and the sulfate ions would again pass across the membrane to form clean sulfuric acid on the anodic side.

A.4 Electrolytic Leaching

The use of MSA to leach lead from a source containing a mixture of lead in different oxidation states (such as recycled lead acid batteries) has already been established [198]. Other processes which use Pb^{2+} ions in methanesulfonic acid require a reducing agent to reduce the PbO_2 to Pb^{2+}. Often the reducing agent is hydrogen peroxide (H_2O_2). In this case, an equal molar quantity of H_2O_2 is required for the amount of Pb to be reduced. This process is a high-cost method of dealing with PbO_2 [71]. This proposed method of reducing PbO_2 to Pb^{2+} uses electrolytic leaching. By using a slurry electrode of PbO_2 in the paste within a methanesulfonic acid (MSA) electrolyte, the following electrode reaction is proposed as the cathodic reaction in an electrolytic cell.

$$PbO_2 + 4H^+ + 2e^- \rightleftharpoons Pb^{2+} + H_2O \tag{A.1}$$

An anodic chamber, separated from the cathodic chamber by a proton exchange membrane, would electrolyse water to produce oxygen gas:

$$H_2O \rightleftharpoons 2H^+ + 1/2O_2 + 2e^- \tag{A.2}$$

As the MSA is not consumed in the reaction, it can be recirculated, so only minimal top-up is required to replace the electrolyte lost during drag out or if degradation occurs.

A.5 Electroplating Lead

There is an established process for electrodepositing lead from a solution Pb^{2+} in MSA [111]. The following electrode reactions are proposed:

$$Pb^{2+} + 2e^- \rightleftharpoons Pb \tag{A.3}$$

$$H_2O \rightleftharpoons 2H^+ + \frac{1}{2}O_2 + 2e^- \tag{A.4}$$

These reactions would occur in a cell separated with a proton exchange membrane. Here, however, the positive reaction could be replaced by the SLFB positive electrode reaction, either permanently or as an addition which would allow the lead recover plant to operate as a battery when market conditions allowed. Building on this, the SLFB could be modified to produce removable Pb and PbO_2 electrodes to be sold or, again to be discharged as en extra revenue stream for the process.

An alternative option is, as a solution of Pb^{2+} in MSA has been made during the leaching process, were an electrochemical recovery process to replace traditional pyrometallurgical plants, this solution could be sold separately as an electrolyte for the SLFB at this point in the process.

A.6 Summary

A novel process for the recovery of Pb from waste lead-acid battery paste using electrochemical techniques has been proposed. This process builds upon work previously documented including electrodeposition of Pb from a Pb^{2+} solution in a methanesulfonic acid electrolyte and the direct recovery of Pb from a paste containing $PbSO_4$ using a slurry electrode. Further to this, a cell using another slurry electrode is proposed to electrochemically leach PbO_2 into methanesulfonic acid to form the Pb^{2+} electrolyte. The relevant electrochemical theory required to understand this process and the equations used to calculate its cost have been discussed. Costs of this process have been estimated using data from H J Enthoven's Darley Dale smelter. This has been compared to the costs of the existing processing route for the same materials. Based on these initial calculations, it is shown that the electrochemical technique may be competitive with the existing process

Appendix B

Adaptive mesh vs moving mesh

When the model geometry changes during a simulation, the mesh change to continue to represent the geometry accordingly. The mesh may maintain the number and general distribution of elements as it deforms, which is termed a moving mesh. Alternatively, as the geometry deforms, a new mesh can be generated to fit the new form, known as an adaptive mesh. It is also possible to set up an adaptive mesh to be refined in areas of interest as the simulation progresses.

In the case of the model presented in Chapter 5, the electrolyte domain to be meshed decreases in size as a charge is simulated. The domain then increases in size again when discharge is simulated. As such, the main benefit of an adaptive mesh compared to a moving mesh is anticipated to be a reduction in the required number of elements in the bulk electrolyte as the domain decreases in size. However, this must be offset against any time taken remeshing.

A preliminary comparison between a moving mesh and an adaptive mesh for this model were therefore made. The same setup as described in Section 5.5 The resulting meshes are shown in Figure B.1. It can be seen that while some remeshing has occurred, in the simulation using an adaptive mesh, the differences are modest. Comparing the maximum current density during the first charge cycle in each of the two methods, as was done for the mesh refinement studies, showed virtually no difference, with a maximum of 36.70 mA cm^{-2} for the moving mesh and 36.68 mA cm^{-2} for the adaptive mesh. Furthermore, the time taken for the adaptive mesh simulation to solve was over

75 minutes compared to 27 minutes for the moving mesh simulation. Hence the it was deemed more beneficial to use a moving mesh method.

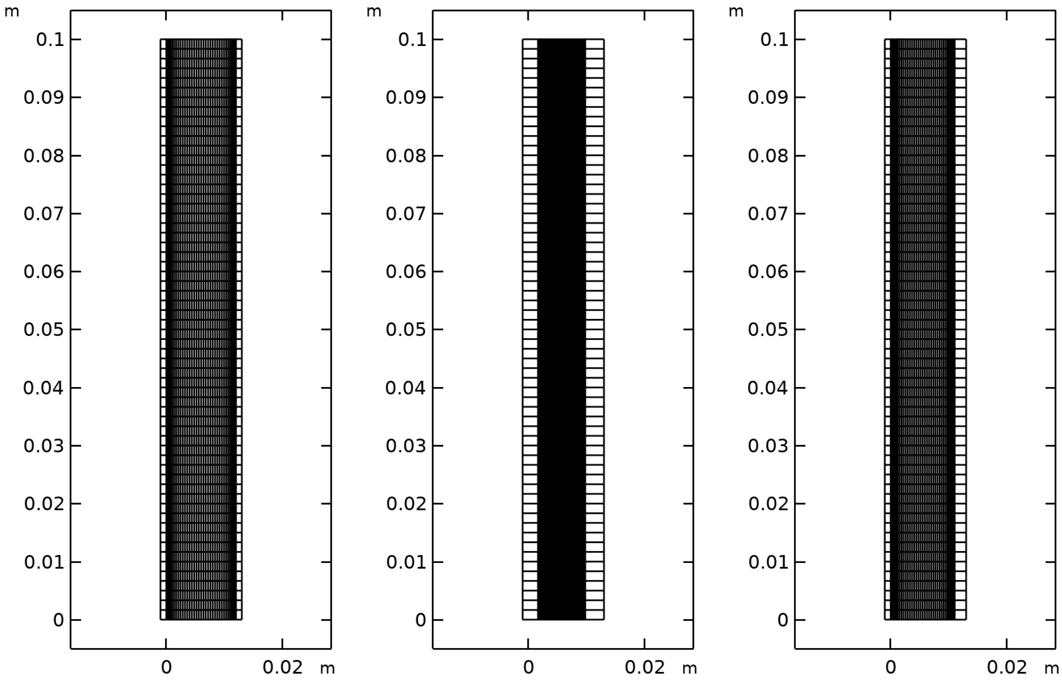

(A) Moving mesh t=0 (B) Moving mesh after first charge (C) Moving mesh after first discharge

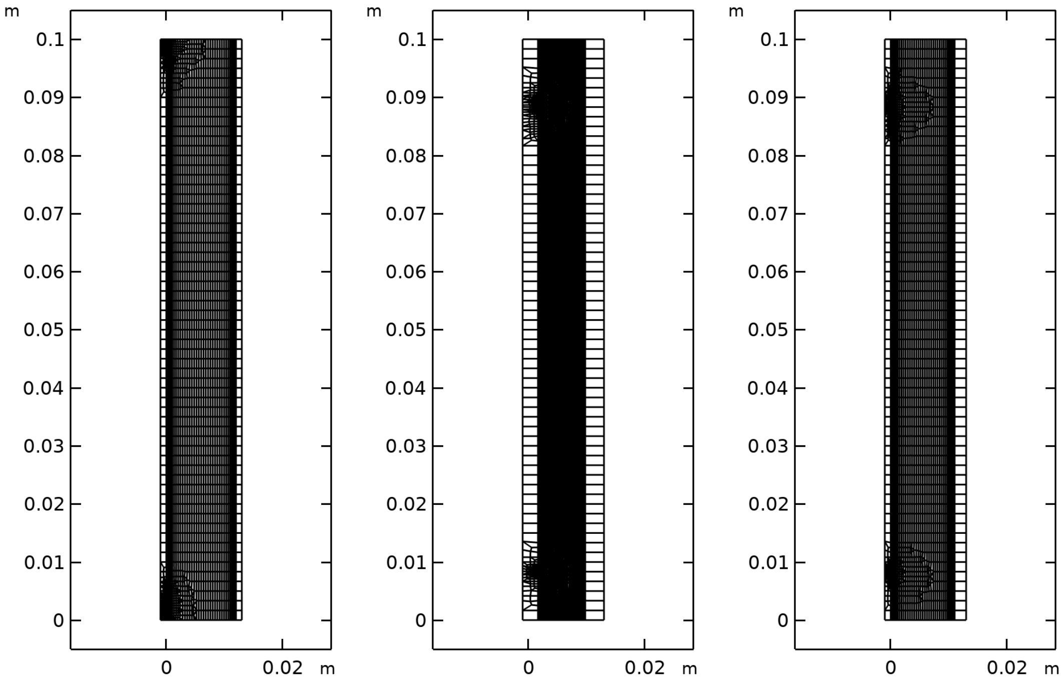

(D) Adaptive mesh t=0 (E) Adaptive mesh after first charge (F) Adaptive mesh after first discharge

FIGURE B.1: Comparison of meshes from simulations using a moving mesh and an adaptive mesh. The times shown are t=0, after a charge step and after a subsequent discharge step. The simulations ran for 24 hours at 20 mA cm^{-2}.

Appendix C

Mesh Sensitivity

The mesh sensitivity results using the method described in Chapter 4 are displayed here showing the maximum current density over the simulation and the computational time required for the simulation vs number, or scale of elements in each dimension/domain.

An example mesh is shown in Figure C.1. The horizontal and vertical elements are shown at the full scale. In the zoomed region, the boundary layer elements are clearer. In the mesh sensitivity the number of boundary layer elements and the growth factor (scale) of the elements is used. The growth factor is the amount by which the boundary layer elements increase in thickness with perpendicular distance from the boundary.

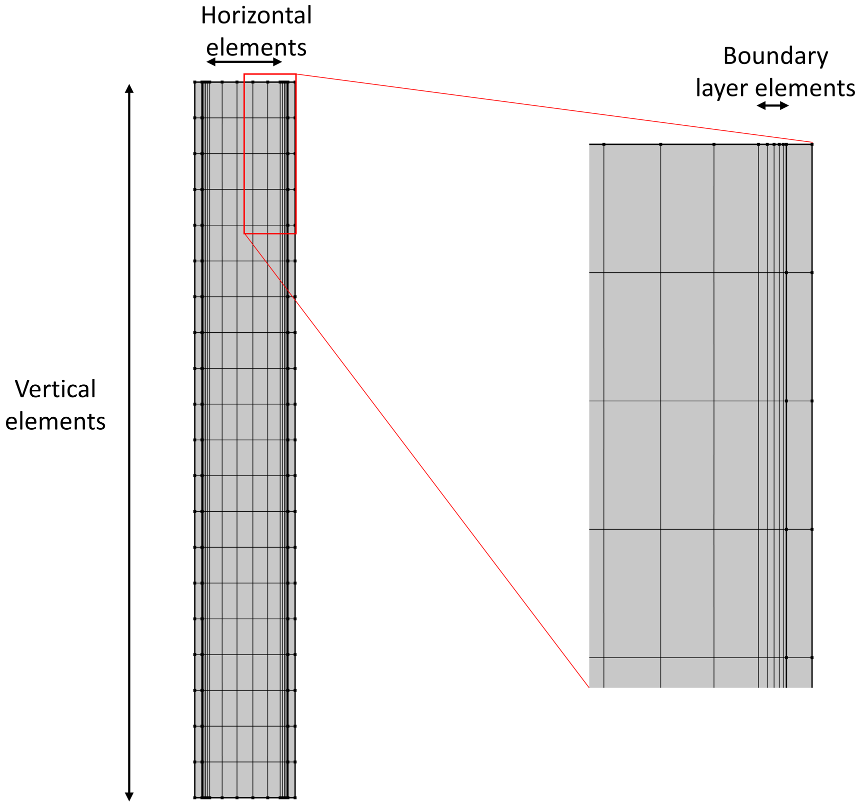

FIGURE C.1: An example mesh showing elements in each dimension. A full mesh is shown on the left and a zoomed region to highlight the boundary layer elements is shown on the right. In this example, there are 5 horizontal elements, 20 vertical elements, 5 boundary layer elements and a growth factor of 1.3.

C.1 Moving mesh

Figure C.2 shows the mesh sensitivity study for the model used in Chapter 5 when a moving mesh was used. The final mesh used 60 vertical elements, 15 horizontal elements, 15 boundary layer elements and a growth factor of 1.05.

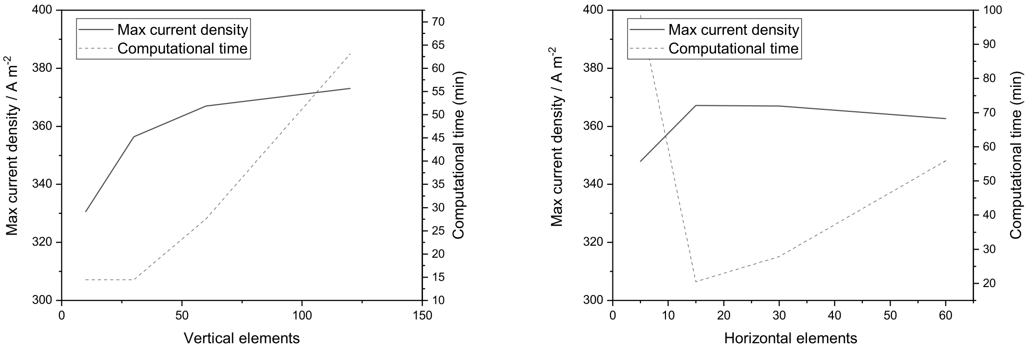

(A) Number of elements in the y-direction (vertical) (B) Number of elements in the x-direction (horizontal) in the electrode domains

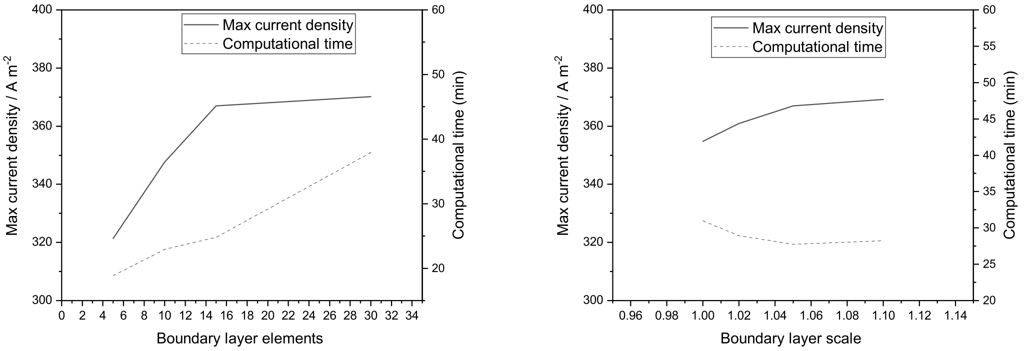

(C) Number of boundary layer elements (D) Boundary layer growth factor

FIGURE C.2: Maximum local current density magnitude (solid lines) and computational time (dashed lines) recorded with when number of elements are varied for the moving mesh model.

C.2 Static mesh

Figure C.3 shows the mesh sensitivity study for the model used in Chapter 5 when a static mesh was used. The final mesh also used 60 vertical elements, 15 horizontal elements, 15 boundary layer elements and a growth factor of 1.05.

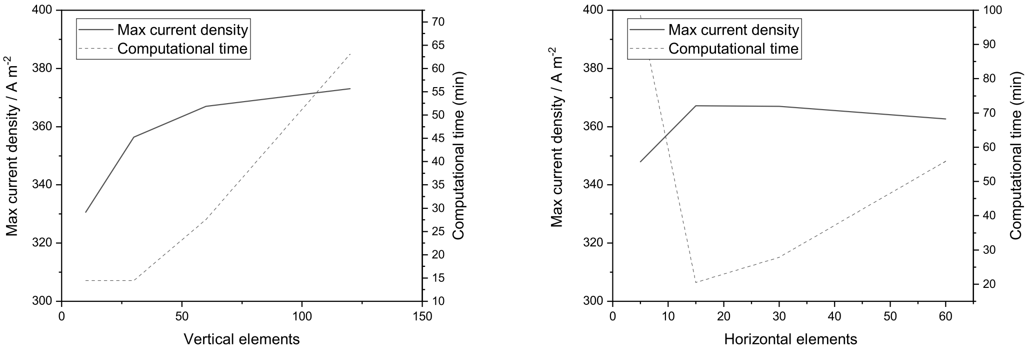

(A) Number of elements in the y-direction (vertical) (B) Number of elements in the x-direction (horizontal) in the electrode domains

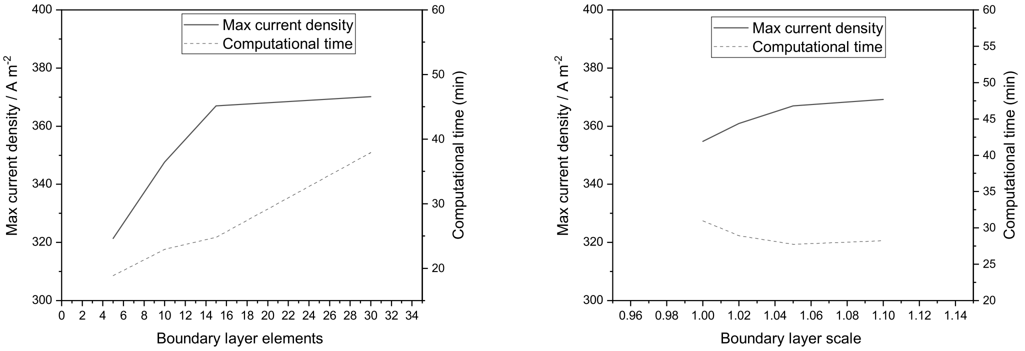

(C) Number of boundary layer elements (D) Boundary layer growth factor

FIGURE C.3: Maximum local current density magnitude (solid lines) and computational time (dashed lines) recorded with when number of elements are varied for the static mesh model.

C.3 Two-dimensional divided cell

Figure C.4 shows the mesh sensitivity study for the two-dimensional divided model used in Chapter 7. The final mesh used 60 vertical elements, 15 horizontal elements (per electrolyte domain), 15 electrode boundary layer elements at the electrode and 5 boundary layer elements at the membrane boundary.

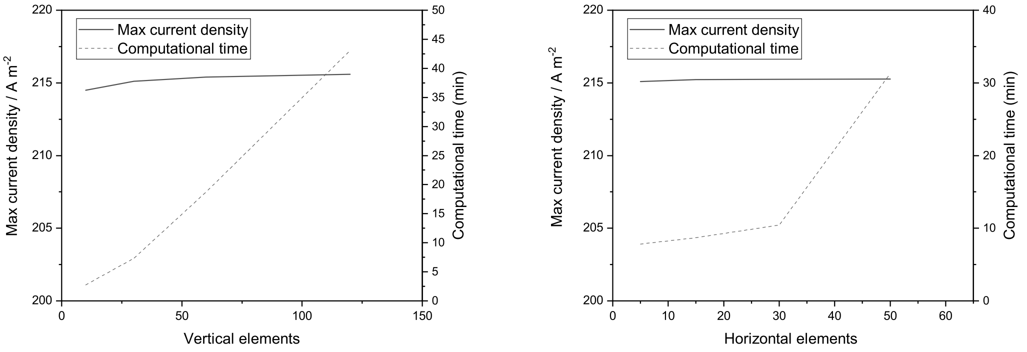

(A) Number of elements in the y-direction (vertical) (B) Number of elements in the x-direction (horizontal) in the electrode domains

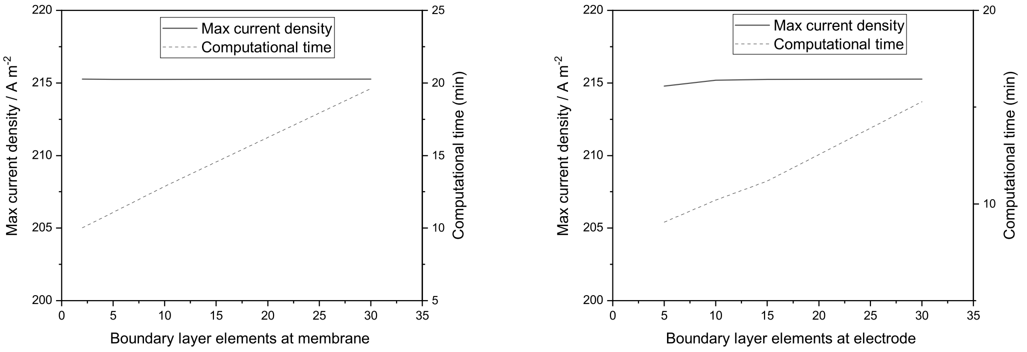

(C) Number of boundary layer elements at the membrane boundary (D) Number of boundary layer elements at the electrode boundary

FIGURE C.4: Maximum local current density magnitude (solid lines) and computational time (dashed lines) recorded with when number of elements are varied for the SLFB with two-dimensional divided model.

Appendix D

Gold

As the thickness of solid deposits that form in the SLFB is limited, the amount of energy it can store for a given electrode area is also capped. Thick deposits are, therefore, advantageous.

In order to ensure thick deposits are possible, the interface between the electrode and the deposit must be considered. Typically, two-dimensional, planar, bipolar carbon-polymer electrodes are used with the SLFB. One method of ensuring thick deposits is to use a three-dimensional electrode, thus increasing the effective electrode area. Oury et al. have produced a cell with a honeycomb-shaped positive electrode to such an effect [96]. Reticulated vitreous carbon (RVC) has also been used as a three-dimensional electrode for the SLFB [47, 95, 98, 199, 200].

Another method is to use improved electrode materials. Nickel electrodes have been used for the SLFB in several studies, most commonly as the negative electrode [47, 79, 94, 95, 201]. Copper electrodes have also been used as a negative electrode [96]. Rough lead deposits formed at the copper electrodes despite the addition of a smoothing additive hexadecyltrimethylammonium hydroxide (HDTMA). However, the electrode material was not the focus of this study.

In this work, gold is used as the surface layer of the electrode. Gold is prohibitively expensive to use as the bipolar plate or in high mass loadings in the electrode. Therefore, small quantities of gold are used at the surface of the electrodes.

D.1 Cell efficiencies

A single cell with plain carbon-polymer electrodes and a cell with gold-leaf plated electrodes were cycled at a current density of 10 mA cm^{-2}. The cells were charged for 15 minutes and discharged to a cut-off voltage of 0.3 V. Figure D.1 (A) shows the coulombic, voltage and energy efficiency of each cycle. All of the efficiencies are low in cycle 1, at 70.1 %, 51.1 % and 35.8 % for the voltage, coulombic and energy efficiencies respectively. All three efficiencies rise over the subsequent 5 – 7 cycles, peaking at 82.3 % in cycle 6, 97.3 % in cycle 8 and 79.93 % in cycle 7 for the voltage, coulombic and energy efficiency respectively. The efficiencies steadily decrease until cycle 27, after which point the coulombic efficiency and hence the energy efficiency decrease more rapidly. The cell is deemed to have failed when the coulombic efficiency drops below 60 % in the 30th cycle.

A similar trend is seen in the results from the plain carbon-polymer electrodes, described in Figure D.1 (B). The coulombic efficiency and hence the energy efficiency in cycle 1 are higher but voltage efficiency was comparable to that seen in the cell with gold leaf plated electrodes with coulombic, voltage and energy efficiencies of 70.7 %, 72.4 % and 51.2 % respectively. However, the efficiency peaks earlier, in cycle 4 and at marginally lower values of 93.3 %, 79.5 % and 74.2 % for the coulombic, voltage and energy efficiencies respectively. The lower efficiencies witnessed during the first few cycles are visible when additives are used [86]. However, this is exacerbated when gold electrodes are used. This could be due to a greater resistance to stripping of the initial deposits at one or both of the electrodes. Alternatively, it may be due to a reduced affinity for deposition due to the additives in the electrolyte and by the gold on the electrodes. The efficiencies decrease steadily, until the 9th cycle when the efficiencies rapidly decrease. The cell is deemed to have failed by the 14th cycle.

Figure D.2 shows the charge voltage and energy efficiencies of cells with a single gold-coated electrode at the positive Figure D.2 (A) and the negative Figure D.2 (B) electrode respectively. The other electrode is a plain carbon-polymer electrode. Figure D.2 (A) shows all three efficiencies are low in cycle 1 at 40.3 %, 71.4 % and 56.4 % for the energy, voltage and coulombic efficiencies respectively. Again, the efficiencies rise, reaching a peak during cycle 8 at 73.7 %, 78.9 % and 93.4 % respectively. The cell had failed by cycle 10, however. In Figure D.2 (B), the efficiencies are again low in cycle 1 at 49.5 %,

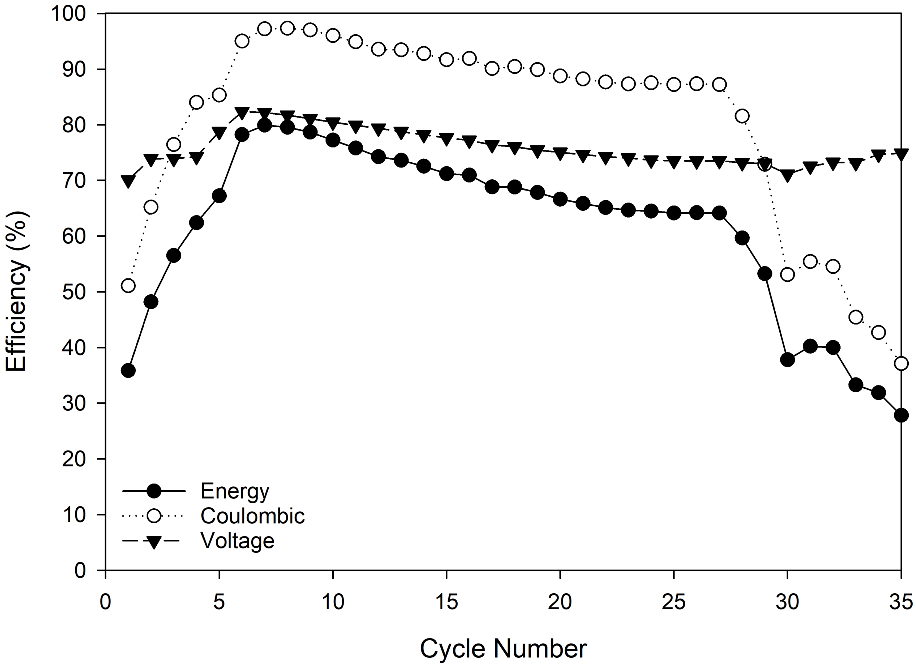

(A) Gold leaf plated carbon polymer

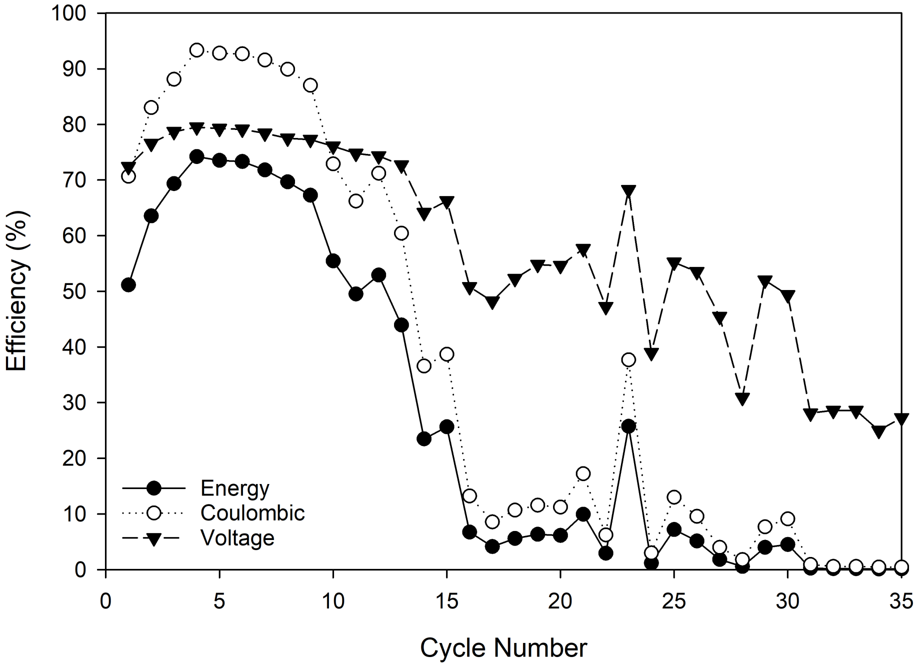

(B) Plain carbon polymer

FIGURE D.1: Charge, voltage and energy efficiencies for each cycle of cells charged at 10 mA cm^{-2} for 15 minutes and discharged to 0.3 V.

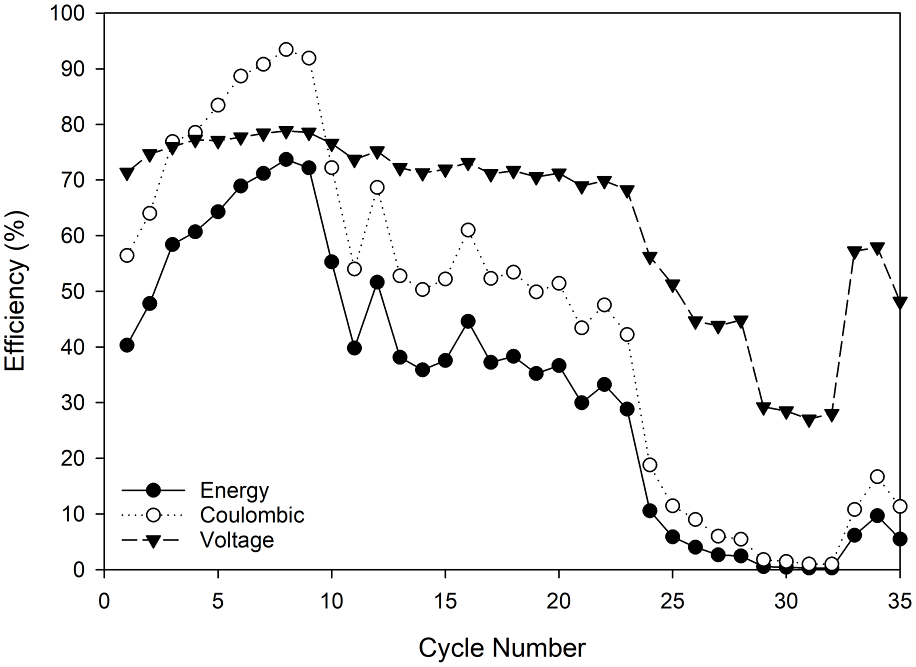

(A) Gold leaf plated positive electrode only

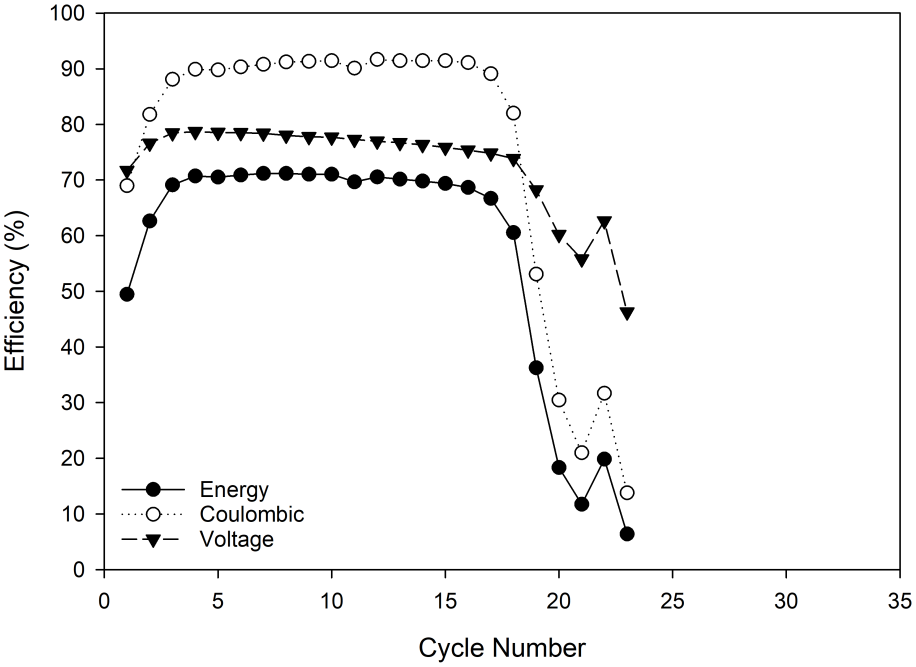

(B) Gold leaf plated negative electrode only

FIGURE D.2: Charge, voltage and energy efficiencies for each cycle of cells using gold leaf plated carbon-polymer electrodes at single electrode only. Cells were charged at 10 mA cm^{-2} for 15 minutes and discharged to 0.3 V

71.7 % and 69.0 % for energy, voltage and coulombic efficiencies respectively. In this cell, however, the efficiencies rose much quicker, reaching a plateau after cycle 3 at 70.7 %, 78.7 % and 89.9 % respectively. The efficiencies remain relatively constant until cycle 17 when all three decrease rapidly. The cell has failed by cycle 19.

D.2 Cell failure

The mode of failure of each of the cells is also of interest. By comparing the cycle during which the voltage efficiency begins to decrease with the cycle during which the coulombic efficiency begins to decrease, it is possible to suggest if the cell failed due to shorting between the electrodes, such as due to a buildup of sludge from materials fallen from the electrode, or from another mode of failure, such as capacity fade due to the complex mechanisms at the positive electrode.

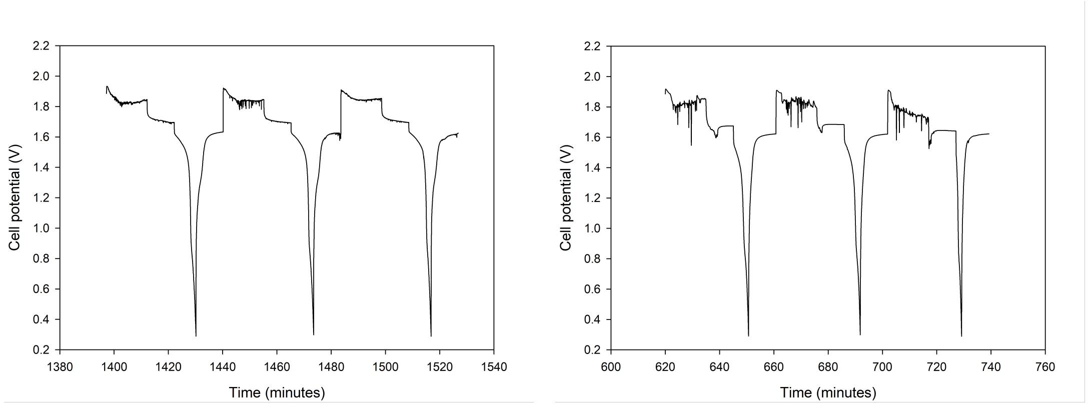

(A) Gold leaf on both electrodes (B) Plain carbon-polymer electrodes

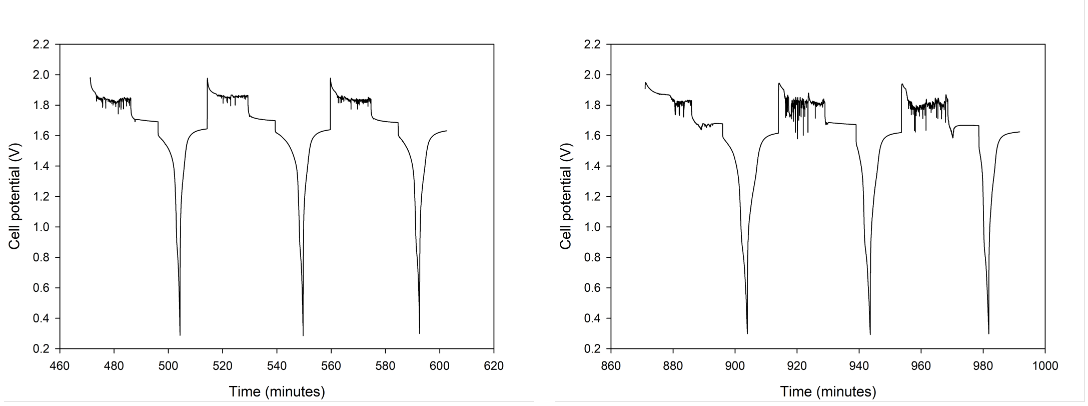

(C) Gold leaf on only the positive electrode (D) Gold leaf on only the negative electrode

FIGURE D.3: Cell potential vs time for the three cycles post failure.

The cells for which the voltage efficiency decreases at a similar time to the coulombic efficiency, the cell using plain carbon-polymer electrodes and the cell with gold at the negative electrode, suggest that the cell failed, at least partly, due to shorting. Cells for which the voltage efficiency remains high after failure, the cell with gold at both electrodes and the cell with gold at the positive electrode, suggests the cell failed due to another mechanism. The voltage curves of the cells shortly after failure, shown in Figure D.3, support this theory. Figure D.3 (A) and Figure D.3 (C) (the cell with gold at both electrodes and the cell with gold at the positive electrode) show little noise in the voltage curve and so suggest that little shorting has occurred. Figure D.3 (B) and Figure D.3 (D) (the cell with plain carbon-polymer electrodes and the cell with gold at the negative electrode) show significantly more noise in the cell potential and hence suggest that there is some shorting of the cells. It is known that sludge can form from material at the positive electrode [47], which, in a static cell would gather at the bottom of the cell and cause a short circuit between the electrodes. This data suggests that gold may prevent, or hinder a buildup of this sludge at the positive electrode. However, further work is required to confirm this theory.

D.3 Economics

The obvious caveat to the use of gold as an additive to electrodes is the price. Using the raw material prices for materials commonly used to manufacture bipolar plate electrodes, gold leaf coating the entire surface of the electrode becomes the significant cost in manufacturing the electrode. Figure D.4 shows the proportion of the costs of components in a typical RFB cell. In this instance, the cell does not include the endplates, the electrolyte or any of the flow circuitry including the pump. The cell is assumed to be part of a stack, so each cell consists of a single bipolar plate (the stack is assumed to be large enough to ignore the extra electrode required at the end of the stack), a cell frame. Four cells are described: an undivided cell with plain electrodes, an undivided cell with gold plated electrodes, a divided cell with plain electrodes and a divided cell with gold plated electrodes. It is assumed that the gold is plated uniformly to a thickness of 0.1 μm on the active area of the electrodes. The separator is assumed to be a Nafion ion exchange membrane. The cell frame is not included due to the amount of material required depending heavily on the design of the flow field and physical form of the electrodes.

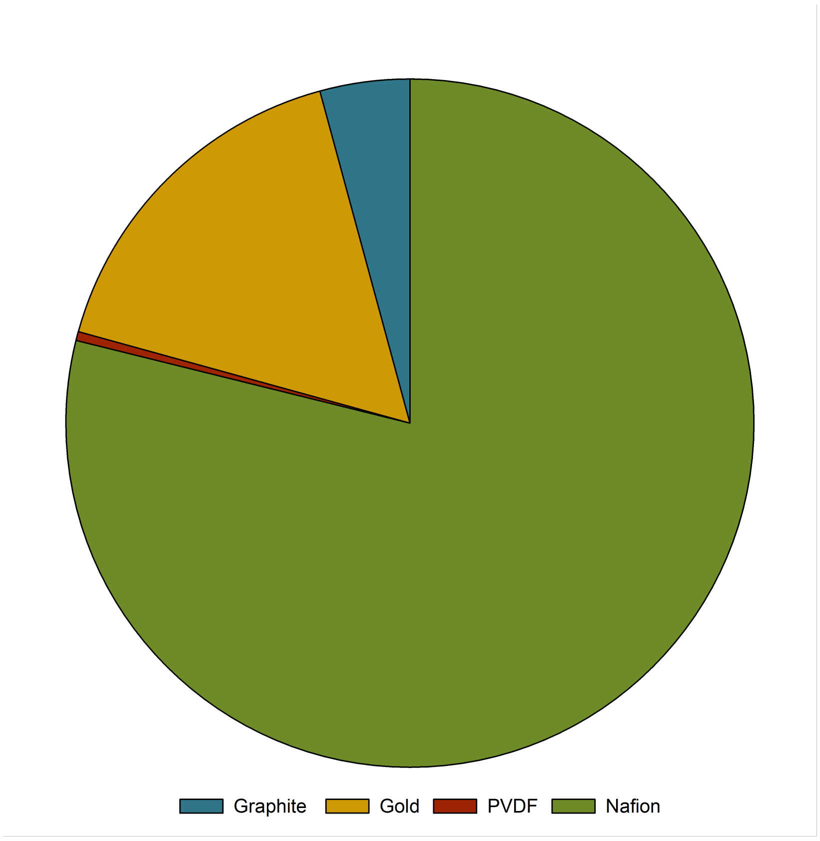

(A) Current

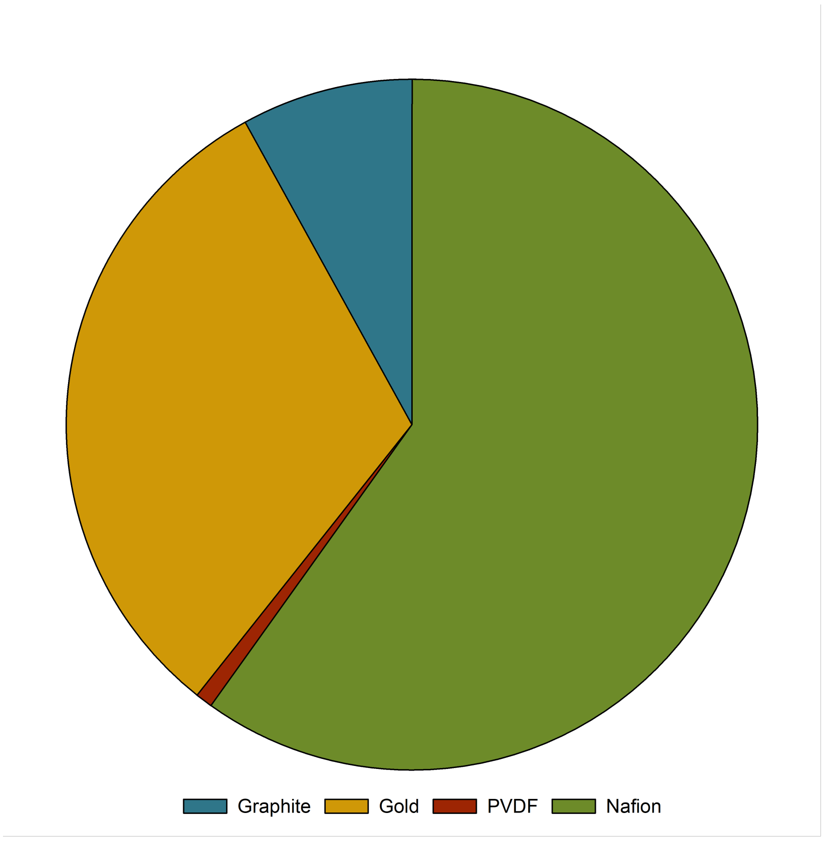

(B) Future

FIGURE D.4: Proportion of cell cost by material using current and a future prediction for the cost of Nafion

The costs of graphite and polyvinylidene difluoride (PVDF) are approximately £8 kg^{-1} and £5.50 kg^{-1} respectively [202]. A plain carbon polymer consisting of graphite with a PVDF binder, assumed to have a ratio of 85:15 respectively and to be 1 mm thick, would cost approximately £20 m^{-2}. The addition of 0.1 μm of gold, the thickness presented in this work, would add a further cost of approximately £60 m^{-2}, a significant increase [203]. A Nafion membrane, however, would cost approximately £300 m^{-2}, potentially reducing to £120 m^{-2} in the future[204]. As the SLFB is able to operate without a membrane, the addition of gold may, therefore, be feasible. Furthermore, gold may be beneficial in much lower mass loadings than represented here. Further work is, however, required.

D.4 Conclusions

These preliminary results show that the use of gold in electrodes for the soluble lead flow battery has promise. When gold is used at both electrodes there is a significant increase in performance. The cycle life is doubled and there are increases in both coulombic and voltage efficiencies. These results were gathered from cells with a static electrolyte at relatively low currents. While this is assumed to be indicative of performance in a flow cell, testing on flow cells over a greater period at higher currents is necessary. The mode of failure when gold is not present appears to be a mode other than shorting. It can be concluded that the addition of gold to the positive electrode may reduce the likelihood of shorting, probably due to a reduced volume of sludge forming at the positive electrode when gold is present. However, further work is required to confirm this theory. Furthermore, the cost of gold in the mass loadings used is significant but not excessive when compared to other components in a flow cell. Further techniques to improve the addition of gold to electrodes and varying the mass loading of gold on the surface of these electrodes is also necessary. Further analysis of the deposits formed on these gold impregnated electrodes would also be beneficial.

References

[1] E. J. Fraser, R. G. Wills, and A. J. Cruden, "The use of gold impregnated carbon-polymer electrodes with the soluble lead flow battery," *Energy Reports*, vol. 6, pp. 19–24, 2020.

[2] E. J. Fraser, K. R. Dinesh, and R. Wills, "Development of a two-dimensional, moving mesh treatment for modelling the reaction chamber of the soluble lead flow battery as a function of state of charge for Pb and PbO_2 deposition and dissolution," *Journal of Energy Storage*, vol. 31, p. 101484, 2020.

[3] E. Fraser, K. Ranga Dinesh, and R. Wills, "A two dimensional numerical model of the membrane-divided soluble lead flow battery," *Energy Reports*, vol. 7, pp. 49–55, 2021, sI: 5th AC-CDTESA.

[4] E. J. Fraser, J. P. Le Houx, K. R. Dinesh, and R. Wills, "Image-based modelling of porous electrodes and simulating their performance in the soluble lead flow battery," submitted to the Journal of Energy Storage.

[5] M. Krishna, E. J. Fraser, R. G. A. Wills, and F. C. Walsh, "Developments in soluble lead flow batteries and remaining challenges: An illustrated review," *Journal of Energy Storage*, vol. 15, pp. 69–90, 2018.

[6] United Nations. World population prospects 2019. (Accessed: 15/05/2021). [Online]. Available: https://esa.un.org/unpd/wpp/DataQuery/

[7] US Energy Information Administration. (2017) International energy outlook. [Online]. Available: https://www.eia.gov/outlooks/ieo/pdf/0484(2017).pdf

[8] British Petroleum. (2020) BP statistical review of world energy 2020. [Online]. Available: https://www.bp.com/content/

dam/bp/business-sites/en/global/corporate/pdfs/energy-economics/statistical-review/bp-stats-review-2020-full-report.pdf

[9] D. M. Etheridge, L. Steele, R. L. Langenfelds, R. J. Francey, J.-M. Barnola, and V. Morgan, “Natural and anthropogenic changes in atmospheric CO_2 over the last 1000 years from air in Antarctic ice and firn,” *Journal of Geophysical Research: Atmospheres*, vol. 101, no. D2, pp. 4115–4128, 1996.

[10] J. F. Mitchell, “The “greenhouse” effect and climate change,” *Reviews of Geophysics*, vol. 27, no. 1, pp. 115–139, 1989.

[11] S. Holgate, J. Grigg, R. Agius, J. R. Ashton, P. Cullinan, K. Exley, D. Fishwick, G. Fuller, N. Gokani, and C. Griffiths, “Every breath we take: The lifelong impact of air pollution, report of a working party.” Royal College of Physicians, 2016.

[12] British Petroleum, “Energy outlook 2020 edition,” 2020.

[13] IEA. (2021) BP world energy outlook 2021. [Online]. Available: https://www.iea.org/reports/world-energy-outlook-2021

[14] M. Ram, M. Child, A. Aghahosseini, D. Bogdanov, A. Lohrmann, and C. Breyer, “A comparative analysis of electricity generation costs from renewable, fossil fuel and nuclear sources in G20 countries for the period 2015-2030,” *Journal of cleaner production*, vol. 199, pp. 687–704, 2018.

[15] D. M. Rosenberg, R. A. Bodaly, and P. J. Usher, “Environmental and social impacts of large scale hydroelectric development: who is listening?” *Global Environmental Change*, vol. 5, no. 2, pp. 127–148, 1995.

[16] E. G. Hertwich, “Addressing biogenic greenhouse gas emissions from hydropower in LCA,” *Environmental science & technology*, vol. 47, no. 17, pp. 9604–9611, 2013.

[17] S. Homan, N. Mac Dowell, and S. Brown, “Grid frequency volatility in future low inertia scenarios: Challenges and mitigation options,” *Applied Energy*, vol. 290, p. 116723, 2021.

[18] Sandia National Laboratories and Department of Energy. (2016) Global energy storage database. (Accessed: 08/03/2017). [Online]. Available: https://www.energystorageexchange.org/

[19] European Comission. Strategic energy technologies. (Accessed: 05/07/2017). [Online]. Available: https://setis.ec.europa.eu/technologies

[20] National Grid ESO, "Future energy scenarios 2021," 2021.

[21] M. S. Ziegler, J. M. Mueller, G. D. Pereira, J. Song, M. Ferrara, Y.-M. Chiang, and J. E. Trancik, "Storage requirements and costs of shaping renewable energy toward grid decarbonization," *Joule*, vol. 3, no. 9, pp. 2134–2153, 2019.

[22] P. Denholm, E. Ela, B. Kirby, and M. Milligan, "The role of energy storage with renewable electricity generation," 2010.

[23] US Department of Energy. (2021) DOE global energy storage database. (Accessed: 08/03/2022). [Online]. Available: https://www.sandia.gov/ess-ssl/global-energy-storage-database/

[24] B. Nykvist and M. Nilsson, "Rapidly falling costs of battery packs for electric vehicles," *Nature climate change*, vol. 5, no. 4, pp. 329–332, 2015.

[25] SBC Energy Institute, "Leading the energy transition: Electricity storage," 2013.

[26] D. Linden and T. Reddy, *Handbook of Batteries*, 3rd ed. McGraw-Hill, 2002.

[27] J. Zhang, Q. Zhou, Y. Tang, L. Zhang, and Y. Li, "Zinc–air batteries: are they ready for prime time?" *Chemical science*, vol. 10, no. 39, pp. 8924–8929, 2019.

[28] M. V. Reddy, A. Mauger, C. M. Julien, A. Paolella, and K. Zaghib, "Brief history of early lithium-battery development," *Materials*, vol. 13, no. 8, p. 1884, 2020.

[29] A.-I. Stan, M. Świerczyński, D.-I. Stroe, R. Teodorescu, and S. J. Andreasen, "Lithium ion battery chemistries from renewable energy storage to automotive and back-up power applications—an overview," in *2014 International Conference on Optimization of Electrical and Electronic Equipment (OPTIM)*. IEEE, 2014, pp. 713–720.

[30] H. S. Hirsh, Y. Li, D. H. Tan, M. Zhang, E. Zhao, and Y. S. Meng, "Sodium-ion batteries paving the way for grid energy storage," *Advanced Energy Materials*, vol. 10, no. 32, p. 2001274, 2020.

[31] M. D. Slater, D. Kim, E. Lee, and C. S. Johnson, "Sodium-ion batteries," *Advanced Functional Materials*, vol. 23, no. 8, pp. 947–958, 2013.

[32] S. Wei, S. Xu, A. Agrawral, S. Choudhury, Y. Lu, Z. Tu, L. Ma, and L. A. Archer, "A stable room-temperature sodium–sulfur battery," *Nature communications*, vol. 7, no. 1, pp. 1–10, 2016.

[33] A. Bito, "Overview of the sodium-sulfur battery for the IEEE stationary battery committee," in *IEEE Power Engineering Society General Meeting, 2005.* IEEE, 2005, pp. 1232–1235.

[34] S. Ha and K. G. Gallagher, "Estimating the system price of redox flow batteries for grid storage," *Journal of Power Sources*, vol. 296, pp. 122–132, 2015.

[35] L. da Silva Lima, M. Quartier, A. Buchmayr, D. Sanjuan-Delmás, H. Laget, D. Corbisier, J. Mertens, and J. Dewulf, "Life cycle assessment of lithium-ion batteries and vanadium redox flow batteries-based renewable energy storage systems," *Sustainable Energy Technologies and Assessments*, vol. 46, p. 101286, 2021.

[36] A. Z. Weber, M. M. Mench, J. P. Meyers, P. N. Ross, J. T. Gostick, and Q. Liu, "Redox flow batteries: a review," *Journal of Applied Electrochemistry*, vol. 41, no. 10, pp. 1137–1164, 2011.

[37] M. Bartolozzi, "Development of redox flow batteries. A historical bibliography," *Journal of Power Sources*, vol. 27, no. 3, pp. 219–234, 1989.

[38] E. Sánchez-Díez, E. Ventosa, M. Guarnieri, A. Trovò, C. Flox, R. Marcilla, F. Soavi, P. Mazur, E. Aranzabe, and R. Ferret, "Redox flow batteries: Status and perspective towards sustainable stationary energy storage," *Journal of Power Sources*, vol. 481, p. 228804, 2021.

[39] A. Parasuraman, T. M. Lim, C. Menictas, and M. Skyllas-Kazacos, "Review of material research and development for vanadium redox flow battery applications," *Electrochimica Acta*, vol. 101, pp. 27–40, 2013.

[40] M. Wu, T. Zhao, H. Jiang, Y. Zeng, and Y. Ren, "High-performance zinc bromine flow battery via improved design of electrolyte and electrode," *Journal of Power Sources*, vol. 355, pp. 62–68, 2017.

[41] B. Amunátegui, A. Ibáñez, M. Sierra, and M. Pérez, "Electrochemical energy storage for renewable energy integration: zinc-air flow batteries," *Journal of Applied Electrochemistry*, vol. 48, no. 6, pp. 627–637, 2018.

[42] L. H. Thaller, “Recent advances in redox flow cell storage systems,” 1979.

[43] C. Ponce de León, A. Frias-Ferrer, J. Gonzalez-Garcia, D. A. Szanto, and F. C. Walsh, “Redox flow cells for energy conversion,” *Journal of Power Sources*, vol. 160, no. 1, pp. 716–732, 2006.

[44] A. Hazza, D. Pletcher, and R. Wills, “A novel flow battery: A lead acid battery based on an electrolyte with soluble lead (II) part I. preliminary studies,” *Physical Chemistry Chemical Physics*, vol. 6, no. 8, pp. 1773–1778, 2004.

[45] J. grosse Austing, C. Nunes Kirchner, E.-M. Hammer, L. Komsiyska, and G. Wittstock, “Study of an unitised bidirectional vanadium/air redox flow battery comprising a two-layered cathode,” *Journal of Power Sources*, vol. 273, no. Supplement C, pp. 1163–1170, 2015.

[46] Y. Xu, Y. Wen, J. Cheng, Y. Yanga, Z. Xie, and G. Cao, “Novel organic redox flow batteries using soluble quinonoid compounds as positive materials,” *1st World Non-Grid-Connected Wind Power and Energy Conference, WNWEC 2009, September 24, 2009 - September 26, 2009*, pp. 475–478, 2009.

[47] R. G. A. Wills, J. Collins, D. Stratton-Campbell, C. T. J. Low, D. Pletcher, and F. Walsh, “Developments in the soluble lead-acid flow battery,” *Journal of Applied Electrochemistry*, vol. 40, no. 5, pp. 955–965, 2010.

[48] K. Divya and J. Østergaard, “Battery energy storage technology for power systems—an overview,” *Electric Power Systems Research*, vol. 79, no. 4, pp. 511–520, 2009.

[49] M. Krishna, L. Wallis, R. Wills, D. Hall, and A. Shah, “Measurement of key electrolyte properties for improved performance of the soluble lead flow battery,” *International Journal of Hydrogen Energy*, vol. 42, no. 29, pp. 18 491–18 498, 2017.

[50] R. Boddula, R. Pothu, A. M. Asiri *et al.*, *Rechargeable Batteries: History, Progress, and Applications*. John Wiley & Sons, 2020.

[51] P. Kurzweil, “Gaston Planté and his invention of the lead–acid battery—the genesis of the first practical rechargeable battery,” *Journal of Power Sources*, vol. 195, no. 14, pp. 4424–4434, 2010.

[52] D. Pavlov, *Lead-Acid Batteries: Science and Technology: A Handbook of Lead-Acid Battery Technology and Its Influence on the Product*, 2nd ed. Elsevier Science, 2017.

[53] W. Zhang, J. Yang, X. Wu, Y. Hu, W. Yu, J. Wang, J. Dong, M. Li, S. Liang, J. Hu *et al.*, "A critical review on secondary lead recycling technology and its prospect," *Renewable and Sustainable Energy Reviews*, vol. 61, pp. 108–122, 2016.

[54] T. W. Ellis and A. H. Mirza, "The refining of secondary lead for use in advanced lead-acid batteries," *Journal of Power Sources*, vol. 195, no. 14, pp. 4525–4529, 2010.

[55] J. Yang, X. Zhu, and R. V. Kumar, "Ethylene glycol-mediated synthesis of pbo nanocrystal from pbso4: A major component of lead paste in spent lead acid battery," *Materials Chemistry and Physics*, vol. 131, no. 1, pp. 336–342, 2011.

[56] L. C. Ferracin, A. E. Chácon-Sanhueza, R. A. Davoglio, L. O. Rocha, D. J. Caffeu, A. R. Fontanetti, R. C. Rocha-Filho, S. R. Biaggio, and N. Bocchi, "Lead recovery from a typical brazilian sludge of exhausted lead-acid batteries using an electrohydrometallurgical process," *Hydrometallurgy*, vol. 65, no. 2-3, pp. 137–144, 2002.

[57] M. Maja, S. Bodoardo, C. Serracane, and R. Baudino, "Dissolution of pastes in lead-acid battery recycling plants," *Journal of applied electrochemistry*, vol. 23, no. 8, pp. 819–826, 1993.

[58] F. Beck, "Lead batteries," US Patent 4 001 037A, 1977.

[59] R. Wurmb, F. Beck, and K. Boehlke, "Secondary battery," US Patent 4 092 463A, 1978.

[60] P. O. Henk and Z. A. Piontkowski, "Lead salt electric storage battery," US Patent 4 331 744A, 1982.

[61] C. P. Zhang, S. M. Sharkh, X. Li, F. C. Walsh, C. N. Zhang, and J. C. Jiang, "The performance of a soluble lead-acid flow battery and its comparison to a static lead-acid battery," *Energy Conversion and Management*, vol. 52, no. 12, pp. 3391–3398, 2011.

[62] M. Gernon *et al.*, "Environmental benefits of methanesulfonic acid. comparative properties and advantages," *Green chemistry*, vol. 1, no. 3, pp. 127–140, 1999.

[63] M. Lanfranconi and H.-J. Lilienhof, “All-lead-flow-batteries as promising candidates for energy storage solutions,” *Journal of Sustainable Development of Energy, Water and Environment Systems*, vol. 7, no. 2, pp. 343–354, 2019.

[64] D. P. Kelly and J. C. Murrell, “Microbial metabolism of methanesulfonic acid,” *Archives of microbiology*, vol. 172, no. 6, pp. 341–348, 1999.

[65] F. C. Walsh and C. Ponce de León, “Versatile electrochemical coatings and surface layers from aqueous methanesulfonic acid,” *Surface and Coatings Technology*, vol. 259, no. Part C, pp. 676–697, 2014.

[66] C. Díaz-Urrutia and T. Ott, “Activation of methane: A selective industrial route to methanesulfonic acid,” *Science*, vol. 363, no. 6433, pp. 1326–1329, 2019.

[67] Radiometer analytical. (Accessed: 27/09/2017). [Online]. Available: http://www.analytical-chemistry.uoc.gr/files/items/6/618/agwgimometria_2.pdf

[68] H. E. Darling, “Conductivity of sulfuric acid solutions,” *Journal of Chemical & Engineering Data*, vol. 9, no. 3, pp. 421–426, 1964.

[69] B. R. Chalamala, T. Soundappan, G. R. Fisher, M. R. Anstey, V. V. Viswanathan, and M. L. Perry, “Redox flow batteries: an engineering perspective,” *Proceedings of the IEEE*, vol. 102, no. 6, pp. 976–999, 2014.

[70] K. Orapeleng, R. G. Wills, and A. Cruden, “Developing electrolyte for a soluble lead redox flow battery by reprocessing spent lead acid battery electrodes,” *Batteries*, vol. 3, no. 2, p. 15, 2017.

[71] J. Collins, X. Li, D. Pletcher, R. Tangirala, D. Stratton-Campbell, F. C. Walsh, and C. Zhang, “A novel flow battery: A lead acid battery based on an electrolyte with soluble lead (II). part IX: Electrode and electrolyte conditioning with hydrogen peroxide,” *Journal of Power Sources*, vol. 195, no. 9, pp. 2975–2978, 2010.

[72] K. Orapeleng, R. G. Wills, and A. Cruden, “Performance of recovered and reagent grade electrolyte in a soluble lead redox cell,” *Journal of Energy Storage*, vol. 20, pp. 49–56, 2018.

[73] Y. Li, S. Yang, P. Taskinen, J. He, Y. Chen, C. Tang, Y. Wang, and A. Jokilaakso, “Spent lead-acid battery recycling via reductive sulfur-fixing smelting and its

reaction mechanism in the $PbSO_4$-Fe_3O_4-Na_2CO_3-C system," *JOM*, vol. 71, no. 7, pp. 2368–2379, 2019.

[74] J. B. Spijkerman and R. J. Groenen, "Process for the recovery of metallic lead from battery paste," GB Patent 9 102 994D0, 1996.

[75] M. Olper, M. Maccagni, and S. Cossali, "Process for producing metallic lead starting from desulfurized pastel," US Patent 8 409 421B2, 2013.

[76] R. Kumar and S. Sonmez, "Recovery of lead from lead waste such as lead battery paste, involves treating lead waste with aqueous citric acid solution, separating obtained lead citrate from solution and converting citrate into lead and/or lead oxide," *Cambridge Enterprise Ltd (Uyca) Univ Cambridge Tech Services Ltd (Uyca) WO2008056125-A1*.

[77] ecobat. (Accessed: 03/02/2022). [Online]. Available: https://www.ecobat.com

[78] L. P. J. Wallis and R. G. A. Wills, "Membrane divided soluble lead battery utilising a bismuth electrolyte additive," *Journal of Power Sources*, vol. 247, no. 0, pp. 799–806, 2014.

[79] D. Pletcher, H. Zhou, G. Kear, C. T. J. Low, F. C. Walsh, and R. G. A. Wills, "A novel flow battery: A lead-acid battery based on an electrolyte with soluble lead(II) part V. studies of the lead negative electrode," *Journal of Power Sources*, vol. 180, no. 1, pp. 621–629, 2008.

[80] J. Collins, J. Bateman, and D. Pletcher, "Emerging energy technologies: Redox flow cells for intelligent grid management, TP no: TP/4/EET/6/I/22296," 2009.

[81] I. Petersson, E. Ahlberg, and B. Berghult, "Parameters influencing the ratio between electrochemically formed α- and β-PbO_2," *Journal of Power Sources*, vol. 76, no. 1, pp. 98–105, 1998.

[82] D. Pletcher, H. Zhou, G. Kear, C. T. J. Low, F. C. Walsh, and R. G. A. Wills, "A novel flow battery: A lead-acid battery based on an electrolyte with soluble lead(II) part VI. studies of the lead dioxide positive electrode," *Journal of Power Sources*, vol. 180, no. 1, pp. 630–634, 2008.

[83] X. Li, D. Pletcher, and F. C. Walsh, "A novel flow battery: a lead acid battery based on an electrolyte with soluble lead (II): Part VII. further studies of the lead dioxide positive electrode," *Electrochimica Acta*, vol. 54, no. 20, pp. 4688–4695, 2009.

[84] I. Sirés, C. Low, C. Ponce de León, and F. Walsh, "The characterisation of PbO_2-coated electrodes prepared from aqueous methanesulfonic acid under controlled deposition conditions," *Electrochimica Acta*, vol. 55, no. 6, pp. 2163–2172, 2010.

[85] A. Hazza, D. Pletcher, and R. Wills, "A novel flow battery: A lead acid battery based on an electrolyte with soluble lead(II) part IV. the influence of additives," *Journal of Power Sources*, vol. 149, no. 0, pp. 103–111, 2005.

[86] M. Krishna, R. Wills, A. Shah, D. Hall, and J. Collins, "The separator-divided soluble lead flow battery," *Journal of Applied Electrochemistry*, vol. 48, no. 9, pp. 1031–1041, 2018.

[87] H. Chen, L. Wu, C. Ren, Q. Luo, Z. Xie, X. Jiang, S. Zhu, Y. Xia, and Y. Luo, "The effect and mechanism of bismuth doped lead oxide on the performance of lead-acid batteries," *Journal of power sources*, vol. 95, no. 1-2, pp. 108–118, 2001.

[88] J. Feng and D. C. Johnson, "Electrocatalysis of anodic oxygen-transfer reactions: Titanium substrates for pure and doped lead dioxide films," *Journal of The Electrochemical Society*, vol. 138, no. 11, pp. 3328–3337, 1991.

[89] C. Low, D. Pletcher, and F. Walsh, "The electrodeposition of highly reflective lead dioxide coatings," *Electrochemistry communications*, vol. 11, no. 6, pp. 1301–1304, 2009.

[90] J. Cao, H. Zhao, F. Cao, J. Zhang, and C. Cao, "Electrocatalytic degradation of 4-chlorophenol on F-doped PbO_2 anodes," *Electrochimica Acta*, vol. 54, no. 9, pp. 2595–2602, 2009.

[91] R. Amadelli, L. Armelao, A. Velichenko, N. Nikolenko, D. Girenko, S. Kovalyov, and F. Danilov, "Oxygen and ozone evolution at fluoride modified lead dioxide electrodes," *Electrochimica Acta*, vol. 45, no. 4, pp. 713–720, 1999.

[92] Y.-T. Lin, H.-L. Tan, C.-Y. Lee, and H.-Y. Chen, "Stabilizing the electrodeposit-electrolyte interphase in soluble lead flow batteries with ethanoate additive," *Electrochimica Acta*, vol. 263, pp. 60–67, 2018.

[93] M. G. Verde, K. J. Carroll, Z. Wang, A. Sathrum, and Y. S. Meng, “Achieving high efficiency and cyclability in inexpensive soluble lead flow batteries,” *Energy & Environmental Science*, vol. 6, no. 5, pp. 1573–1581, 2013.

[94] J. Collins, G. Kear, X. Li, C. T. J. Low, D. Pletcher, R. Tangirala, D. Stratton-Campbell, F. C. Walsh, and C. Zhang, “A novel flow battery: A lead acid battery based on an electrolyte with soluble lead(II) part VIII. the cycling of a 10 cm × 10 cm flow cell,” *Journal of Power Sources*, vol. 195, no. 6, pp. 1731–1738, 2010.

[95] D. Pletcher and R. Wills, “A novel flow battery: A lead acid battery based on an electrolyte with soluble lead (II) part II. flow cell studies,” *Physical Chemistry Chemical Physics*, vol. 6, no. 8, pp. 1779–1785, 2004.

[96] A. Oury, A. Kirchev, and Y. Bultel, “Cycling of soluble lead flow cells comprising a honeycomb-shaped positive electrode,” *Journal of Power Sources*, vol. 264, pp. 22–29, 2014.

[97] L. Arenas, C. P. de León, and F. Walsh, “Critical review—the versatile plane parallel electrode geometry: An illustrated review,” *Journal of The Electrochemical Society*, vol. 167, no. 2, p. 023504, 2020.

[98] A. Banerjee, D. Saha, T. N. G. Row, and A. K. Shukla, “A soluble-lead redox flow battery with corrugated graphite sheet and reticulated vitreous carbon as positive and negative current collectors,” *Bulletin of Materials Science*, vol. 36, no. 1, pp. 163–170, 2013.

[99] R. Suman, M. K. Ravikumar, N. Jaiswal, S. Patil, and A. K. Shukla, “On extending cycle-life of the soluble lead redox flow battery,” in *Meeting Abstracts*. The Electrochemical Society, 2018, pp. 221–221.

[100] A. B. Velichenko, R. Amadelli, E. V. Gruzdeva, T. V. Luk’yanenko, and F. I. Danilov, “Electrodeposition of lead dioxide from methanesulfonate solutions,” *Journal of Power Sources*, vol. 191, no. 1, pp. 103–110, 2009.

[101] X. Luo, Z. Liu, B. Jiang, and D. Ji, “High efficiency of the lead methanesulfonate flow battery achieved by changing the characteristics of PbO_x under potentiostatic conditions,” *Journal of Energy Storage*, vol. 24, p. 100771, 2019.

[102] R. Wills. An overview of the relcobatt project. (Accessed: 15/09/2021). [Online]. Available: https://www.faraday2020.org.uk/exhibition-area/richard-wills/

[103] S. Suresh, M. Ulaganathan, N. Venkatesan, P. Periasamy, and P. Ragupathy, "High performance zinc-bromine redox flow batteries: Role of various carbon felts and cell configurations," *Journal of Energy Storage*, vol. 20, pp. 134–139, 2018.

[104] T. L. M. Exchange. Lme gold. (Accessed: 01/04/2022. [Online]. Available: https://www.lme.com/en/metals/precious/lme-gold#Trading+day+summary

[105] J. Friedrich, C. Ponce de León, G. Reade, and F. Walsh, "Reticulated vitreous carbon as an electrode material," *Journal of Electroanalytical Chemistry*, vol. 561, pp. 203–217, 2004.

[106] F. Walsh, L. Arenas, C. Ponce de León, G. Reade, I. Whyte, and B. Mellor, "The continued development of reticulated vitreous carbon as a versatile electrode material: Structure, properties and applications," *Electrochimica Acta*, vol. 215, pp. 566–591, 2016.

[107] J. Wang and H. Dewald, "Deposition of metals at a flow-through reticulated vitreous carbon electrode coupled with on-line monitoring of the effluent," *Journal of the Electrochemical Society*, vol. 130, no. 9, p. 1814, 1983.

[108] J. Newman and N. P. Balsara, *Electrochemical systems*. John Wiley & Sons, 2021.

[109] A. Ford, *Modeling the environment: an introduction to system dynamics models of environmental systems*. Island press, 1999.

[110] K. Rogers. (2012) Scientific modeling. (Accessed: 21/09/2020). [Online]. Available: https://www.britannica.com/science/scientific-modeling

[111] Q. Zheng, X. Li, Y. Cheng, G. Ning, F. Xing, and H. Zhang, "Development and perspective in vanadium flow battery modeling," *Applied energy*, vol. 132, pp. 254–266, 2014.

[112] B. K. Chakrabarti, E. Kalamaras, A. K. Singh, A. Bertei, J. Rubio-Garcia, V. Yufit, K. M. Tenny, B. Wu, F. Tariq, and Y. S. Hajimolana, "Modelling of redox flow battery electrode processes at a range of length scales: a review," *Sustainable Energy & Fuels*, 2020.

[113] Y. Zhang, R. Xiong, H. He, and M. G. Pecht, "Lithium-ion battery remaining useful life prediction with box–cox transformation and monte carlo simulation," *IEEE Transactions on Industrial Electronics*, vol. 66, no. 2, pp. 1585–1597, 2018.

[114] S. Nejad, D. Gladwin, and D. Stone, "A systematic review of lumped-parameter equivalent circuit models for real-time estimation of lithium-ion battery states," *Journal of Power Sources*, vol. 316, pp. 183–196, 2016.

[115] H. Al-Fetlawi, A. Shah, and F. Walsh, "Modelling the effects of oxygen evolution in the all-vanadium redox flow battery," *Electrochimica Acta*, vol. 55, no. 9, pp. 3192–3205, 2010.

[116] G. Qiu, A. S. Joshi, C. Dennison, K. Knehr, E. Kumbur, and Y. Sun, "3-d pore-scale resolved model for coupled species/charge/fluid transport in a vanadium redox flow battery," *Electrochimica Acta*, vol. 64, pp. 46–64, 2012.

[117] B. Craig, C.-K. Skylaris, T. Schoetz, and C. P. de León, "A computational chemistry approach to modelling conducting polymers in ionic liquids for next generation batteries," *Energy Reports*, vol. 6, pp. 198–208, 2020.

[118] J. Badeda, M. Huck, D. Sauer, J. Kabzinski, and J. Wirth, *Basics of lead–acid battery modelling and simulation*. Elsevier, 2017, pp. 463–507.

[119] K.-J. Euler, R. Kirchhof, and H. Metzendorf, "Electronic conductivity of battery active masses—a limiting factor?" *Journal of Power Sources*, vol. 5, no. 3, pp. 255–262, 1980.

[120] D. Simonsson, "Current distribution in the porous lead dioxide electrode," *Journal of The Electrochemical Society*, vol. 120, no. 2, p. 151, 1973.

[121] P. Ekdunge and D. Simonsson, "The discharge behaviour of the porous lead electrode in the lead-acid battery. II. mathematical model," *Journal of applied electrochemistry*, vol. 19, no. 2, pp. 136–141, 1989.

[122] W. Gu, C.-Y. Wang, and B. Y. Liaw, "Numerical modeling of coupled electrochemical and transport processes in lead-acid batteries," *Journal of The Electrochemical Society*, vol. 144, no. 6, p. 2053, 1997.

[123] D. U. Sauer, "Modelling of local conditions in flooded lead/acid batteries in photovoltaic systems," *Journal of power sources*, vol. 64, no. 1-2, pp. 181–187, 1997.

[124] Y. Ashraf Gandomi, D. Aaron, J. Houser, M. Daugherty, J. Clement, A. Pezeshki, T. Ertugrul, D. Moseley, and M. Mench, “Critical review—experimental diagnostics and material characterization techniques used on redox flow batteries,” *Journal of The Electrochemical Society*, vol. 165, no. 5, p. A970, 2018.

[125] M. Miyabayashi, K. Sato, T. Tayama, Y. Kageyama, and H. Oyama, “Redox flow type battery,” US Patent 5 851 694, 1998.

[126] C. Bengoa, A. Montillet, P. Legentilhomme, and J. Legrand, “Flow visualization and modelling of a filter-press type electrochemical reactor,” *Journal of applied electrochemistry*, vol. 27, no. 12, pp. 1313–1322, 1997.

[127] A. Wragg and A. Leontaritis, “Local mass transfer and current distribution in baffled and unbaffled parallel plate electrochemical reactors,” *Chemical Engineering Journal*, vol. 66, no. 1, pp. 1–10, 1997.

[128] J. Rubio-Garcia, A. Kucernak, and A. Charleson, “Direct visualization of reactant transport in forced convection electrochemical cells and its application to redox flow batteries,” *Electrochemistry Communications*, vol. 93, pp. 128–132, 2018.

[129] J. Houser, J. Clement, A. Pezeshki, and M. M. Mench, “Influence of architecture and material properties on vanadium redox flow battery performance,” *Journal of Power Sources*, vol. 302, pp. 369–377, 2016.

[130] A. A. Wong, M. J. Aziz, and S. Rubinstein, “Direct visualization of electrochemical reactions and comparison of commercial carbon papers in operando by fluorescence microscopy using a quinone-based flow cell,” *ECS Transactions*, vol. 77, no. 11, p. 153, 2017.

[131] J. Escudero-González and P. Amparo López-Jiménez, “Redox cell hydrodynamic modelling: Towards real improved geometry based on CFD analysis,” *Engineering Applications of Computational Fluid Mechanics*, vol. 8, no. 3, pp. 435–446, 2014.

[132] J. Escudero-González and P. A. López-Jiménez, “Methodology to optimize fluid-dynamic design in a redox cell,” *Journal of Power Sources*, vol. 251, pp. 243–253, 2014.

[133] M. D. Kok, R. Jervis, T. G. Tranter, M. A. Sadeghi, D. J. Brett, P. R. Shearing, and J. T. Gostick, “Mass transfer in fibrous media with varying anisotropy for flow battery

electrodes: Direct numerical simulations with 3d x-ray computed tomography," *Chemical Engineering Science*, vol. 196, pp. 104–115, 2019.

[134] M. D. Kok, A. Khalifa, and J. T. Gostick, "Multiphysics simulation of the flow battery cathode: cell architecture and electrode optimization," *Journal of The Electrochemical Society*, vol. 163, no. 7, p. A1408, 2016.

[135] S. Liu, M. Kok, Y. Kim, J. L. Barton, F. R. Brushett, and J. Gostick, "Evaluation of electrospun fibrous mats targeted for use as flow battery electrodes," *Journal of The Electrochemical Society*, vol. 164, no. 9, p. A2038, 2017.

[136] D. F. Elger, B. A. LeBret, C. T. Crowe, and J. A. Roberson, *Engineering fluid mechanics*. John Wiley & Sons, 2020.

[137] D. A. Nield and A. Bejan, *Convection in porous media*. Springer, 2006, vol. 3.

[138] S. Whitaker, "Flow in porous media I: A theoretical derivation of Darcy's law," *Transport in porous media*, vol. 1, no. 1, pp. 3–25, 1986.

[139] H. Brinkman, "A calculation of the viscous force exerted by a flowing fluid on a dense swarm of particles," *Flow, Turbulence and Combustion*, vol. 1, no. 1, p. 27, 1949.

[140] H. Brinkman, "On the permeability of media consisting of closely packed porous particles," *Flow, Turbulence and Combustion*, vol. 1, no. 1, p. 81, 1949.

[141] A. Shah, H. Al-Fetlawi, and F. Walsh, "Dynamic modelling of hydrogen evolution effects in the all-vanadium redox flow battery," *Electrochimica Acta*, vol. 55, no. 3, pp. 1125–1139, 2010.

[142] J. Picalek and J. Kolafa, "Molecular dynamics study of conductivity of ionic liquids: The Kohlrausch law," *Journal of Molecular Liquids*, vol. 134, no. 1-3, pp. 29–33, 2007.

[143] G. M. Kontogeorgis, B. Maribo-Mogensen, and K. Thomsen, "The Debye-Hückel theory and its importance in modeling electrolyte solutions," *Fluid Phase Equilibria*, vol. 462, pp. 130–152, 2018.

[144] P. M. Monk, *Fundamentals of electroanalytical chemistry*. John Wiley & Sons, 2001.

[145] L. Onsager, "Report on a revision of the conductivity theory," *Transactions of the Faraday Society*, vol. 23, pp. 341–349, 1927.

[146] W. Tiedemann and J. Newman, "Maximum effective capacity in an ohmically limited porous electrode," *Journal of The Electrochemical Society*, vol. 122, no. 11, p. 1482, 1975.

[147] J. R. Varcoe, P. Atanassov, D. R. Dekel, A. M. Herring, M. A. Hickner, P. A. Kohl, A. R. Kucernak, W. E. Mustain, K. Nijmeijer, K. Scott *et al.*, "Anion-exchange membranes in electrochemical energy systems," *Energy & environmental science*, vol. 7, no. 10, pp. 3135–3191, 2014.

[148] T. Xu, "Ion exchange membranes: state of their development and perspective," *Journal of membrane science*, vol. 263, no. 1-2, pp. 1–29, 2005.

[149] B. Tjaden, S. J. Cooper, D. J. Brett, D. Kramer, and P. R. Shearing, "On the origin and application of the bruggeman correlation for analysing transport phenomena in electrochemical systems," *Current opinion in chemical engineering*, vol. 12, pp. 44–51, 2016.

[150] H. Ohshima, "Chapter 2. potential distribution around a soft particle," *Theory of Colloid and Interfacial Electric Phenomena, ed. h. Ohshima*, vol. 12, pp. 39–55, 2006.

[151] M. Paunovic and M. Schlesinger, *Fundamentals of electrochemical deposition*, 2nd ed., ser. The electrochemical society series. Wiley, 1998.

[152] M. N. Nandanwar and S. Kumar, "Modelling of effect of non-uniform current density on the performance of soluble lead redox flow batteries," *Journal of The Electrochemical Society*, vol. 161, no. 10, pp. A1602–A1610, 2014.

[153] COMSOL. (Accessed: 05/03/2022). [Online]. Available: https://www.comsol.com

[154] Ansys. (Accessed: 05/03/2022). [Online]. Available: https://www.ansys.com

[155] A. A. Shah, X. Li, R. G. Wills, and F. C. Walsh, "A mathematical model for the soluble lead-acid flow battery," *Journal of The Electrochemical Society*, vol. 157, no. 5, pp. A589–A599, 2010.

[156] A. Bates, S. Mukerjee, S. C. Lee, D.-H. Lee, and S. Park, "An analytical study of a lead-acid flow battery as an energy storage system," *Journal of Power Sources*, vol. 249, pp. 207–218, 2014.

[157] A. Oury, A. Kirchev, and Y. Bultel, "A numerical model for a soluble lead-acid flow battery comprising a three-dimensional honeycomb-shaped positive electrode," *Journal of Power Sources*, vol. 246, pp. 703–718, 2014.

[158] M. Nandanwar and S. Kumar, "Charge coup de fouet phenomenon in soluble lead redox flow battery," *Chemical Engineering Science*, vol. 154, pp. 61–71, 2016.

[159] M. Nandanwar and S. Kumar, "A modelling and simulation study of soluble lead redox flow battery: Effect of presence of free convection on the battery characteristics," *Journal of Power Sources*, vol. 412, pp. 536–544, 2019.

[160] M. N. Nandanwar, K. S. Kumar, S. Srinivas, and D. Dinesh, "Pump-less, free-convection-driven redox flow batteries: Modelling, simulation, and experimental demonstration for the soluble lead redox flow battery," *Journal of Power Sources*, vol. 454, p. 227918, 2020.

[161] D. Ji, Z. Liu, B. Jiang, and X. Luo, "Temperature adaptability of the lead methanesulfonate flow battery," *Journal of Energy Storage*, vol. 28, p. 101218, 2020.

[162] P. Alotto, M. Guarnieri, and F. Moro, "Redox flow batteries for the storage of renewable energy: A review," *Renewable and sustainable energy reviews*, vol. 29, pp. 325–335, 2014.

[163] P. Leung, X. Li, C. Ponce de León, L. Berlouis, C. T. J. Low, and F. C. Walsh, "Progress in redox flow batteries, remaining challenges and their applications in energy storage," *RSC Advances*, vol. 2, no. 27, pp. 10 125–10 156, 2012.

[164] L. Arenas, C. Ponce de León, and F. Walsh, "Engineering aspects of the design, construction and performance of modular redox flow batteries for energy storage," *Journal of Energy Storage*, vol. 11, pp. 119–153, 2017.

[165] G. Nikiforidis, L. Berlouis, D. Hall, and D. Hodgson, "A study of different carbon composite materials for the negative half-cell reaction of the zinc cerium hybrid redox flow cell," *Electrochimica Acta*, vol. 113, pp. 412–423, 2013.

[166] V. Viswanathan, A. Crawford, D. Stephenson, S. Kim, W. Wang, B. Li, G. Coffey, E. Thomsen, G. Graff, P. Balducci, M. Kintner-Meyer, and V. Sprenkle, "Cost and performance model for redox flow batteries," *Journal of Power Sources*, vol. 247, pp. 1040–1051, 2014.

[167] ARPA-e. (2010). [Online]. Available: https://arpa-e.energy.gov/sites/default/files/documents/files/GRIDS_ProgramOverview.pdf

[168] ARPA-e. (2010). [Online]. Available: https://arpa-e.energy.gov/sites/default/files/documents/files/BEEST_ProgramOverview.pdf

[169] J. A. Mellentine, W. J. Culver, and R. F. Savinell, "Simulation and optimization of a flow battery in an area regulation application," *Journal of Applied Electrochemistry*, vol. 41, no. 10, pp. 1167–1174, 2011.

[170] D. Pletcher and R. Wills, "A novel flow battery: A lead acid battery based on an electrolyte with soluble lead(II) part III. the influence of conditions on battery performance," *Journal of Power Sources*, vol. 149, no. 0, pp. 96–102, 2005.

[171] SGL Carbon. (2019) (Accessed: 17/03/2019). [Online]. Available: https://www.sglcarbon.com/en/markets-solutions/material/sigracell-bipolar-plates-and-end-plates/

[172] R. C. Weast, M. J. Astle, and W. H. Beyer, *CRC handbook of chemistry and physics*. CRC press Boca Raton, FL, 1988, vol. 69.

[173] X. Li, D. Pletcher, and F. C. Walsh, "Electrodeposited lead dioxide coatings," *Chemical Society Reviews*, vol. 40, no. 7, pp. 3879–3894, 2011.

[174] A. Oury, A. Kirchev, Y. Bultel, and E. Chainet, "PbO_2/Pb^{2+} cycling in methanesulfonic acid and mechanisms associated for soluble lead-acid flow battery applications," *Electrochimica Acta*, vol. 71, pp. 140–149, 2012.

[175] J. Newman and K. E. Thomas-Alyea, *Electrochemical systems*. John Wiley & Sons, 2012.

[176] V. Vand, "Viscosity of solutions and suspensions. i. theory," *The Journal of Physical Chemistry*, vol. 52, no. 2, pp. 277–299, 1948.

[177] J. Kovacik, "Electrical conductivity of two-phase composite material," *Scripta materialia*, vol. 39, no. 2, pp. 153–157, 1998.

[178] K. Knehr, E. Agar, C. Dennison, A. Kalidindi, and E. Kumbur, "A transient vanadium flow battery model incorporating vanadium crossover and water transport through the membrane," *Journal of The Electrochemical Society*, vol. 159, no. 9, p. A1446, 2012.

[179] S. Wen, R. R. Corderman, F. Seker, A.-P. Zhang, L. Denault, and M. L. Blohm, "Kinetics and initial stages of bismuth telluride electrodeposition," *Journal of the Electrochemical Society*, vol. 153, no. 9, p. C595, 2006.

[180] C. Frantz, N. Stein, Y. Zhang, E. Bouzy, O. Picht, M. Toimil-Molares, and C. Boulanger, "Electrodeposition of bismuth telluride nanowires with controlled composition in polycarbonate membranes," *Electrochimica Acta*, vol. 69, pp. 30–37, 2012.

[181] J. Schoenleber, N. Stein, and C. Boulanger, "Influence of tartaric acid on diffusion coefficients of biiii, sbiii, teiv in aqueous medium: Application of electrodeposition of thermoelectric films," *Journal of Electroanalytical Chemistry*, vol. 724, pp. 111–117, 2014.

[182] T. Luo, S. Abdu, and M. Wessling, "Selectivity of ion exchange membranes: A review," *Journal of membrane science*, vol. 555, pp. 429–454, 2018.

[183] L. F. Arenas, R. P. Boardman, C. Ponce de León, and F. C. Walsh, "X-ray computed micro-tomography of reticulated vitreous carbon," *Carbon*, vol. 135, pp. 85–94, 2018.

[184] J. Le Houx and D. Kramer, "OpenImpala: OPEN source IMage based PArallisable Linear Algebra solver," *SoftwareX*, vol. 15, p. 100729, 2021.

[185] D. W. Green and M. Z. Southard, *Perry's chemical engineers' handbook*. McGraw-Hill Education, 2019.

[186] J. Cook, M. Laubitz, and M. Van der Meer, "Thermal conductivity, electrical resistivity, and thermoelectric power of pb from 260 to 550 k," *Journal of Applied Physics*, vol. 45, no. 2, pp. 510–513, 1974.

[187] W. Mindt, "Electrical properties of electrodeposited pbo2 films," *Journal of The Electrochemical Society*, vol. 116, no. 8, p. 1076, 1969.

[188] J. Le Houx and D. Kramer, "X-ray tomography for lithium ion battery electrode characterisation—a review," *Energy Reports*, vol. 7, pp. 9–14, 2021.

[189] C. A. Schneider, W. S. Rasband, and K. W. Eliceiri, "NIH image to ImageJ: 25 years of image analysis," *Nature methods*, vol. 9, no. 7, pp. 671–675, 2012.

[190] J. Le Houx, M. Osenberg, M. Neumann, J. R. Binder, V. Schmidt, I. Manke, T. Carraro, and D. Kramer, "Effect of tomography resolution on calculation of microstructural properties for lithium ion porous electrodes," *ECS Transactions*, vol. 97, no. 7, p. 255, 2020.

[191] X. Lu, A. Bertei, D. P. Finegan, C. Tan, S. R. Daemi, J. S. Weaving, K. B. O'Regan, T. M. Heenan, G. Hinds, E. Kendrick *et al.*, "3D microstructure design of lithium-ion battery electrodes assisted by x-ray nano-computed tomography and modelling," *Nature communications*, vol. 11, no. 1, pp. 1–13, 2020.

[192] M. Doube, M. M. Kłosowski, I. Arganda-Carreras, F. P. Cordelières, R. P. Dougherty, J. S. Jackson, B. Schmid, J. R. Hutchinson, and S. J. Shefelbine, "BoneJ: free and extensible bone image analysis in ImageJ," *Bone*, vol. 47, no. 6, pp. 1076–1079, 2010.

[193] C. D. Iacovangelo and F. G. Will, "Parametric study of zinc deposition on porous carbon in a flowing electrolyte cell," *Journal of The Electrochemical Society*, vol. 132, no. 4, p. 851, 1985.

[194] G. Tomazic and M. Skyllas-Kazacos, *Chapter 17 - Redox Flow Batteries*. Amsterdam: Elsevier, 2015, pp. 309–336. [Online]. Available: https://www.sciencedirect.com/science/article/pii/B9780444626165000176

[195] A. Masliy, N. Poddubny, A. Z. Medvedev, and V. Lukyanov, "Analysis of the distribution of geometrical current density along the direction of solution flow inside flow-by porous electrodes," *Journal of Electroanalytical Chemistry*, vol. 757, pp. 128–136, 2015.

[196] Y. Qi, T. Jang, V. Ramadesigan, D. T. Schwartz, and V. R. Subramanian, "Is there a benefit in employing graded electrodes for lithium-ion batteries?" *Journal of The Electrochemical Society*, vol. 164, no. 13, p. A3196, 2017.

[197] L. Lu, J. Pan, and D. Zhu, "Quality requirements of iron ore for iron production," in *Iron Ore*. Elsevier, 2015, pp. 475–504.

[198] S. Fassbender, D. Dreisinger, and Z. Wu, "Recovering lead from a mixed oxidized material," US Patent 9 322 104B2, 2016.

[199] A. Czerwiński and M. Żelazowska, “Electrochemical behavior of lead deposited on reticulated vitreous carbon,” *Journal of Electroanalytical Chemistry*, vol. 410, no. 1, pp. 55–60, 1996.

[200] A. Czerwiński and M. Żelazowska, “Electrochemical behavior of lead dioxide deposited on reticulated vitreous carbon (rvc),” *Journal of Power Sources*, vol. 64, no. 1–2, pp. 29–34, 1997.

[201] M. Schlesinger and M. Paunovic, *Modern electroplating*. John Wiley & Sons, 2011, vol. 55.

[202] J. F. Peters, A. Peña Cruz, and M. Weil, “Exploring the economic potential of sodium-ion batteries,” *Batteries*, vol. 5, no. 1, p. 10, 2019.

[203] Bloomberg. (2019) XAU-GBP x-rate. (Accessed: 29/05/2019). [Online]. Available: https://www.bloomberg.com/quote/XAUGBP:CUR

[204] C. Minke and T. Turek, “Economics of vanadium redox flow battery membranes,” *Journal of Power Sources*, vol. 286, pp. 247–257, 2015.